University of Nevada, Reno

Hydrothermal Footprint of Carlin-type Gold Deposits at the District Scale: Jerritt Canyon Mining District, Elko County, Nevada

A thesis submitted in partial fulfillment of the

requirements for the degree of Master of Science in

Geology

by

Lucia Maria Patterson

Dr. John L. Muntean/Thesis Advisor

May 2009

THE GRADUATE SCHOOL

University of Nevada, Reno
Statewide • Worldwide

We recommend that the thesis
prepared under our supervision by

LUCIA MARIA PATTERSON

entitled

**Hydrothermal Footprint Of Carlin-Type Gold Deposits At The District Scale:
Jerritt Canyon Mining District, Elko County, Nevada**

be accepted in partial fulfillment of the
requirements for the degree of

MASTER OF SCIENCE

John L. Muntean Ph. D., Advisor

Tommy B. Thompson, Ph. D., Committee Member

Jill S. Heaton, Ph. D., Graduate School Representative

Marsha H. Read, Ph. D., Associate Dean, Graduate School

May, 2009

Abstract

Carlin-type gold deposits in Nevada are among the leading gold producing deposits in the United States and constitute 8% of world production, making the United States one of the leading gold producing countries in the world. The Jerritt Canyon district, located in northeastern Nevada, hosts several Carlin-type deposits and has produced over 7 million ounces of gold.

Many studies have been completed documenting the hydrothermal footprint of Carlin-type deposits at the deposit scale. However, maps depicting the hydrothermal footprint of a Carlin-type deposit at the district scale are lacking. The extent of the hydrothermal footprint of Carlin-type deposits is unclear. Maps depicting hydrothermal products such as alteration, veining, geochemistry, and isotopic data are regularly used in epithermal and porphyry deposits as they commonly form distinct patterns around ore. Maps depicting the hydrothermal footprint of Carlin-type deposits could be used in a similar fashion for exploration and could improve the existing model for these deposit types.

In 2000, Anglo Gold collected a data set consisting of multielement analyses from 6,416 drill holes, from one stratigraphic interval at the bottom 5 feet of the Roberts Mountains Formation, directly above the Saval Discontinuity in the Jerritt Canyon district. The lithology along the base of the Roberts Mountains Formation is predominantly calcareous siltstones; thus, the data set eliminates the effect that variable lithology may have on a hydrothermal footprint. Mapping and core-logging completed during this study are consistent with the interpretation that the Saval discontinuity is a subaerial paleokarst that has been locally structurally activated. In addition, Yukon-

Nevada Gold supplied their data set which consisted of previously logged geology corresponding to the Anglo Gold data set. A sub-set of holes were re-logged to document and obtain data on the Saval discontinuity, and to generate maps depicting patterns of alteration, veining, mineralization, carbonate isotopes, and clay distribution with respect to known mineralization. The geochemical data set was analyzed visually and statistically to document associations between gold and other elements.

Analysis of the geochemical data set has defined two groups of elements. The first group, which consists of gold, arsenic, mercury, thallium, and tellurium, is the elemental suite most closely associated with the Carlin-type gold mineralization. The Carlin-type elements are spatially and statistically associated with each other and are elevated within and outboard of the vertical projection of known gold deposits. The second group is composed of elements common in black shales and consists of two subgroups. The first subgroup consists of uranium, phosphorous, lanthanum, and gallium; and the second group is comprised of zinc, uranium, molybdenum, vanadium, nickel, copper, cadmium, and silver. The black shale elements are statistically and spatially associated with each other and do not exhibit any relationship with the Carlin-type elements.

Re-logged geology, previously logged geology, and XRD analysis all indicate that silicified and decarbonatized rock, along with quartz veining are localized in areas within or near the vertical projection of the gold deposits. $\delta^{18}O$ values from rock carbonate are depleted within and around the vertical projections of the gold deposits, whereas $\delta^{13}C$ values show no pattern with respect to mineralization. Ferroan dolomite and ankerite

identified by carbonate staining and XRD analysis exhibit the most continuous halo to mineralized areas.

The key findings from this study were identification of major centers of fracture controlled fluid upwelling responsible for Carlin-type mineralization, a pre-ore black shale elemental signature, and a suite of vectoring tools which could aid in the exploration of Carlin-type deposits. The major center of upwelling fluids appears to be under the Steer/Saval/SSX area as evidenced by pervasive elevated values of the Carlin-type elements and depletions in $\delta^{18}O$ values. The pervasive, spotty or irregular distribution of the Carlin-type elements and, especially, logged alteration features, in and around the deposits at Jerritt Canyon, suggests complex fracture control of the hydrothermal fluids. The group one black shale elemental signature (P, U, La, Ga) reflects formation of apatite by upwelling oceanic waters during a transgressive cycle. However, the group two black shale signature most likely originated from the migration of basinal brines and petroleum under conditions similar to MVT deposits. Previous petrographic work has documented an intimate association between potential iron bearing dolomite and MVT mineralization indicating that the basinal brine responsible for MVT mineralization would have also been capable of producing ferroan dolomite, which would have been a critical rock preparation event for later Carlin-type mineralization. The most important exploration tools to come out of this study are the identification of halos of ferroan dolomite, depleted $\delta^{18}O$ values in rock carbonate, and continuous, elevated, arsenic, mercury, thallium, and to a lesser extent, tellurium concentrations around the vertical projection of the gold deposits and the zone of gold values greater than 300 ppb along the Saval.

Acknowledgements

Table of Contents

List of Tables

List of Figures

Introduction

Carlin-type gold deposits are epigenetic, disseminated auriferous pyrite deposits characterized by carbonate dissolution, argillization, and silicification of mainly sedimentary rocks (Hofstra and Cline, 2000; Cline *et al*. 2005). Current production from Carlin-type deposits dominates gold production in the country and constitutes 8% of world production, making the United States one of the leading gold-producing countries in the world (Nevada Bureau of Mines and Geology, 2007).

The principal exploration targeting tools utilized to delineate Carlin-type deposits to date are recognition of structure, geochemical pathfinder elements, alteration, and lithology. Most Carlin-type deposits have been discovered by recognition of structural windows through thrust faults, which are interpreted to have acted as aquitards at regional and possibly local scales, and by recognition of high-angle structural culminations. However, geochemical anomalies of Carlin-type pathfinder elements such as arsenic, mercury, thallium, tellurium, antimony, gold, and locally silver, have also led to the discovery of many Carlin-type deposits (e.g., Wells *et al*., 1969; Birak and Hawkins, 1985; Bettles, 2002). Many deposits have also been discovered by the recognition of jasperiod outcrops, which is a common alteration phase in Carlin-type deposits (Ilchik, 1990; Harlan *et al*., 2002; Dobak *et al*., 2002). Though these tools have been successful in the discovery of many Carlin-type deposits, especially of deposits exposed at the surface, most deposits in the future will likely have to be discovered underneath cover. Development of additional exploration tools and improved genetic models for Carlin-type deposits are necessary to improve the efficiency in exploring for these blind deposits.

In order to effectively explore, it is important to know the extent of the hydrothermal system of the targeted deposit type. Documentation of visible and cryptic attributes of hydrothermal systems such as alteration, veining, carbonate staining, apatite fission-tracks, isotopic signatures, clay mineralogy, and trace elements are common methods of defining hydrothermal footprints. The lateral and vertical extent of these attributes away from ore can vary from a few feet to possibly a few miles, and understanding the extents and patterns of these attributes can be valuable tools when trying to vector into a deposit, either laterally or vertically. For example, zoning patterns in alteration and trace elements are widely used in exploration of other deposit types, namely porphyry and epithermal deposits, but have not nearly been as successfully applied in the exploration for Carlin-type deposits.

The hydrothermal extent of Carlin-type deposits, especially at the district scale, is not well documented. A significant amount of research is underway to document alteration and geochemical patterns within and outboard of Carlin-type deposits. Vertical and lateral trace element zoning patterns between gold and associated trace elements have been documented most recently by Heitt *et al*. (2003). Correlations between gold and clay minerals in Carlin-type hydrothermal systems have been documented by Kuehn and Rose (1992), Cail and Cline (2001), and Heitt *et al*. (2003). Depletion halos in the $\delta^{18}O$ values of carbonate around known Carlin-type gold deposits were demonstrated by Stenger *et al*. (1998), and Arehart and Donelick (2006). Eocene partial annealing of apatite fission-tracks in areas of Carlin-type mineralization has been documented by Chakurian *et al*. (2003), Cline *et al*., (2005), and Arehart and Donelick (2006).

Though these studies are critical to understanding the hydrothermal footprint of Carlin-type deposits, most have been done at the scale of individual deposits. There have been few studies at the district scale and, to my knowledge; no integrated studies have been published that show district-scale maps of geochemistry, alteration, mineralogy, and isotopes. It is important to step out from localized areas of study to potentially illustrate the characteristics of hydrothermal systems at a larger or district scale. District-scale data sets could have many scientific implications. For example, multiple zones of $\delta^{18}O$ depletion in carbonates could indicate multiple zones of upwelling hydrothermal fluids rather than significant lateral fluid flow. District-scale assessment of hydrothermal systems may indicate subtle features which could have controlled where the gold was deposited and would help to find other districts with potential for Carlin-type deposits.

The Jerritt Canyon district in northeastern Nevada contains several Carlin-type deposits within an area of approximately 100 square miles (Fig. 1). The total gold endowment of the district is nearly 10 million ounces (Jones, 2005). In 2000, Anglo Gold Corporation, then the operator of the Jerritt Canyon mine, collected a data set consisting of multielement geochemical analyses of 6,416 drill samples collected from 5-foot intervals, in a single stratigraphic unit and lithology (calcareous siltstone), at the base of the Roberts Mountains Formation, directly above the Saval discontinuity (Fig. 2). The Saval discontinuity marks the contact with the underlying Hanson Creek Formation (Fig. 2). Rocks along the Saval discontinuity are commonly altered and anomalous in trace elements, suggesting that it once served as an aquifer and played a key role with respect to fluid flow. This data set eliminates the effect of variable lithologies allowing for a more defined picture of the hydrothermal footprint of the Carlin-type deposits at Jerritt

Canyon. Furthermore, Jerritt Canyon is an ideal location, because, unlike many other districts which host Carlin-type deposits, there are no Mesozoic intrusions and associated hydrothermal alteration and mineralization that would interfere with the hydrothermal alteration, trace elements, and geochemical signature of the Carlin-type mineralization.

Yukon-Nevada Gold, the current operator of the Jerritt Canyon mine, supplied its drill-hole database, from which logged geological data were queried from the same 5 foot intervals of the 6,416 drill holes from which Anglo Gold collected the trace element data. These data, in combination with new data collected during this study, were used to generate maps documenting patterns of trace elements, hydrothermal alteration, veining, mineralogy, and isotopes in the northern half of the Jerritt Canyon district. The map patterns were then analyzed to develop exploration targeting tools and to gain insights into the history and hydrology of hydrothermal activity in the district.

Research for this project focused on the multi-element dataset, preexisting logged geology, and generating an internally consistent logging data base. Anglo-Gold's data set was combined with Yukon-Nevada Gold's logging data base to look at elemental patterns with respect to previously logged geology. A sub-set of 247 core and rotary drill holes in the northern half of the Jerritt Canyon district, were re-logged to generate an internally consistent data set. Logging included documentation of alteration, lithology, veining, mineralization, and the staining characteristics of carbonate. SEM analyses were completed to verify and document minerals and alteration types identified during logging. In addition, logging, as well as surface mapping of selected localities, focused on documenting the characteristics of the Saval Discontinuity. Carbon and oxygen isotope data were collected on carbonates from 179 of the 247 holes. X-ray diffraction analyses

were also completed on the pulps from 297 chip and core holes, which include most of the 247 logged holes. Patterns are evident from trace elements, veining, alteration, isotopes, XRD, and carbonate staining that could be efficient vectoring tools, and have yielded new information with respect to the mineralization history in the Jerritt Canyon district as detailed below.
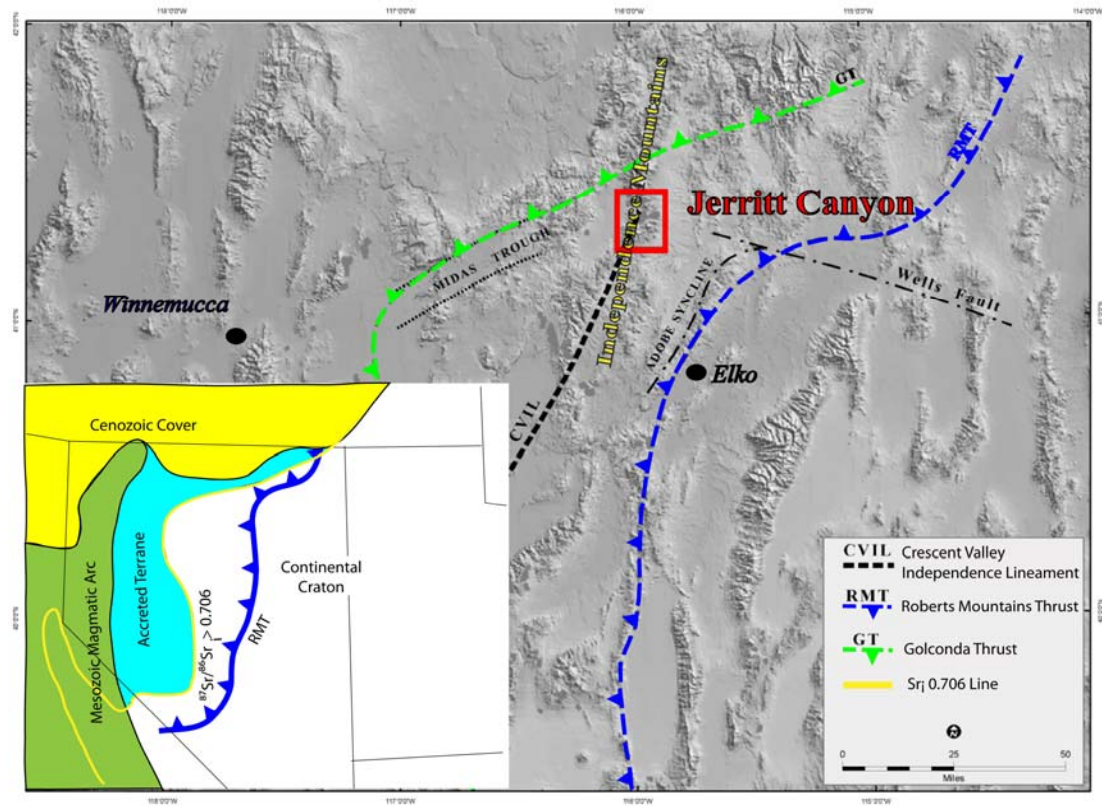
Figure 1: Location map of the Jerritt Canyon district in relation to the Sr_i 0.706 line, the Roberts Mountains thrust, the Golconda thrust and Crescent Valley Independence lineament. Modified from Eliason and Wilton (2005).
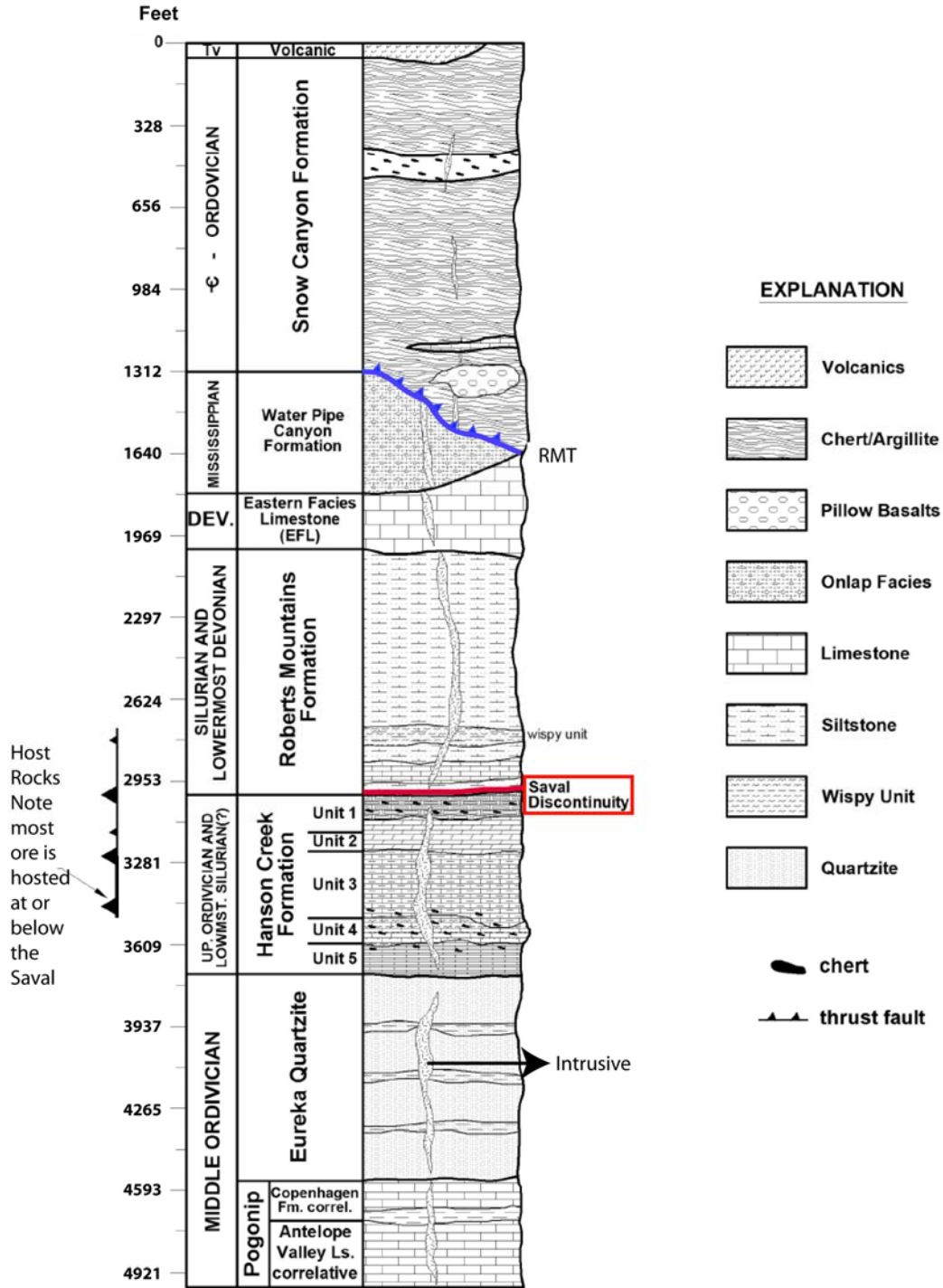
Figure 2: Jerritt Canyon stratigraphic section. Location of the sample interval for Anglo Gold data set highlighted in red, and the Roberts Mountains thrust (RMT) is highlighted in blue. Modified from Eliason and Wilton (2005).

District History

The Jerritt Canyon district is located in northeastern Nevada, 45 miles northeast of Elko in the Independence Mountains (Fig. 1). Historic exploration activity in the Jerritt Canyon district was concentrated on antimony with minimal production during the early 1900's (Lawrence, 1963). The discovery of gold mineralization in the district was preceded by an antimony exploration program initiated by FMC Inc. in 1971 (Birak and Hawkins, 1985). The initial gold discovery in the district was made in 1973 when geologists recognized similarities between the geology of the Jerritt Canyon area and the nearby Carlin gold deposit (Hawkins, 1982). Mapping, sampling, and geochemical analysis led to the discovery of a gold anomaly along the north fork of Jerritt Creek (Birak and Hawkins, 1985). A joint-venture agreement in 1976 between Freeport Exploration Co. and FMC led to an expanded mapping, sampling and drilling program that resulted in the delineation of several deposits and commencement of production in 1981 (Birak and Hawkins, 1985). Several companies have managed the Jerritt Canyon mine since Freeport including Independence Mining Company (1990-1999), Anglo Gold (1999-2003), Queenstake Resources (2003-2007), and currently Yukon-Nevada Gold Corporation.

To date, Jerritt Canyon has produced over seven million ounces of gold. Annual production has been mainly between 170,000 ounces and 350,000 ounces of gold (Nevada Bureau of Mines and Geology, 2007). Proven and probable reserves currently stand at 3.1552 million tons at 0.227 opt gold (Nevada Bureau of Mines and Geology, 2007).

Regional Geology

During active rifting of the continental margin, clastic sediments were deposited, burying the Precambrian crystalline basement (Stewart, 1972; Poole *et al*., 1992). Following active rifting, a sequence of dominantly miogeosynclinal carbonates were deposited on the shelf; silty carbonate rocks were deposited on the slope; and eugeosynclinal siliciclastic and volcanic rocks were deposited on oceanic rock to the west. The approximate location of the buried margin has been suggested to be best represented by the Sr_i 0.706 line defined by Farmer and Depaolo (1983) and Kistler and Peterman (1973) (Fig. 1).

The late Devonian and early Mississippian Antler Orogeny juxtaposed eugeosynclinal sediments eastward over miogeosynclinal sediments along the Roberts Mountains Thrust (Roberts *et al*., 1958; Stewart, 1980). Loading from the Antler allochthon on the miogeosynclinal sediments totaled several kilometers, and created a foredeep basin east of the Antler highland (Miller *et al*., 1992). Early Mississippian and Pennsylvanian synorogenic and postorogenic sediments respectively filled the foredeep basin (Poole *et al*., 1992). Intermittent extensional and shortening events, commonly referred to as the Humboldt orogeny (Ketner, 1977; Theodore *et al*., 2004), occurred from the Mississippian to the Permian, culminating in the late Permian-early Triassic Sonoma Orogeny. The Sonoma Orogeny thrust eugeoclinal sediments eastward over the Roberts Mountains allochthon along the Golconda thrust (Silberling and Roberts, 1962; Silberling 1975).

During the late Triassic an Andean-type margin was established on the western margin of North American. Several additional orogenies occurred in the Mesozoic.

From oldest to youngest, these include the Nevadan, Elko, and Sevier orogenies. Significant intrusive activity in Nevada began in the Jurassic and continued until the late Cretaceous at which time magmatism ceased due to shallow subduction of the Farallon plate, which resulted in the Laramide orogeny to the east in the Rocky Mountains and attendant crustal thickening and uplift in eastern Nevada (cf. Cline *et al.*, 2005). Renewed calc-alkaline magmatism and associated extension began in the Eocene, which was associated with removal or rollback of the Farallon plate, and swept southward through northeastern Nevada between about 45 and 35 Ma. (Humphreys, 1995; Jones *et al.*, 1998; Liu and Shen, 1998; Rahl *et al.*, 2002; Breitsprecher *et al.*, 2003; Humphreys *et al.*, 2003). The extensional tectonics began to break up high-elevation, low-relief terrain that was covered by many large shallow lakes that had developed in northeastern Nevada during the Cretaceous and early Tertiary (Hofstra and Cline, 2000). Fluvial-alluvial and lacustrine sediments, ash-flow tuffs, lavas, and volcaniclastic rocks filled broad depressions developed during this time (Cline *et al.*, 2005).

At about 17 Ma the extensional style throughout Nevada changed (Stewart, 1980; Zoback *et al.*, 1981), resulting in the basins and ranges seen today. Since this time bimodal basalt-rhyolite magmatism associated with basin and range extension, has been predominant throughout much of north-central and northeastern Nevada (Christiansen and Lipman, 1972). Local low-sulfidation epithermal gold-silver-mercury mineralization accompanied this bimodal magmatism in northeastern Nevada (John, 2001).

District Geology

The geology of the Jerritt Canyon district has been presented in several publications (i.e., Kerr, 1962; Birak and Hawkins, 1985; Daly, 1991; Hofstra, 1994;

Wilton, 2004; Muntean and Henry, 2007). The district is about 100 km west of the leading edge of the Roberts Mountains thrust (Fig. 1). Paleozoic stratigraphy is characterized by eugeosynclinal (upper plate) rocks that have been thrust eastward over the miogeosynclinal (lower plate) rocks along the Roberts Mountains Thrust produced during the Antler orogeny (Figs. 1, 2, & 3).

Lower Plate Rocks

The lower plate rocks consist of Ordovician and Silurian siltstone, limestone, chert, and quartzite. The oldest lower plate rocks exposed in the Jerritt Canyon district are part of the Ordovician Pogonip Group, which consists of dark gray, commonly fossiliferous limestone, calcareous shales, and lesser amounts of dolomite. Overlying the Pogonip Group is the Ordovician Eureka Quartzite which is one of the major cliff-forming units in the district (Fig. 2). The Eureka Quartzite is a medium-grained, light gray to white, massive quartzite. Overlying the Eureka Quartzite is the main host rock of the district, which is the Silurian to Ordovician Hanson Creek Formation (SOhc). It has a maximum thickness of about 750 feet and is divided informally into five units (Fig. 2). The lowermost unit, Unit 5 ($SOhc_5$), is 15-100 feet thick and consists of chert, limestone, and laminated calcareous siltstones. Unit 4 ($SOhc_4$), which averages about 250 feet in thickness, is a carbonaceous, medium to coarse-grained limestone, commonly with pods and lenses of black chert. Unit 3 ($SOhc_3$) is up to 300 feet thick and consists of interbedded carbonaceous micritic limestone and argillaceous dolomitic limestone. It hosts much of the ore in the district, and commonly does not crop out. Unit 2 ($SOhc_2$) is a light gray limestone, up to 100 feet thick, and is commonly fossiliferous and dolomitized. It is comprised of thick- bedded, fine-grained limestone, thin-bedded to

nodular limestone, oolitic limestone, and wavy laminated limestone. Unit 1 (SOhc$_1$), is the uppermost unit of the Hanson Creek Formation and is a 10 to 130 feet thick sequence of rhythmically interbedded black chert and carbonaceous limestone. Bedding thickness averages 5 cm. SOhc$_1$ is a common cliff-former due to pervasive silicification. The Roberts Mountains Formation (DSrm), of Silurian to Devonian age, unconformably overlies the SOhc (Fig. 2). The unconformity separating the Roberts Mountains and Hanson Creek formations is locally referred to as the Saval discontinuity as mentioned above (Fig. 2). The lower parts of the DSrm host significant ore in the district. It is predominantly a laminated, calcareous to dolomitic, carbonaceous siltstone. A 30-50 foot thick laminated to thin-bedded silty limestone commonly occurs near the base. Thickness of the entire Roberts Mountains section is not known due to structural thickening and thinning, but it is at least 325 feet thick and may be greater than 670 feet thick in some places. A detailed description of the bottommost 5 foot of the DSrm, the focus of much of this study, will be discussed below.
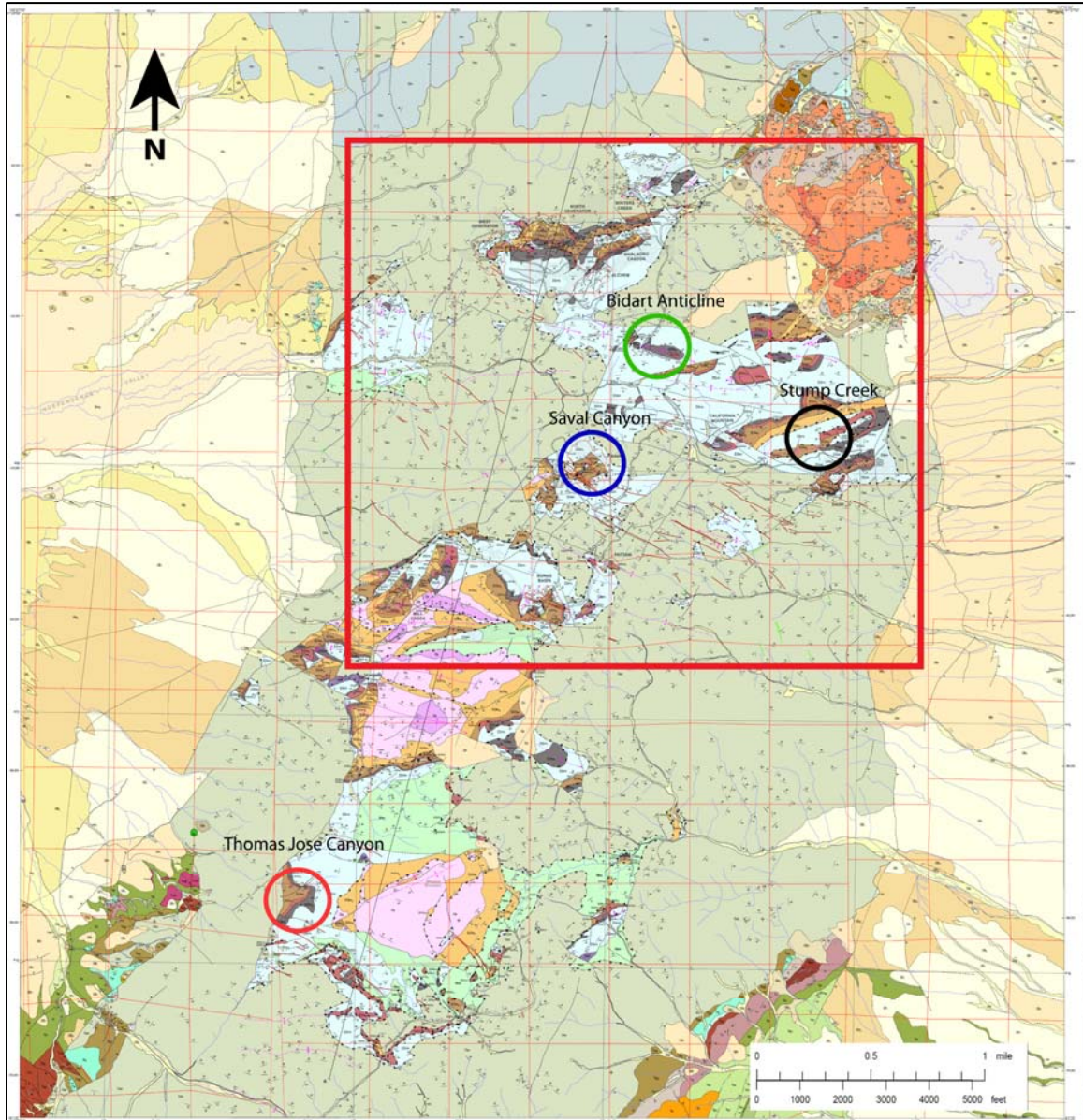
Figure 3: Geologic map of the Jerritt Canyon district taken from Muntean and Henry (2007). Circles indicate the surface areas that were mapped for this project. The red box encloses the study area for this project. In general, light blue is the DSrm, maroon-yellow-brown-gray is the SOhc, shades of green are upper plate rocks, orange is Tertiary volcanic rocks, and yellow-tan Quaternary sediments. The maroon lines generally trending west-northwest are mostly Pennsylvanian dikes.

Locally, overlying unconformably the Roberts Mountains Formation is a Mississippian foredeep sequence called the Water Pipe Canyon Formation (Fig. 2). The Water Pipe

Canyon Formation consists of basal greywacke with interbedded carbonaceous shale, chert pebble conglomerate, and bedded chert. The upper part is argillaceous sandstone interbedded with quartz siltstone and fine-grained greywacke. The Waterpipe Formation attains a maximum thickness of about 330 m. Peters *et al*. (2003) identified Mississippian radiolarians from the Water Pipe Canyon Formation. Locally in the Jerritt Canyon district, a Devonian limestone is found between the Roberts Mountains and Water Pipe Canyon formations.

Upper Plate Rocks

Upper plate rocks in the Jerritt Canyon district include the Snow Canyon Formation and McAfee Quartzite. The Snow Canyon formation consists of a basal sequence of limestone, chert, and greenstone (metabasalt), a middle unit of chert, argillite, siltstone, shale, local bedded barite, and an upper unit of primarily poorly bedded turbiditic quartzite (Fig. 2). The thickness of the Snow Canyon Formation is about 370 m thick but may achieve a maximum thickness of 600 to 700 m. The McAfee Quartzite is a fine-grained, white to light gray, cliff-forming massive quartzite with minor shale and chert. The McAfee Quartzite appears to conformably overlie the Snow Canyon Formation. Maximum thickness of this unit is about 1080 m. Based on published age data, the formations are considered to be late Cambrian to Ordovician in age. However, ongoing work, which has demonstrated ages as young as upper Devonian (P. Noble, personal communication, 2007), is showing that the upper plate rocks at Jerritt Canyon are even more complex than originally thought.

Igneous Rocks

Dikes in the Jerritt Canyon district have been placed into four age-composition groups, as most recently described by Eliason and Wilton (2005). The first group consists of Early Pennsylvanian dikes. The dikes are basaltic in composition, intrude west-northwesterly trending structures, cut all stratigraphic units within the upper plate and lower plate rocks, cut imbricated sections, are strongly altered, and commonly host gold mineralization. The basalt dikes have been dated using the K-Ar on biotite concentrates, the K-Ar and $^{40}Ar/^{39}Ar$, which yielded dates ranging from 318 to 325 Ma (Hofstra, 1994; Phinisey, 1995; Hofstra *et al.*, 1999). The second group consists of Eocene basalt dikes, from which $^{40}Ar/^{39}Ar$ dates were obtained on plagioclase separates and whole rock samples, which yielded age dates of 40.8 ± 0.1 Ma (Hofstra, 1994; Phinisey *et al.*, 1996; Folger *et al.*, 1996; Hofstra *et al.*, 1999). The third group consists of Eocene quartz monzonite dikes which have been dated at 39.2 ± 0.1, 39.9 ± 2.3, and 43.7 ± 2.6 Ma using the $^{40}Ar/^{39}Ar$ and K-Ar on hornblende concentrates and the $^{40}Ar/^{39}Ar$ on zeolites (Phinisey *et al.*, 1996; Hofstra, 1994). The Eocene dikes have northeast trends and are not found in west-northwest trending structures. They locally are altered and mineralized. The final group consists of a Miocene basalt dike intersected near Burns Creek from which $^{40}Ar/^{39}Ar$ dates on plagioclase yielded an age of 17.2 ± 0.8 Ma (Hofstra, unpublished report, 1999). The Miocene basalt dikes are unmineralized and unaltered (Eliason and Wilton, 2005).

Tertiary rock units unconformably overlie the Paleozoic rocks along the flanks of the range on the northeast, southeast, and southwest sides of the Jerritt Canyon district (Fig. 3; Muntean and Henry, 2007). The oldest Tertiary rocks are Eocene sedimentary

rocks, which have been broken into two units. A lower conglomerate consists of poorly exposed, poorly indurated boulder to pebble chert-quartzite or quartzite conglomerate with a sandy or muddy matrix. Overlying the lower conglomerate is the early tuff which is a poorly-non-welded porphyritic ash-flow tuff containing 10% crystal fragments of mostly altered feldspar and lesser biotite and quartz, with local interbeds of conglomerate. Above the early tuff is a cream to light gray finely laminated micritic Eocene limestone that overlies and is locally interbedded with the upper part of the lower conglomerate and contains ostracods, oolites, gastropods, and reed fragments. Finally, the youngest of the sedimentary rock sequence is very finely laminated "paper" shale-calcareous shale with sandstone channels and leaf impressions of metasequoia. Volcanic rocks overlie the Eocene sedimentary rocks. In the area known locally as the Millsite Volcanics at the northeastern end of the Jerritt Canyon district, the volcanic rocks are predominantly rhyolite tuffs with dacite tuffs and lavas. The Eocene volcanic unit is the Eocene Rhyolite tuff that is a densely welded, low-high silica dacite ash-flow tuff, with a basal vitrophyre, 25-30% crystal fragments that are dominantly plagioclase and lesser biotite, with minor hornblende, clinopyroxene, orthopyroxene, and magnetite. The Eocene dacite tuffs and lavas are abundantly porphyritic and makes up most of the rock of the Mill Site Volcanics. Crystal fragments of plagioclase, hornblende, biotite, orthopyroxene, clinopyroxene, and magnetite make up 30-50% of the rock. The dacite tuff and lava have been dated as being 40.4 ± 0.1 Ma, and 40.6 ± 0.2 Ma using $^{40}Ar/^{39}Ar$ on hornblende and biotite, respectively (Hofstra, 1994). The pre-volcanic sedimentary rocks and the volcanic rocks are not mineralized.

Structure

The structure of the Jerritt Canyon district is characterized by multiple episodes of thrusting, folding, and high angle faulting and has been described by Birak and Hawkins (1985), Daly (1991), Hofstra (1994); Peters *et al*., (2003), Wilton (2004); and Eliason and Wilton (2005). While absolute ages cannot be given to many of the structures observed in the district, ages have been constrained using cross-cutting relationships observed between dikes, faults, and folds as will be discussed below.

Lower plate stratigraphy is commonly imbricated and locally interleaved with thin slices of the upper plate Snow Canyon Formation. High-angle faults also have complicated histories and show evidence for normal, strike-slip and reverse faulting. They have geometries consistent with inversion of original normal faults (Muntean *et al*., 2007). The Antler orogeny is manifested in Jerritt Canyon by the juxtaposition of the Ordovician Snow Canyon Formation over Ordovician to Mississippian lower plate rocks along the Roberts Mountains Thrust as described above (Fig. 2).

Based on the geology of areas surrounding Jerritt Canyon district this area probably has experienced deformation from the Sonoma, Nevadan, and Sevier orogenies. Evidence for the Sonoma orogeny is present just north of the Jerritt Canyon district, where rocks of the Golconda allochthon are thrust over a Devonian to Permian overlap sequence that overlies the Roberts Mountain Allochthon and lower plate rocks. Just east of the Independence Mountains is the Adobe syncline which is thought to have formed in the hinterland of the Sevier orogeny (Fig. 1).

Despite the fact that there is structural evidence for the Sonoma, Nevadan, and Sevier orogenies in close proximity to Jerritt Canyon the folds present in the Jerritt

Canyon district are interpreted as being older than 321 Ma, as Pennsylvanian dikes were intruded along west-northwesterly trending high-angle faults that cut folds, all interpreted thrust faults, and repeated sections through out the district (Fig. 2) (Hofstra *et al.*, 1999; Hofstra, 1994; Phinisey, 1995). The fact that the dikes are near vertical in most cases indicates that most of the deformation present in the Jerritt Canyon district can be attributed to the Antler orogeny (Hofstra, 1994).

Post-ore structures are mainly related to basin and range extension. In general basin and range faults trend north-south and displace orebodies, dikes, and volcanics. Range-front faults are the largest extensional structures in the area exhibiting displacement from basin and range faulting.

Ore Bodies

Ore bodies in the Jerritt Canyon district occupy many of the pre-Tertiary high and low-angle structures, including both extensional and compressional structures. They are also found in imbricated sections. Extensional structures, where mineralization is localized, could be due to incipient extension in the Eocene shortly before the Carlin-mineralizing event.

Gold mineralization at Jerritt Canyon has been described by many workers (Birak and Hawkins, 1985; Daly *et al.*, 1991; Bratland, 1991; Hofstra, 1994; Phinisey *et al.*, 1996; Dewitt, 1999; Hofstra *et al.*, 1999; Hutcherson, 2002; Wilton, 2004). Gold deposits were first found in lower plate windows, where orebodies are hosted mainly by the Hanson Creek and Roberts Mountains formations, and in Pennsylvanian and Eocene-aged dikes (Figs. 2 & 3). In the last 18 years, deposits have been found in lower plate rocks covered by upper plate rocks. The deposits tend to be tabular in morphology, but

are commonly highly irregular. Deposit geometry is controlled by intersections of favorable lithologies with a complex array of structures. The highest grades and largest deposits occur where west-northwest-trending high-angle faults, dikes, and fold structures intersect northeast-striking, high-angle faults in combination with favorable lithologies. In nearly all cases the ore is refractory (due to carbon and pyrite), although oxidized supergene ore zones were present in the Alchem, California Mountain, and Marlboro Canyon deposits. The age of the gold deposits has been constrained to be younger than 40.8 Ma due to the fact that the Pennsylvanian andesite dikes and the Eocene basalt dikes are mineralized but the 17.8 Ma basalt dike is not mineralized (Eliason and Wilton, 2005).

The Saval Discontinuity

As described above, the Saval discontinuity marks the contact between the DSrm and underlying SOhc (Fig. 2). Missing sections of SOhc are common below the Saval. The DSrm is commonly found in direct contact with $SOhc_2$, $SOhc_3$, or $SOhc_4$. It is also common to see, significant variation in the thickness of units below the Saval. The Saval discontinuity has been interpreted as a low-angle structural feature (Bratland, 1991; Eliason and Wilton, 2005), a tectonically activated disconformity (Daly *et al*., 1991), and an erosional karsted disconformity (Peters *et al*., 2003).

Rocks along the Saval are commonly altered and anomalous in trace elements, suggesting it once served as a paleo-aquifer. Silicification of the $SOhc_1$ underneath the Saval is very common. Hofstra (1994) identified 17 stages of quartz in the jasperiod of $SOhc_1$ and summarized them into three silicification events:

1. Event 1: Formed prior to gold mineralization by remobilization of silica from chert beds in $SOhc_1$ during diagenesis. Considered to be is regional extent.

2. Event 2: Formed during gold mineralization. It is volumetrically smaller than event 1, is not directly associated with stratigraphy, is well developed in chert-poor and chert-bearing units of SOhc and DSrm, and is found in the vicinity of ore zones near high-angle faults, thrust faults, and fault intersections.

3. Event 3: Formed after gold mineralization, is widespread through out Jerritt Canyon but is volumetrically very small, and consists of several stages of drusy quartz, along with euhedral barite, stibnite, and late calcite.

In this study, the Saval was characterized by mapping five surface exposures of the discontinuity, visiting and noting observations of other surface exposures, and logging its characteristics in core from 67 diamond drill holes and chips from 197 reverse circulation holes. The five areas were mapped at a scale of ~1:2,500 and included Stump Creek, two road-cuts at the Bidart anticline, Thomas Jose Canyon, and Saval Canyon (Fig. 3). Field maps not presented below can be found in Appendix 1. Samples were taken from mapped areas and core that was logged for further characterization of the Saval in hand-sample and thin-section.

The Saval commonly has karst features such as caves and cave fill (Fig. 4). Karst features were observed in all the areas mapped and visited. It is very important to note that no clasts of the DSrm were documented in the breccia that is present at the top of the $SOhc_1$. Observed caves exhibited a wide range of sizes. The smallest caves were documented at Saval Canyon and were typically11 inches long and 6-12 inches high. At Thomas Jose Canyon and Stump Creek the caves were anywhere between 1-20 feet long

and 1-5 feet high (Figs. 4 & 5). The largest cave feature was documented at the Bidart Anticline, with a zone of cave fill that is about 60 feet long and 15-20 feet wide (Fig. 6). The large cave at the Bidart anticline was filled with very finely laminated and very fine-grained silty material interpreted to be cave fill. Angular to subangular clasts, 0.5-6 mm long, were found in the cave fill (Fig. 7). The breccia in Figure 7 exhibited fine laminations and no clast sorting. In thin section the cave fill is dominated by finely laminated, silt-sized, angular to sub-angular quartz with minor calcite, and clay. Minor remnants of cave fill material were also found at Saval Canyon and Stump Creek in the bottom of cave structures.
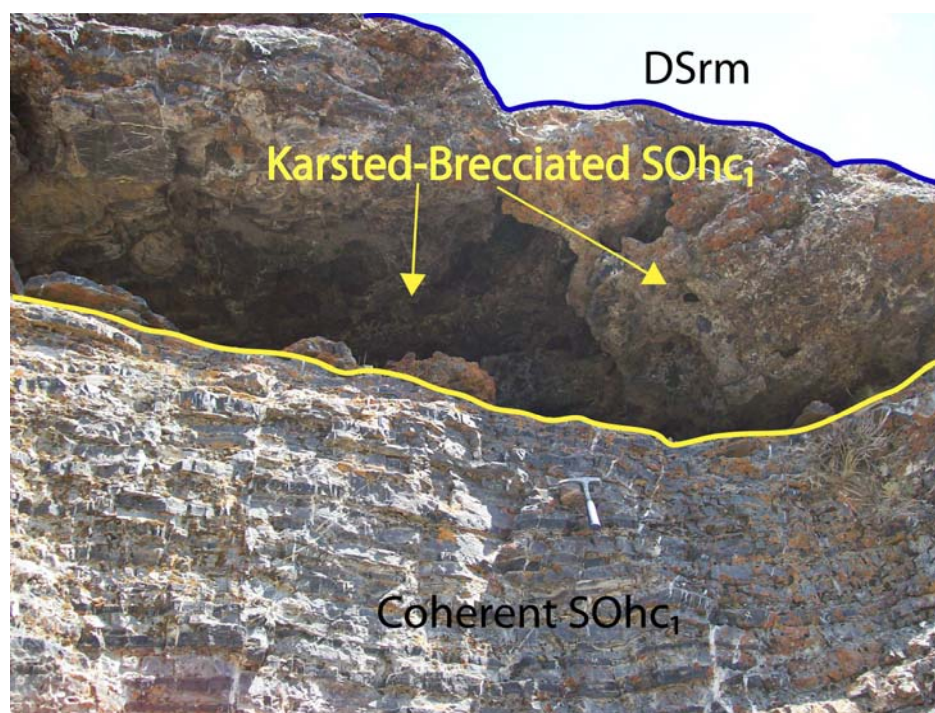
Figure 4: Caves that resulted from karsting at Stump Creek. The DSrm is not shown in the photo but does poorly crop out directly above the cave.
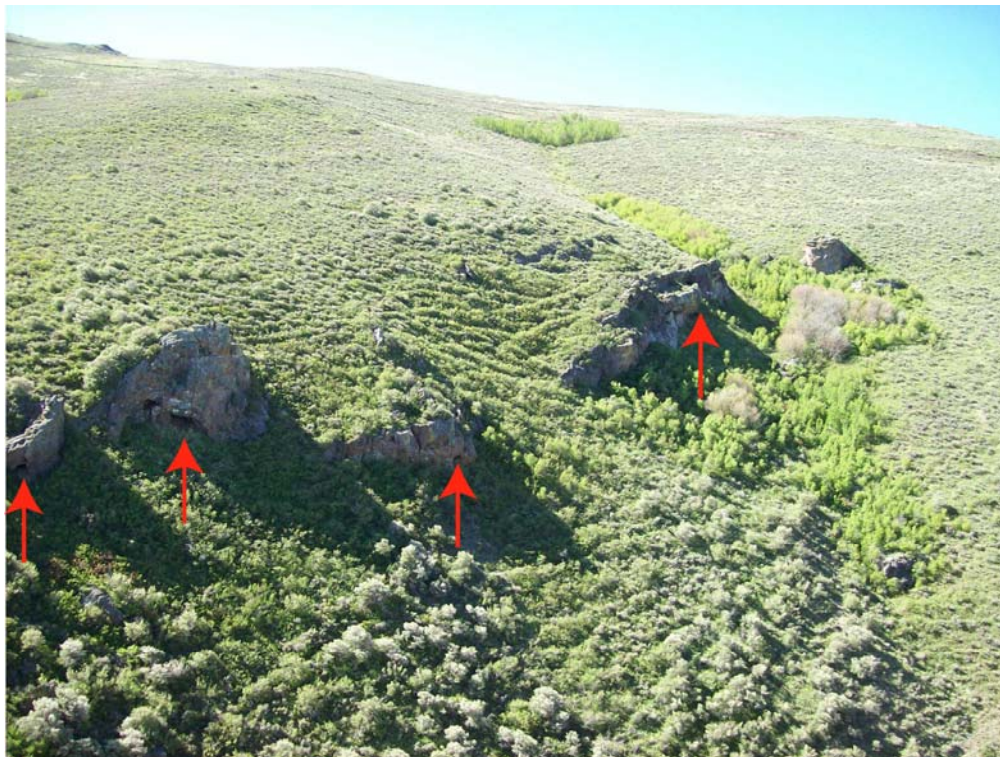
Figure 5: Red arrows point to karsted caves in the SOhc$_1$ as observed at Thomas Jose Canyon.
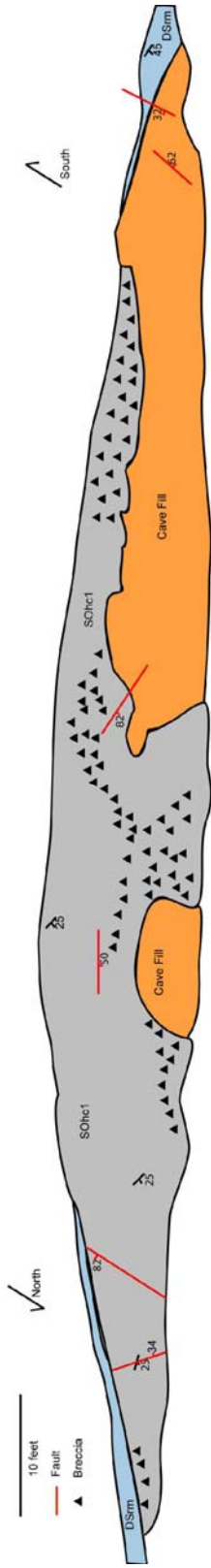
Figure 6: Sketch of road cut geology exposed at the Bidart anticline showing the extent of the caves and cavefill in SOhc$_1$.

Figure 7: Entire picture showing cave fill observed at the Bidart Anticline. Note the black chert clasts directly above the rock hammer

The $SOhc_1$ is commonly brecciated along the Saval. Locally other units of the SOhc are brecciated at this contact, but $SOhc_1$ is more commonly brecciated than any other unit. At Stump Creek, Thomas Jose Canyon, and the Bidart Anticline the uppermost 5-10 feet of the $SOhc_1$ was brecciated with coherent interbedded limestone and chert beneath the brecciated top (Fig. 4). Brecciation in the $SOhc_1$ was documented in 142 out of the 267 drill holes that were logged. It should be noted that brecciation is not easily distinguishable in chip holes; therefore, brecciation in some of the logged reverse circulation hole could have been overlooked. The breccia is mostly monolithic and matrix supported with samples commonly having at least 60 percent matrix material. Most of the clasts that were observed during this study consist of angular to subangular chert that are 0.5 to 3 inches long and derived from the $SOhc_1$ (Fig. 8a). Limestone clasts were observed in only a few places. Features of the matrix are commonly masked by silicification. In thin section the matrix is dominated by fine-grained quartz of replacement origin, or silicified rock that is commonly cross-cut by quartz veins, many of which exhibit open-space growth (Fig. 8b). Commonly, clasts are composed of microcrystalline quartz (chert), which are surrounded by the jigsaw-textured quartz (Fig. 8c). Where the DSrm was found in direct contact with brecciated $SOhc_2$, $SOhc_3$, or $SOhc_4$, structural zones are present and/or intrusions. Therefore, it is inferred that missing section observed during this study is mostly the result of structural processes.

The dominant DSrm lithology type that was encountered in the 5 foot interval of interest to this study was a calcareous siltstone. The calcareous siltstone was very reactive with a 10% solution of hydrochloric acid (HCl). In hand-sample, the rock is finely planar-laminated with alternating layers of silt and lighter colored calcareous

material which was composed mostly of calcite. The layers were on average 1 mm thick. In thin-section the rock is dominated by about 70% calcite with up to 28% subrounded to subangular quartz and 2% illite (Fig. 9). The amount of dolomite present in the samples is highly variable depending on the degree of dolomitization in a given sample. There were three occurrences of a silty limestone and one occurrence of calcareous sandstone. In hand-sample the silty limestone consists of finely laminated silt-sized material interbedded with finely crystalline limestone. In hand-sample the calcareous sandstone consists of medium grained (1/8 - 1/4 mm), rounded to subrounded quartz grains in a calcite cement. Detrital potassium feldspar was also identified during SEM analyses, and is present in very minor amounts in the DSrm (Fig. 10). The bottom 5 feet of the DSrm commonly has black lenses, ~0.5 to 1 inches wide and ~2 inches long, which were identified by SEM analyses to be phosphate (Fig. 11a). The phosphate lenses were most common in the bottommost 10 feet of the DSrm. In thin section these lenses consist of dark carbonaceous material with minor detrital quartz and lesser amounts of illite. Based on data obtained from energy dispersive spectroscopy (EDS) using the SEM, the black lenses are comprised of mostly apatite with carbon, quartz, and minor illite (Figs. 11b, 11c). Phosphate lenses and nodules in the lowermost 5 feet of the DSrm were observed at the Bidart Anticline and were observed in 34 of the 247 drill holes logged during this study. There was also a maroon clay found right along the Saval discontinuity at Saval Canyon and the Bidart anticline (Fig. 12). It consists mainly of fluroapatite and quartz with minor amounts of calcite, illite, muscovite, dolomite, and ankerite, based on x-ray diffraction (XRD) analyses. The clay is consistent with being a paleosol, which would be expected in a subaerial karst environment (*e.g.*, Wright, 1982).

Mullens (1980) described the regional characteristics of the DSrm in detail. The Laminated Limestone unit from Mullens (1980), which is interpreted here to be a close analog to the interval of interest, consists of carbonaceous material and extremely fine grained pyrite that forms one set in a pair of laminations. The "average" laminated limestone consists of 40 % calcite, 23 % dolomite, 26 % quartz, 2 % potassium-feldspar, and 7 % clay minerals (Mullens, 1980). However, compositional differences in laminations are common where calcite only makes up 9 % of the sample and dolomite makes up 52 % of the sample (Mullens, 1980). The variation in calcite and dolomite contents in the DSrm is why the unit is commonly referred to a dolomitic siltstone.
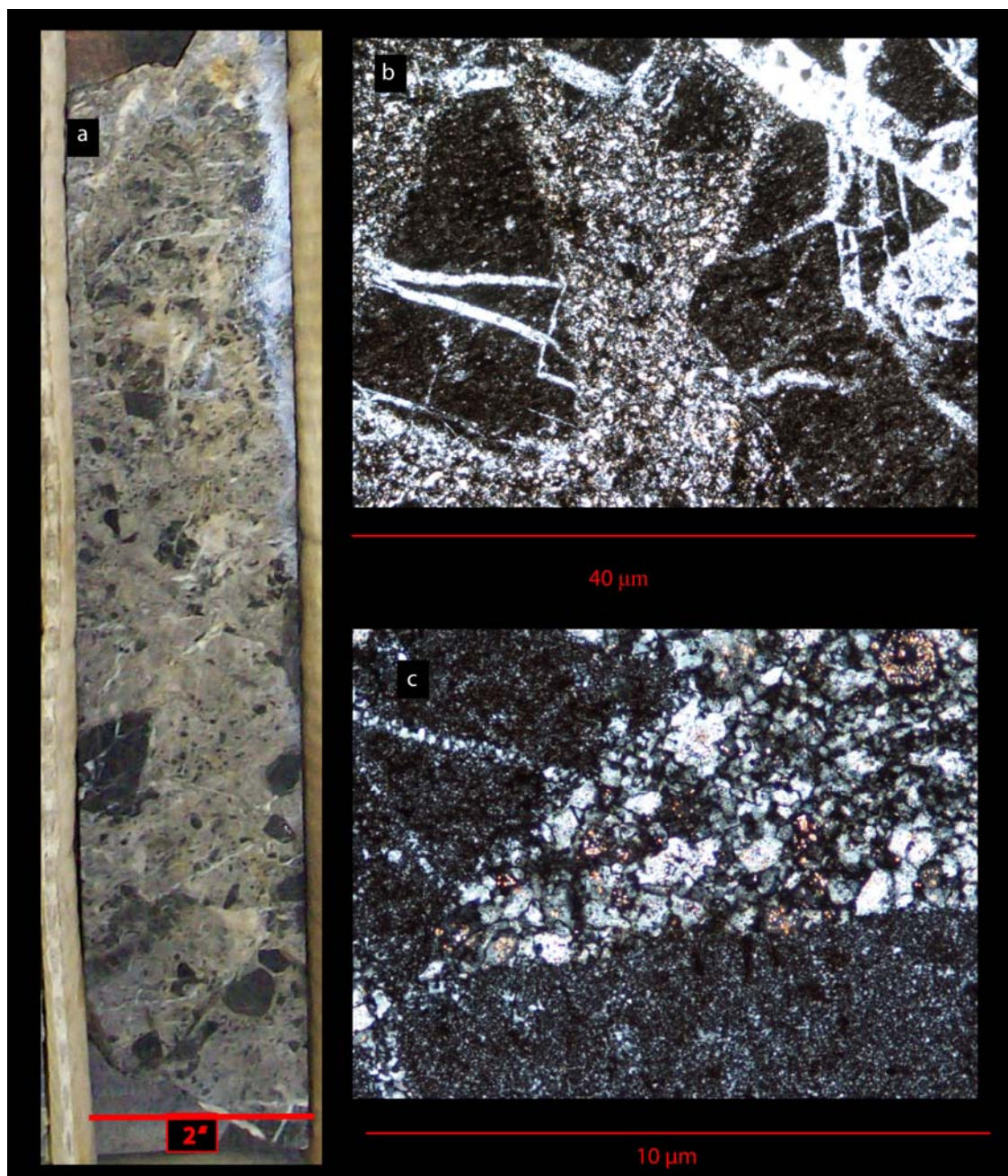
Figure 8. A. Drill core showing brecciated SOhc$_1$. The darker clasts are the angular to subangular chert

fragments. B. Thin section photomicrograph showing brecciated SOhc$_1$ under cross nicols. The black

fragments are the angular to sub-angular chert fragments found in the breccia of SOhc$_1$. The lighter or

white material is the silicified matrix of the SOhc$_1$ breccia. c. Brecciated SOhc$_1$ under cross nicols show

the jigsaw texture of the quartz that is commonly observed in the matrices of the SOhc$_1$ breccias. The black

material is the brecciated angular to sub-angular chert fragments.
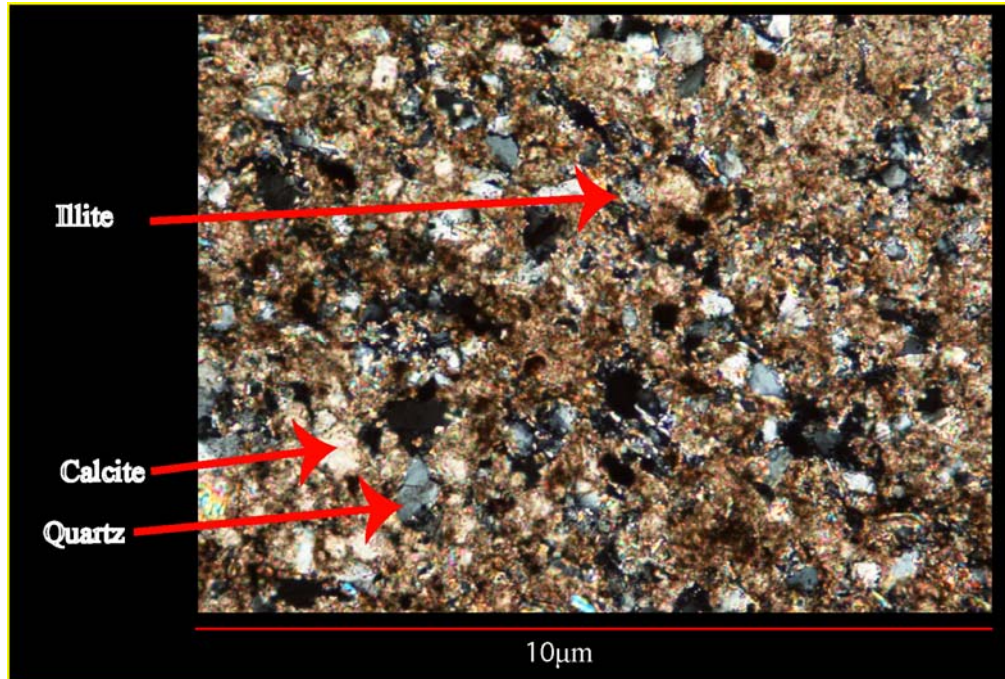
Figure 9: Photomicrograph taken of unaltered DSrm. Quartz is the less birefringent material as indicated by the bottom red arrow and calcite is the higher birefringent material indicated by the lighter colored material. The needle-like platelets are illite and the opaque mineral is pyrite.
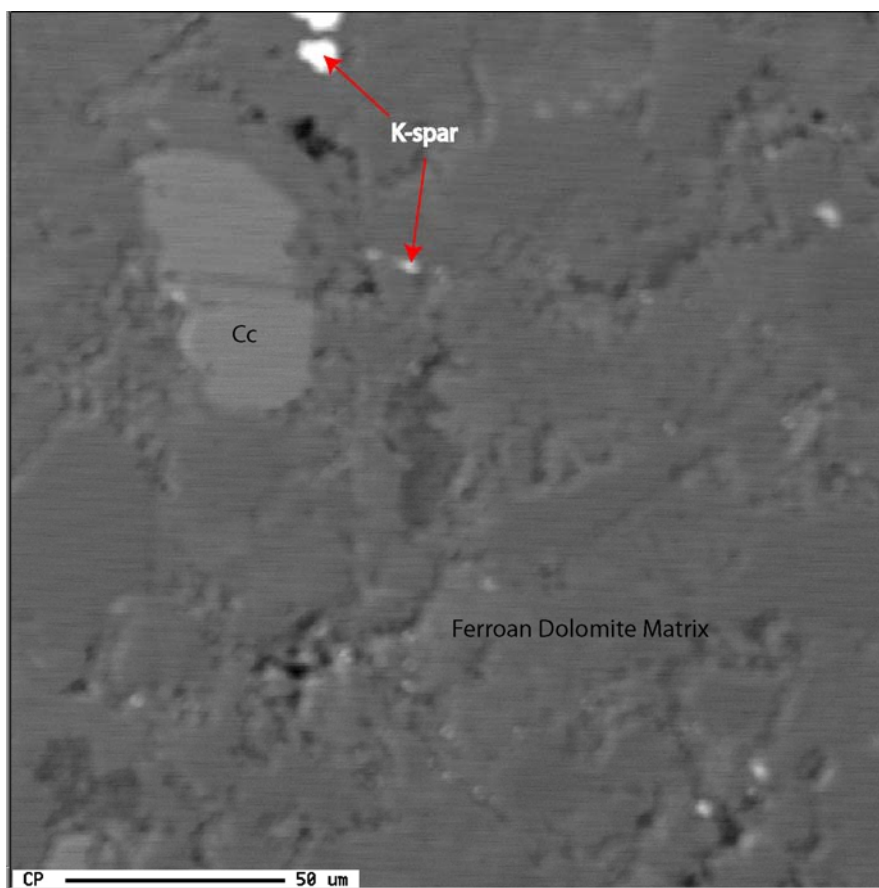
Figure 10: Back-scattered electron (BSE) image of K-feldspar that was found in the DSrm. The K-feldspar

is the bright phase. The matrix of the rock is dominated by ferroan dolomite (medium gray) with minor

calcite (light gray).
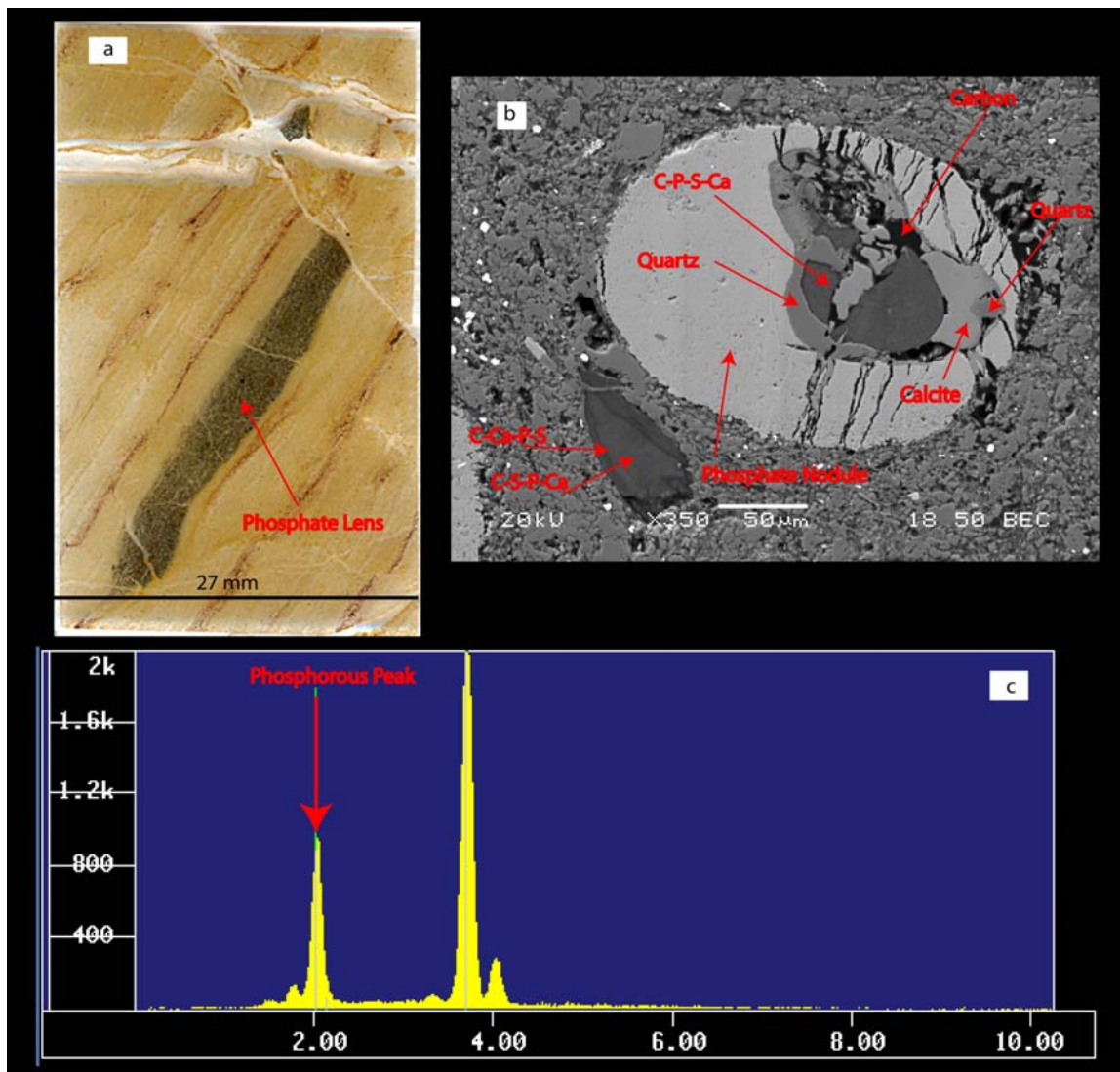
Figure 11:

a. Scanned image of a thin-section showing a phosphate lens (black material) within the bedding of DSrm.

b. Backscattered electron image of phosphate nodule.

c. EDS spectra taken from the phosphate nodule in 9b.
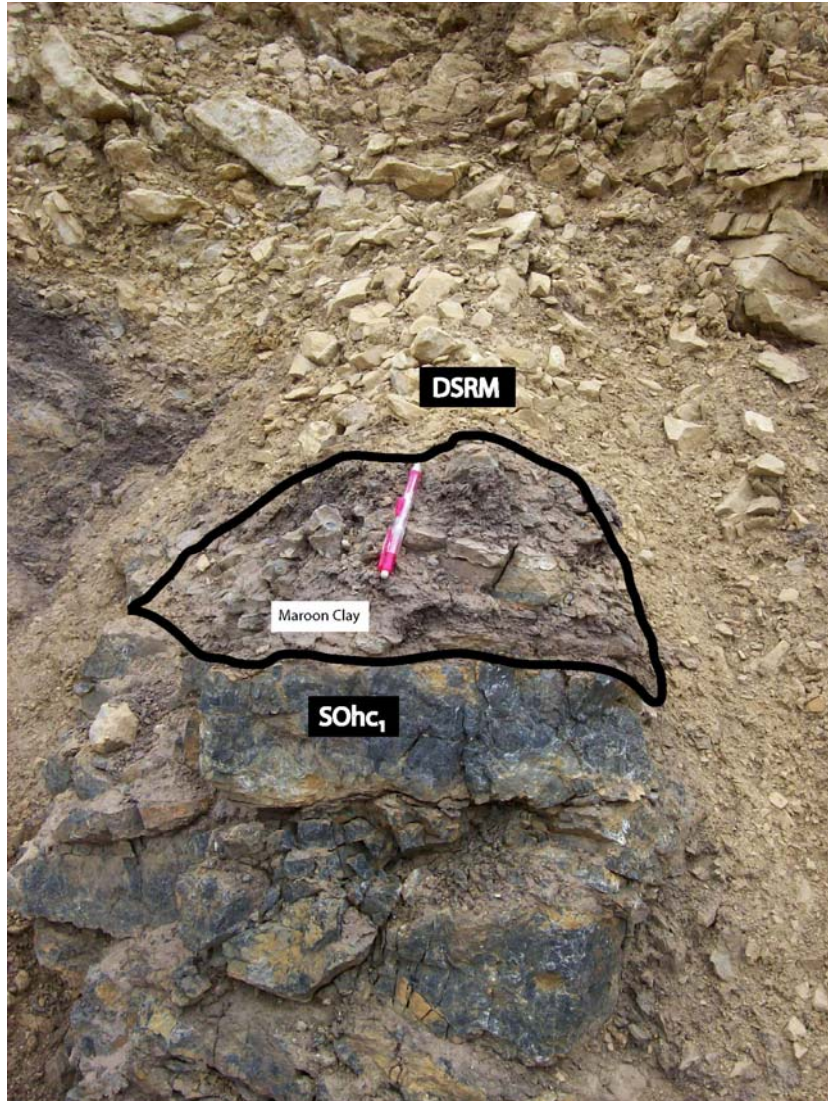
Figure 12: Maroon Clay observed at Saval Canyon.

Deformation along the Saval was not well documented in the mapped areas mapped because the DSrm is generally poorly exposed. The best example of deformation along the Saval was observed in the California Mountain pit, where a recumbent fold in the DSrm is exposed directly at the contact with underlying $SOhc_1$ (Fig. 13). Deformation in the DSrm directly above the Saval was also documented in the logging.

Of the 247 holes logged, 44 holes exhibited structural zones in the 5 foot interval directly above the Saval, which were composed of carbon rich broken rock with zones of disrupted bedding. Most of these structural zones closely correspond spatially to interpreted high-angle structures previously mapped at Jerritt Canyon (Muntean and Henry, 2007).

Silicified rock was observed in the $SOhc_1$ at all mapped surface exposures. Of the five areas that were mapped, silicified DSrm was only observed at Thomas Jose Canyon, where it occurred in close proximity to a high-angle structure. Of the 267 holes logged, 126 holes had silicified rock in the top most five feet of $SOhc_1$ and 48 had silicified rock in the bottom most five feet of DSrm. Silicification both destroys and preserves textures. Most of the texture-preserving silicification is interpreted to be event 1 silicification (after Hofstra, 1994), because it is restricted to chert rich units such as the SOhc1. In thin section silicified rock exhibits a jigsaw texture (Fig. 8c). Texture-destructive silicification is associated with mineralized areas and high angle structures. This silicification type is interpreted to be Hoftra's (1994) Event 2 silicification. Event 3 silicification was best exhibited at Thomas Jose and the Bidart Anticline by euhedral quartz filling vugs of $SOhc_1$ accompanied by euhedral calcite and stiboconite (Figs. 13a, 13b, & 13c). Calcite and barite from event 3 silicification was also observed in logged core as the matrix around brecciated $SOhc_1$ chert fragments. Silicified rocks of the lowermost DSrm and its spatial relationship with the gold deposits, trace elements and other alteration types is described in more detail below.
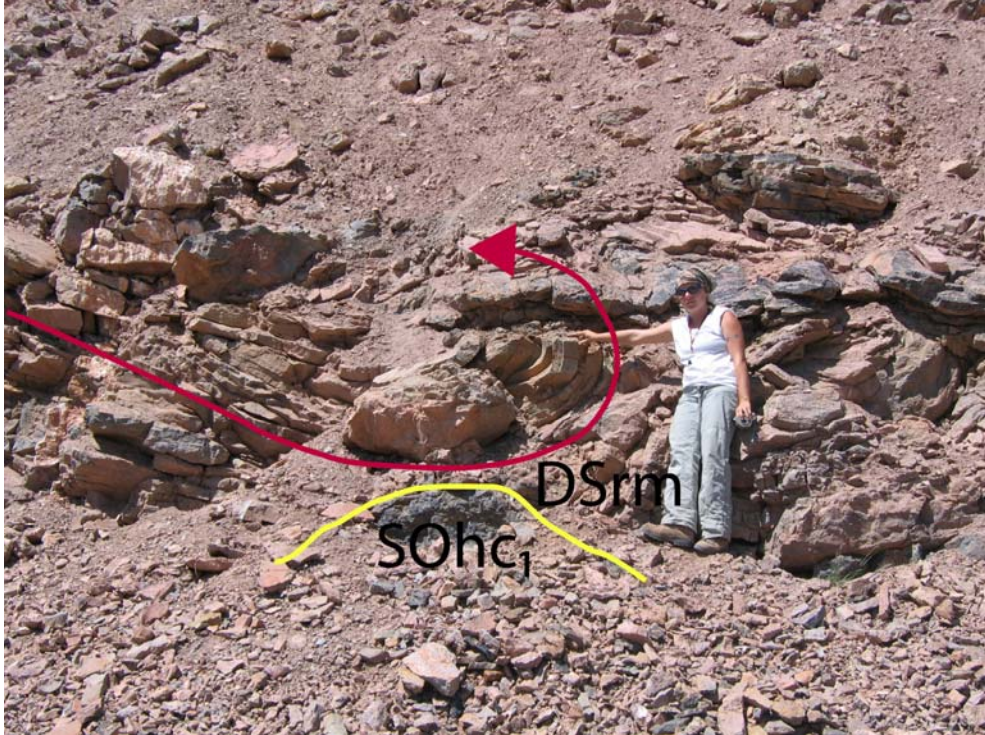
Figure 13: Recumbent fold in the DSrm directly above the Saval Discontinuity at California Mountain.

Figure 14: A. Picture of drusy quartz filling a vuggy sample taken from Thomas Jose Canyon. B. Picture of platy calcite that is filling a karst vug at the Bidart Anticline. C. Picture of stibiconite that was found within the brecciated SOhc$_1$ at Saval Canyon.

Features of the $SOhc_1$ along the Saval described above are consistent with subaerial karstification prior to deposition of the DSrm. Peters *et al.* (2003) made a similar interpretation, suggesting initial deposition of $SOhc_1$ took place in shallow waters where black, siliceous, laminated algal beds of stromatolites were sub-aerially exposed and karstified. Others have noted the occurrence of chert and have pointed out stratigraphic evidence for regional hiatus in deposition and subaerial erosion at the top of Hanson Creek throughout much of Nevada (Roberts *et al.*, 1967; Armstrong *et al.*, 1998). Regional conodont data indicate the top of the Hanson Creek is early Silurian (middle Llandovery) and the base of the Roberts Mountain Formation is late Llandovery (late Early Silurian), indicating a hiatus of 3 to 5 million years (Armstrong *et al.*, 1998).

Though the hiatus supports the hypothesis of karsting during subaerial exposure of the Hanson Creek, formation of chert fragments during such karsting is problematic. Several studies have indicated that the transition of opal-A to opal-CT to quartz requires temperatures on the order to 35 to 110°C, with the actual temperature being a complex function of many factors (cf. Hesse, 1988). If higher temperatures are simply a function of burial and a typical geothermal gradient, formation of chert in the $SOhc_1$ would require approximately 500 to 3,000 m of cover prior to deposition of the DSrm, clearly an unreasonable amount.

However, other studies have proposed models for direct precipitation of quartz or recrystallization of opaline phases to quartz under subaerial conditions, mainly by the mixing of seawater and meteoric water (Land, 1979; Laschet, 1984). Besides higher temperatures, high pH and ionic strength appear to enhance the transformation rates of opaline phases to quartz. Direct precipitation of quartz can occur in local, highly alkaline

evaporitic environments (Laschet, 1984). Land (1979) investigated the formation of chert in a Miocene chalk unit that was deposited in a slope environment off the north Jamaican coast. Later faulting subaerially exposed the chalk unit and down-faulted parts of it into the Cayman Trench. Chert in the down-faulted part of the slope consists of opal-CT nodules, whereas the subaerially exposed nodules are composed of quartz. He argued that the conversion of opal-CT to quartz was a result of temperature increase as the Miocene slope was uplifted through warm surface waters of the ocean, or by changes in pore fluid chemistry once interstitial seawater was replaced with meteoric water. In a similar fashion, mixing of warm, alkaline, silica-rich marine waters in a supratidal to intertidal environment with meteoric waters during uplift and subaerial exposure likely allowed the formation of quartz-bearing chert under near-surface conditions in the $SOhc_1$ at Jerritt Canyon. Meteoric waters likely dissolved the interbedded carbonates in $SOhc_1$ during karsting, resulting in volume loss and formation of collapse breccias containing fragments of chert. H. Cook (personal commun., 2008) indicated that stromatolites are a major constituent of the $SOhc_1$ cherts. Cook emphasized that stromatolites produce siliceous skeletons which would result in chert without burial or special conditions.

Phosphatic materials are commonly associated with unconformities and are seen today forming in areas of oceanic upwelling where a deep-ocean reservoir allows continuous growth of organisms which supply phosphatic material (Krumbein and Sloss, 1951; Boggs, 2006). The maroon clay and the phosphatic nodules documented in the bottommost 5 feet of the DSrm are likely indicating the beginning of a trangressive sequence (initial flooding) following sub-areal exposure of the $SOhc_1$.

Timing of the brecciation seems to be pre-Eocene and possibly pre-Pennsylvanian, as will be argued below. First, minerals that are products of the late ore stage Carlin fluids, such as calcite, stibnite, barite, and quartz commonly fill karst features and occur in the matrices of breccias, which indicates the karsting features were present prior to this event (Fig. 14a & 14b). Second, there was one hole in which a Pennsylvanian dike was observed cutting through the Saval between the DSrm and $SOhc_1$. However, there were no clasts of the dike in the underlying breccia of the $SOhc_1$ or in any other hole logged for this project which further indicates that karsting was pre-Pennsylvanian. Third, and most important, there were no clasts of DSrm observed in the karst breccias of the $SOhc_1$. If brecciation were to have taken place after deposition of the DSrm there should be some evidence of heterolithic collapse breccias consisting of the DSrm and $SOhc_1$ fragments. It is important to note that Tertiary karsting has been documented in the Jerritt Canyon district by Hofstra (1994). Tertiary karsting was also observed in one core hole from Saval Canyon during this study however, the breccia was distinctly different than that commonly observed in $SOhc_1$. In this core hole the breccia had angular to sub-angular clasts of the DSrm and SOhc formations in a clay matrix that made up 75 percent of the sample. However, stibnite was present on the $SOhc_1$ breccia clasts. This coincides with Hofstra's (1994) interpretation that Tertiary karsting was present at Jerritt Canyon but occurred after the Carlin mineralizing event.

In summary, the Saval discontinuity is interpreted here to be an unconformity formed by subaerial exposure, erosion and karstificiation that occurred during a lowstand in sea level during the early Silurian. The unconformity was subsequently, locally structurally activated as a low-angle fault, as evidenced by structural deformation of the

DSrm directly above the Saval (Fig. 13). Initial deposition of $SOhc_1$ in shallow water as siliceous laminated algal beds (cf. Peters *et al.*, 2003) was followed by a 3 to 5 million year long low-stand during the early Silurian (Fig. 15) (cf. Blatt and Tracy, 1995; Armstrong *et al.*, 1998; Cook and Corboy, 2006). This global low stand resulted in the subaerial exposure of the $SOhc_1$ and the mixing of warm, alkaline, silica-rich marine waters with meteoric waters to form chert by directly precipitating quartz or precipitating opal, which rapidly transformed to quartz in the shallow subsurface. Soon after, dissolution of carbonate by meteoric waters initiated karsting and caused brecciation of the chert layers. Following subaerial karsting, rapid transgression was marked by cooling upwelling waters and the formation of phosphates and the deposition of DSrm in a relatively deep slope or basin environment. Burial and subsequent loading of the Roberts Mountain allochthon likely was responsible for inducing event 1 silicification and other events described below.
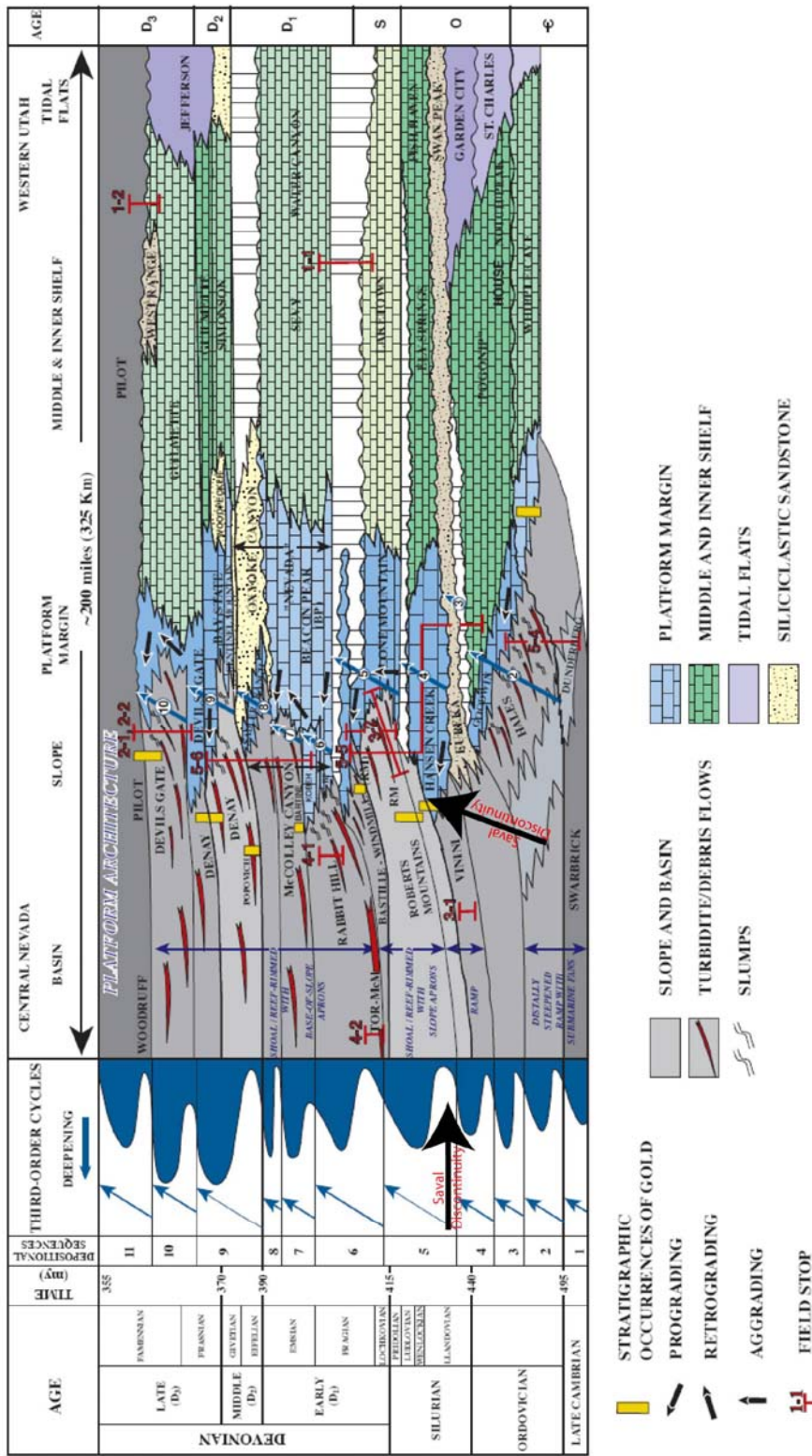
Figure 15: Black arrow to the left indicating approximate position of the Saval discontinuity and showing a global low-stand. The arrow to the right also shows the position of the Saval Discontinuity within the sedimentary pile of north eastern Nevada. Note disconformity above the Hanson Creek Formation. Modified from Cook and Corboy (2003).

Geochemistry

<u>Elemental Grids</u>

As stated earlier, Anglo Gold in 2000 collected a data set consisting of 6,416 drill samples (core and chips) with multielement geochemistry from the bottom 5 feet of the Roberts Mountains Formation directly above the Saval discontinuity. In drill holes with imbricated sections the samples were taken from the five foot interval directly above the first downhole occurrence of the Saval. Because of imbrication, not all the samples may be time equivalent. Attempts were made to separate conodonts from seven samples, to determine whether or not samples were time equivalent. No conodonts were found. Nevertheless, the samples are assumed here to be time-equivalent.

All analyses were completed by ALS Chemex. Gold was determined by fire assay with an AA finish, whereas other elements were analyzed by ICP-MS, using nitric-aqua regia digestion. Elements not completely digested by nitric-aqua regia include aluminum, barium, beryllium, calcium, chromium, gallium, potassium, lanthanum, sodium, strontium, titanium, and tungsten. If an analysis was less than the detection limit for a given element, a value of half the detection limit of that given element was entered into the database. Titanium, germanium, and boron are not included in the analysis of the data below, because very few samples have values exceeding the detection limit.

In order to establish background, 79 holes were chosen from the dataset, which had low values of gold, arsenic, mercury, thallium, and tellurium. These elements are most closely related to gold mineralization as outlined below. Elemental values were considered low if gold values were below <5 ppb (the detection limit for gold), <10 ppm arsenic, <2 ppm mercury, <0.25 ppm thallium, <13 ppm antimony, and <0.15 ppm

tellurium. The means were calculated for all the elements in the 79 holes, and thus, represent the estimated background values prior to Carlin-type gold mineralization in the Eocene (Table 1). The analyses of the 79 samples, used to calculate the background values can be found in Appendix 2.

From the Anglo Gold data set, point maps were produced first in order to look at patterns in elemental distribution in and around known areas of known mineralization. Each element was displayed in ESRI's GIS software package, ArcMap, as color coded point maps with red indicating high elemental values and purple indicating low elemental values (Fig. 16). Elemental populations were determined using breaks in slope or inflection points from logarithmic distribution curves for each individual element. Though point maps can be useful, the vast amount of data made it difficult to distinguish elemental patterns.

Gridded images of the data were made to reveal the spatial patterns in the elements. The gridded images were made in ArcMap using Target software, an add-on to ArcMap developed by Geosoft. A log-linear kriging method was used for elements that had log-normal population distributions and a linear kriging method was used for normal elemental distributions. A 150 foot cell size and search radius was used to calculate the grid points. Once grids were made, they were displayed in ArcMap as classified images with discrete changes in the colors representing breaks in the population of a given element (Fig. 17). Classified images not shown below can be found in Appendix 3. The reader should be cautioned that model diagnostics for the gridding were not run; therefore, some patterns may be misleading, especially in areas of low data density along the margins of the grids.

Only the northern portion of the Jerritt Canyon district will be discussed, as most of the data are concentrated in this area (Fig. 18). About 300 samples were available for the southern most portion of the district and were too widely distributed to generate a meaningful grid. For the purposes of this study the northern portion of the Jerritt Canyon district will be broken into two areas. The first area is the Murray-Winters Creek area which consists of the Murray, North Generator, West Generator, Marlboro Canyon, Alchem, and Winters Creek deposits (Fig. 19). The second is the SSX-Smith area which includes the Steer, Saval, SSX, Smith, DASH, California Mountain, Burns Basin, and Mill Creek deposits (Fig. 19). Other geologic and geographic locations that will be included in the following discussion are shown in figure 19 which includes Wright Window, the New Deep Fault, and the South Boundary Fault.

Of the 6,416 samples in the Anglo Gold data set only 2,130 samples were taken from the Murray-Winters Creek area. The relative lack of data in the Murray-Winters Creek area is because SOhc cropped out in several places and the Saval discontinuity was not present (Fig. 18).

Element	Au ppb	Al%	Sb ppm	As ppm	Ba ppm	Be ppm	Bi ppm	Cd ppm
Average	2.50	0.29	2.58	5.37	258.01	0.35	0.05	0.87

Element	Ca%	Cr ppm	Co ppm	Cu ppm	Ga ppm	Fe %	La ppm	Pb ppm
Average	12.53	29.58	3.33	14.17	0.80	0.72	8.63	5.46

Element	Mg %	Mn ppm	Hg ppm	Mo ppm	Ni ppm	P ppm	K %	Sc ppm
Average	3.96	154.56	0.31	5.34	18.52	1545.70	0.13	1.76

Element	Se ppm	Ag ppm	Na %	Sr ppm	S %	Te ppm	Tl ppm	W ppm
Average	1.52	0.21	0.01	362.89	0.45	0.04	0.08	0.26

Element	U ppm	V ppm	Zn ppm
Average	3.96	32.27	77.75

Table 1: Average background values for all elements prior to Carlin-type mineralization, based on samples with low values of gold, arsenic, mercury, thallium, and tellurium. See text for discussion.
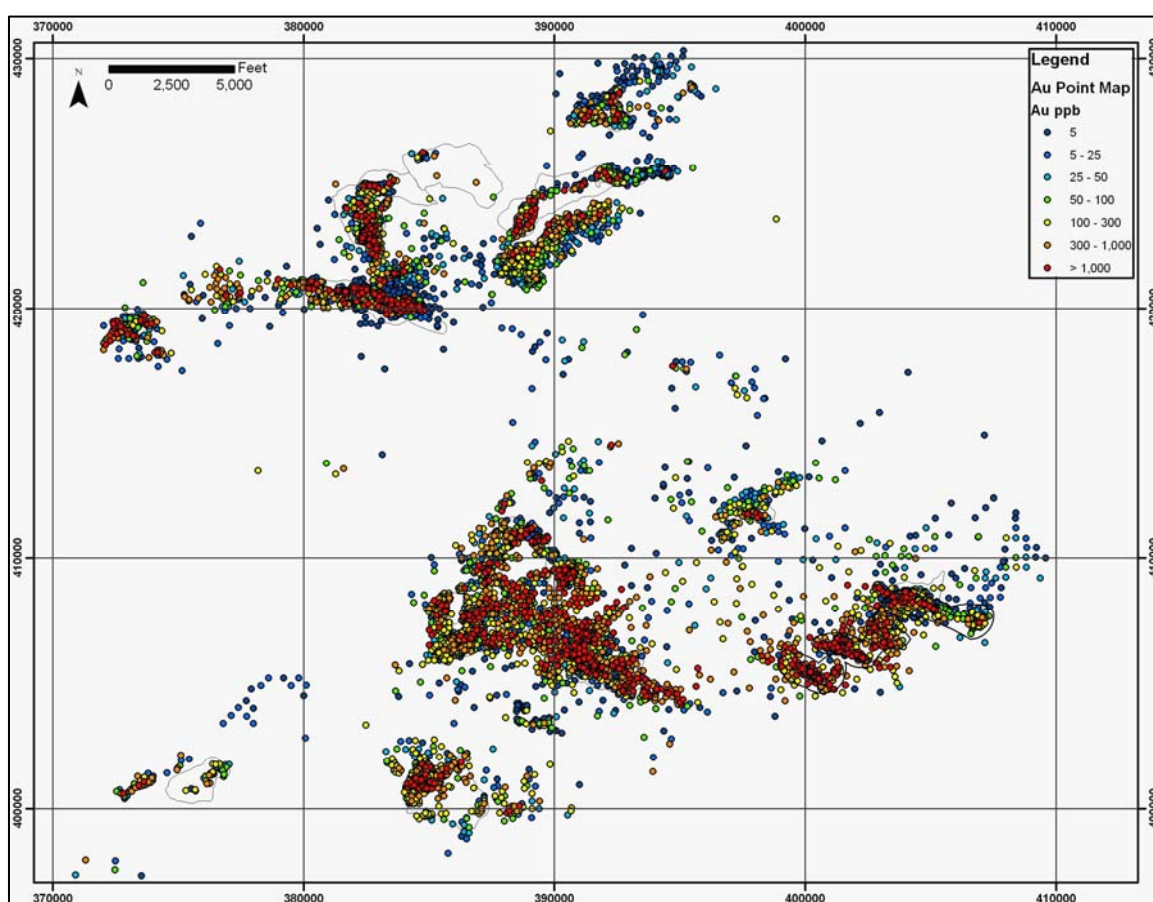
Figure 16: Elemental point map for gold. Fine black lines outline the deposits
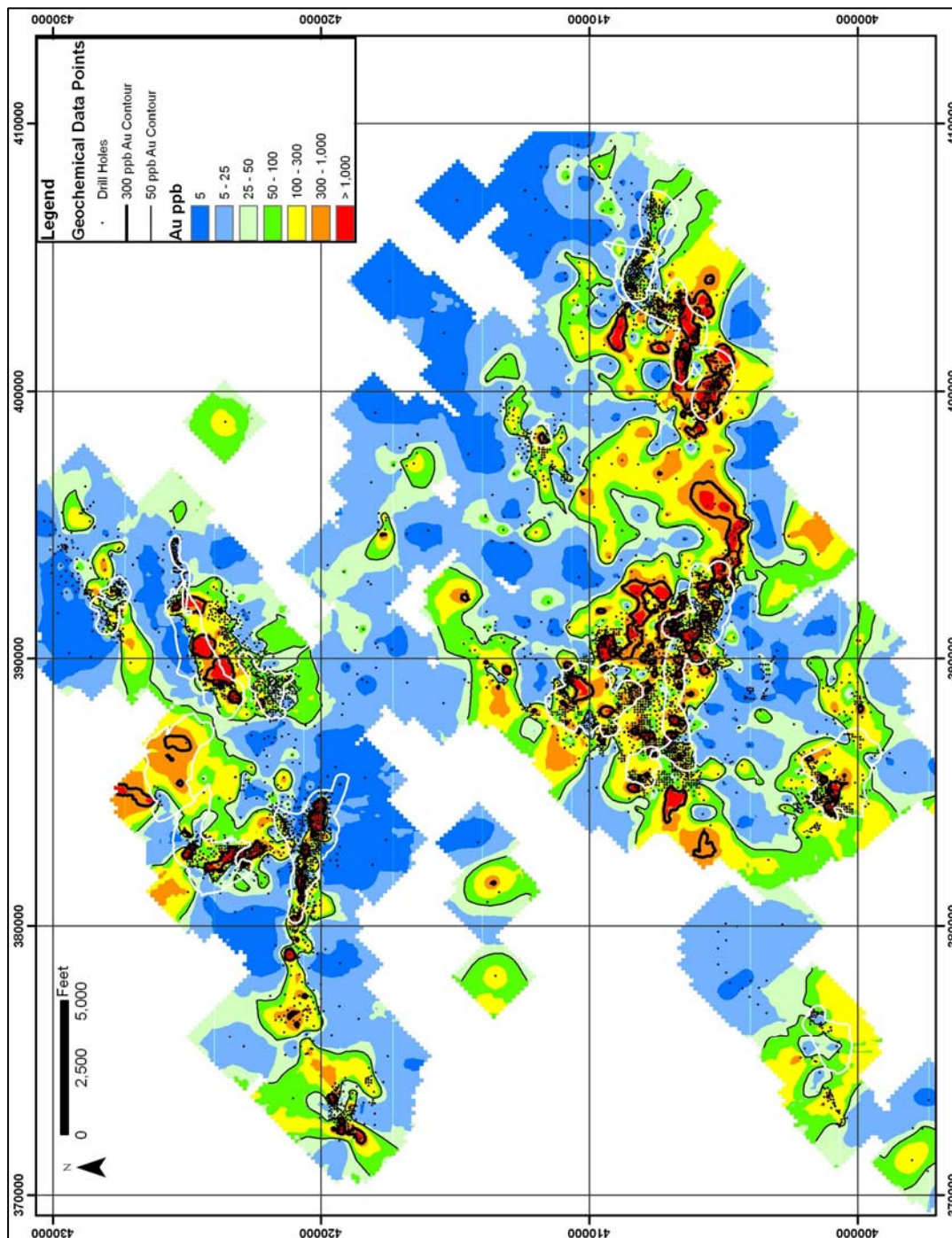
Figure 17: Classified grid for gold values. The white lines outline the deposits.
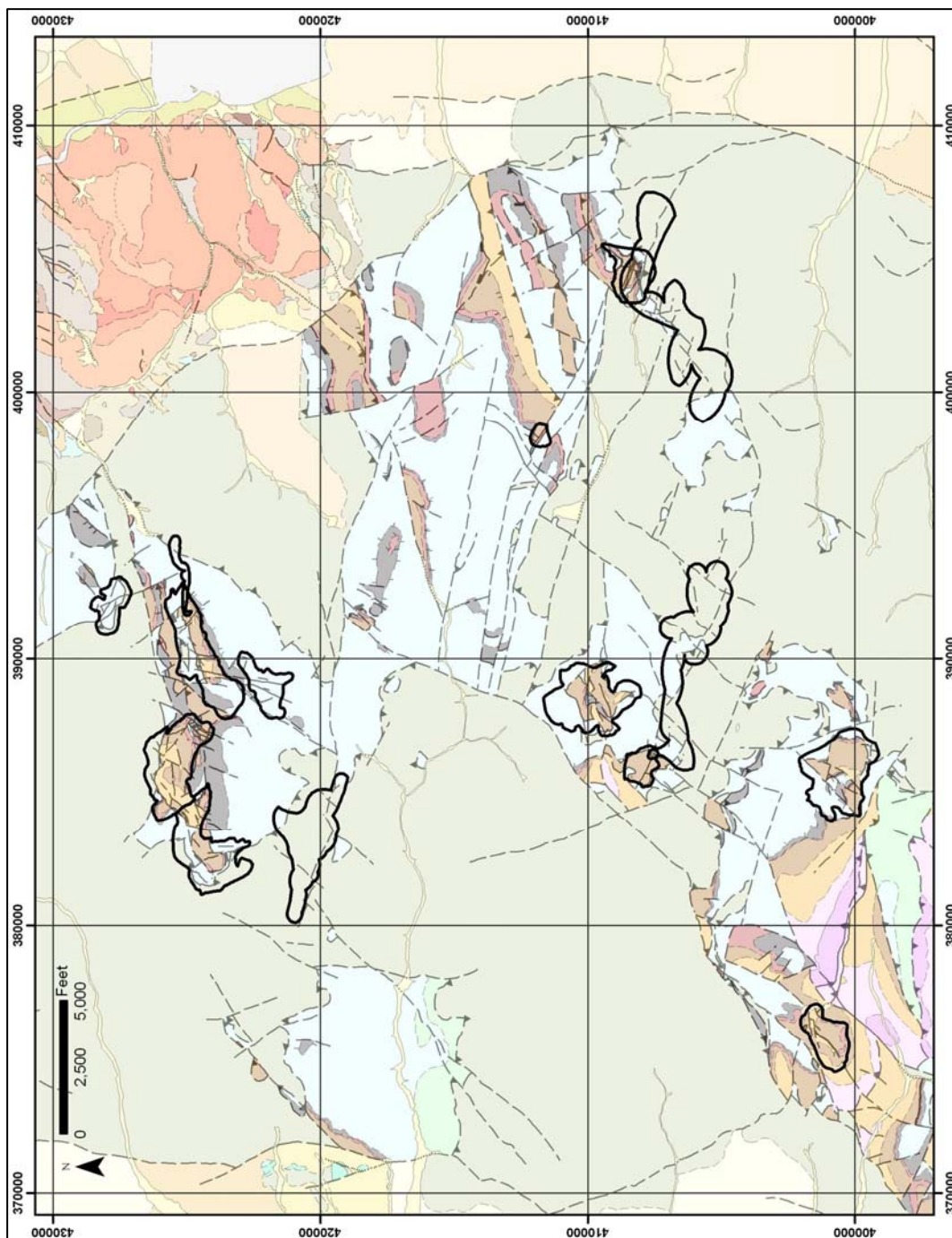
Figure 18: Map showing geographic locations of gold deposits (black outlines) and geology. See figure 3 for explanation of the map.
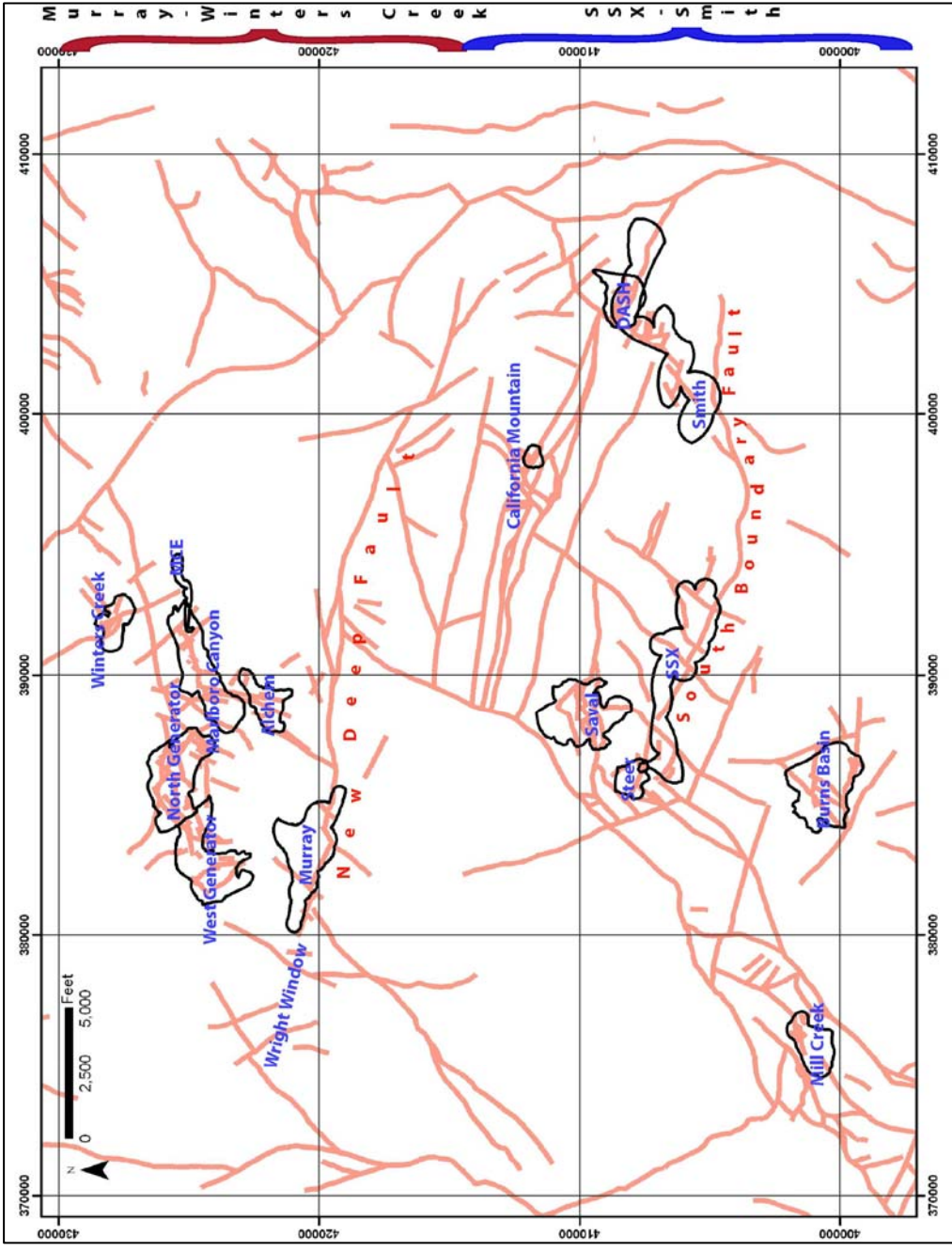
Figure 19: Maps showing deposit outlines with name designations, geographic, and geologic features referred to in text. High-angle structures are indicated by the red lines. Also shown to the right is the division of the northern portion of the Jerritt Canyon district as it will be referred to in the text.

It is important to note that the geochemical data base along the Saval, in most cases, does not represent ore, but rather a halo to ore. The deposits and their relative position with respect to the Saval are summarized in Table 2. In the North Generator, Mill Creek (Fig. 20, Table 2), and SSX deposits ore is primarily hosted in $SOhc_3$ any where from 30-300 feet below the Saval (Fig. 20, Table 2). In Winters Creek, Marlboro Canyon, Alchem, West Generator, Steer, Saval, Murray, and California Mountain ore is hosted mostly in the DSrm anywhere from 0-100 feet above the Saval (Fig. 20, Table 2). It is also important to note that these deposits are not stratiform, they are strongly controlled by structure; therefore, areas of mineralization are commonly found transecting through units of the SOhc and extending up into the DSrm (Fig. 20). For the purposes of this discussion the outlines of the deposits will be presented on most of the maps and halos above or below the Saval will be addressed as the vertical projection of the deposits.
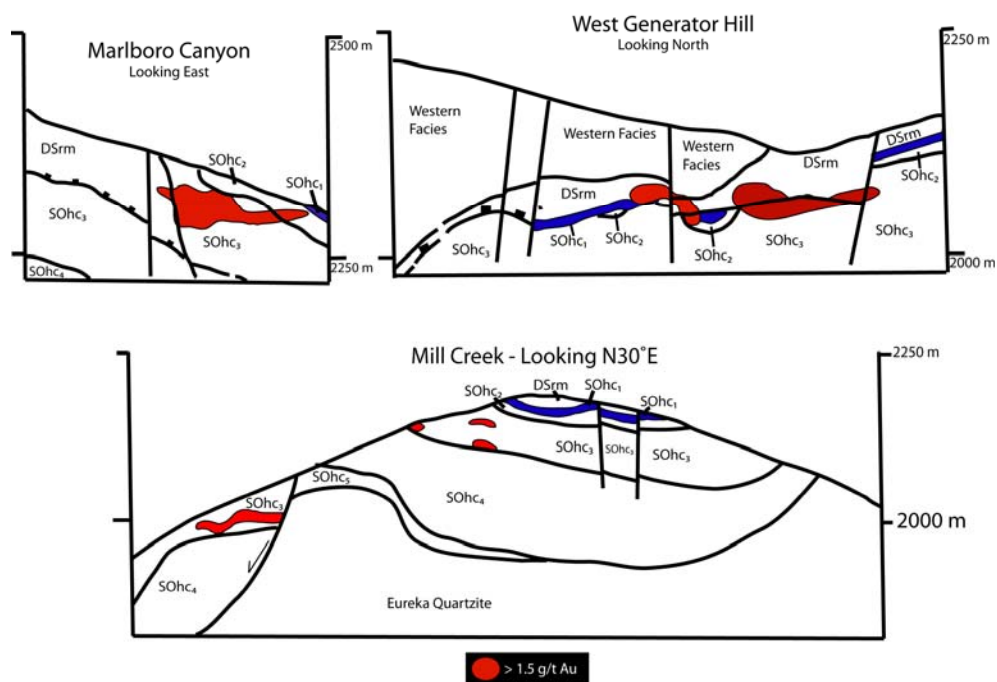
Figure 20: (Modified from Daly *et al*., 1991) Examples of ore body morphology and position with respect to the Saval discontinuity (top of the blue outline) for Marlboro Canyon (top left), West Generator Hill (top right), and Mill Creek (bottom). The blue is the $SOhc_1$.

Deposit	Host Rock	Position Relative to the Saval
Winters Creek	DSrm	50-100 ft above
Alchem	DSrm	40-120 ft above
DASH	SOhc 2&3	0-100 ft below
Burns Basin	DSrm & SOhc 3	Straddles
Saval	DSrm	0-100 ft below
North Generator	SOhc 3	30-70 ft below
West Generator	DSrm	0-75 ft above
Marlboro Canyon	SOhc 3 DSRM SOhc4	Straddles
Mill Creek	SOhc 3	~190 ft below
Steer/Saval	SOhc 3 DSrm	Straddles
California Mountain	SOhc 3	0-100 ft below
Murray	DSrm & SOhc 3	Straddles
Smith	SOhc 2&3	0-100 ft below
SSX	SOhc 2&3	75-100 ft below

Table 2: Table lists all deposits in the Jerritt Canyon district in the left-hand column, the host rock for each deposit in the center column, and the position of the ore body with respect to the Saval Discontinuity in the right-hand column.

Elements associated with Carlin-type gold mineralization will first be presented; then elements associated with hydrothermal alteration related to Carlin-type gold mineralization; and finally a group of mainly redox-sensitive elements that commonly are associated with black shales. The reasoning for this grouping will be further discussed following the presentation of statistical analyses. To draw out additional patterns that might form halos to the deposits, ratios were calculated and gridded using the same process that was used for the elements. Where applicable, ratio patterns from the gridded images will be discussed.

Spatial Patterns of Elements Related to Gold Mineralization

The maps presented below show that gold, arsenic, mercury, thallium, and to a lesser extent tellurium exhibit a similar spatial distribution. It is likely that gold, arsenic, mercury, thallium and tellurium were deposited at the same time during the Eocene Carlin-type gold mineralization event. Table 3 shows the spatial relationships exhibited by arsenic, mercury, thallium, and tellurium with respect to gold. Table 4 shows the pattern of gold, arsenic, mercury, thallium, and tellurium in terms of actual values and the attenuation of the elements away from elevated values.

Gold shows two distinct types of patterns, based on values greater than 50 ppb (Fig. 17). The first pattern type characterizes the Murray mine and the second pattern is a large west-northwest-trending zone in the SSX-Smith area (Fig. 17). Gold values greater than 50 ppb exhibit a west-northwest linear trend through the Murray deposit, which extends westward into the northern portion of the Wright Window area. This trend is 14,000 feet long and about 800 feet wide following the strike of the New Deep Fault. At West Generator gold values greater than 50 ppb exhibit a north-northwest linear trend

through the deposit that is 4,000 feet long and 900 feet wide. Marlboro Canyon exhibits a northeast trend of gold values greater than 50 ppb that is roughly 5,000 feet long and 1,700 feet wide. Winters Creek has circular or pod-like distributions of gold values greater than 50 ppb which are no larger than 600 feet in diameter. Gold values above 50 ppb extend from the Steer/Saval/SSX area 25,000 feet east-southeast through the Smith/DASH mines and possibly 20,000 feet northwestward if the trend is extended up towards Wright Window. Gold values above 50 ppb are much more extensive and evenly distributed in the SSX-Smith areas than they are in the Murray-Winters Creek area. Gold values greater than 50 ppb appear to be truncated to the south against the South Boundary Fault (Figs. 17 & 19).

Thallium forms a pattern very similar to the patterns exhibited by gold. Thallium values greater than 0.3 ppm are locally present in the Murray-Winters Creek area (Fig. 21a). Thallium values greater than 0.3 ppm occurs in a large/pervasive area around the SSX-Smith area and, like gold, are extensive and evenly distributed. At the Murray mine there is a west-northwest linear trend of thallium values greater than 0.3 ppm through Murray trailing out to the northern portion of the Wright Window area following the strike of the New Deep Fault. Relatively continuous thallium values greater than 0.3 ppm occur in a zone through the Murray mine that is 6,400 feet long and 700 feet wide. West Generator exhibits a north-northwest linear trend of thallium values greater than 0.3 ppm which is 3,000 feet long and 900 feet wide. In Marlboro Canyon thallium values greater than 0.3 ppm occur in circular pods, which have a maximum diameter of 800 feet. In Winters Creek there are isolated areas that exhibit thallium values greater than 0.3 ppm. Thallium values above 0.3 ppm are much more pervasively distributed in the SSX-Smith

area. Thallium values greater than 0.3 ppm form a large continuous pattern that extends from the Steer/Saval/SSX area 25,000 feet east-southeast through the Smith/DASH mines. Similar to gold, thallium values greater than 0.3 ppm are truncated to the south against the South Boundary Fault. Thallium values greater than 2 ppm are strictly confined to areas where gold values are greater than 300 ppb (Fig. 21a). In the Murray-Winters Creek and SSX-Smith areas thallium values between 0.3 ppm and 2 ppm extend out an average of 1,500 feet from gold values greater than 300 ppb (Fig. 21a). Thallium values between 0.3 and 0.5 form the most continuous halo to gold values greater than 300 ppb. Figure 21b shows that within the 50 ppb gold contour the thallium to gold ratios are consistently low with values between zero and ten, indicating that gold and thallium are decreasing in concentration laterally away from the deposits at a similar rate; however, beyond the 50 ppb gold contour thallium to gold ratios increased suggesting higher mobility of thallium compared to gold.

Mercury (Fig. 21c) values above 0.3 ppm are present throughout most of the study area. In the Murray mine mercury values greater than 1 ppm form a linear west-north west trend through Murray extending out to the northern portion of the Wright Window area, forming a continuous, linear trend that is 7,000 feet long and 500 feet wide. In West Generator mercury values greater than 1 ppm make a north-northwest trend that is 5,000 feet long by 2,000 feet wide. Marlboro Canyon and Winters Creek both exhibit northeast-trending linear patterns of mercury values greater than 1 ppm, which are about 6,500 feet long and 1,500 feet wide. Mercury values greater than 3 ppm are much more pervasively distributed in and around the SSX-Smith area than they are in the Murray-Winters Creek area. Mercury values greater than 3 ppm extend from the

Steer/Saval/SSX area 25,000 feet east-southeast through the Smith/DASH mines Mercury values above 10 ppm are mainly confined to areas where gold values are greater than 300 ppb (Fig. 21c). In the Murray-Winters Creek area mercury values between 3 and 10 ppm make a spotty halo to gold values greater than 300 ppb which extends out an average of 300 feet (Fig. 21c). Mercury values between 3 and 10 ppm extend out from gold values greater than 300 ppb 100 to 500 feet in the Steer/Saval/SSX and Burns Basin areas (Fig. 21c). In the Smith/DASH area mercury values between 3 and 10 ppm extend northward from the Smith/DASH area upwards of 2,500 feet from gold values greater than 300 ppb. Elevated mercury values are also truncated by the South Boundary fault. Figure 21c indicates that within the 50 ppb gold contour the mercury to gold ratio has consistently low ratio values between 0.1 and 0.3. The ratio patterns in figure 21d again indicate that gold and mercury both attenuate away from mineralized areas at the same rate, however, beyond the 50 ppb gold contour mercury to gold ratios increased suggesting greater mobility and/or background values of mercury compared to gold.

Arsenic values above 10 ppm are present throughout almost the entire study area (Fig. 21e). In the Murray mine arsenic values greater than 50 ppm form a continuous west-northwest linear trend along the New Deep fault that is 8,000 feet long and 600 feet wide extending out to the north end of Wright Window. In West Generator arsenic values greater than 50 ppm form a north-northwest trend that is 4,000 feet long and 800 feet wide. Arsenic values greater than 50 ppm extend through Alchem and Marlboro Canyon in a northeast trend that is 8,500 feet long. The width of the trend averages about 800 feet wide in the eastern extension of Marlboro Canyon widening to a width of 3,000 feet in-between Alchem and Marlboro Canyon. In Winters Creek arsenic values above

50 ppm form another northeast trend that is 4,000 feet long and 600-1000 feet wide. Arsenic values above 50 ppm are much more extensive in and around the SSX-Smith area than they are in the Murray-Winters Creek area. Arsenic values greater than 50 ppm extend from the Steer/Saval/SSX area 25,000 feet east-southeast through the Smith/DASH mines in an almost continuous linear trend that truncates southward against the South Boundary Fault. The east-southeast trend of arsenic values is not as continuous as the gold, thallium, and mercury trends in and around the Smith-DASH areas (Figs. 17, 21a, 21c, & 21e). Arsenic values greater than 100 ppm are mostly confined to areas where gold values are greater than 300 ppb but do make spotty halos around the greater than 300 ppb gold contour (Fig. 21e). Arsenic values greater than 100 ppm generally extend out from gold values greater than 300 ppb to an average of 0 to 100 feet in the Murray-Winters Creek area and 0 to 350 feet in the SSX-Smith area (Fig. 21e). Arsenic values between 50 and 150 ppm form the best defined, most continuous halo to gold values greater than 300 ppb (Fig. 21e). The 50 to 150 ppm arsenic halo extends out up to 1,500 feet in the SSX-Smith area and 800 feet in the Murray-Winters Creek area from gold values greater than 300 ppb (Fig. 21e). Figure 21f shows the arsenic to gold ratio consistently displays low ratio values between 0.5 and 400 within the 300 ppb gold contour. However, the arsenic to gold ratio grid also shows that right at, or about 300 feet outboard of the 300 ppb gold contour, gold values decrease more rapidly than arsenic values, which raises the arsenic to gold ratio to values between 400 and 5,000. Similar to mercury, beyond the 50 ppb gold contour arsenic to gold ratios increased suggesting greater mobility and/or background values of arsenic compared to gold.

Local zones of tellurium values greater than 0.2 ppm are generally present in and around areas where gold values are greater than 300 ppb (Figs. 21g). Pods of tellurium values greater than 0.2 ppm form a west-northwest linear trend through the Murray mine along the strike of the New Deep fault trailing out to the northern portion of the Wright Window area. The linear trend through the Murray mine is 5,000 feet long and an average of 600 feet wide. Tellurium values that are greater than 0.1 ppm exhibit a north-northwest linear trend in the southern portion of the West Generator mine that is 3,000 feet long and 600 feet wide. Tellurium values greater than 0.1 ppm are present in and around the Marlboro Canyon and Winters Creek deposits in broad east-northeast trends. The largest zone of elevated tellurium values occurs in the Steer/Saval/SSX area. Tellurium values greater than 0.2 ppm make a continuous east-southeast trend from Steer/Saval down through SSX that diminishes towards the Smith/DASH deposits and truncates southward against the South Boundary Fault. The east-southeast trend at Steer/Saval/SSX consists of tellurium values greater than 0.2 ppm and is 14,000 feet long by 4,000 feet wide. Tellurium values greater than 0.5 ppm are restricted, almost exclusively, to areas where gold values are greater than 300 ppb (Fig. 21g). In the Murray-Winters Creek area tellurium values between 0.15 and 0.5 are also restricted to areas where gold values are greater than 300 ppb (Fig. 21g). Tellurium values that are between 0.05 and 0.15 ppm extend out an average of 600 feet in the Murray-Winters Creek area from the 300 ppb contour (Fig. 21g). In the Steer/Saval/SSX area tellurium values that are between 0.05 and 0.5 extend out an average of 1,000 feet from gold values greater than 300 ppb (Fig. 21g). The 0.05 to 0.1 ppm tellurium halo forms the most continuous halo to gold values greater than 300 ppb. Figure 21h shows that within the

300 ppb gold contour the tellurium to gold ratio is uniform, but generally increases within about 10 to 500 feet of the 50 ppb gold contour, indicating gold values are attenuating at a greater rate than tellurium (Fig. 21h). This is best observed in the Steer/Saval/SSX area.

Antimony, mainly as stibnite, is common throughout the Jerritt Canyon district, but generally does not share the similar patterns exhibited by gold, thallium, mercury and arsenic. Elevated antimony values above 5 ppm are present throughout much of the study area (Fig. 21i). Antimony values greater than 25 ppm occur in the vertical projection of known gold deposits in the Murray-Winters Creek area, and in an east-southeast trend above the SSX mine. However, the west-northwest trend of elevated antimony values greater than 25 ppm is displaced about 1,100 feet northeast of the vertical projection of SSX (Fig. 21i). Elevated antimony values are mostly closely associated with gold values greater than 300 ppb in the Murray deposit (Fig. 21i) An almost antithetic pattern between antimony and gold, thallium, mercury, arsenic, and tellurium is presented by the elemental maps, with broad antimony concentrations (>25 ppm) outboard of areas where the gold related elements are elevated (Figs. 17, 21a, 21c, 21e, 21g, & 21i).

	Distance from the Vertical Projection of the Gold Deposits in the SSX-DASH area	Distance from the Vertical Projection of the Gold Deposits in the Murray-Winters Creek area	Distance from the 300 ppb Au Contour (SSX-DASH)	Distance from the 300 ppb Au Contour (Murray-Winters Creek Area)	Distance from the 50 ppb Au Contour (SSX-DASH area)	Distance from the 50 ppb Au Contour (Murray-Winters Creek Area)
Au > 1,000 ppb	0 - 1,900 ft	0 - 300 ft	NA	NA	NA	NA
Au 300-1,000 ppb Halo	0 - 3,700 ft	0 - 1,000 ft	NA	NA	NA	NA
Au 100-300 ppb halo	0 - 4,000 ft	0 - 3,500 ft	NA	NA	NA	NA
Au 25-50 ppb Halo	0 - 2,700 ft	0 - 8,000 ft	NA	NA	NA	NA
Tl > 5 ppm	0 - 1,700 ft	0 - 1,700 ft	NA	NA	NA	NA
Tl 2-5 ppm	0 - 2,800 ft	0 - 1,400 ft	0 - 400- ft (S)	0 - 235 ft (S)	NA	NA
Tl 1-2 ppm	0 - 2,900 ft	0 - 1,300 ft	0 - 500 ft (S)	0 - 450 ft (S)	0 - 400 ft (S)	0 - 50 ft (S)
Tl 0.75-1 ppm	0 - 3,300 ft	0 - 1,400 ft	0 - 550 ft (S)	0 - 470 ft (S)	0 - 500 ft (S)	0 - 350 ft (S)
Tl 0.5-0.75 ppm	0 - 3,600 ft	0 - 1,500 ft	0 - 630 ft (S)	0 - 600 ft (SC)	0 - 900 ft (S)	0 - 450 ft (S)
Tl 0.3 - 0.5 ppm	0 - 4,000ft	0 - 1,600 ft	0 - 1,500 ft (C)	0 - 900 ft (C)	0 - 1,500 ft (S)	0 - 750 ft (S)
As > 500 ppm	200 - 2,000 ft	0 - 1,200 ft	0 - 150 ft (S)	NA	NA	NA
As 200-500 ppm	0 - 2,200 ft	0 - 1,400 ft	0 - 300 ft (S)	0 - 250 ft (S)	NA	0 - 100 ft (S)
As 150-200 ppm	0 - 2,500 ft	0 - 1,500 ft	0 - 350 ft (SC)	0 - 275 ft (S)	0 - 100 ft (S)	0 - 120 ft (S)
As 100-150 ppm	0 - 2,700 ft	0 - 1,600 ft	0 - 600 ft (SC)	0 - 400 ft (SC)	0 - 300 ft (S)	0 - 150 ft (S)
As 50-100 ppm	0 - 3,000 ft	0 - 2,800 ft	0 - 1,500 ft (C)	0 - 800 ft (C)	0 - 900 ft (S)	0 - 400 ft (S)
Hg > 25 ppm	0 - 1,200 ft	NA	0 - 150 ft (S)	NA	NA	NA
Hg 15-25 ppm	0 - 1,500 ft	NA	0 - 230 ft (S)	NA	NA	0 - 50 ft
Hg 10-15 ppm	0 - 2,000 ft	0 - 1,300 ft	0 - 400 ft (S)	NA	NA	0 - 100 ft
Hg 3-10 ppm	0 - 4,000 ft	0 - 1,500 ft	0 - 2,000 ft (C)	0 - 300 ft (S)	0 - 1,000 ft (S)	0 - 800 ft (S)
Hg 1-3 ppm	0 - 5,000 ft	0 - 2,700 ft	0 - 2,500 ft (C)	0 - 1,000 ft (C)	0 - 1,500 ft (S)	0 - 900 ft (S)
Te > 2 ppm	0 - 2,300 ft	0	0 - 300 ft (S)	0 - 400 ft (S)	NA	NA
Te 0.5-2 ppm	0 - 2,400 ft	0 - 400 ft	0 - 370 ft (S)	0 - 300 ft (S)	NA	NA
Te 0.2-0.5 ppm	0 - 2,600 ft	0 - 800 ft	0 - 500 ft	0 - 350 ft (S)	NA	NA
Te 0.15-0.2 ppm	0 - 2,800 ft	0 - 850 ft	0 - 525 ft (S)	0 - 375 ft (S)	0 - 50 ft (S)	0 - 50 ft (S)
Te 0.1 - 0.15 ppm	0 - 3,000 ft	0 - 950 ft	0 - 650 ft (SC)	0 - 400 ft (S)	0 - 450 ft (S)	0 - 300 ft (S)
Te 0.05-0.1 ppm	0 - 3,700 ft	0 - 1,500 ft	0 - 1,000 ft (C)	0 - 600 ft (C)	0 - 800 ft (S)	0 - 1,200 ft (S)

(C) : Continuous   (SC) : Semi-Continuous   (S) : Spotty

Table 3: Attenuation of gold related elements from 300 and 50 ppb gold and the vertical projection of known gold deposits.

	Gold							
In South Jerritt								
The	300 - 1000	ppb	Gold halo extends out an average of	100	feet from the	> 1000 ppb	ppb	halo.
The	100 - 300	ppb	Gold halo extends out an average of	100 - 150	feet from the	300 - 1000	ppb	halo.
The	50 - 100	ppb	Gold halo extends out an average of	50 - 75	feet from the	100 - 300	ppb	halo.
The	25 - 50	ppb	Gold halo extends out an average of	50	feet from the	50 - 100	ppb	halo.
The	2.5 - 25	ppb	Gold halo extends out an average of	unknown	feet from the	25 - 50	ppb	halo.
In North Jerritt								
The	300 - 1000	ppb	Gold halo extends out an average of	100	feet from the	> 1000 ppb	ppb	halo.
The	100 - 300	ppb	Gold halo extends out an average of	50 - 100	feet from the	300 - 1000	ppb	halo.
The	50 - 100	ppb	Gold halo extends out an average of	50 - 75	feet from the	100 - 300	ppb	halo.
The	25 - 50	ppb	Gold halo extends out an average of	50	feet from the	50 - 100	ppb	halo.
The	2.5 - 25	ppb	Gold halo extends out an average of	50 - 100	feet from the	25 - 50	ppb	halo.
	Arsenic							
In South Jerritt								
The	200 - 500	ppm	Arsenic halo extends out an average of	100 - 150	feet from the	> 500	ppm	halo.
The	150 - 200	ppm	Arsenic halo extends out an average of	50 - 100	feet from the	200 - 500	ppm	halo.
The	100 - 150	ppm	Arsenic halo extends out an average of	100	feet from the	150 - 200	ppm	halo.
The	50 - 100	ppm	Arsenic halo extends out an average of	100 - 200	feet from the	100 - 150	ppm	halo.
The	10 - 50	ppm	Arsenic halo extends out an average of	unknown	feet from the	50 - 100	ppm	halo.
In North Jerritt								
The	200 - 500	ppm	Arsenic halo extends out an average of	~75	feet from the	> 500	ppm	halo.
The	150 - 200	ppm	Arsenic halo extends out an average of	50	feet from the	200 - 500	ppm	halo.
The	100 - 150	ppm	Arsenic halo extends out an average of	70	feet from the	150 - 200	ppm	halo.
The	50 - 100	ppm	Arsenic halo extends out an average of	50 - 200	feet from the	100 - 150	ppm	halo.
The	10 - 50	ppm	Arsenic halo extends out an average of	100 - 200	feet from the	50 - 100	ppm	halo.
Mercury								
In South Jerritt								
The	15 - 25	ppm	Mercury halo extends out an average of	50 - 100	feet from the	> 25	ppm	halo.
The	10 - 15	ppm	Mercury halo extends out an average of	50 - 75	feet from the	15 - 25	ppm	halo.
The	3 - 10	ppm	Mercury halo extends out an average of	100 - 300	feet from the	10 - 15	ppm	halo.
The	1 - 3	ppm	Mercury halo extends out an average of	170	feet from the	3 - 10	ppm	halo.
The	0.3 - 1	ppm	Mercury halo extends out an average of	unknown	feet from the	1 - 3	ppm	halo.
In North Jerritt								
The	15 - 25	ppm	Mercury halo extends out an average of	50	feet from the	> 25	ppm	halo.
The	10 - 15	ppm	Mercury halo extends out an average of	25 - 50	feet from the	15 - 25	ppm	halo.
The	3 - 10	ppm	Mercury halo extends out an average of	100	feet from the	10 - 15	ppm	halo.
The	1 - 3	ppm	Mercury halo extends out an average of	100 - 200	feet from the	3 - 10	ppm	halo.
The	0.3 - 1	ppm	Mercury halo extends out an average of	100 - 200	feet from the	1 - 3	ppm	halo.
Thallium								
In South Jerritt								
The	2 - 5	ppm	Thallium halo extends out an average of	50 - 80	feet from the	> 5	ppm	halo.
The	1 - 2	ppm	Thallium halo extends out an average of	50 - 75	feet from the	2 - 5	ppm	halo.
The	0.75 - 1	ppm	Thallium halo extends out an average of	50	feet from the	1 - 2	ppm	halo.
The	0.5 - 0.75	ppm	Thallium halo extends out an average of	50 - 100	feet from the	0.75 - 1	ppm	halo.
The	0.1 - 0.5	ppm	Thallium halo extends out an average of	unknown	feet from the	0.5 - 0.75	ppm	halo.
In North Jerritt								
The	2 - 5	ppm	Thallium halo extends out an average of	50-80	feet from the	> 5	ppm	halo.
The	1 - 2	ppm	Thallium halo extends out an average of	50	feet from the	2 - 5	ppm	halo.
The	0.75 - 1	ppm	Thallium halo extends out an average of	25	feet from the	1 - 2	ppm	halo.
The	0.5 - 0.75	ppm	Thallium halo extends out an average of	30	feet from the	0.75 - 1	ppm	halo.
The	0.1 - 0.5	ppm	Thallium halo extends out an average of	unknown	feet from the	0.5 - 0.75	ppm	halo.
Tellurium								
In South Jerritt								
The	0.5 - 2	ppm	Tellurium halo extends out an average of	50 - 75	feet from the	> 2	ppm	halo.
The	0.2 - 0.5	ppm	Tellurium halo extends out an average of	50 - 100	feet from the	0.5 - 2	ppm	halo.
The	0.15 - 0.2	ppm	Tellurium halo extends out an average of	50	feet from the		ppm	halo.
The	0.1 - 0.15	ppm	Tellurium halo extends out an average of	50 - 80	feet from the		ppm	halo.
The	0.05 - 0.1	ppm	Tellurium halo extends out an average of	100 - 150	feet from the		ppm	halo.
In North Jerritt								
The	0.5 - 2	ppm	Tellurium halo extends out an average of	100	feet from the	> 2	ppm	halo.
The	0.2 - 0.5	ppm	Tellurium halo extends out an average of	80	feet from the	0.5 - 2	ppm	halo.
The	0.15 - 0.2	ppm	Tellurium halo extends out an average of	30	feet from the	0.2 - 0.5	ppm	halo.
The	0.1 - 0.15	ppm	Tellurium halo extends out an average of	100	feet from the	0.15 - 0.2	ppm	halo.
The	0.05 - 0.1	ppm	Tellurium halo extends out an average of	100 - 120	feet from the	0.1 - 0.15	ppm	halo.

Table 4: Table showing the patterns of gold, arsenic, mercury, thallium and tellurium, in terms of actual values, and the attenuation of the elements away from high values.

Figure 21:

a. Thallium classified grid with 300 and 50 ppb gold contours and white deposit outlines. b. Classified grid of the thallium to gold ratio with 300 and 50 ppb gold contours and white deposit outlines. Legends are for calculated grid values, not actual values.

c. Mercury classified grid with 300 and 50 ppb gold contours and white deposit outlines. d. Classified grid of the Mercury to gold ratio with 300 and 50 ppb gold contours and white deposit outlines. Legends are for calculated grid values, not actual values.

e. Arsenic classified grid with 300 and 50 ppb gold contours and white deposit outlines. f. Classified grid of the arsenic to gold ratio with 300 and 50 ppb gold contours and white deposit outlines. Legends are for calculated grid values, not actual values.

g. Tellurium classified grid with 300 and 50 ppb gold contours and white deposit outlines. h. Classified grid of the tellurium to gold ratio with 300 and 50 ppb gold contours and white deposit outlines. Legends are for calculated grid values, not actual values.

i. Antimony classified grid with 300 and 50 ppb gold contours and white deposit outlines. Legends are for calculated grid values, not actual values.
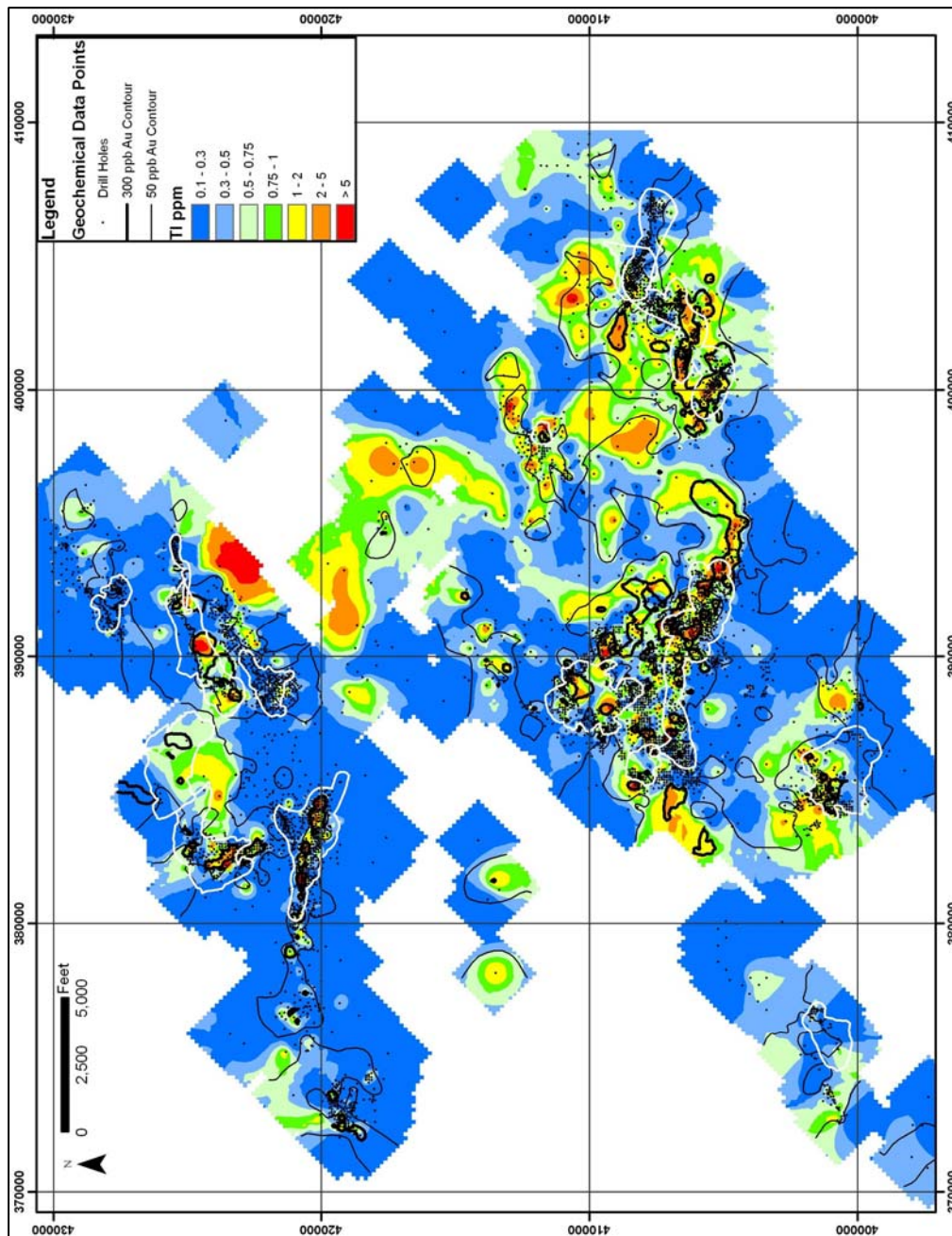
Figure 21a

Figure 21b

Figure 21c

Figure 21d

Figure 21e

Figure 21f
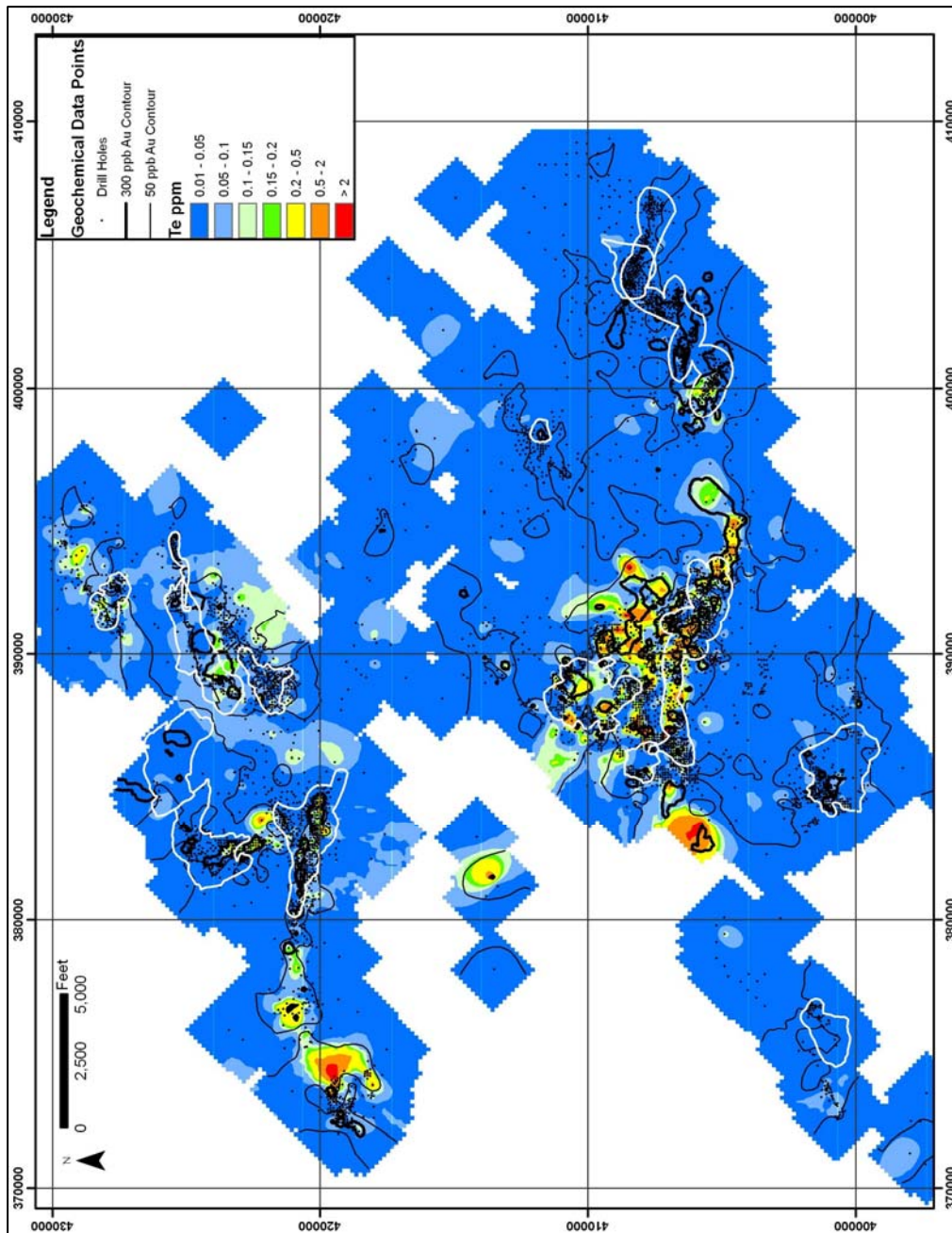
Figure 21g
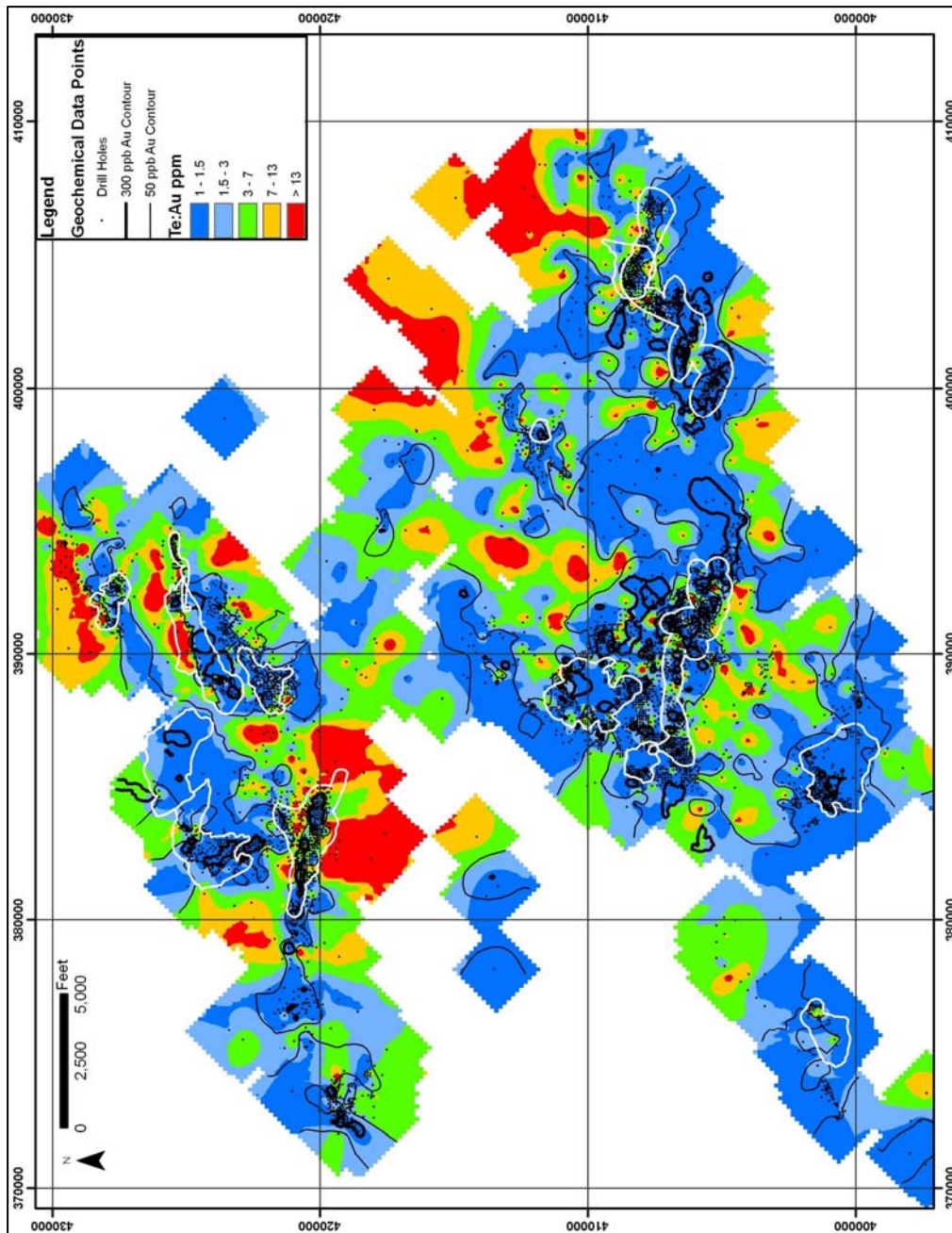
Figure 21h
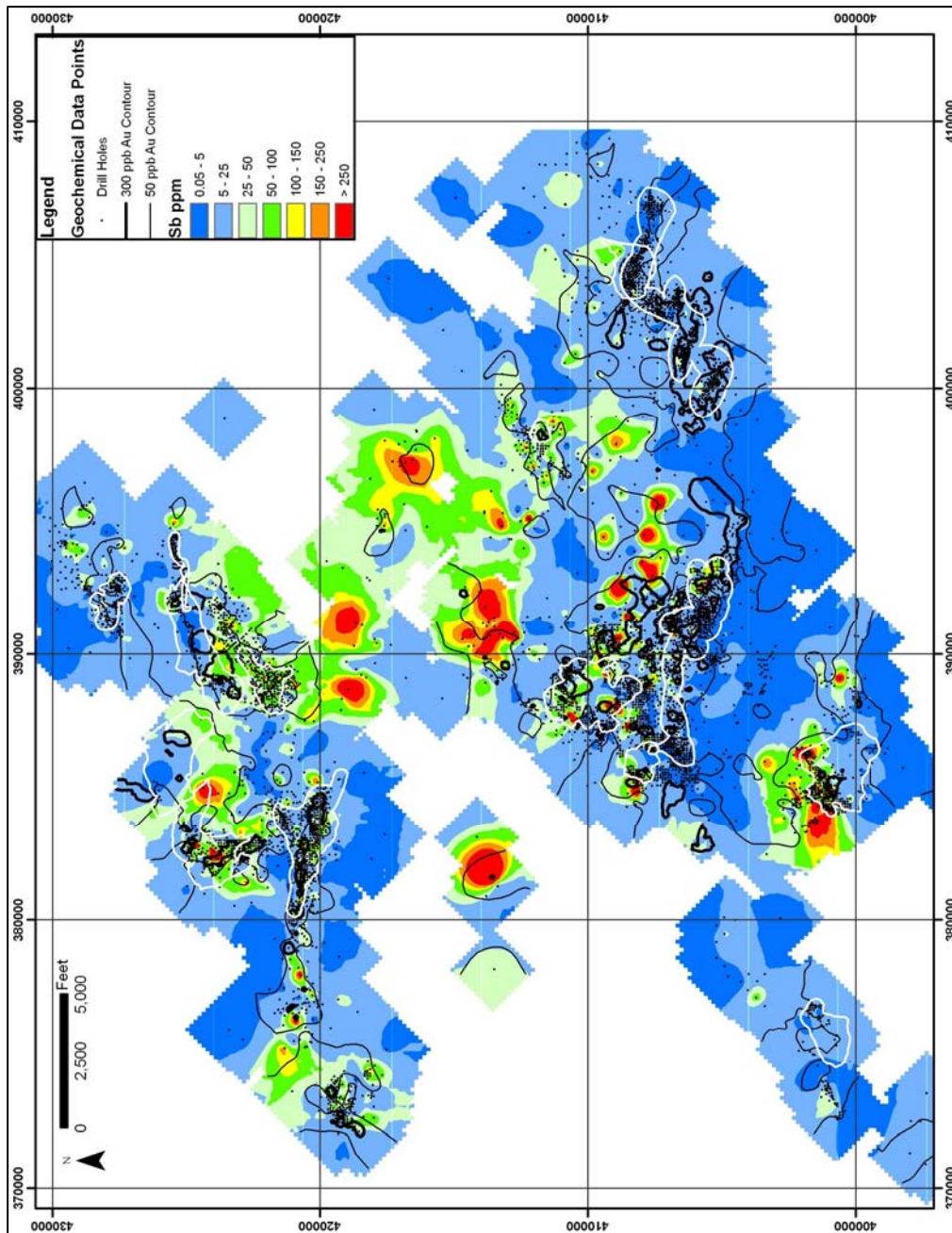
Figure 21i

Spatial Patterns of Elements Related to Hydrothermal Alteration

The elemental grids validate decarbonatization as the main alteration type associated with the Carlin-type gold deposits at Jerritt Canyon. Decarbonatization is the process by which dissolution of carbonates and removal of elements such as magnesium, calcium, and strontium occurs. Therefore, areas of depleted calcium, magnesium, and strontium are good proxies for identifying localities where decarbonatization has taken place. In the vertical projection of known gold deposits calcium, magnesium, and strontium values are low or depleted (Fig. 22a, 22b, & 22c). Also, where gold values are greater than 50 ppb calcium, magnesium, and strontium values are low or depleted (Fig. 22a, 22b, & 22c). A good example of this relationship can be examined in the Murray mine and in the Steer/Saval/SSX area. In general, where gold values are greater than 50 ppb, calcium is less than 8%, magnesium is less than 3.5% (except the Smith and Dash deposits), and strontium is less than 100 ppm (Figs. 22a, 22b, & 22c). The calcium to gold ratio grid shows that within the 300 ppb contour the gold values are extremely higher than calcium values with a ratio minimum of 355 (Fig. 22d). In the SSX-Smith areas calcium values begin to rise within 500 feet of the 300 ppb contour (Fig. 22d). In the Murray-Winters Creek area calcium values begin to rise 0 to 800 feet from the 300 ppb contour (Fig. 22d). The ratio of calcium to gold + thallium + mercury + arsenic + tellurium (CTEs) was also taken and is shown in figure 25h. The calcium to CTEs ratio shows that ratio values begin to increase, but not consistently, 0 to 600 feet in the SSX-Smith area and 0 to 1,000 feet from gold values greater than 300 ppb (Fig 22e). Both the ratio images show that calcium values increase more rapidly then gold CTE values decrease outboard of the deposits.

Figure 22:

a. Calcium classified grid with 300 and 50 ppb gold contours and white deposit outlines. Legend is for calculated grid values, not actual values.

b. Magnesium classified grid with 300 and 50 ppb gold contours and white deposit outlines. Legend is for calculated grid values, not actual values.

c. Strontium classified grid with 300 and 50 ppb gold contours and white deposit outlines. Legend is for calculated grid values, not actual values.

d. Ca:Au ratio grid with 300 and 50 ppb gold contours and white deposit outlines. Legend is for calculated grid values, not actual values.

e. Ca:CTE ratio grid with 300 and 50 ppb gold contours and white deposit outlines. Legend is for calculated grid values, not actual values.

Figure 22a

70
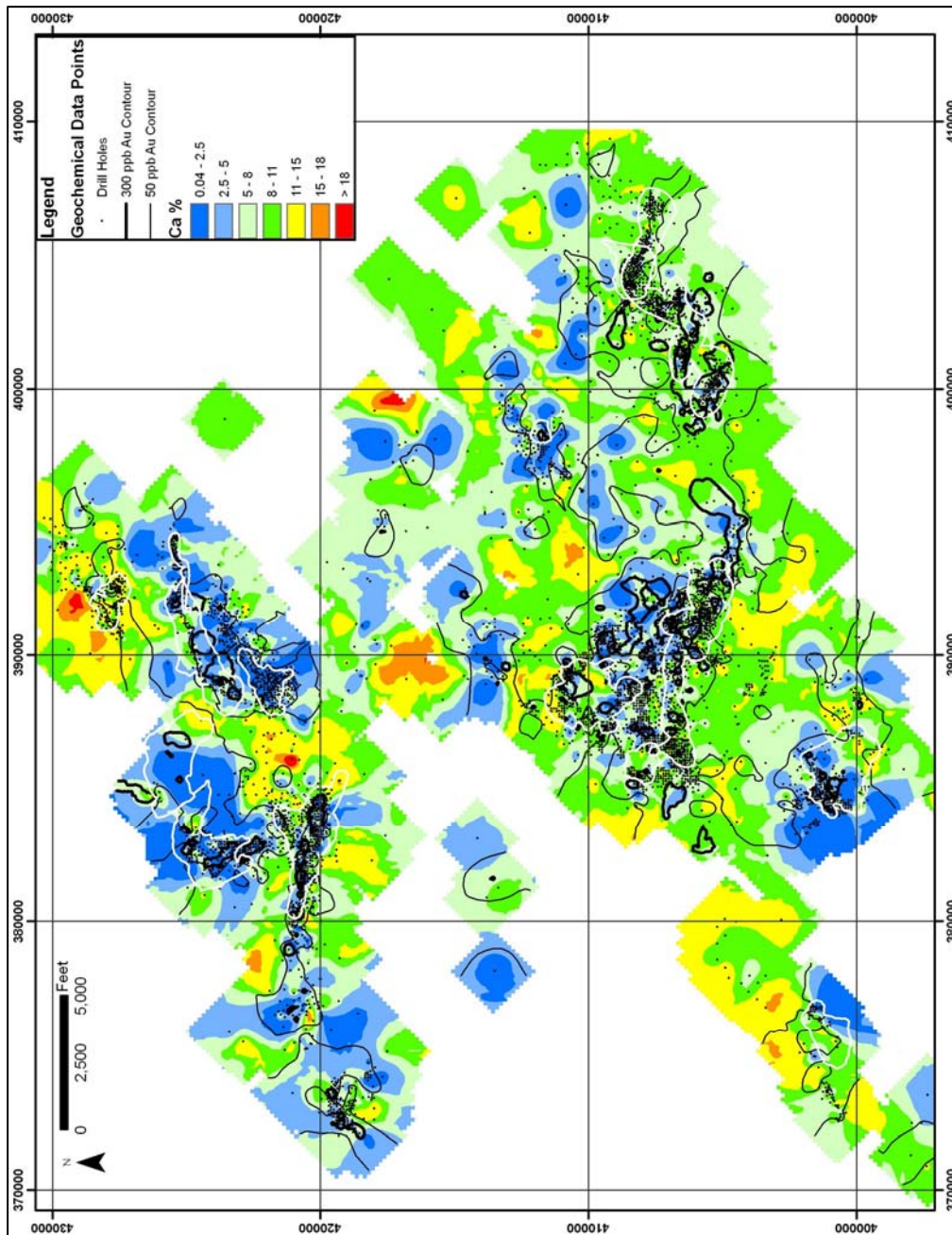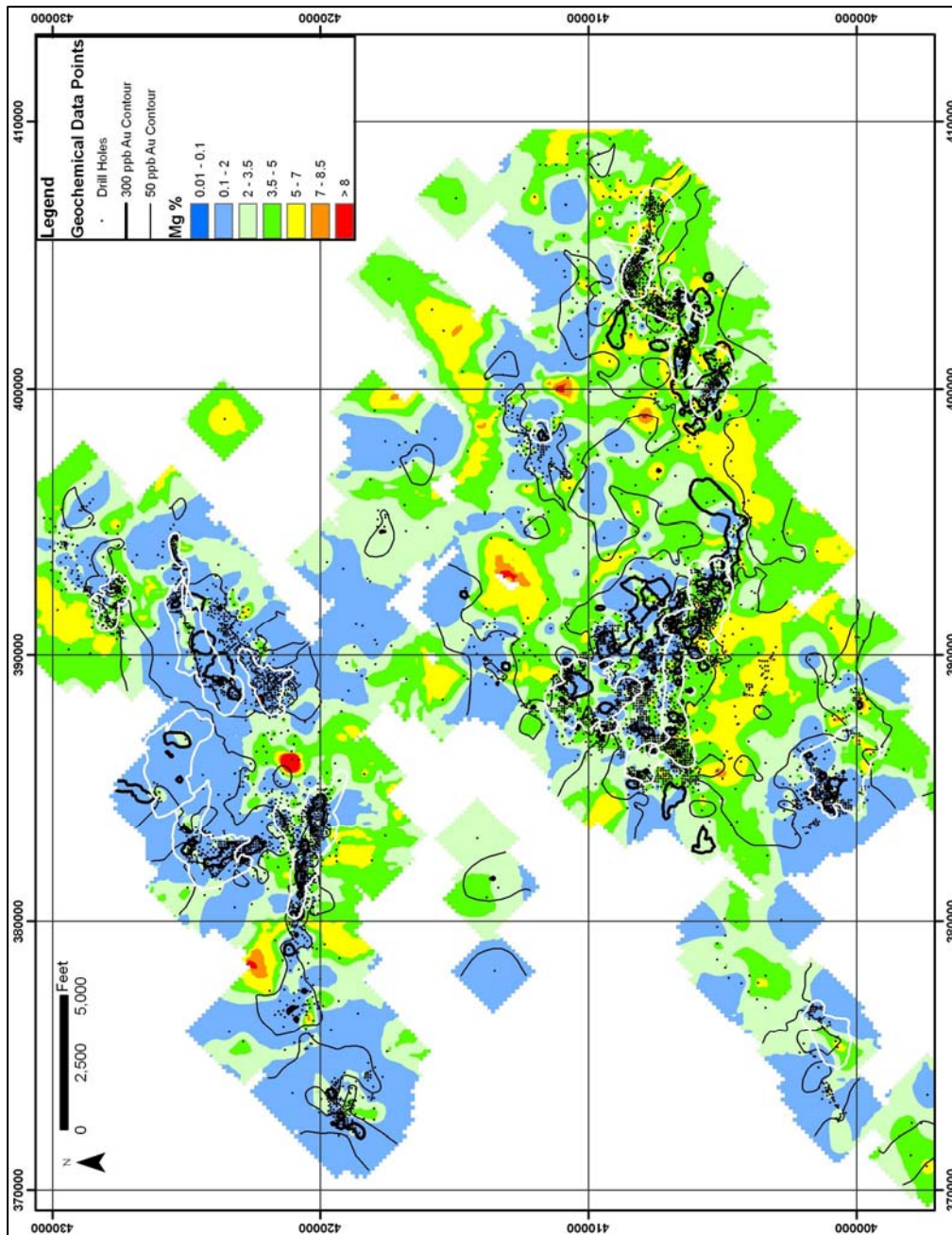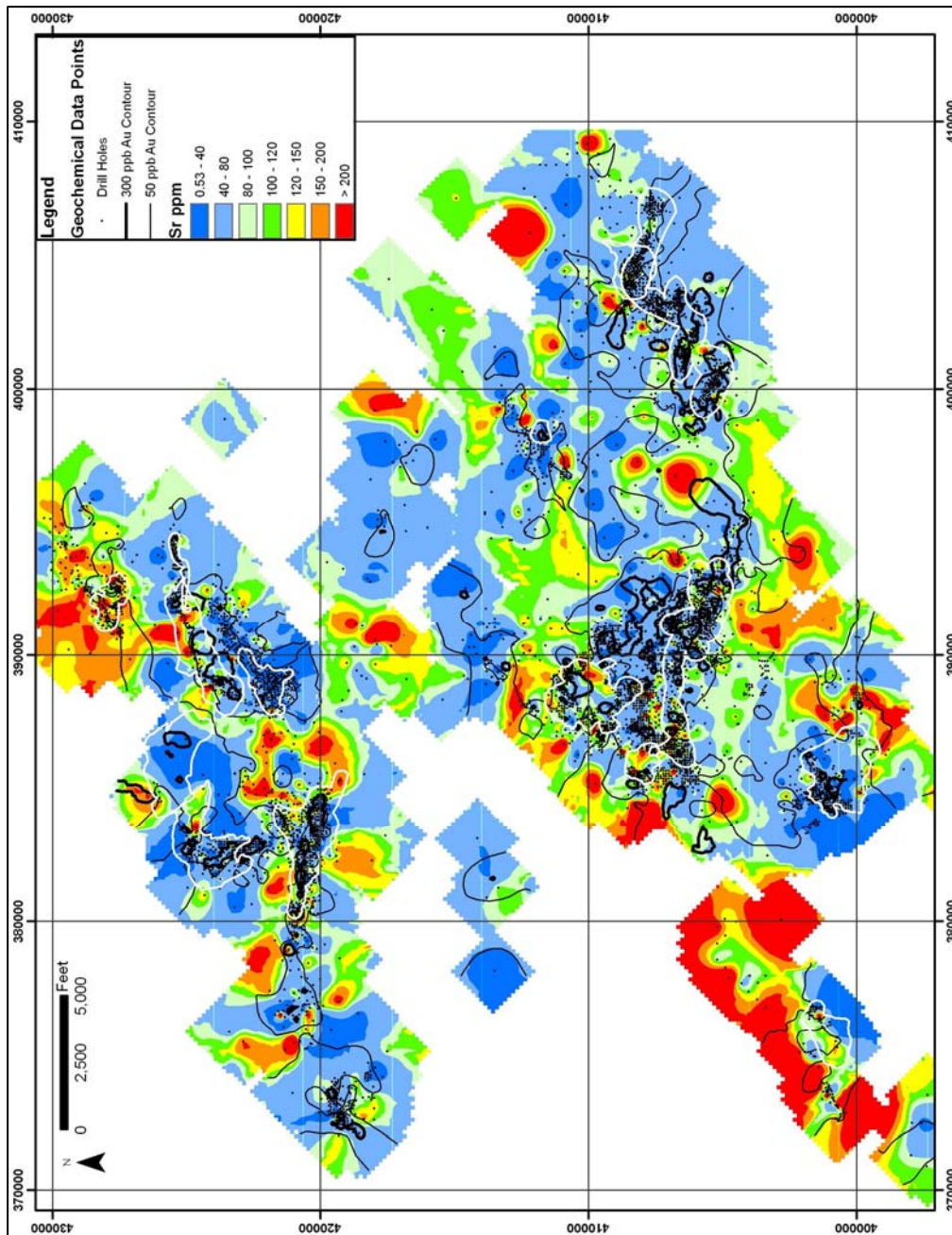
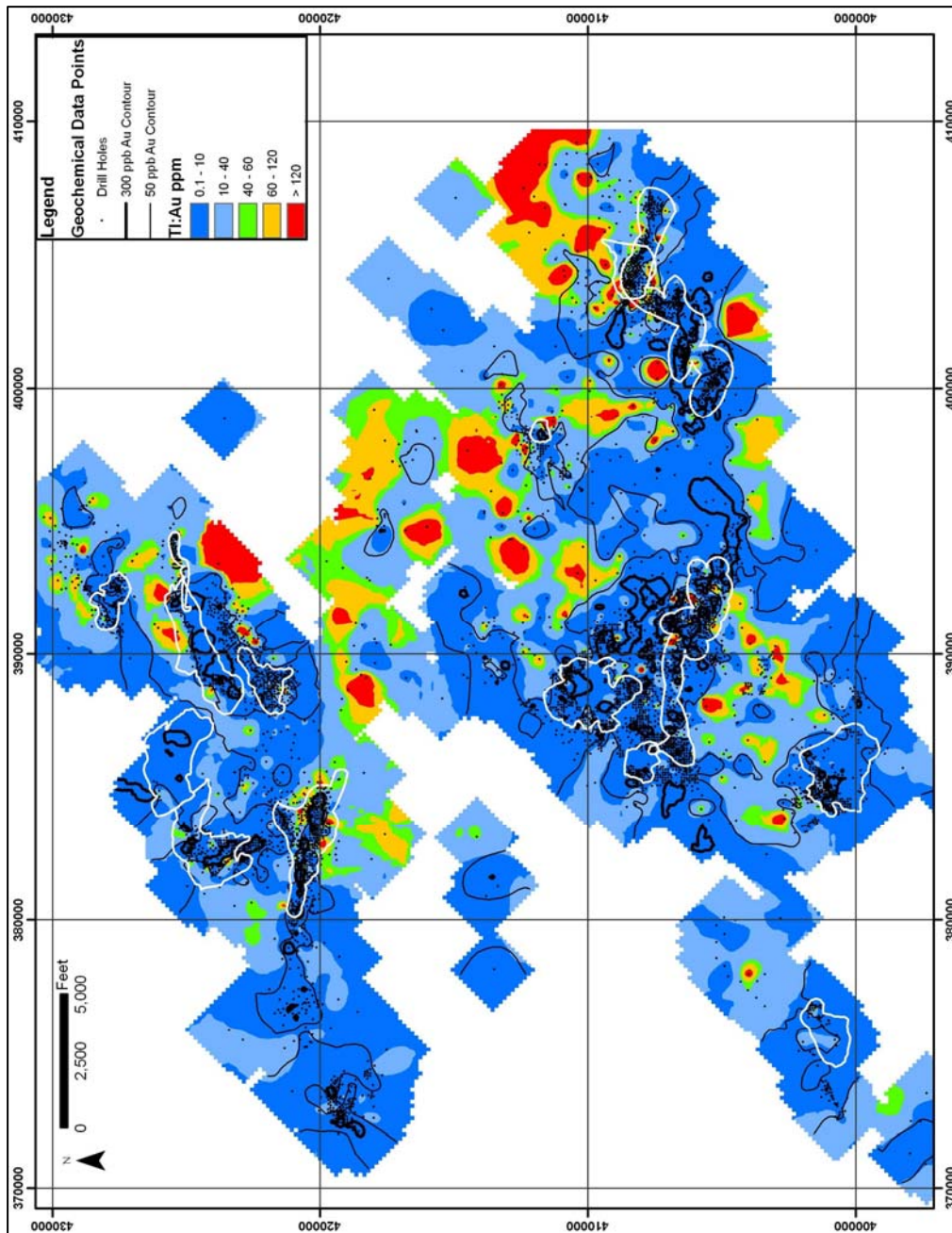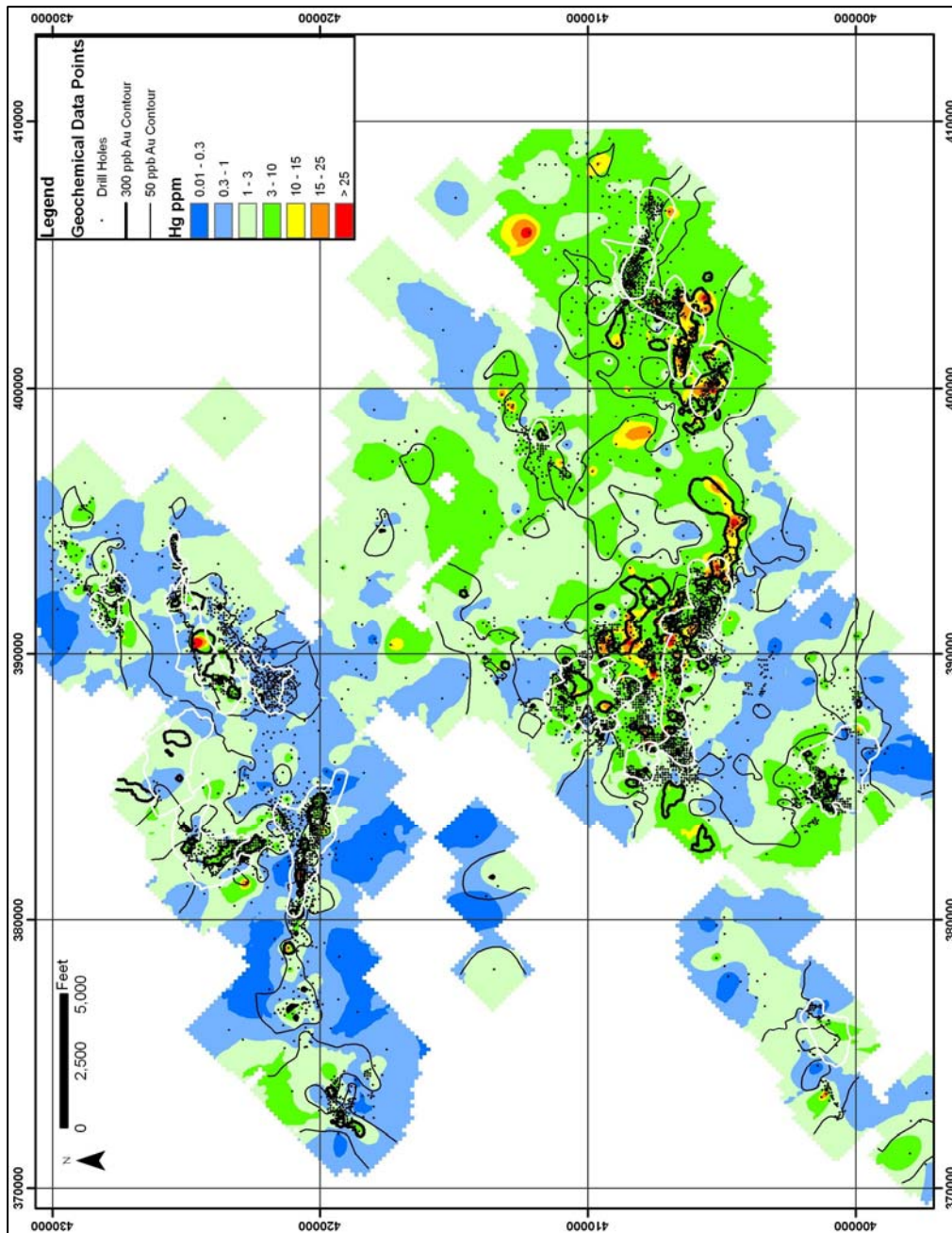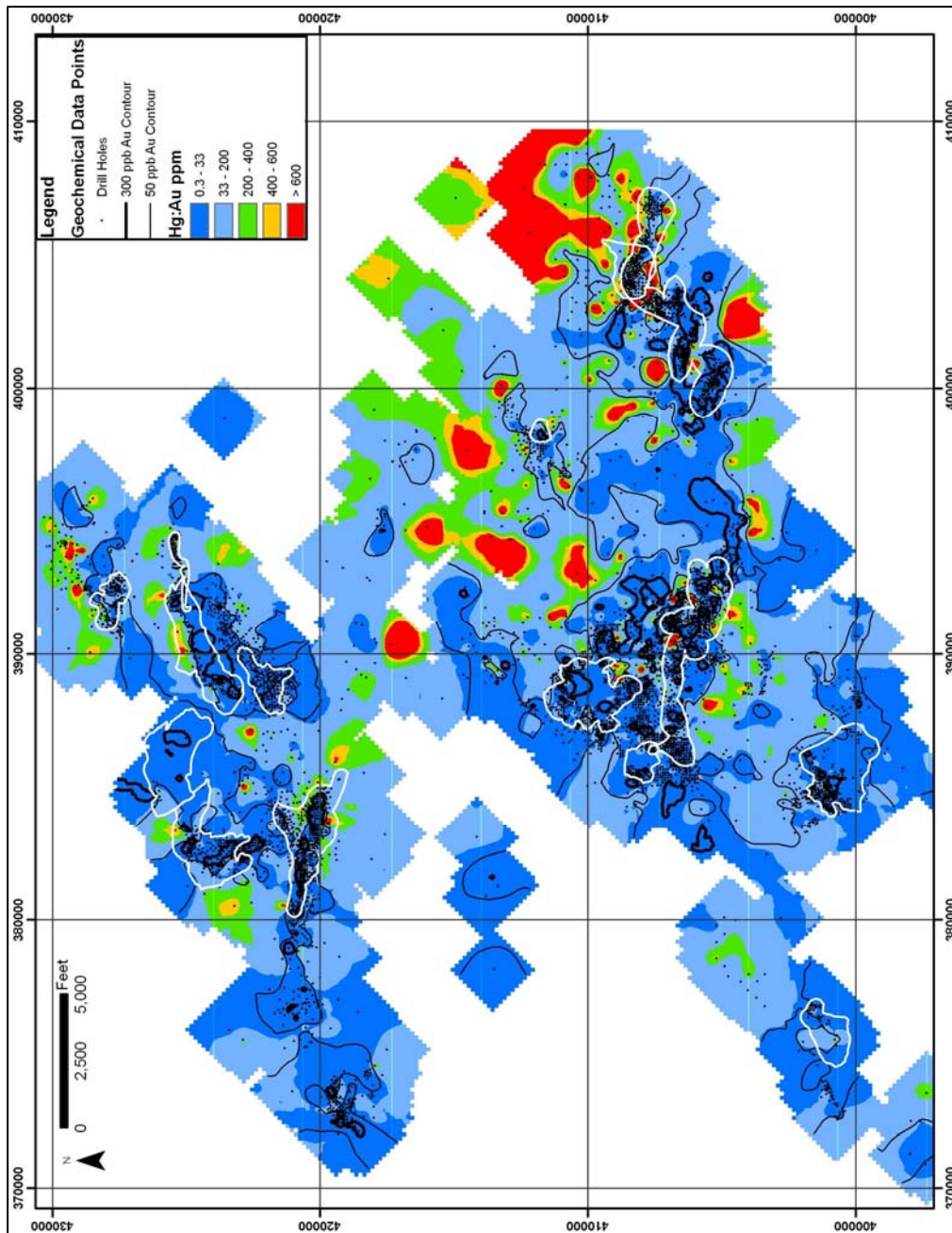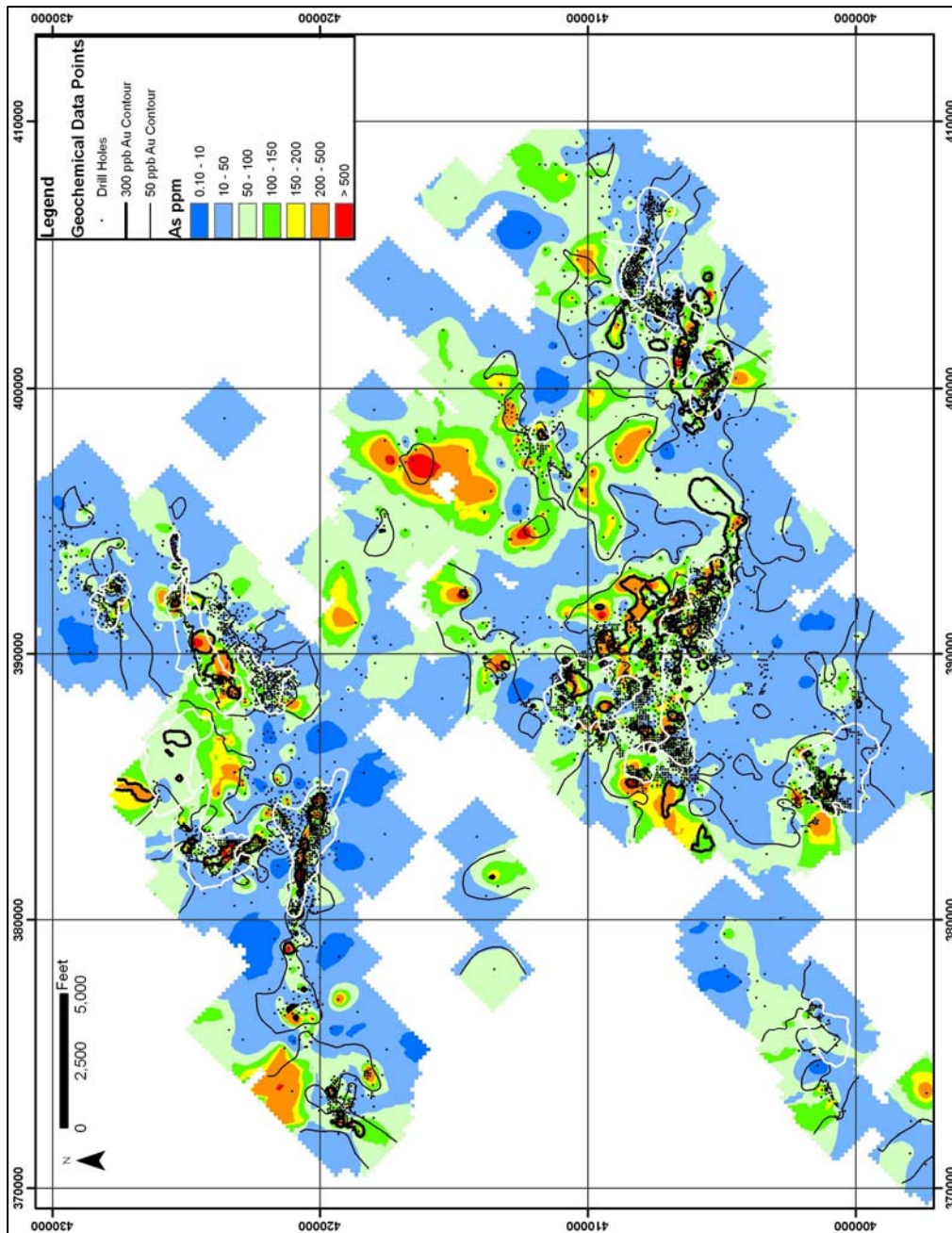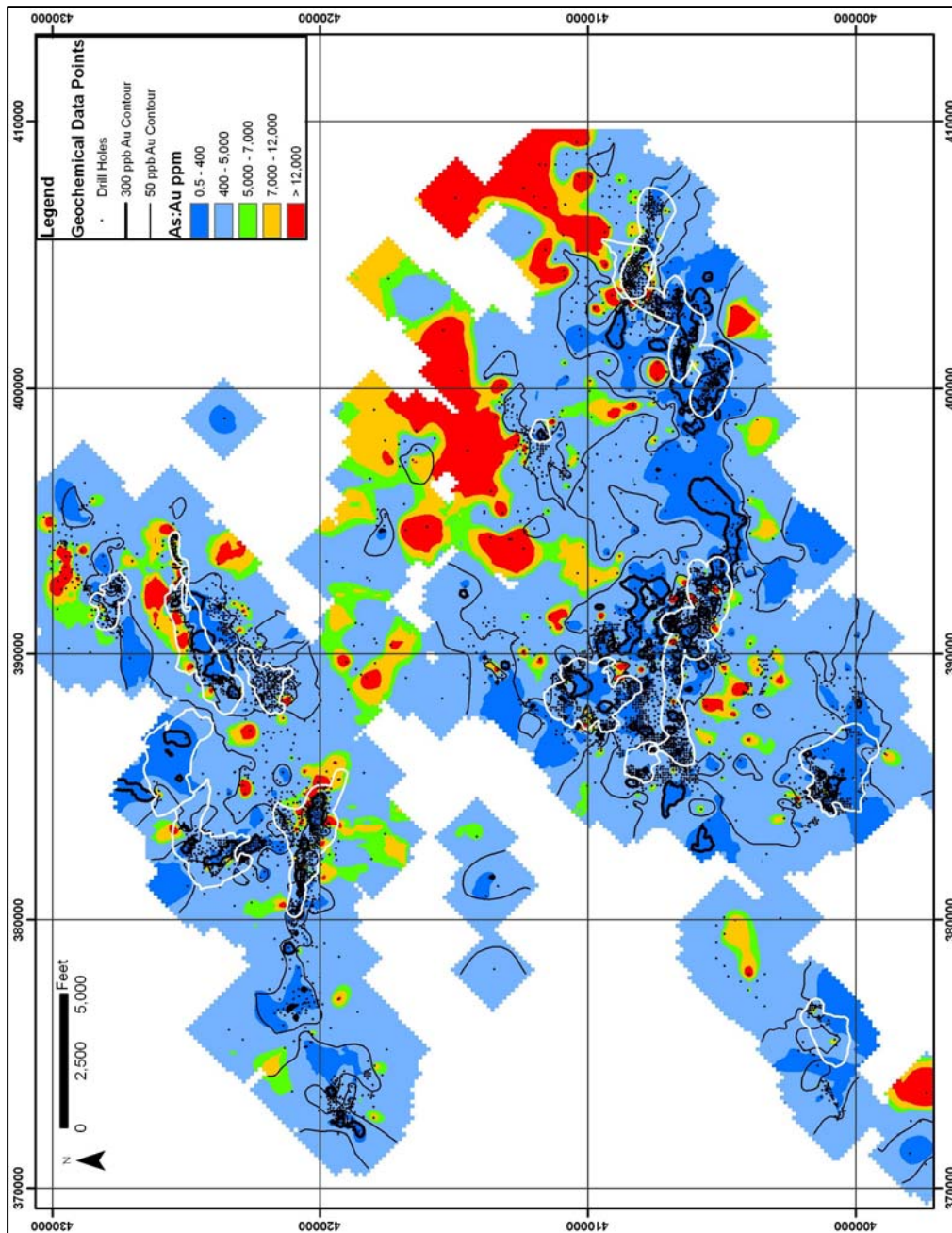Figure 22b

Figure 22c
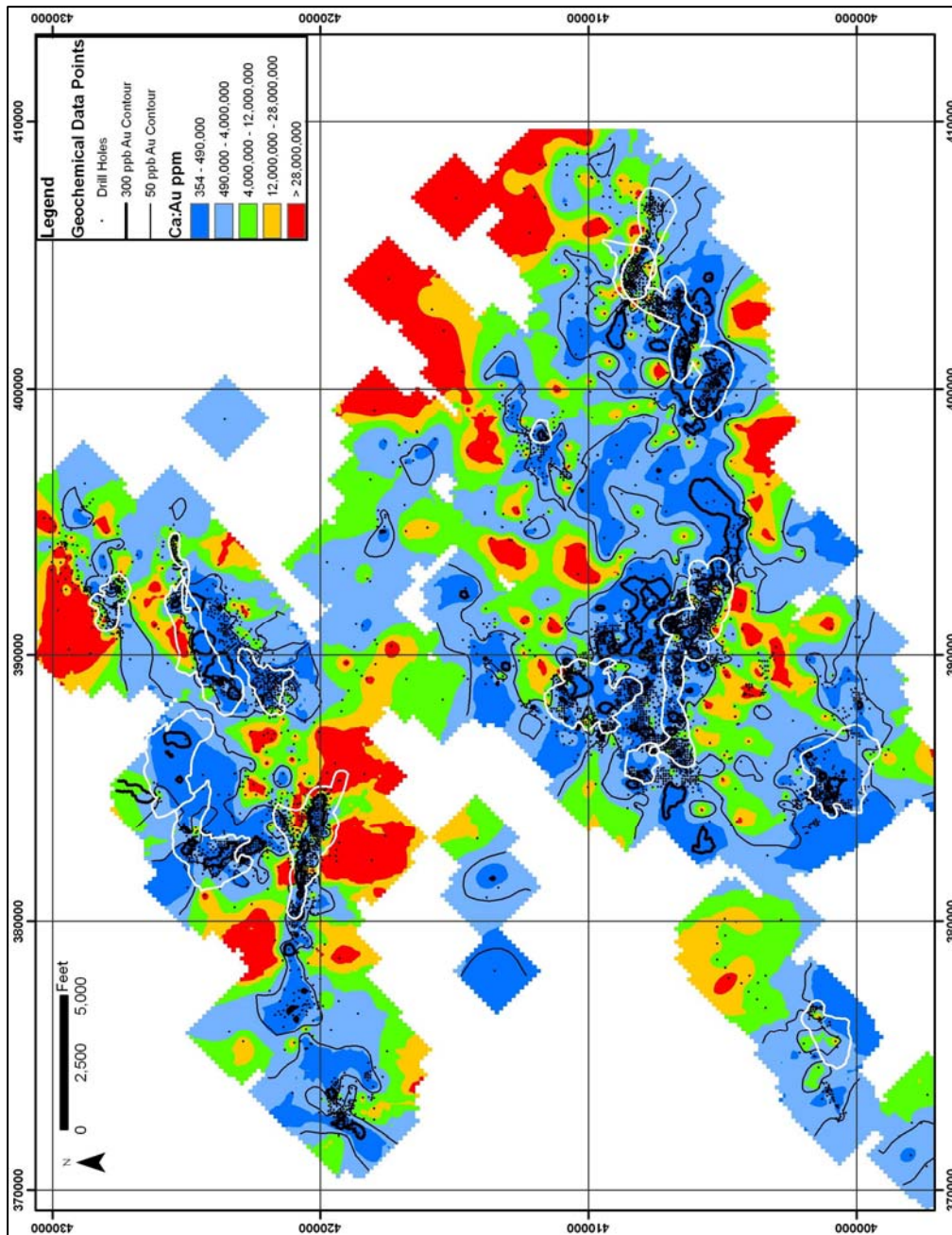
Figure 22d
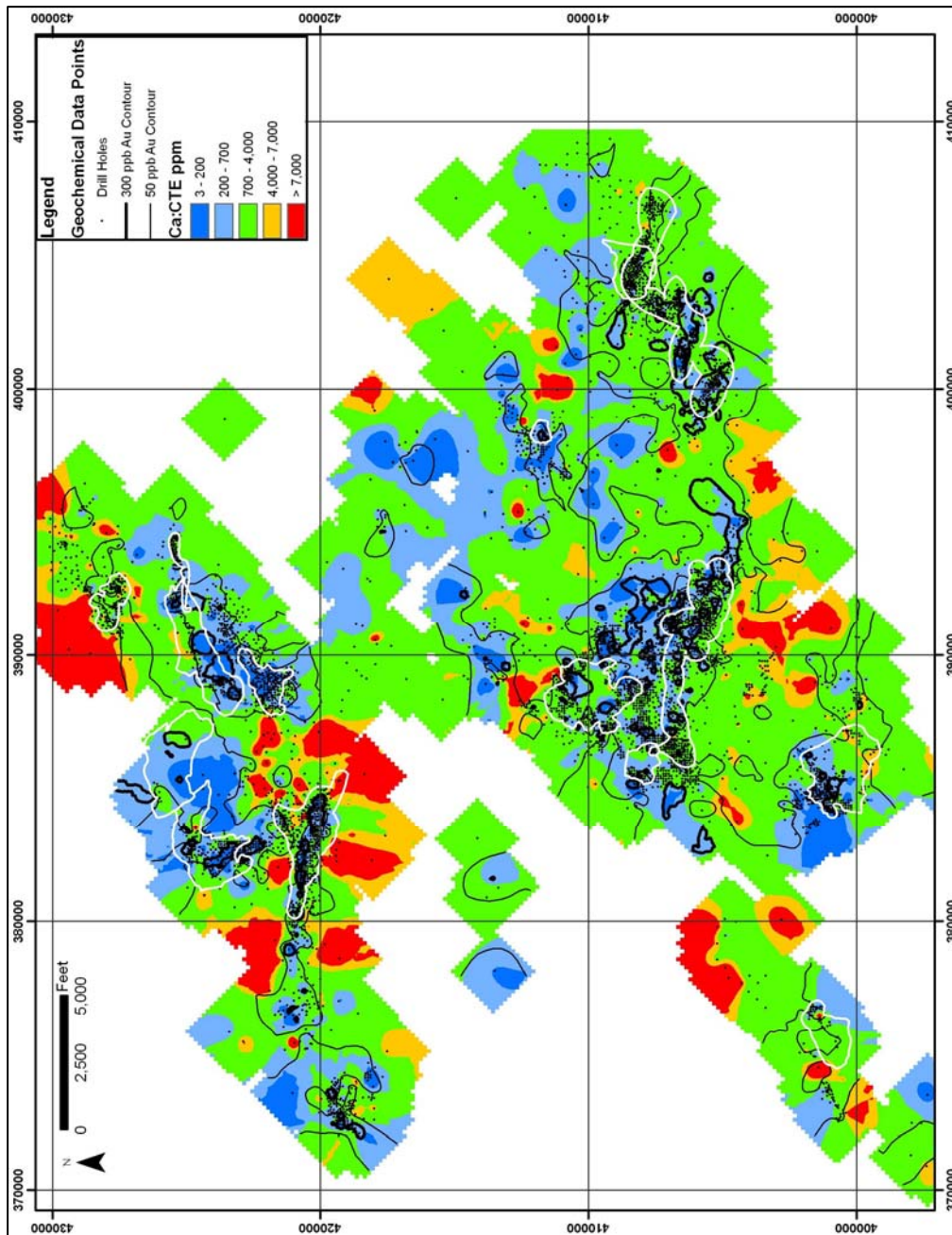
Figure 22e

Black Shale Elements-Gridding Patterns

The following discussion addresses a group of mainly redox-sensitive elements that are commonly enriched in the organic component of many black shales world wide and share a similar spatial distribution in the Jerritt Canyon district. The group is herein termed the black shale elements (BSEs) and includes uranium, vanadium, zinc, molybdenum, phosphorous, lanthanum, bismuth, selenium, nickel, copper, cadmium, and silver (Figs. 23a, 23b, 23c, 23d, 23e, 23f, 23g, 23h, 23j, 23k, and 23l, respectively). These elements exhibit high values in the Murray-Winters Creek area, and Burns Basin area. The Burns Basin and Winters Creek areas are the only localities where bismuth, selenium, nickel, copper and cadmium exhibit thier highest values (23f, 23g, 23h, 23j, and 23k). The highest values exhibited by all of the BSEs are in and around the Winters Creek deposit. The Murray mine is the only deposit where black shale elements share a similar spatial pattern to elements associated with gold mineralization. At Murray, uranium, molybdenum, and phosphorous all exhibit the same west-northwest linear trend as the elements associated with gold mineralization. The black shale elements excluding silver are all locally elevated in the vicinity of the SSX-Smith mines, exhibiting discontinuous, spotty patterns. Silver does exhibit a spatial distribution similar to gold in the SSX-Smith areas (Fig. 23l); however, the relationship is not statistically validated as will be addressed below. All the black shale elements are elevated at Winters Creek and exhibit an almost identical pattern in this area, forming a northeast trend that extends for about 7,000 feet. Phosphorous, lanthanum, and uranium form similar pattern, which is expected because they are commonly found together in apatite.

Figure 23: All images shown with deposit outlines. Legends are for calculated grid values, not actual values.

a. Uranium classified gridded image.

b. Vanadium classified gridded image.

c. Zinc classified gridded image.

d. Molybdenum classified gridded image.

e. Phosphorous classified gridded image.

f. Lanthanum classified gridded image.

g. Bismuth classified gridded image.

h. Selenium classified gridded image.

i. Nickel classified gridded image.

j. Copper classified gridded image.

k. Cadmium classified gridded image.

l. Silver classified gridded image.
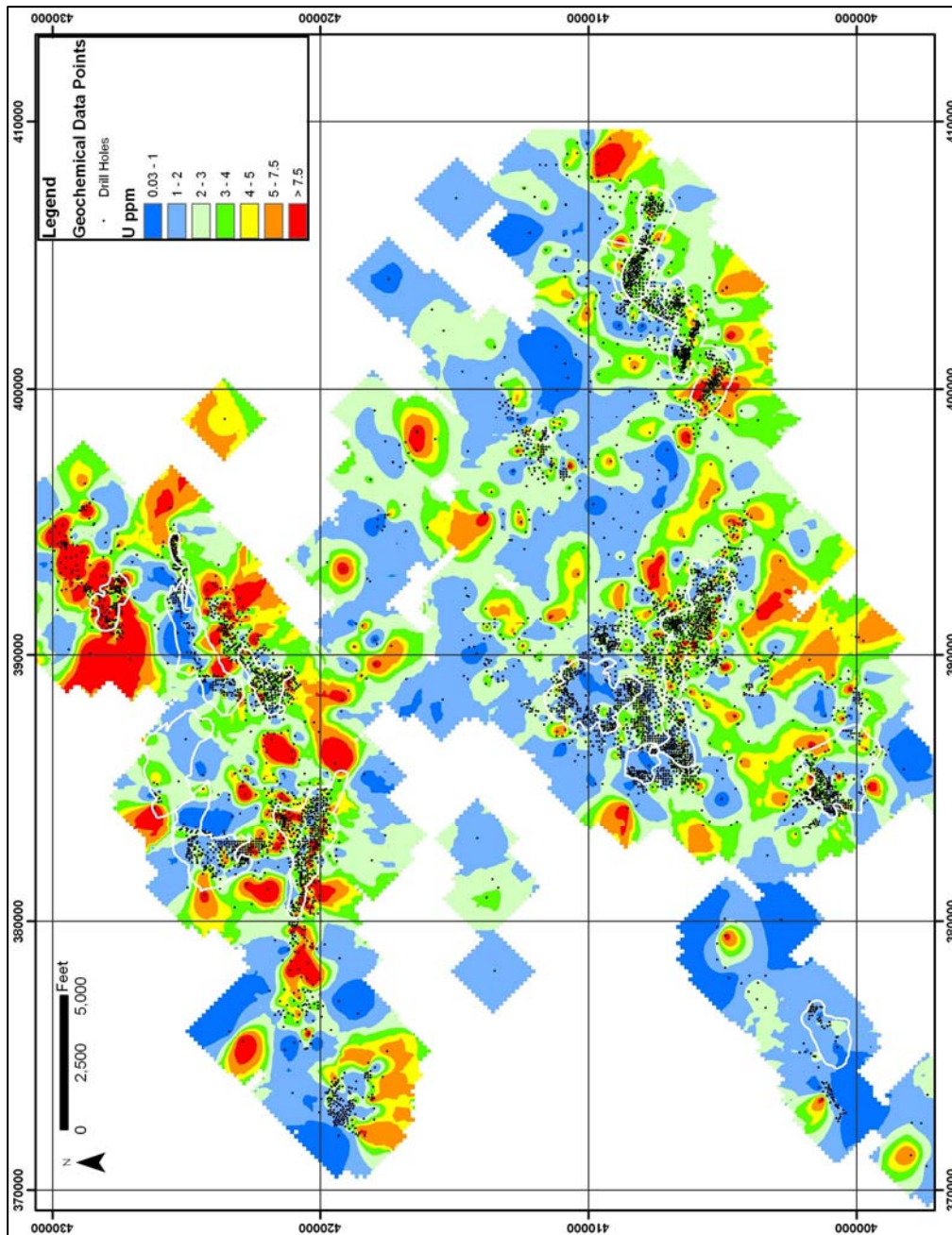
Figure 23a
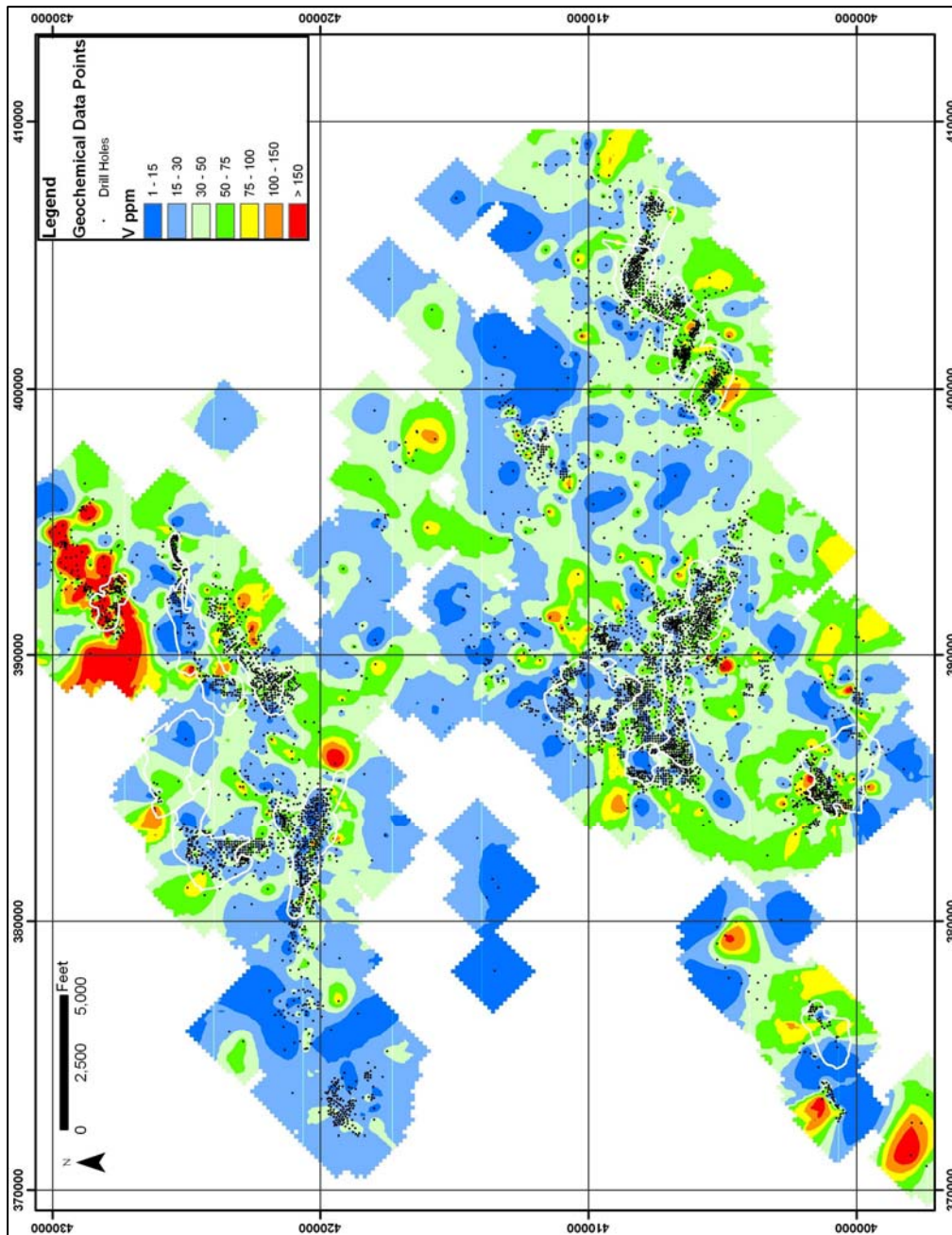
Figure 23b
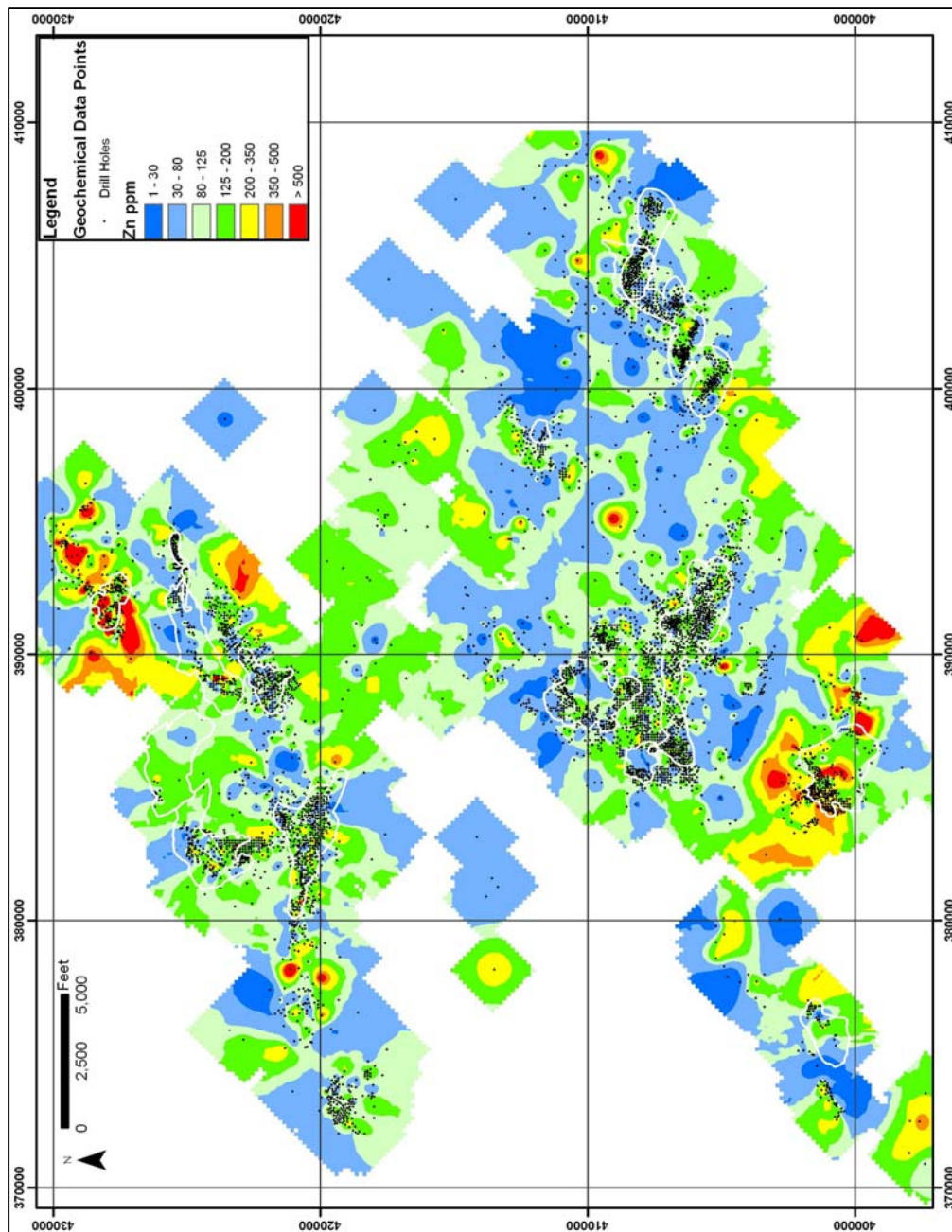
Figure 23c

Figure 23d

Figure 23e
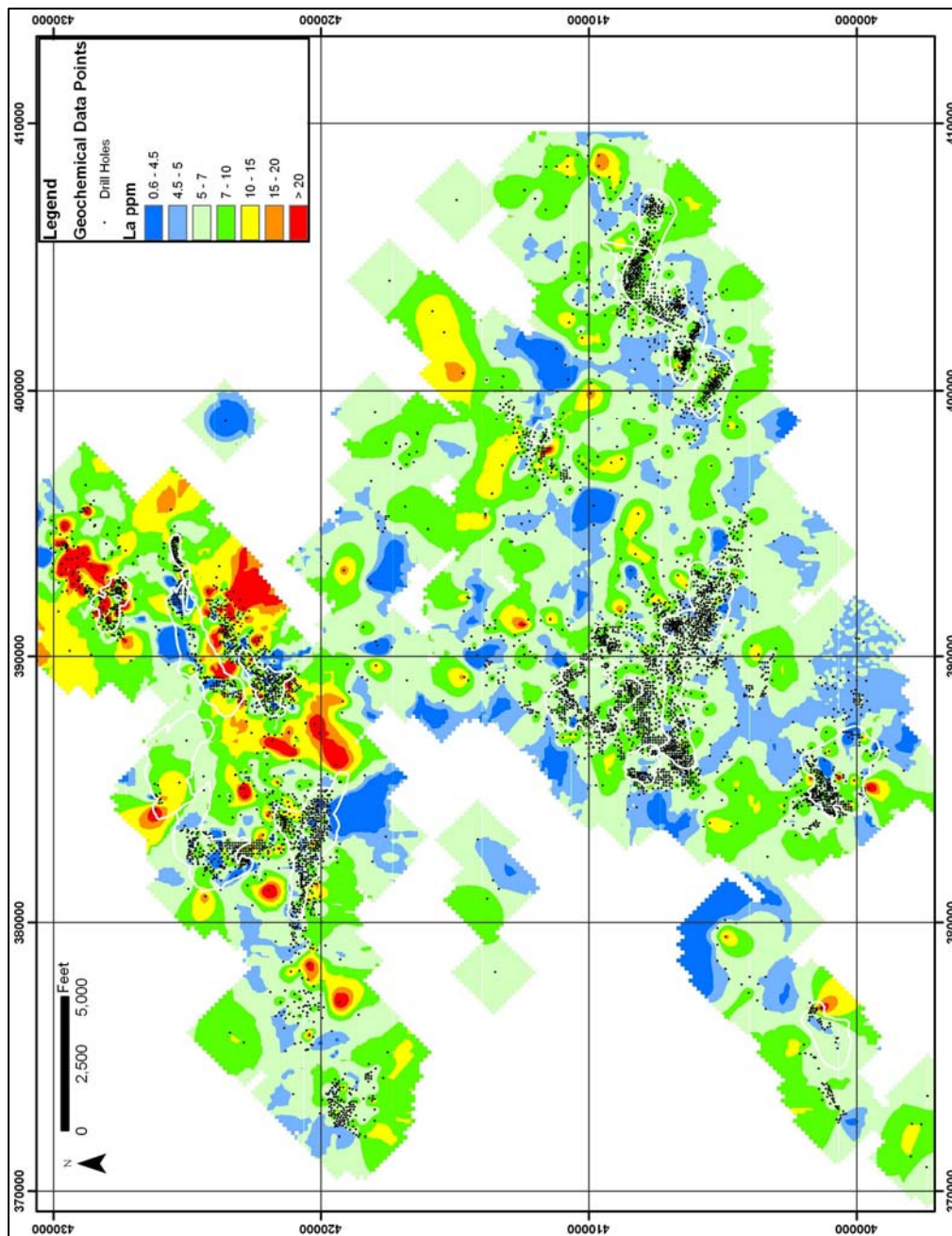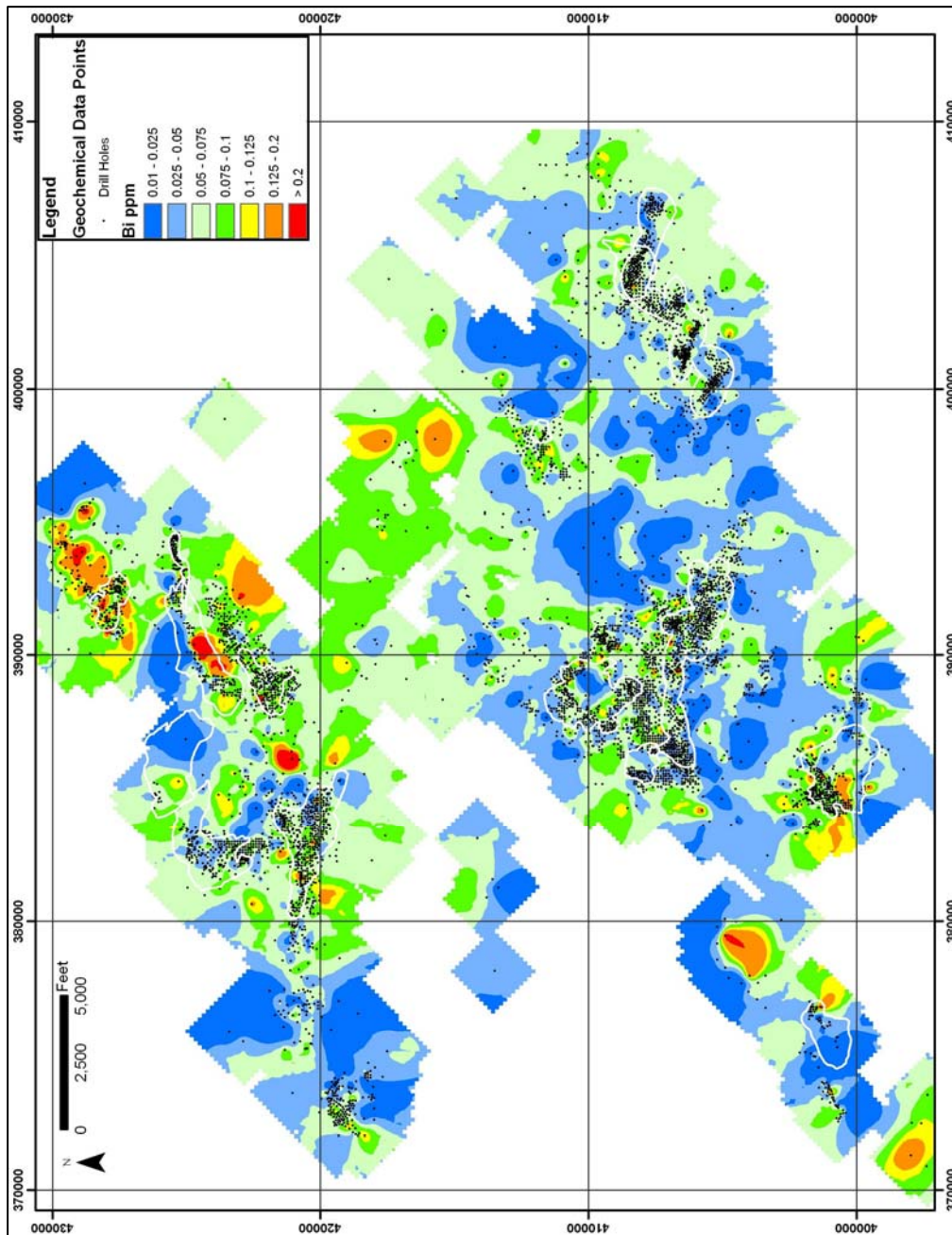
Figure 23f

Figure 23g
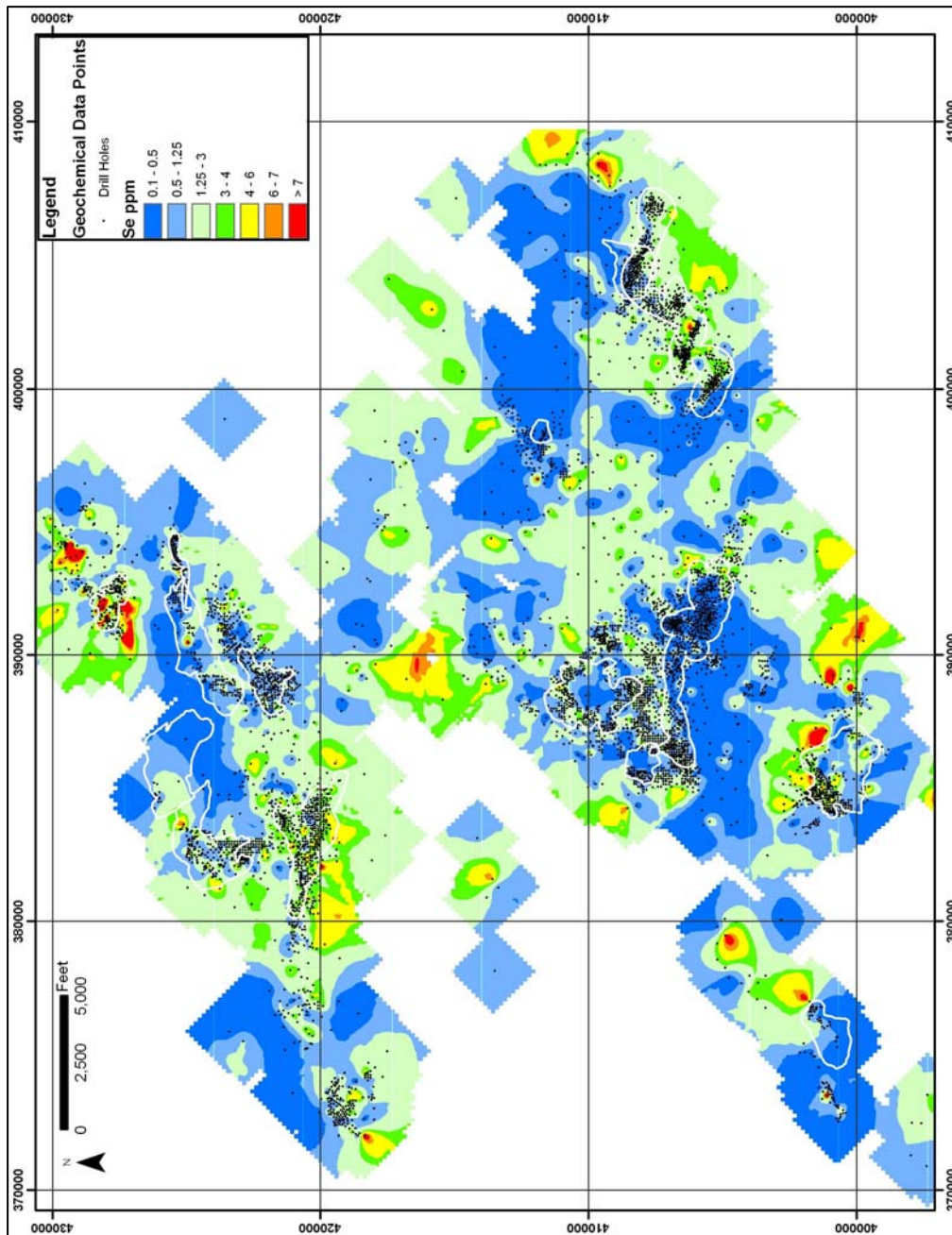
Figure 23h
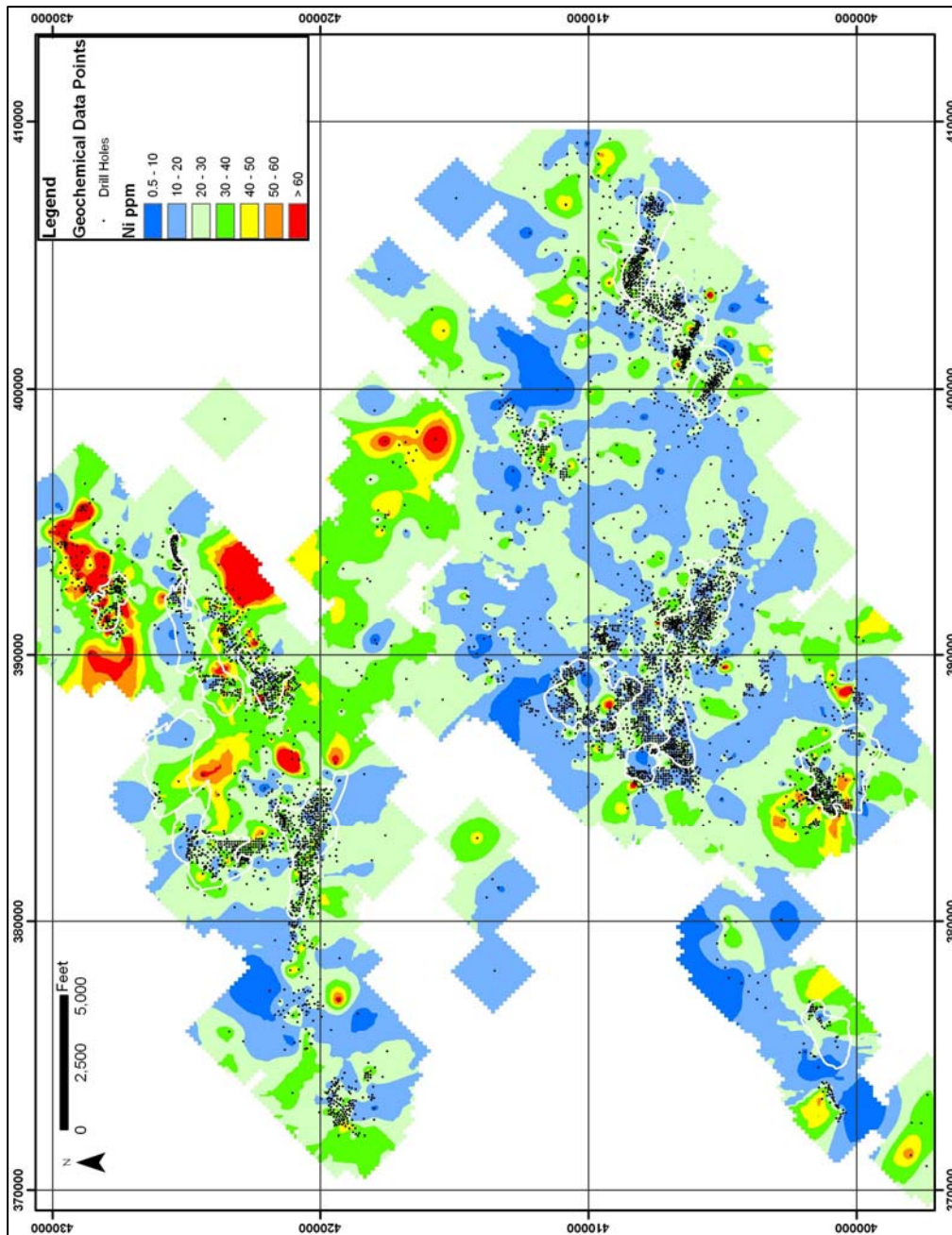
Figure 23i
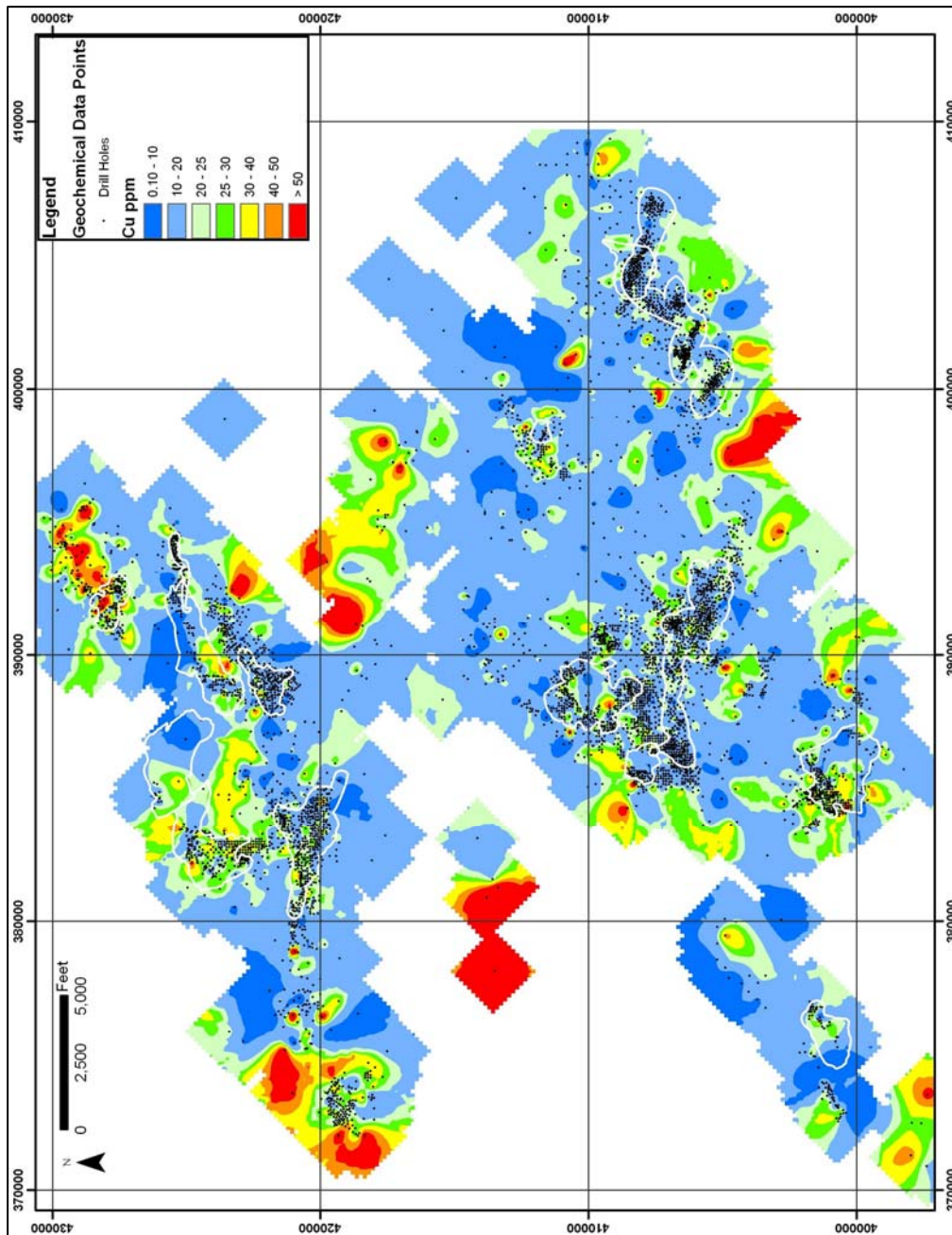
Figure 23j
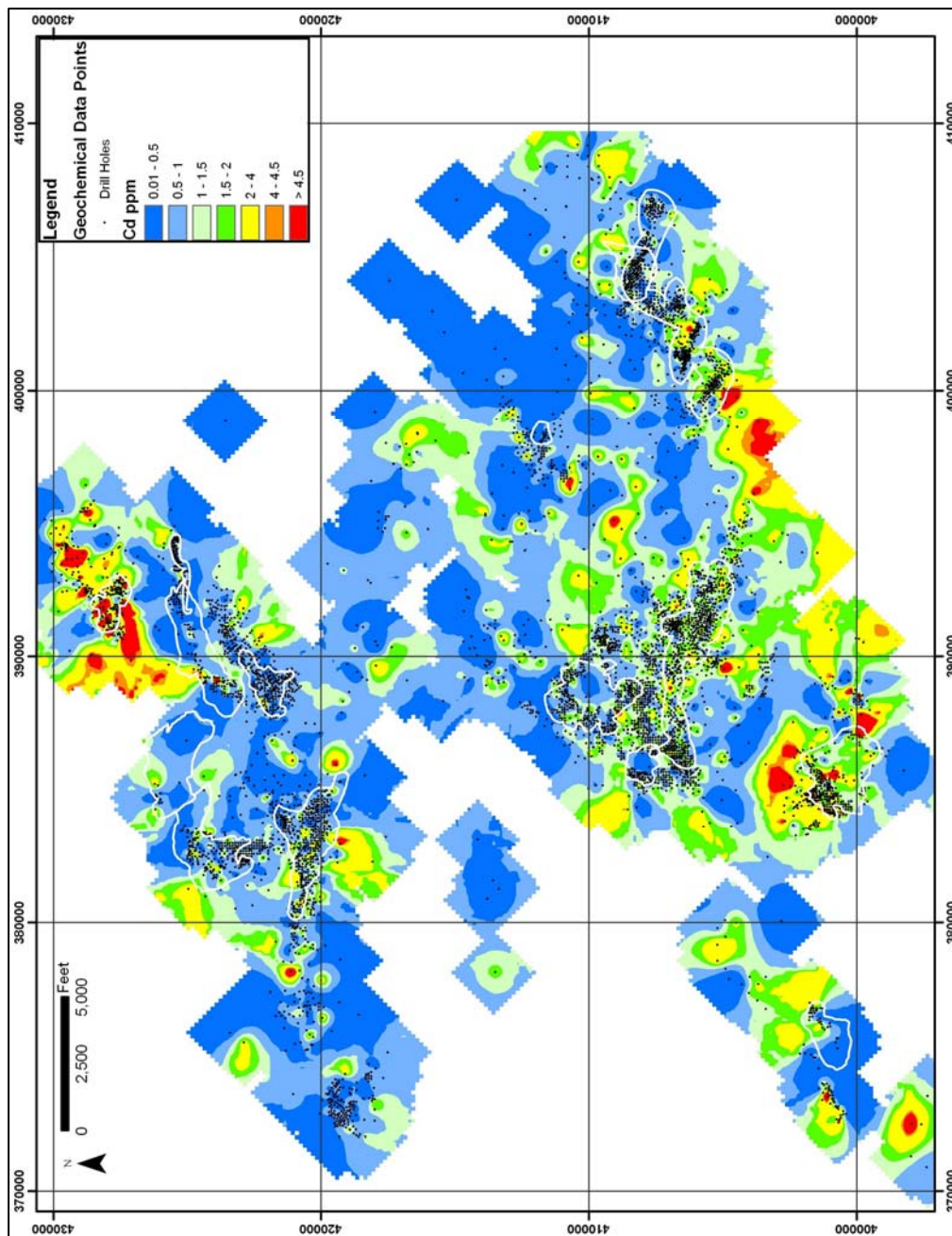
Figure 23k
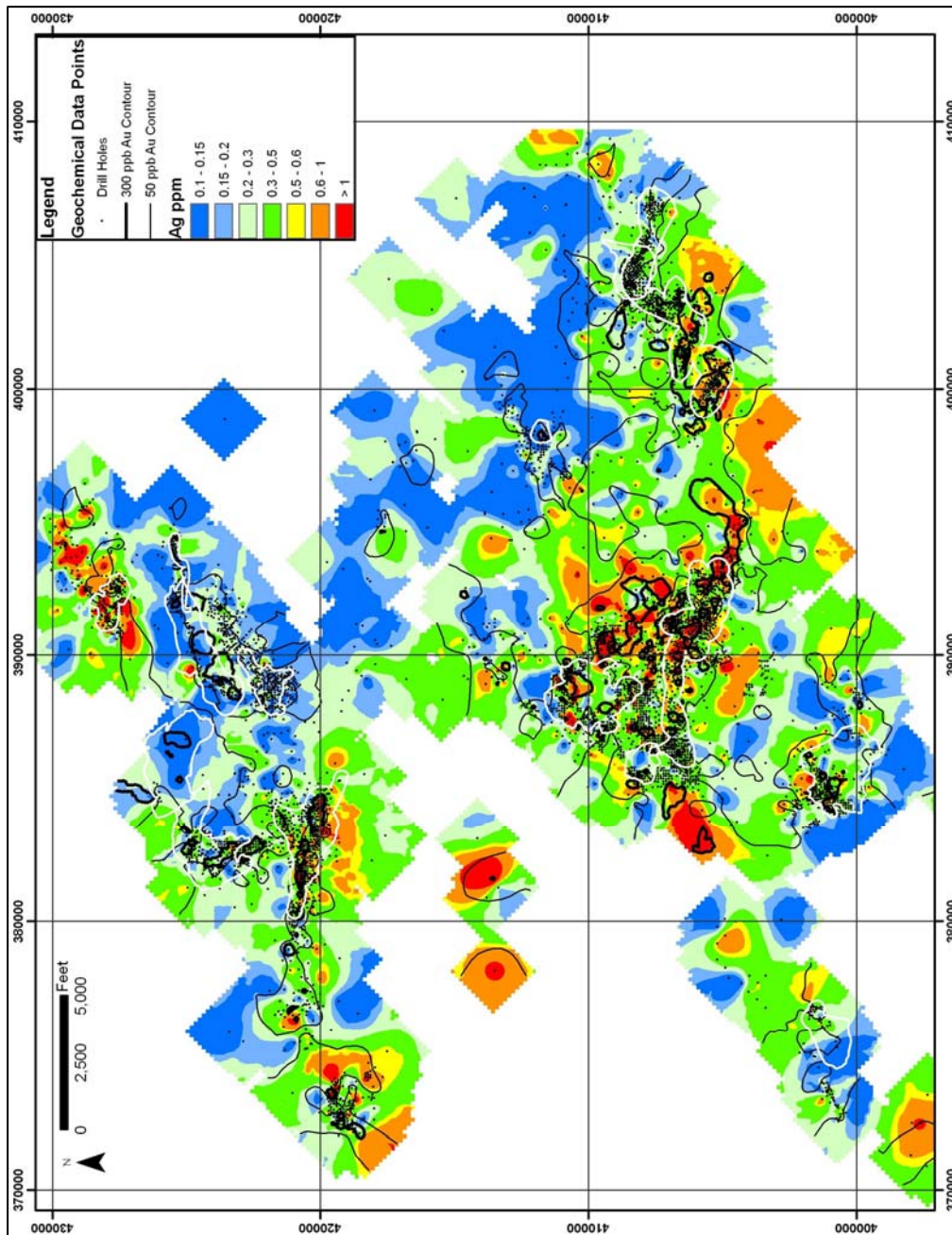
Figure 23

<u>Effects on Elemental Distributions Due to Oxidation</u>

It is important to address whether or not supergene oxidation had any effect on the distribution of the elements observed in the gridded images. Most of the rocks logged during this study were unoxidized. When limonite was present the entire rock was oxidized and there was no evidence of leached cavities or limonite after pyrite. To further validate whether or not elements were remobilized during supergene oxidation, cumulative distribution plots were generated for gold, arsenic, uranium, zinc, and copper (Fig. 24a, 24b, 24c, 24d, & 24e, respectively) from samples that were logged in the Yukon-Nevada Gold logging data base as unoxidized, weakly oxidized, moderately oxidized or strongly oxidized. Arsenic, uranium, zinc and copper are mobile in an oxidizing environment. All of the cumulative distribution plots are similar, do not show evidence for significant elemental enrichments or depletions, and suggest that mobility of these elements was insignificant during oxidation. The cumulative distribution plots establish that supergene oxidation has had little to no effect on the distribution of the elements in the bottommost 5 feet of the DSrm, and the observed patterns are the result of hypogene processes.

Figure 24:

a. Cumulative distribution plot of gold values versus nature of oxidation.

b. Cumulative distribution plot of arsenic values versus nature of oxidation.

c. Cumulative distribution plot of uranium values versus nature of oxidation.

d. Cumulative distribution plot of zinc values versus nature of oxidation.

e. Cumulative distribution plot of copper values versus nature of oxidation.
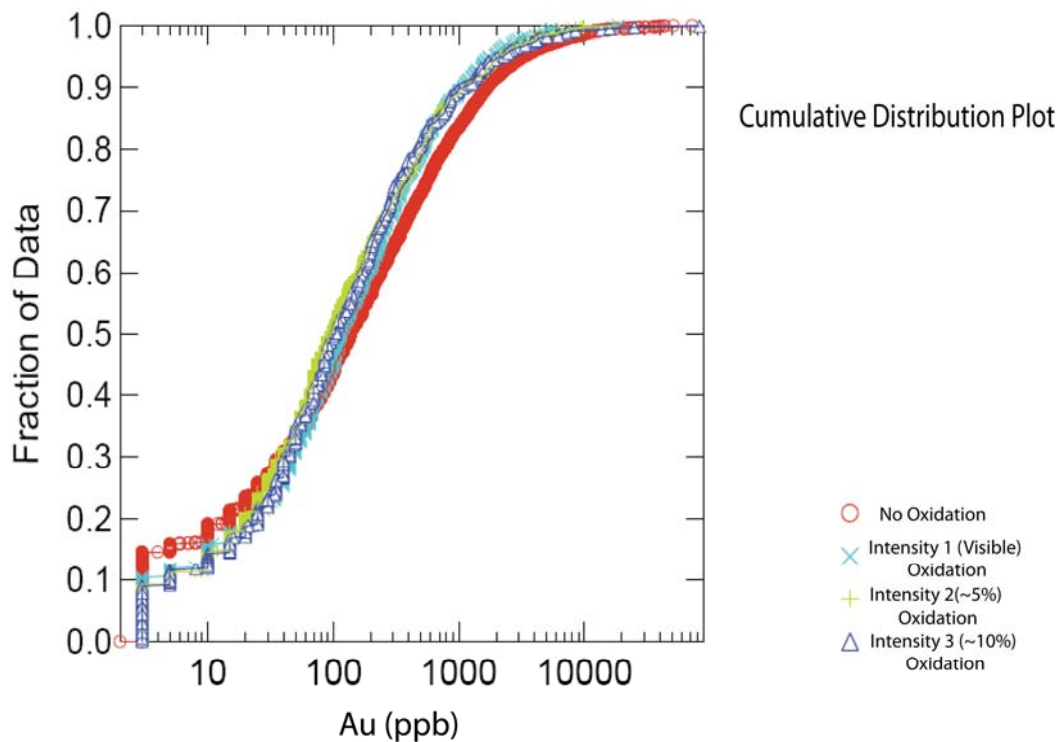
Figure 24a
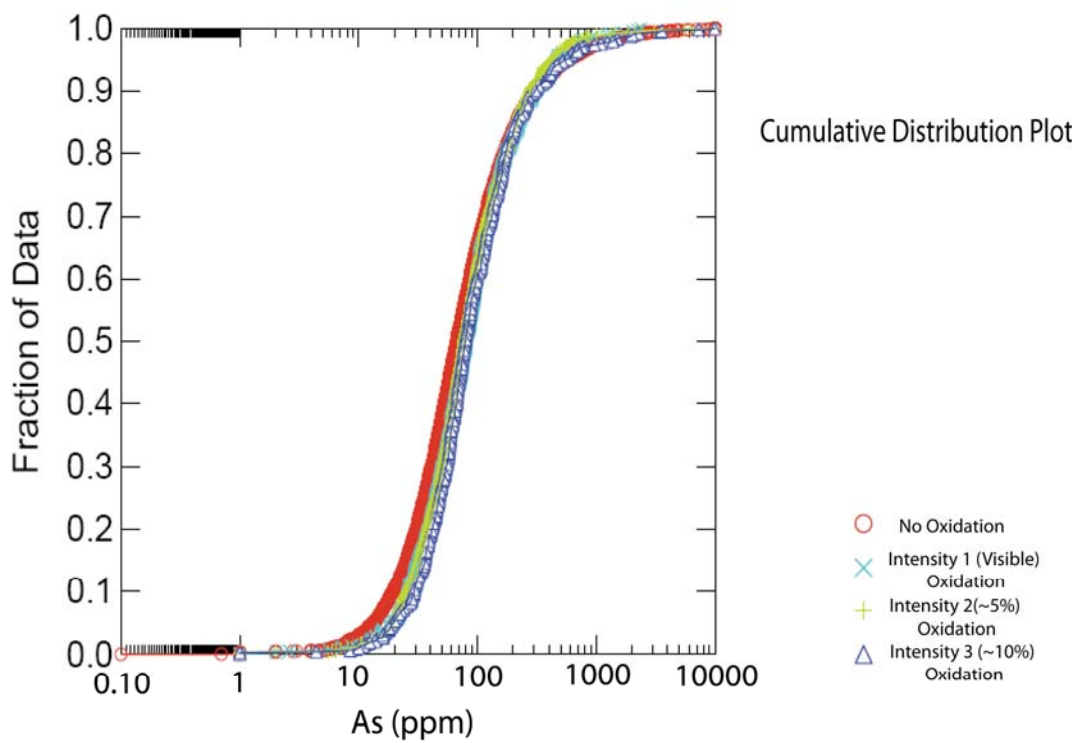
Figure 24b
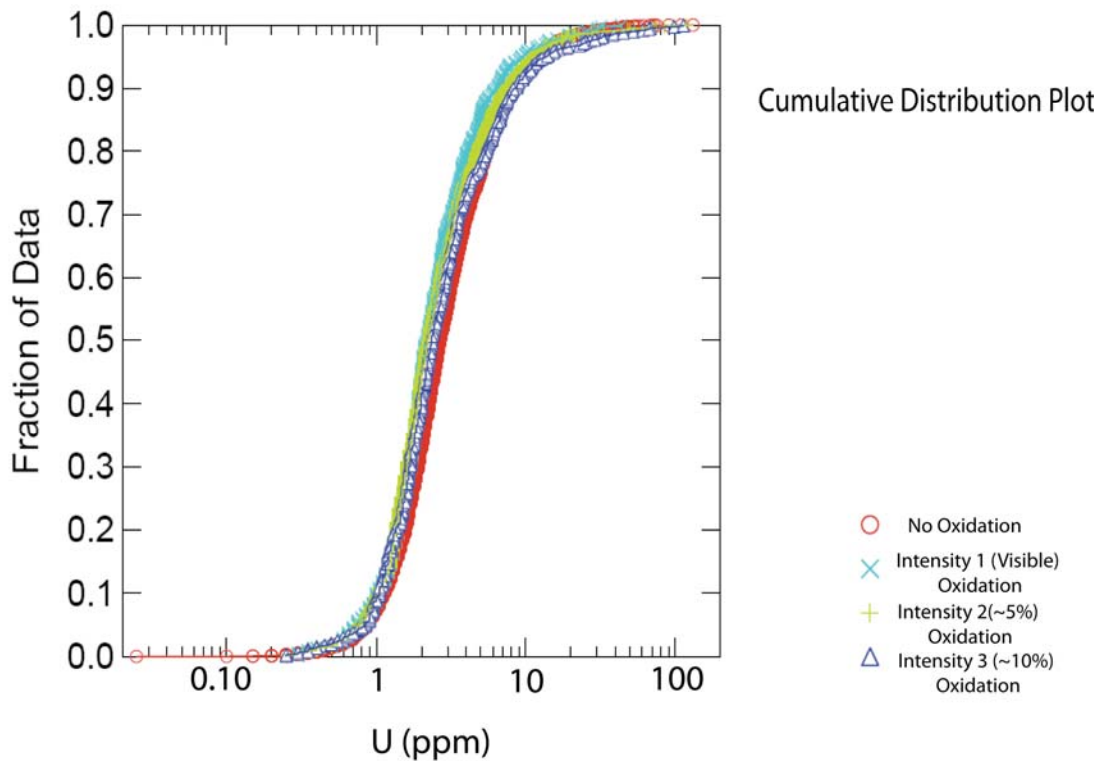
Figure 24c
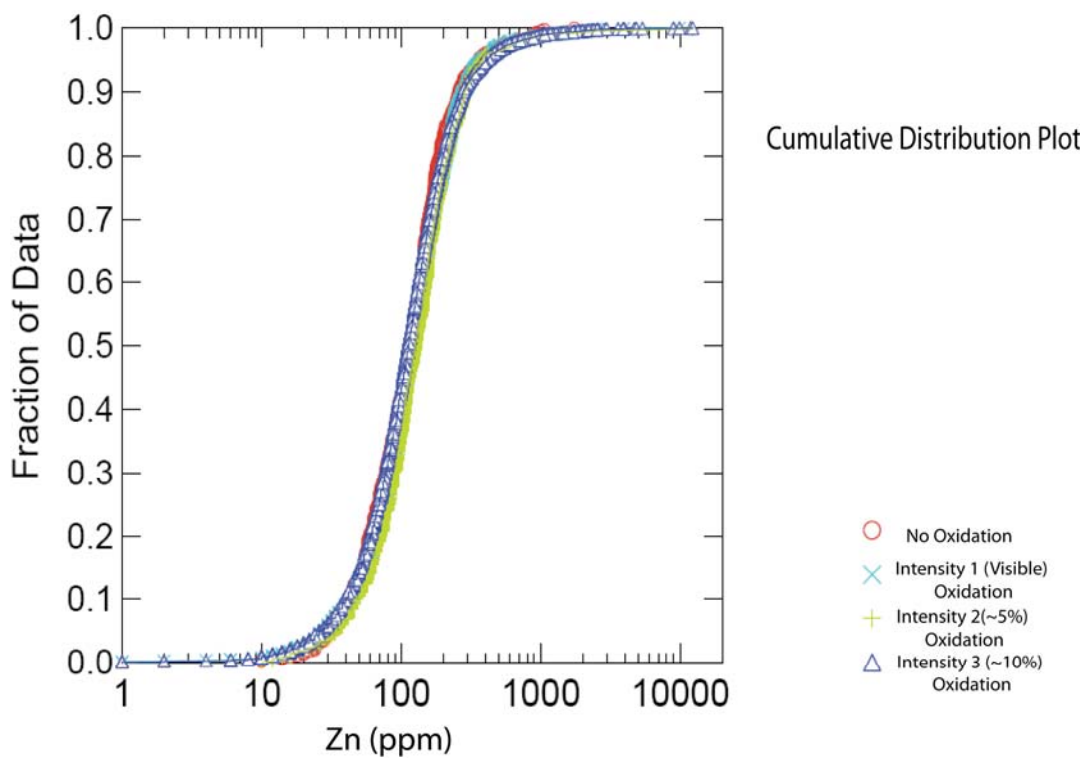
Figure 24d
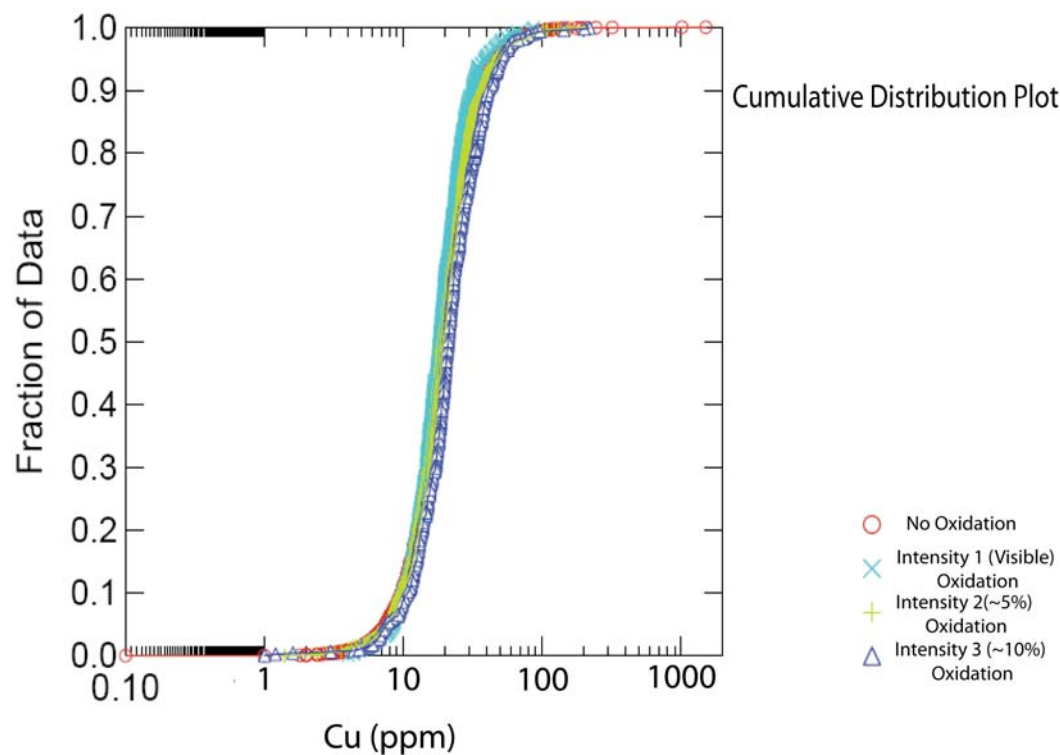
Figure 24e

|	Au	Al	Sb	As	Ba	Be	Bi	Cd	Ca	Cr	Co	Cu
N of cases	6,416	6,416	6,416	6,416	6,416	6,416	6,416	6,416	6,416	6,416	6,416	6,416
Minimum	2.50	0.01	0.05	0.10	0.50	0.03	0.01	0.01	0.04	1.00	0.10	0.10
Maximum	82,859.00	52.70	10,000.00	10,000.00	4,270.00	6.25	5.00	115.50	33.00	734.00	92.60	1,515.00
Range	82,856.50	52.69	9,999.95	9,999.90	4,269.50	6.22	4.99	115.49	32.96	733.00	92.50	1,514.90
Median	125.00	0.30	13.28	71.40	240.00	0.40	0.06	0.98	7.38	48.00	3.20	19.00
Mean	732.74	0.36	81.64	178.96	586.65	0.44	0.08	1.74	7.17	71.08	3.88	22.48
Standard Dev	2,783.24	0.69	456.67	571.40	827.23	0.28	0.13	3.78	4.16	68.55	3.83	27.26
Skewness	13.50	67.16	15.44	11.91	2.19	3.93	22.93	13.62	0.12	2.53	8.11	34.08

	Ga	Fe	La	Pb	Mg	Mn	Hg	Mo	Ni	P	K	Sc
N of cases	6,416	6,416	6,416	6,416	6,416	6,416	6,416	6,416	6,416	6,416	6,416	6,416
Minimum	0.03	0.03	0.60	0.60	0.01	2.00	0.01	0.10	0.50	10.00	0.01	0.10
Maximum	16.00	11.30	450.00	802.00	120.00	4,990.00	4,370.00	184.00	2,030.00	10,000.00	3.00	27.00
Range	15.97	11.27	449.40	801.40	119.99	4,988.00	4,369.99	183.90	2,029.50	9,990.00	2.99	26.90
Median	1.00	0.94	5.00	6.90	3.21	120.00	2.69	5.20	24.00	1,600.00	0.14	2.00
Mean	1.20	1.04	8.21	9.59	3.12	143.94	6.89	7.45	28.43	2,270.80	0.16	2.29
Standard Dev	0.91	0.58	10.41	18.69	2.89	130.56	57.01	8.40	36.90	2,179.75	0.09	1.66
Skewness	4.34	4.91	17.10	20.83	19.41	11.38	70.36	5.61	38.72	2.01	6.43	3.77

	Se	Ag	Na	Sr	S	Te	Tl	W	U	V	Zn	
N of cases	6,416	6,416	6,416	6,416	6,416	6,416	6,416	6,416	6,416	6,416	6,416	
Minimum	0.10	0.01	0.01	0.53	0.01	0.01	0.01	0.03	0.03	1.00	1.00	
Maximum	50.20	26.70	79.00	1,925.00	5.00	26.40	160.00	762.00	131.50	3,120.00	12,300.00	
Range	50.10	26.69	78.99	1,924.47	4.99	26.39	159.99	761.97	131.47	3,119.00	12,299.00	
Median	1.50	0.35	0.01	70.00	0.30	0.05	0.48	0.85	2.55	39.00	112.00	
Mean	2.21	0.58	0.03	96.57	0.46	0.22	1.64	1.53	4.23	57.03	169.38	
Standard Dev	2.75	1.12	1.19	129.41	0.53	1.01	6.33	11.00	6.59	111.42	364.86	
Skewness	4.85	10.29	59.71	6.59	2.76	14.79	13.21	56.77	8.16	13.45	18.98	

Table 5: Descriptive statistics for all elements analyzed during this study.

Statistics

To further define elemental associations within the data set, a variety of common statistical analyses were completed. Table 5 shows the descriptive statistics for each element. In addition, Spearman rank correlation, correspondence analysis, and traditional R-mode factor analysis were completed.

Spearman rank correlation matrices were completed using the statistical software package SYSTAT 11. The Spearman method of generating correlation matrices was used because it shows whether one variable has an effect on another set of variables, without constraining the correlation to be linear. For example, outliers can strongly influence traditional linear Pearson correlation coefficients. A correlation coefficient greater than 0.400 was considered to be significant in this study. Spearman rank correlation matrices were completed for the following cases: 1) the entire Saval data set (entire data set); 2) samples that are within the vertical projections of known gold deposits (only deposits); and 3) samples outside the vertical projections of known gold deposits (district excluding deposits) (Figs. 25a, 25b, & 25c).

Correspondence analysis was completed in DATAVIEW 07 (Carr, 2002). Correspondence analysis is a method used to graphically display unbiased relationships between variables. The axes of the graph are made perpendicular so that elemental relationships are not distorted. This is done via eigen decomposition which yields eigen vectors that define the axes and make the graph perpendicular. The principal components with the highest eigen values represent the most data and are factors 1 and 2. Like the Spearman rank correlation matrices, correspondence analysis was also completed for the entire Saval data set, for samples within the vertical projections of the known gold

deposits, and for samples outside the vertical projection of the deposits (district excluding deposits) (Figs. 26a, 26b, & 26c).

Factor analysis for the entire dataset was completed using SYSTAT 11 (Table 6). Traditional R-mode factor analysis was completed using varimax rotation and a minimum eigen value of 1.00. Varimax rotation was used because it maximizes the variance that each factor represents (Abdi, 2003). Because most of the elements showed log-normal distributions, the log values for each element were used for the factor analysis, because factor analysis is based on the assumption of normal populations. Factor scores for each of the 8 calculated factors were calculated for each sample in the dataset by summing the product of the concentration and loading for each element. The factor scores for each factor were then gridded and imaged by stretching the grid, using two standard deviations. For a given factor, elements with the highest factor loadings (strongest statistical association) have the highest factor scores in the gridded images. Table 6 shows the 8 calculated factors and the associated factor loadings for the entire data set. Elements with factor loading greater than 0.400 in a given factor are considered significant.

Figure 25: Spearman rank correlation matrixes for:

a. The entire Anglo Gold data set.

b. Samples from the Anglo Gold data set that are completely contained by the vertical projection of known gold deposits.

c. Samples from the Anglo Gold data set that are not completely contained by the vertical projection of known gold deposits.

Figure 25a

Figure 25b

Correlation Coefficient > 0.400

Figure 25c

Figure 26: Correspondence analysis for:

a. The entire Anglo Gold data set.

b. Samples from the Anglo Gold data set that are completely contained by the vertical projection of known gold deposits.

c. Samples from the Anglo Gold data set that are not completely contained by the vertical projection of known gold deposits.
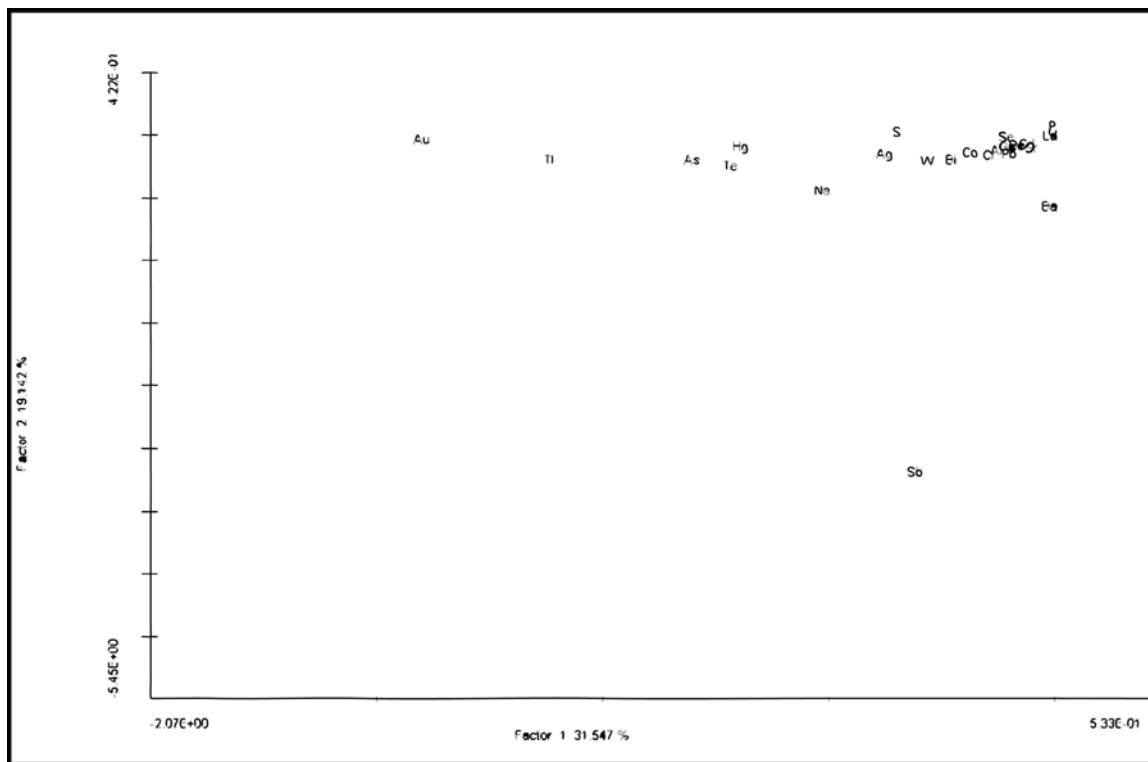
Figure 26a
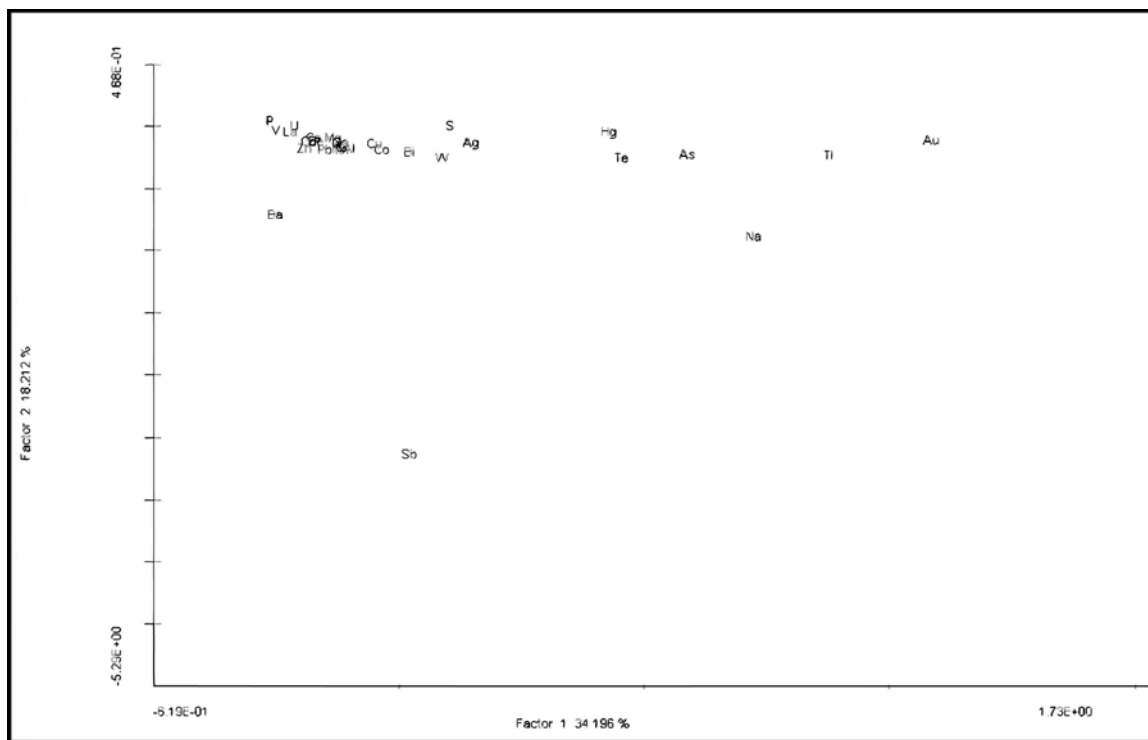
Figure 26b
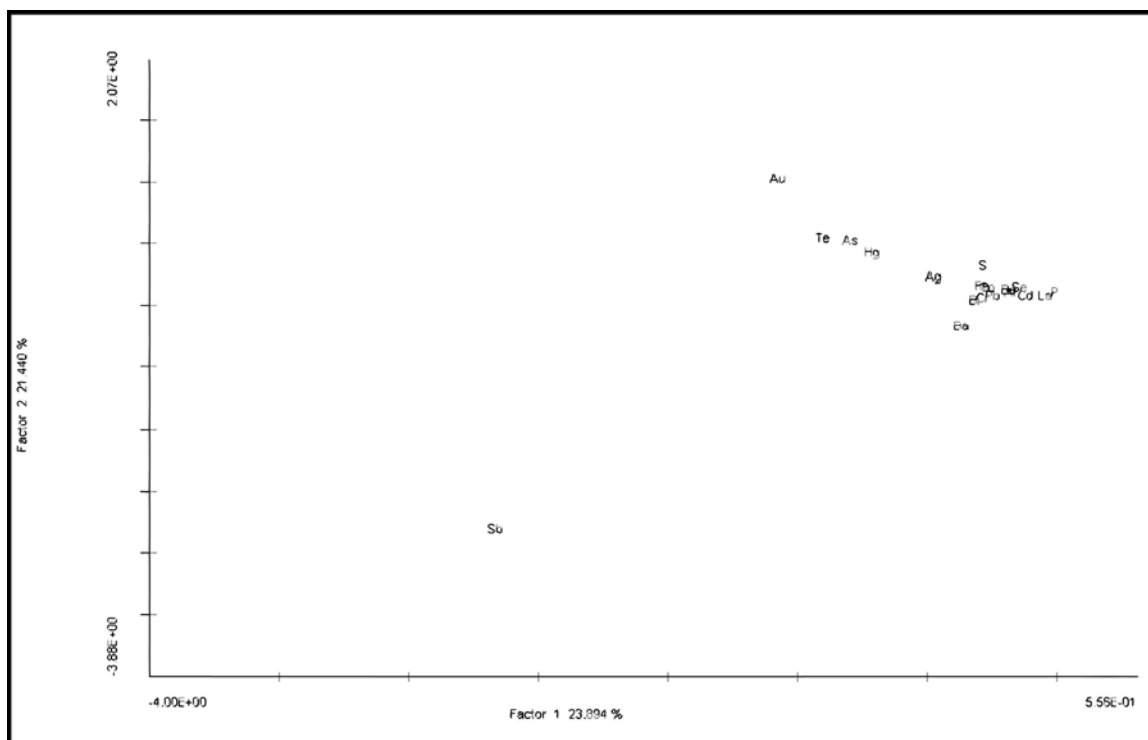
Figure 26c

Gold Related Elements + Antimony

Spearman rank correlation matrices show similar elemental associations between gold-related elements as were observed in the gridded images (Figs. 25a, 25b, & 25c). In all three cases, gold correlates with thallium, arsenic and mercury; with the lowest correlation coefficient being 0.450. Gold, arsenic, and thallium have the highest correlation coefficients, up to 0.684, in the case using the data that are within the vertical projection of the deposits (Fig. 25b). Tellurium correlates with gold to a lesser extent in all three cases, with coefficients ranging from 0.390 to 0.417. However in the Steer/Saval/SSX area, where the spatial relationship is strongest in the gridded image, the correlation coefficient calculated for all samples completely contained by the vertical projection of the SSX deposit was 0.690. Consistent with the lack of spatial relationship in the gridded images, correlation coefficients between silver and gold and antimony and gold were below 0.4 and 0.3, respectively in all three cases.

All the correspondence analyses show gold, mercury, arsenic, thallium, and tellurium are separated from the main grouping of elements (Figs. 26a, 26b, & 26c). They are not closely clustered together in any of the graphs, but it is clear that they are not statistically associated with the other elements. Antimony consistently plots away from, or shows no statistical relationship with any of the elements (Figs. 26a, 26b, & 26c). Even when analyses were completed for only gold, arsenic, tellurium, thallium, mercury, and antimony the elements exhibited a pattern similar to that shown in figures 26a, 26b, and 26c where antimony was completely removed from the other elements.

The statistical association between the gold-related elements is also evident in Factor 3 in the factor analysis of the entire dataset (Table 6). The highest loadings for

Factor 3 were for mercury (0.848), thallium (0.829), gold (0.787) and arsenic (0.766) (the four elements with the strongest spatial association in the gridded images). As expected, tellurium has a lower factor loading than any of the other gold related elements (0.580). Figure 27 is the gridded image of the factor scores for Factor 3. The factor score for a given sample is calculated by taking the sum of each elements factor loading from the factor of interest multiplied by each elements geochemical value for a given sample. The gridded image for factor 3 shows where the gold-thallium-mercury-arsenic-tellurium-antimony association is strongest (Fig. 27). The value of factor analysis stems from showing where the association is strong even if gold is low. For example, if the gold value is low for a given sample, but the thallium, mercury and arsenic values are high, the sample may still have a high score for the Factor 3. In other words, when looking for areas where gold mineralization may be present, one should pay attention to the areas where high factor scores for Factor 3 are present and not just high gold values. Like the gridded images for the individual gold-related elements, high Factor 3 scores are more spatially restricted in the Murray-Winters Creek area, showing the same west-northwest trend in the Murray mine trailing out to Wright Window along the New Deep Fault (Figs. 17, 21a, 21d, 21g, 21j, & 27). Also, the SSX-Smith area shows a more extensive, continuous zone of high Factor 3 than the Murray-Winters Creek area. Though antimony's factor loading of 0.416 for Factor 3 suggests a statistical association with the gold related elements, the factor loading is significantly less than gold, arsenic, mercury, thallium, or tellurium (Table 6). This is consistent with the gridded images which show that antimony does have some spatial association with the gold related elements but it is not consistent and is not observed in all deposits. The gridded images, Spearman rank

correlation matrices, correspondence analysis, and the factor analysis all suggest antimony is not spatially or statistically associated with any of the other elements.

Carlin-type Hydrothermal Alteration Associated Elements

Calculated Spearman rank correlation coefficients are consistent with what would be expected from hydrothermal alteration associated with Carlin-type mineralization, namely decarbonatization (Figs 25a, 25b, & 25c). Calcium, magnesium, and strontium positively correlate in all cases considered with a minimum correlation coefficient of 0.728 which is consistent with the carbonate-bearing Roberts Mountains Formation. Factor analysis also exhibits a negative correlation between gold and the gold-related elements with calcium, magnesium, and strontium, evident from the low loadings for calcium (-0.142), magnesium (-0.083) and strontium (-0.181) in Table 6.

District Factor Analysis-Factor Loadings

	Factor 1	Factor 2	Factor 3	Factor 4	Factor 5	Factor 6	Factor 7	Factor 8
Zn	0.073	0.031	0.076	0.737	0.333	-0.226	-0.164	-0.049
W	0.301	0.293	0.374	0.152	0.016	-0.027	-0.455	-0.078
V	0.423	-0.030	-0.039	0.663	0.389	-0.024	-0.006	0.120
U	0.739	0.054	0.091	0.498	0.027	0.120	-0.094	0.174
Tl	-0.117	0.037	0.829	-0.055	0.128	-0.057	-0.195	-0.052
Te	0.127	0.123	0.580	0.189	-0.039	-0.046	0.253	0.169
Sr	0.220	-0.785	-0.181	-0.143	0.083	-0.041	0.046	0.008
Se	0.094	-0.009	-0.116	0.433	0.281	0.385	0.042	-0.118
Sc	-0.032	-0.263	-0.012	0.112	0.680	0.121	-0.181	0.064
Sb	0.112	0.470	0.416	0.076	0.071	-0.211	-0.355	0.053
S	-0.121	-0.375	0.254	0.181	0.040	0.561	0.330	-0.129
Pb	0.120	0.173	-0.043	0.231	0.312	-0.137	-0.301	0.262
P	0.765	0.077	0.048	0.301	0.280	0.015	0.037	-0.156
Ni	0.217	0.097	0.059	0.520	0.526	0.058	-0.406	0.104
Na	0.008	-0.048	-0.001	0.048	0.091	0.086	0.012	0.864
Mo	0.322	0.067	0.132	0.675	0.002	0.169	-0.235	0.120
Mn	-0.262	-0.751	0.053	0.040	0.212	-0.060	-0.177	-0.159
Mg	-0.074	-0.863	-0.083	0.095	-0.003	0.135	0.138	0.045
La	0.721	-0.095	-0.145	0.066	0.367	-0.063	-0.090	0.092
K	0.182	-0.126	0.088	0.070	0.869	-0.051	0.224	0.060
Hg	0.068	0.035	0.848	0.150	0.089	0.099	0.025	-0.001
Ga	0.425	0.128	0.138	0.217	0.750	-0.096	0.042	-0.022
Fe	-0.195	0.053	0.312	0.162	0.718	0.170	-0.217	-0.124
Cu	0.100	0.122	0.225	0.464	0.559	0.032	-0.125	-0.111
Cr	0.376	0.514	0.186	0.294	-0.126	0.137	0.044	-0.131
Co	-0.137	-0.171	0.102	0.167	0.621	0.147	-0.463	-0.079
Cd	0.077	-0.083	0.098	0.828	0.243	-0.122	0.074	0.052
Ca	0.113	-0.930	-0.142	0.016	-0.019	0.050	0.038	0.063
Bi	0.149	0.138	0.102	0.296	0.614	0.097	-0.128	0.229
Be	0.089	-0.313	-0.010	0.189	0.695	-0.043	0.028	0.021
Ba	-0.056	-0.019	0.021	0.134	-0.004	-0.792	0.071	-0.151
Au	-0.031	0.115	0.787	0.046	0.006	0.041	0.085	-0.018
As	-0.019	0.128	0.766	0.019	0.302	0.000	-0.239	-0.065
Al	0.282	0.023	0.061	0.097	0.870	-0.097	0.142	0.072
Ag	0.110	0.055	0.353	0.628	0.256	0.117	0.387	-0.040
% Varience	8.15	11.12	10.95	11.72	16.75	4.15	4.52	3.35

Factor loadings > 0.400

Higest factor loadings < 0.400 (highest in factor if none > 0.400)

4 lowest factor loadings

Table 6: Table showing the factor loadings for each factor. The elements with the highest factor loadings are considered to be statistically associated with each other.
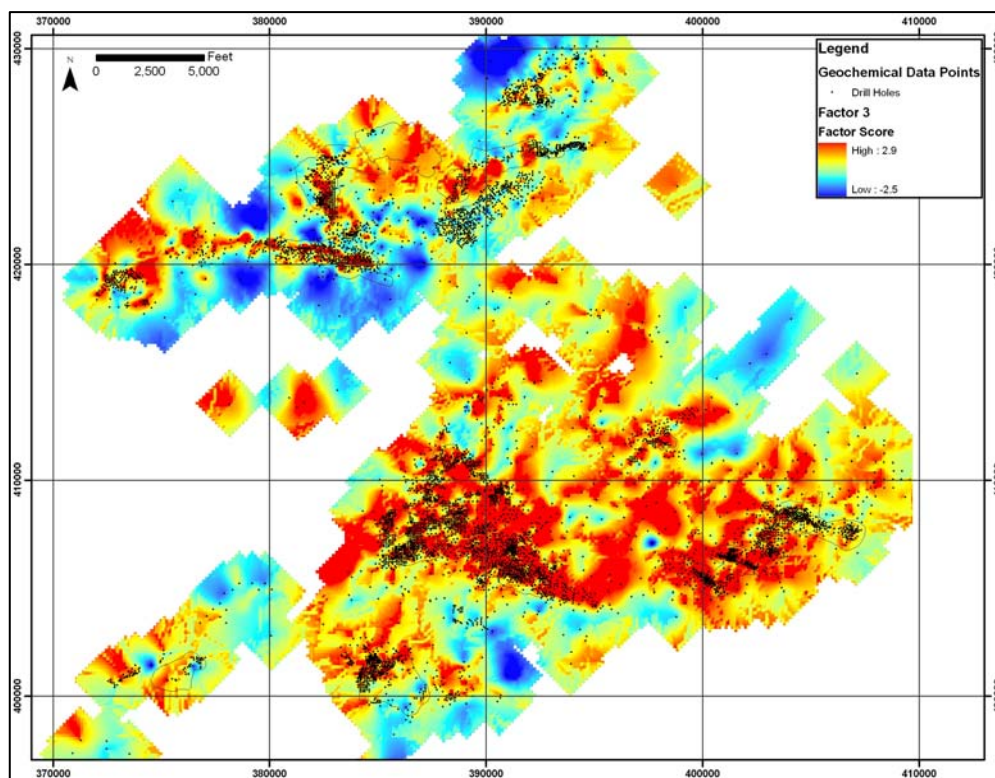
Figure 27: Stretched gridded image for Factor 3 (Au, As, Hg, Tl, Te ± Sb) shown in Table 6.

Black Shale Elements

Spearman rank correlation matrices demonstrated a similar elemental association between the black shale elements as was observed in the gridded images (Figs. 25a, 25b, & 25c). Uranium correlates with molybdenum and phosphorous in all 3 cases with a minimum correlation coefficient of 0.487. Vanadium correlates with zinc, uranium, bismuth, silver, molybdenum and phosphorous in all cases with a minimum correlation coefficient of 0.457. Silver correlates with cadmium, copper, selenium, and vanadium in all cases considered with a minimum correlation coefficient of 0.402.

Again, uranium, vanadium, molybdenum, zinc, and phosphorous were part of the large cluster of elements shown on graphs produced via correspondence analysis (Figs.

26a, 26b, & 26c). However, it can be observed that silver is slightly displaced from the main grouping of elements which is probably insignificant because gold, arsenic, mercury, thallium, and tellurium are further displaced from each other than silver is from the large grouping of elements but gold and the gold related elements have sufficient evidence supporting their associated with each other.

Factor analysis revealed two groups of black shale elements (Table 6). The first group, Factor 1, consists of lanthanum, phosphorous, uranium, gallium, and vanadium. The second group, Factor 4, consists of zinc, vanadium, uranium, selenium, nickel, molybdenum, copper, cadmium, and silver. Factor 1 has high pervasive factor scores throughout much of the Murray-Winters Creek area, which become lower and less pervasive towards the SSX-Smith area (Fig. 28a). High Factor 4 scores occur at Winters Creek and in Burns Basin and are spotty in the Steer/Saval/SSX-Smith/Dash area (Fig. 28b).

Figure 28:

Figure 28a: Stretched gridded image for Factor 1 (lanthanum, phosphorous, uranium, gallium, and vanadium) shown in Table 6. Figure 28b: Stretched gridded image for Factor 4 (Zinc, vanadium, uranium, selenium, nickel, molybdenum, copper, cadmium, and silver) shown in Table 6.

Figure 28b: Stretched gridded image for Factor 4 (Zinc, vanadium, uranium, selenium, nickel, molybdenum, copper, cadmium, and silver) shown in Table 6.
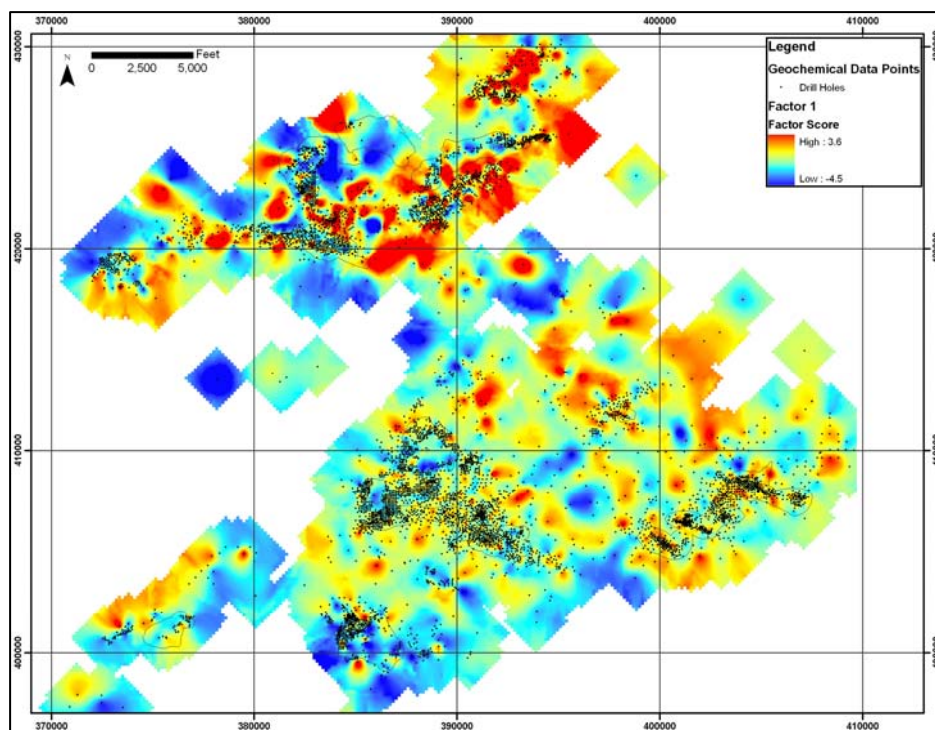
Figure 28a
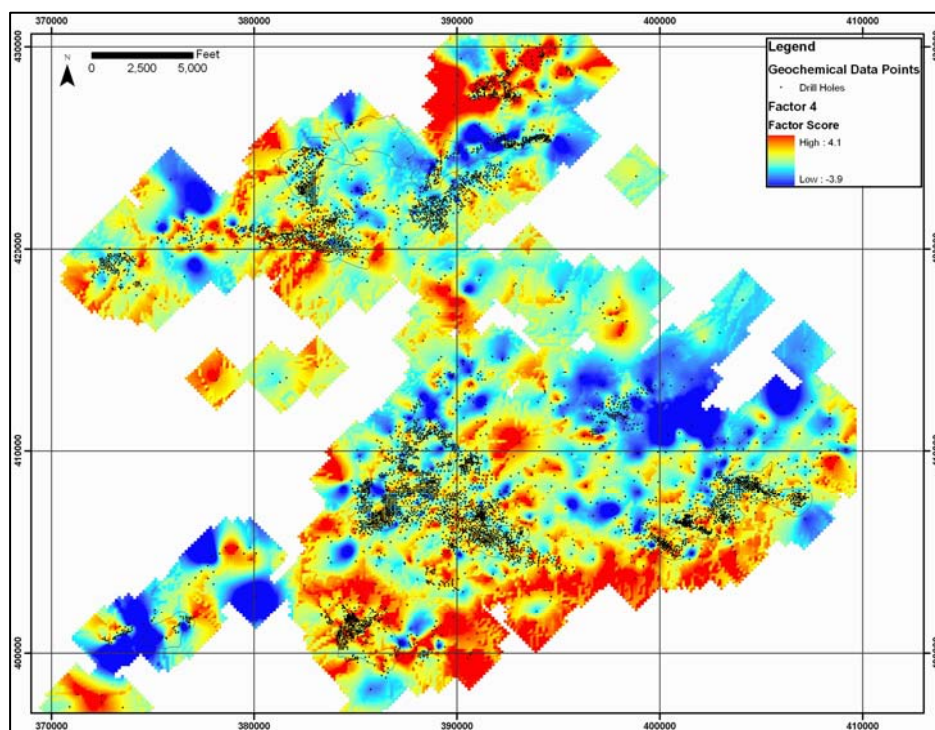
Figure 28b

Other Factors

      Though not yet discussed, Factor 5 represents 16.75% of the variance in the data set (Table 6). The elements which define this factor are scandium, nickel, potassium, gallium, iron, copper, chromium, cobalt, bismuth, beryllium, and aluminum. These elements suggest an mafic igneous signature. However, comparing figure 3 with figure 29 validates a lack of any discernable pattern or spatial association with igneous rocks in the Jerritt Canyon district. Also, the pattern shown in figure 29 is not consistent with any of the patterns observed in the gridded image. An explanation for the origin of the elements that constitute factor 5 is not offered herein.
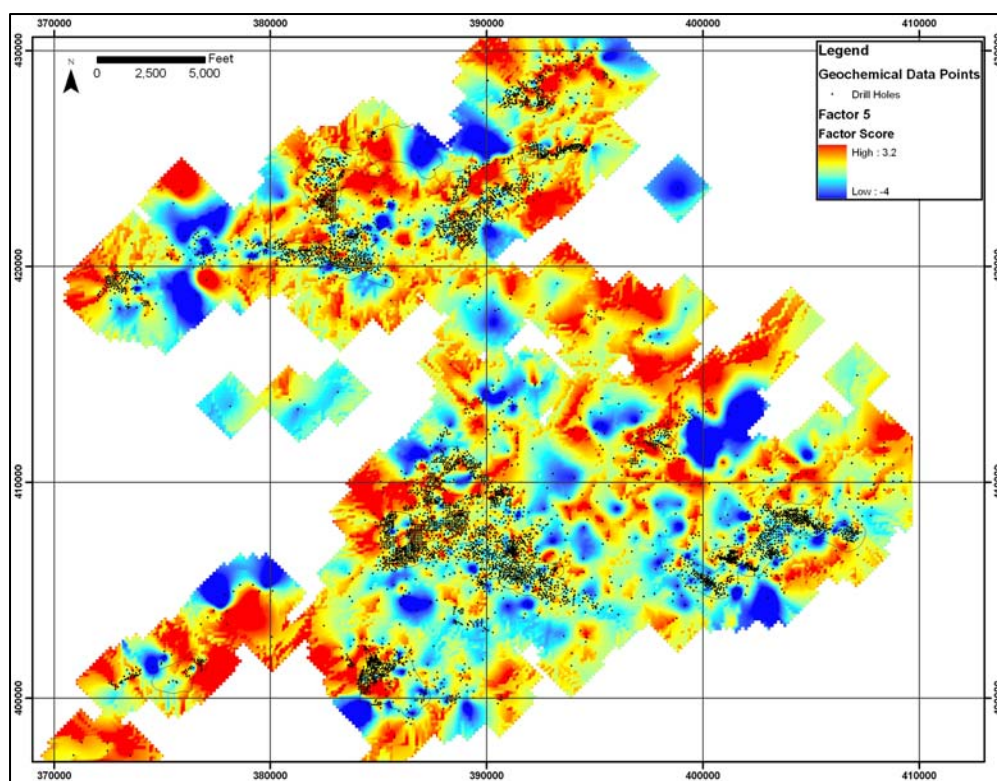
Figure 29: Stretched gridded image for factor 5 (scandium, nickel, potassium, gallium, iron, copper, chromium, cobalt, bismuth, beryllium, and aluminum) shown in Table 6.

Discussion

The gridded images and statistical analyses indicate at least two groups of elements. The first group of elements, are herein termed Carlin-type elements (CTEs) and consist of gold, thallium, mercury, arsenic, and tellurium. The second group is a broad group of elements, the Black Shale elements (BSEs) which has two subgroups: 1): uranium, phosphorous, lanthanum, and gallium; and 2) zinc, uranium, molybdenum, vanadium, nickel, copper, cadmium, and silver.

The Carlin-type elements correlate with each other in the Spearman rank correlation matrices and are statistically associated with each other in the correspondence and factor analysis. Antimony exhibits a weak statistical association but little to no spatial relationship with the Carlin-type elements. Antimony is present at Jerritt Canyon mainly as stibnite, which is a late ore-stage mineral that post-dates most of the gold deposition. The Carlin-type elements are inversely associated with calcium, strontium, and magnesium, spatially and statistically. Decarbonatization during Carlin-type mineralization is the cause for the inverse relationship.

As mentioned before, the BSEs are composed of 2 subsets. The first group consists of, phosphorous, lanthanum, uranium, gallium, and vanadium, which is consistent with a phosphatic signature produced during anoxic conditions and formation of phosphate lenses and nodules described above (Fig. 11a, 11b, & 11c). The second group consists of cadmium, zinc, molybdenum, vanadium, silver, nickel, uranium, selenium, and copper, which is consistent with transport by an oxidized brine and precipitation by reduction. High values of both subsets of BSEs elements are widespread in the Murray-Winters Creek and Burns Basin areas, with spotty areas of elevated values

throughout the SSX-Smith area. The highest values are at Winters Creek where all the BSEs show a similar spatial pattern in the gridded images. Thin sections of samples from Winters Creek were examined with the SEM. Two samples from Winters Creek had sphalerite and V-As-Zn-(Pb) sulfides associated with pyrobitumen with a minor sulfur peak (Fig. 30). One sample from California Mountain had a quartz vein with carbon and sphalerite (Fig. 31).
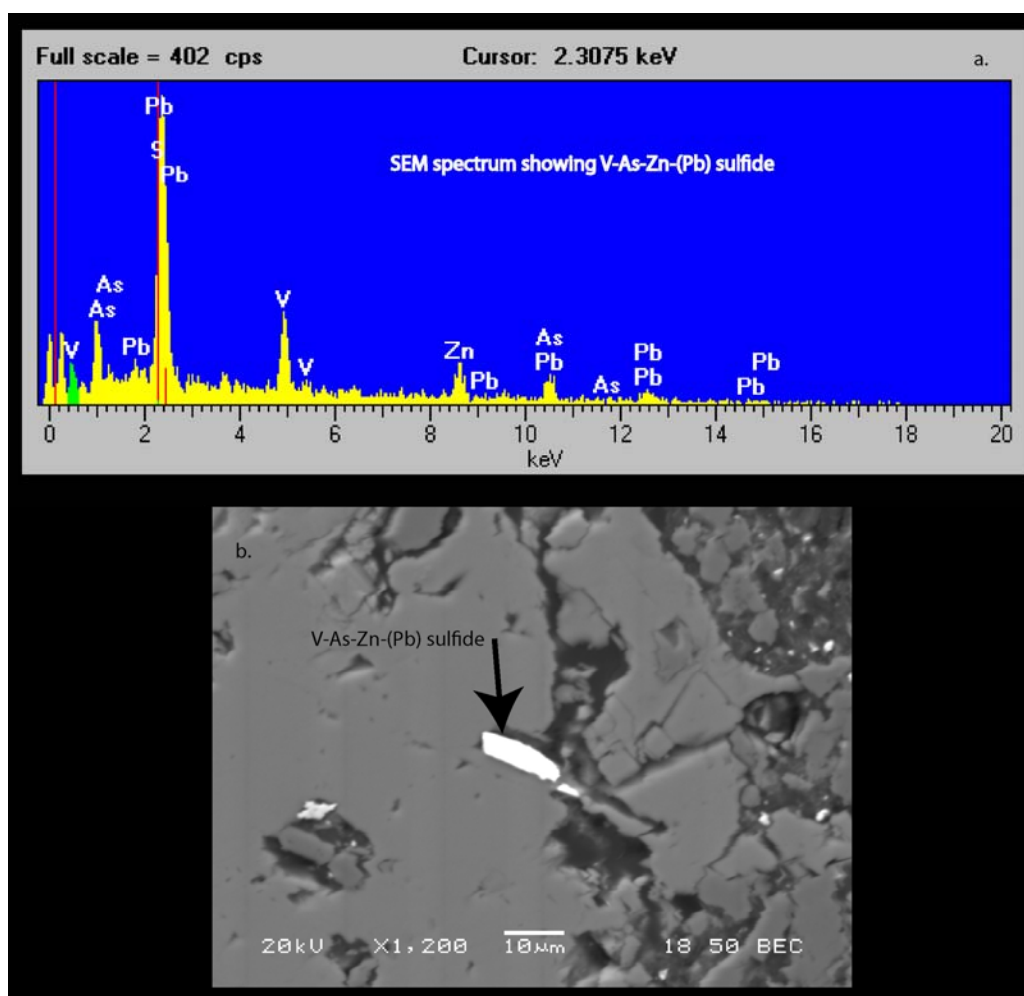
Figure 30: Figure showing the V-As-Zn-(Pb) sulfide from the Winters Creek area.

a. Top image is the EDS spectrum from the V-As-Zn-(Pb) sulfide.

b. Bottom image is an EDS image of a carbon rich vein with a bright V-As-Zn-(Pb) sulfide.
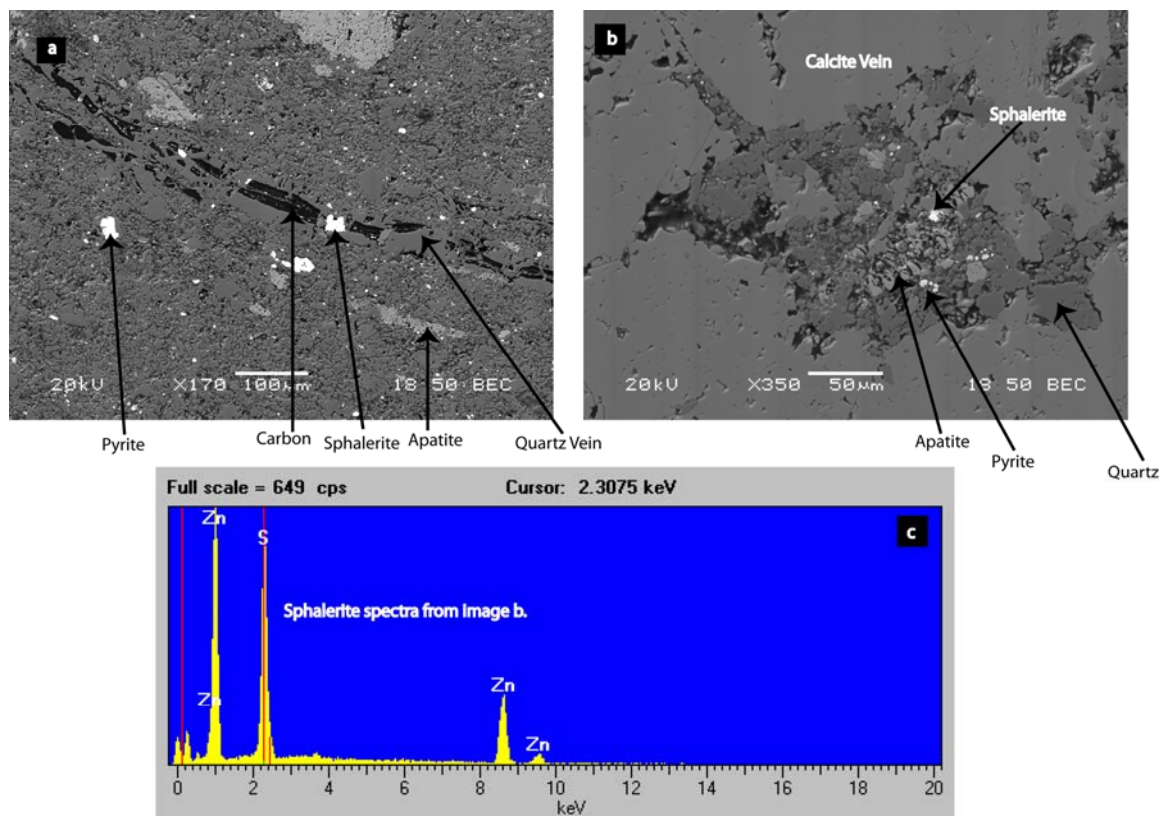
Figure 31: Figure showing the quartz vein with carbon and sphalerite found in a sample from California Mountain.

a. EDS image of a quartz vein with carbon and sphalerite in the center of the vein and apatite and pyrite in the DSrm.

b. EDS image of sphalerite, pyrite, apatite, and quartz in the center of a calcite vein.

c. EDS spectrum from the sphalerite that was found in the calcite vein.

Alteration, Mineralization, and Veining

In order to document patterns of logged geologic features with respect to areas of known gold mineralization and to further define the hydrothermal footprint of the Jerritt Canyon Carlin-type mineralization system, Yukon-Nevada Gold Corporation supplied their logging data-base for this project. Yukon-Nevada Gold's logging data base and Anglo Gold's geochemical data-base were combined in order to generate point maps in ArcMap. The point maps allowed for characterization of the geologic features with respect to trace element geochemistry along the Saval in the bottommost 5 feet of the DSrm.

The geologic features that were previously logged include formations and lithologies, alteration, along with vein and mineral types. Alteration types that were previously logged include oxidized, silicified, decarbonatized, and dolomitized rocks. Vein and mineral types that were previously logged include calcite, pyrite, realgar, orpiment, stibnite, quartz, barite, and dolomite. A problem that exists with Yukon-Nevada Gold's data set is lack of consistency; one person did not log all 6,416 drill holes.

In order to maintain consistency, 40 foot intervals from 247 holes (67 core holes and 180 chip holes) were logged (Fig. 32) using uniform criteria. The 247 holes were chosen to generate a pseudo-grid of the northern potion of the Jerritt Canyon district. The average spacing of the holes chosen is about 1,000 feet. Fifteen feet above the assay interval from Anglo Gold's data base, the assay interval, and twenty feet below the assay interval were logged. The logged features were brought into ArcMap to visually display the data as point maps. The logged features from the assay interval will be the only interval discussed here.

A description of the criteria used to log alteration, lithologies, veining, and mineralization is shown in Appendix 4 as well as examples of completed logs. The logged geologic features included formations and lithologies, alteration (decarbonatized, silicified, dolomitized, and oxidized rocks), minerals (pyrite, stibnite, realgar, orpiment, and barite), veining (dolomite, ferroan dolomite, calcite, ferroan calcite, and quartz), veining intensity, staining features of rock carbonate, and deformation (structures, breccias, stylolites). An example of the data brought into ArcMap can be found in Appendix 5. Furthermore, in order to confirm some of characteristics observed while logging, petrographic work and SEM analyses were completed on 20 thin sections.
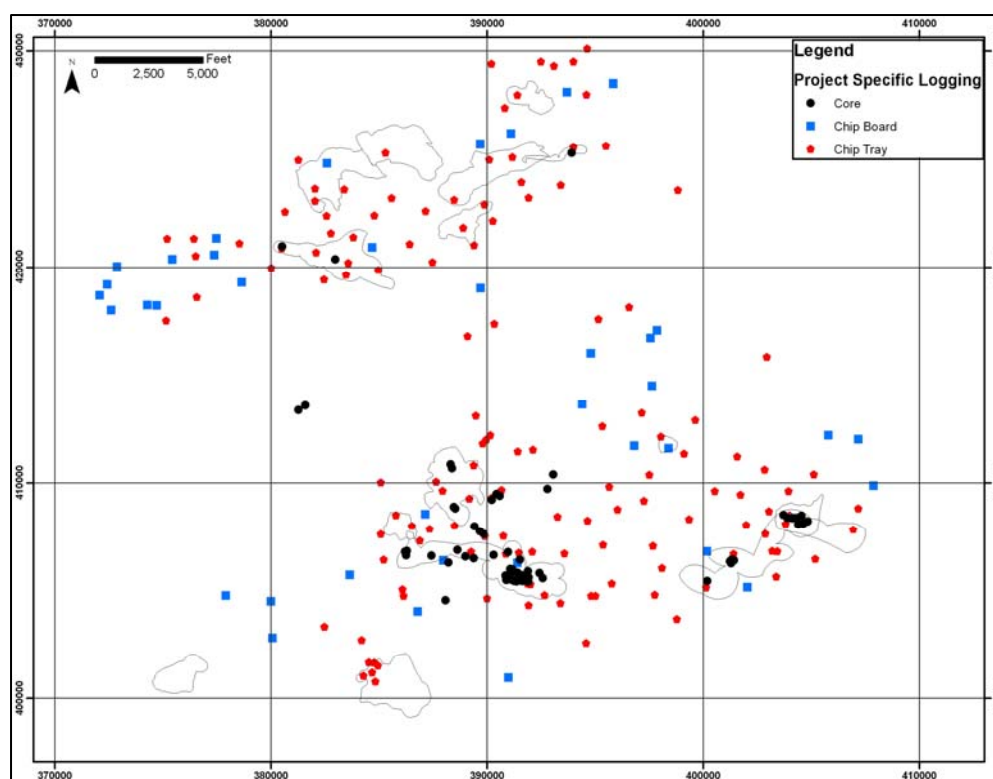
Figure 32: Map showing the distribution of the drill hole that were logged during this study, which included drill core, chip trays, and chip boards.

Carbonate staining (Hitzman, 1999) was implemented to document the carbonate mineralogy present in the veins and rock. A 2% HCl with Alizarin red S and potassium ferricyanide were used for the solution. The exact concentrations of chemicals in the solution are shown in Appendix 6. Four general types of rock and vein staining were observed: 1) a pink stain which indicates calcite; 2) a lilac to lavender stain which indicates ferroan calcite; 3) no stain which indicates dolomite; and 4) a blue stain, typically cretean blue, which indicates ferroan dolomite.

Alteration types observed during logging and thin section petrography included decarbonatized, argillized, and silicified rock. These are the characteristic alteration types observed in Carlin-type deposits (cf. Hofstra and Cline, 2000; Cline *et al*., 2005). Decarbonatized rock is characterized by dissolution of carbonate rocks by acidic hydrothermal fluids. Commonly, where intense decarbonatization has taken place, collapse breccias form which increases fluid-rock reaction, porosity, and permeability. Argillization is characterized by the alteration of silicate minerals to clays, such as kaolinite ± dickite ± illite (Cline *et al*., 2005). Silicification is characterized by the replacement of carbonate by quartz (jasperoid) and fine drusy quartz lining vugs.

Decarbonatized rock was observed in several samples. Decarbonatization includes dissolution of all carbonates including calcite, dolomite, and ankerite. In ore zones most of the aforementioned minerals were probably dissolved during the Carlin-event. Weakly decarbonatized rock was characterized in this study by a moderate to strong reaction with HCl, presence of ~5-10% clay, porous or sanded appearance and formation of minor stylolites and/or disrupted bedding suggestive of minor volume loss. Moderately decarbonatized rock was identified by the presence of increased stylolites and

volume loss, ~10-60% clay, and a weak to moderate reaction with 10% HCl. Figure 33 shows a major stylolite cutting a calcareous rock in SOhc$_3$, which had a moderate to weak reaction with 10% HCl. Most of the styolites that were present consisted of carbonaceous clay-like material with pyrite. Strongly decarbonatized was characterized by no reaction with HCl and the presence clay and quartz silt. Argillically altered rocks were included with decarbonatized rocks as they likely represent the same processes where one represents the dissolution of carbonates and the other is the argillization of silicates.

Silicified rock was logged in several drill holes, but it was much more common in the units of the SOhc, particularly SOhc$_1$, than it was in the Roberts Mountains Formation where it is much less widespread. In hand-sample, weakly silicified rock was logged where the rock was locally silicified in close proximity to quartz veins. Moderately silicified rock was characterized by rock that had a weak reaction with 10% HCl and could not easily be scratched. In thin-section, moderately silicified rock was characterized by about a 50:50 mixture of jigsaw textured quartz that was intergrown with carbonate (Fig. 34). Strongly silicified rock was characterized by the inability to scratch the sample and the presence of silica etching, or angular voids of missing material. Intensely silicified rock was documented where textures were destroyed and the rock could not be scratched. Figure 35 shows strongly silicified SOhc$_3$, in which jigsaw textured quartz has almost completely replaced all carbonate. The silicification events outlined by Hofstra (1994), which were discussed above in the description of the Saval Discontinuity section, could not be distinguished by logging.

Dolomitized rock was documented in most of the holes that were logged for this project. Weakly dolomitized rock was documented during logging by a 1-3 second delay in the reaction of the rock with 10% HCl and a stronger immediate reaction when the sample was scratched and contacted with 10 % HCl. In thin-section and in EDS images of samples logged as weakly dolomitized, a ~1:3 ratio of dolomite to calcite is observed (Fig. 36). Moderately dolomitized rock was documented during logging by a 3-5 second delayed reaction by the rock with 10 % HCl and a stronger immediate reaction when the sample was scratched and contacted with 10 % HCl. In thin section moderately dolomitized rock is characterized by a ~1:1 ratio of dolomite to calcite. Strongly dolomitized rock was best observed in hand sample where the rock, which appeared porous or sanded, would not react with 10% HCl. In thin-section, strongly dolomitized rock is characterized by mostly anhedral to euhedral dolomite that is intergrown with calcite euhedra which appear more granular and fractured compared to that in unaltered DSrm.
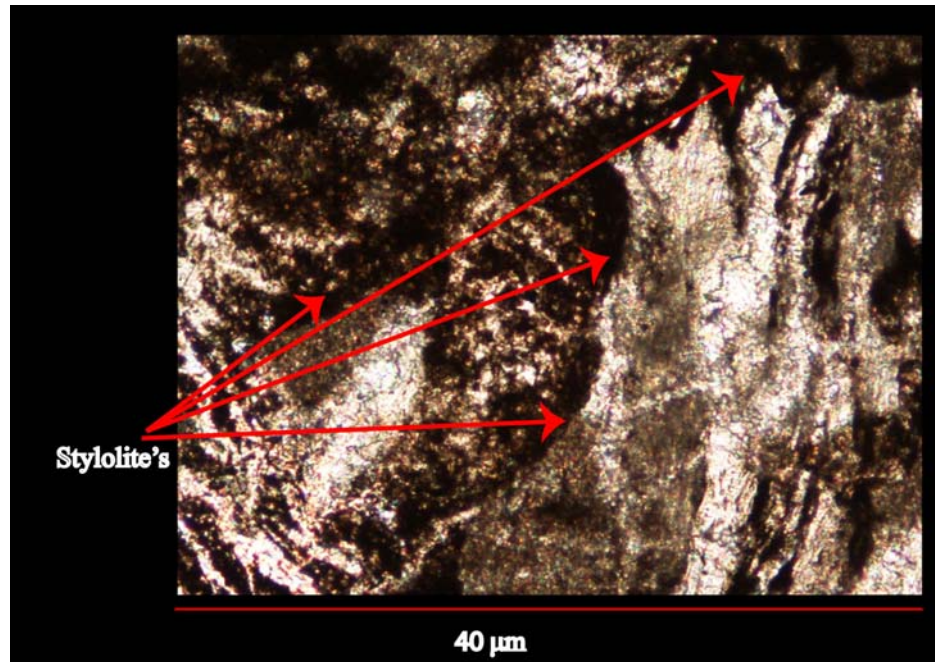
Figure 33: Photomicrograph of a stylolite in SOhc$_3$. The dark material is the stylolite that is composed of carbonaceous material and pyrite.
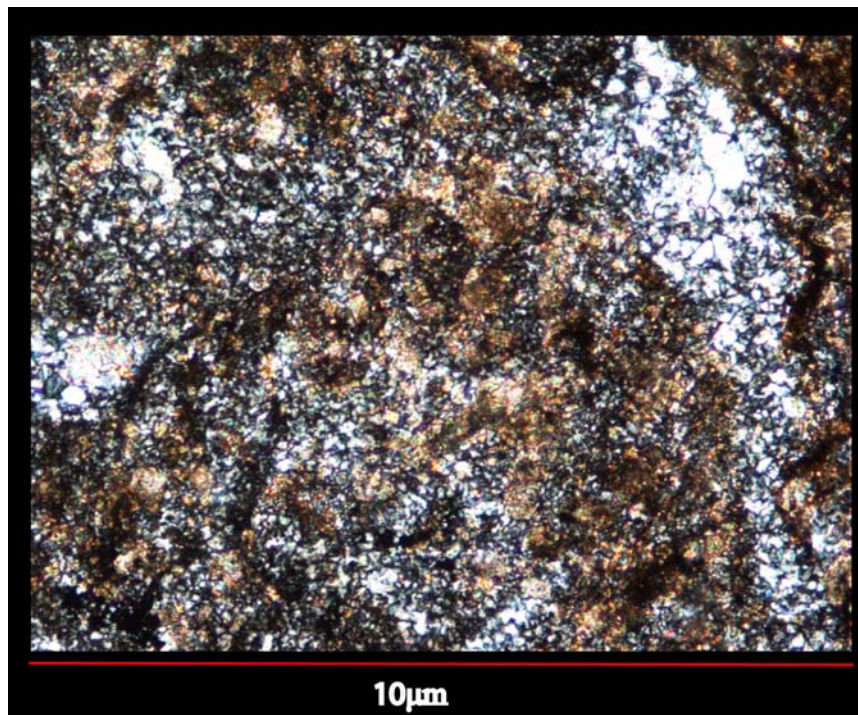
Figure 34: Photomicrograph showing moderately silicified rock. The higher birefrengent mineral is calcite which is surrounded by the lower birefrengent quartz. Note the jig-saw texture of the quartz.
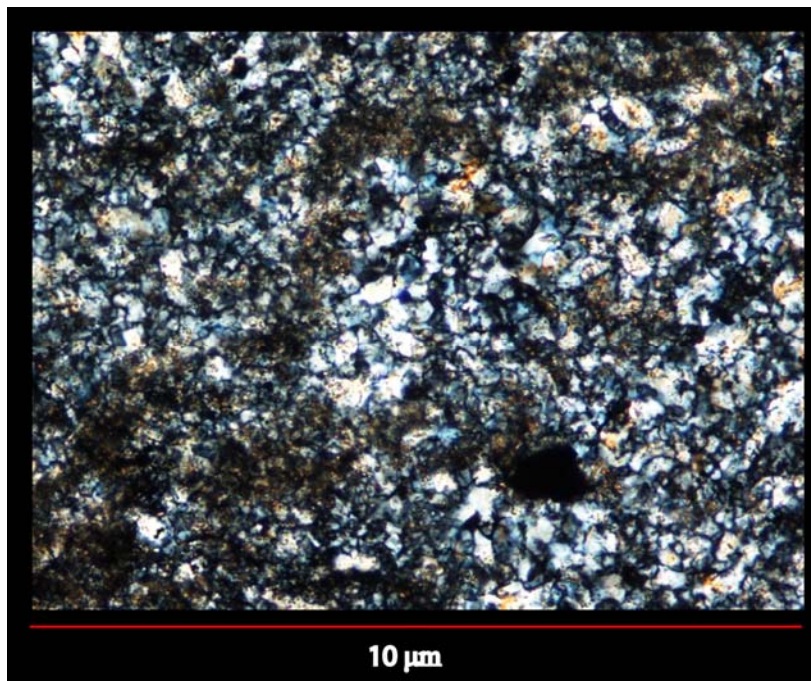
Figure 35: Strongly silicified rock of a carbonate host rock. Note that the section is dominated by low birefrengent jig-saw textured quartz.
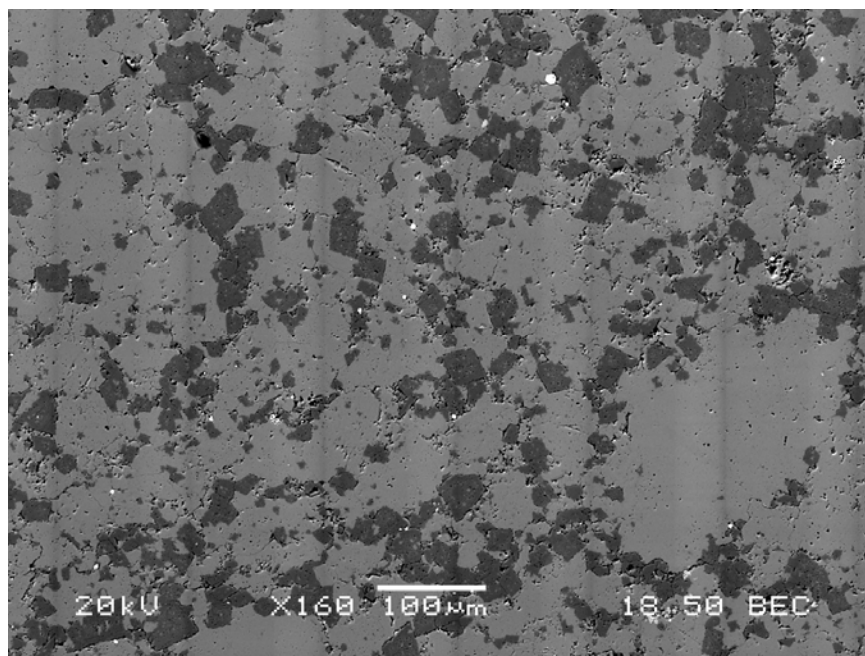
Figure 36: BSE/SEM image showing weakly dolomitized rock, note the dark gray dolomite rhombs in a lighter gray calcite matrix.

The dominant vein types encountered during this study were calcite, dolomite, ferroan dolomite, quartz, and two samples with ferroan calcite. The veins were between 0.1 mm and 1 cm wide, with smaller veins having matching vein walls and larger veins having irregular vein walls. Veins were composed of single mineral phases and multiple mineral phases. The most common vein type observed was calcite. Quartz was commonly found with dolomite and calcite. Pyrite was locally found in and along calcite, quartz, dolomite, and ferroan dolomite veins. All vein types were examined with the SEM, using energy dispersive spectroscopy (EDS), to validate the presence of iron indicated by staining of the dolomite and calcite-bearing veins. The calcite veins stained pink. When analyzed with EDS using the SEM, the pink calcite veins gave a spectrum which would be expected for pure calcite (Fig. 37). Calcite veins commonly cut all other vein types. Dolomite veins did not stain and exhibited an EDS spectrum which would be expected for pure dolomite using the SEM. The ferroan dolomite veins stained blue and had a minor iron peak, along with magnesium and calcium peaks in the EDS spectra obtained using the SEM (Fig. 38). Dolomite and ferroan dolomite veins in some samples appeared to be altered. The dolomite in such veins appears etched and clay-like, with pink-staining calcite occurring as late fillings in the veins (Fig. 39). In two samples, calcite veins stained purple, suggesting they contain iron. However, these veins did not show any iron peaks when analyzed by EDS using the SEM. This does not preclude that iron is absent, because the stain is more sensitive to iron than EDS, which only is sensitive to about 1 wt% of a given element. A microprobe, using wavelength dispersive spectroscopy (WDS), would be required to confirm whether iron is present in these purple-staining calcite veins.
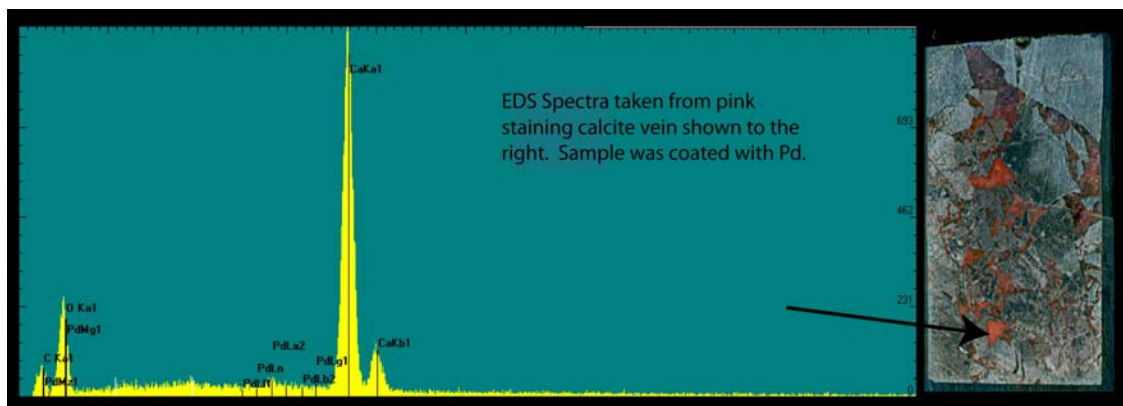
Figure 37: EDS spectra taken from the pink staining calcite shown in the billet to the right.
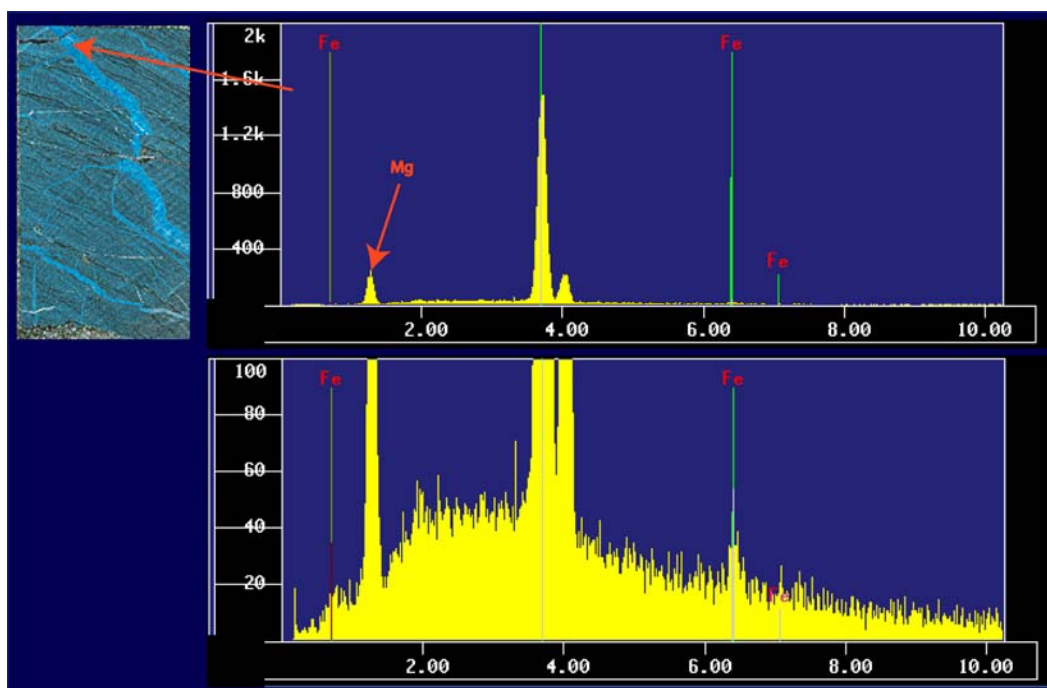
Figure 38: EDS spectra taken from the blue staining ferroan dolomite vein in the billet to the left. Note iron peak in the zoomed EDS spectra in the bottom of the figure.
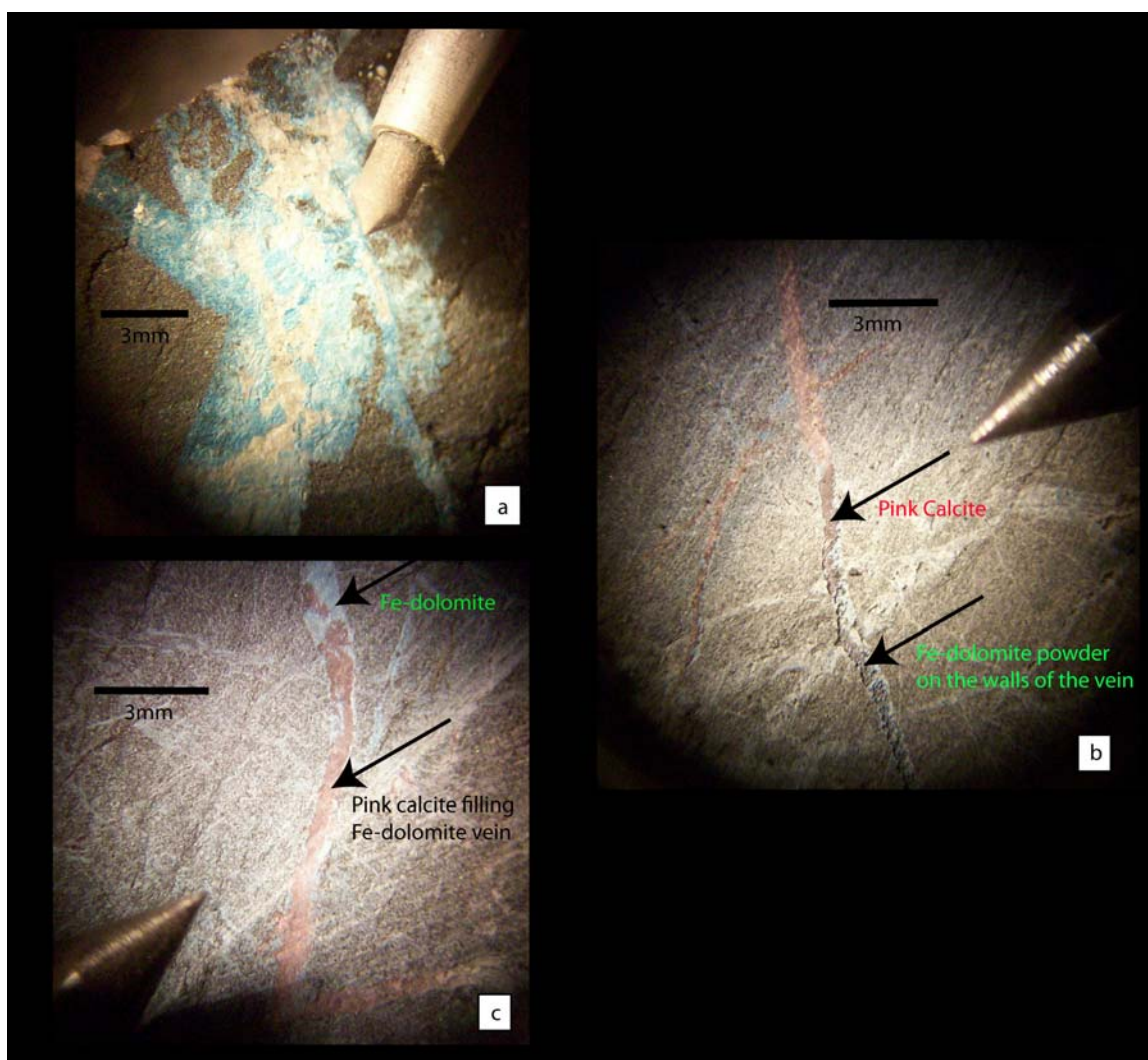
Figure 39:

a. Photograph showing altered dolomite and ferroan dolomite veins. Note the etched, clay-like appearance of both the dolomite and ferroan dolomite.

 b. Photograph showing where pink staining calcite is filling a leached dolomite vein. Remnants of altered ferroan dolomite occur along on the walls of the vein.

c. Another example of pink calcite filling a leached dolomite vein. The light blue material in vein in the top portion of the photograph is etched ferroan dolomite.

As mentioned above, all of the logging data was brought into ArcMap and plotted as point maps to compare the data to the vertical projection of known gold deposits and gold assays within the bottom 5 feet of the DSrm. The following discussion will address patterns observed by alteration, veining, and mineralization from the point maps with respect to mineralized areas. Patterns observed from Yukon-Nevada Gold's data set will be discussed, followed by observations made from the logging completed during this study.

The distribution of previously logged decarbonatized rock from the Yukon-Nevada database is mostly restricted to areas where gold values are greater than 300 ppb (Fig. 40a). Decarbonatized rock seems discontinuous and irregular because there are holes that were documented as being intensely decalcified within 50 feet from samples that were not logged as being altered. Decarbonatized rock logged during this project shows a similar pattern but much less extensive than what was logged previously (Fig. 40b).

Like decarbonatized rock, silicified rock is mostly restricted to areas where gold values are greater than 300 ppb (Fig. 40c). Silicified rock was logged locally outside the 300 ppb gold contour and the intensity of silicification does not systematically vary with respect to proximity of mineralized areas. Samples that are silicified commonly have samples within 50 feet of them that are unaltered, which again exhibits the discontinuous and irregular nature of alteration. Similar patterns of silicified rock were also observed in logging completed during this study, albeit the patterns are not as clear because of the fewer amount of data points (Fig. 40d).

Dolomitized rock is very sparse and no patterns were displayed in the previously logged data; however, the lithology type originally logged as dolomitic siltstone is very likely the dolomitized rock logged during this study (Fig. 40e). Dolomitic siltstone was originally logged in the SSX-Smith areas and along a northeast trend through Marlboro Canyon (Fig. 40e). The logging completed during this study shows that dolomitized rock is more pervasive throughout the study area than originally logged (Fig. 40f). There is no consistent relationship between the intensity of dolomitization and gold values. The intensity of dolomitization is stronger and is more pervasive in the SSX-Smith areas than in the Murray-Winters Creek area. Dolomitized rock is not as discontinuous or as restricted as the distribution of decarbonatized and/or silicified rocks. The magnesium and calcium analyses from the geochemical database along the Saval can also be used to show the distribution and degree of dolomitization. A gridded image of the magnesium to calcium molar ratio is shown in figure 40g. A molar ratio of one indicates pure dolomite and molar ratios less than one indicates a mixture of calcite and dolomite. The gridded image clearly supports the logging completed in this study and shows there is more dolomite in the SSX-Smith areas than there is in the Murray-Winters Creek area.

Oxidized, limonite-bearing rock was commonly documented in the previous logging and shouldn't be considered as a vectoring tool in the Jerritt Canyon district (Fig. 40h). Oxidized rock does not show a spatial relationship with elevated gold values (Fig. 40h). The type of oxidation was not documented in the previous logging, but during the project specific logging goethite was the main oxidation product that was logged. Hematite was logged in very few holes. Oxidation was pervasive and was generally less than 10% of the samples. Leached cavities were not documented.

Veining that was previously logged does not show much of a pattern. Several samples logged during this project had veins that were not monominerallic, but were not broken out in the maps generated in this project. For example, samples with quartz + calcite veins are displayed on the quartz vein map and on the calcite vein map.

In Yukon-Nevada Gold's database, monomineralic calcite veins were not distinguished from calcite+quartz veins so it is unknown whether the veins contain calcite+quartz or if there were monominerallic calcite and quartz veins present. Very few calcite+quartz veins were previously logged (Fig. 40i). New logging shows that calcite veining is very abundant and pervasive throughout the study area (Fig. 40j). Calcite veins occur almost entirely outboard of areas where gold values are greater than 300 ppb (Fig. 40j), rather than showing any spatial correlation to areas of gold concentration.

In Yukon Nevada Gold's database, dolomite veining, as originally logged, was entered as dolomite or dolomite+quartz veins, was sparsely logged, and shows no pattern with respect to mineralization (Fig. 40i). The logging completed during this study shows dolomite is commonly found within, but not restricted to, areas of greater than 50 ppb gold (Fig. 40k). However, ferroan dolomite veins documented during this study are more restricted to areas where gold values are greater than 50 ppb, and form a continuous halo to gold values that are greater than 300 ppb upwards of 100 feet (Fig. 40l). The ferroan dolomite halo is best exhibited in the SSX/Steer/Saval-Smith/Dash deposits but is also present in the Murray and Winters Creek deposits. As shown in Table 4, the 50-300 ppb gold halo extends out an average of 50-75 feet from the 300 pbb gold contour. On the other hand, ferroan dolomite forms a relatively continuous halo of about 100 feet

outboard from the 300 ppb gold contour, and a discontinuous halo upwards of 200 feet from gold values greater than 50 ppb (Fig. 40l).

Quartz veins that were previously logged and logged during this study occur mainly in areas of greater than 300 ppb gold (Figs. 40i & 40m). Unlike ferroan dolomite quartz does not make a halo to mineralization.

Veining density was logged in this study by visually estimating the volume percent of the 5 foot interval that consisted of vein material. The estimate includes all vein types within a given five foot interval. The gridded image and point map of the estimated vein densities show densities are generally lower within the vertical projection of known gold deposits and seem to increase slightly outboard of deposits (Figs. 40n & 40o). Low veining densities in the deposits and higher veining densities outboard of mineralized areas is best observed in the SSX-Smith/DASH deposits.

Results of staining the carbonate in the rock also seem to show spatial associations with the vertical projection of known gold deposits (Fig. 40p). Blue-staining rock, containing ferroan dolomite, commonly occurs proximal to deposits and has a very similar spatial distribution to the ferroan dolomite veins. Blue-staining rock is more closely associated to areas where gold values are greater than 300 ppb than non-staining or pink-staining rock. Pink-staining, calcite-bearing rock commonly occurs more than 600 feet outboard of the vertical projection of the deposits in the SSX-Smith area (Fig. 40p). However, in the Murray-Winters Creek area, pink and non-staining rock commonly occurs within 500 feet outboard of the deposits. Not all non-staining rock is dolomite-bearing. In many cases the rock was either too carbonaceous to see the stain or was silicified. It should be noted that one needs to be cautious in interpreting the results

of staining the rock. Iron from pyrite, limonite, or iron-bearing clays can cause the rock to stain blue. The DSrm has a significant amount of pyrite therefore the blue stain of the rock could be due to bleeding iron from the pyrite. Nevertheless, SEM/EDS analyses that were completed on blue-staining rock validated the presence of ferroan dolomite.

Sulfates and sulfides, including barite, pyrite, stibnite, realgar, and orpiment, were observed only locally in the previous logging and the logging completed during this study (Figs. 40q & 40r). Visually recognizable pyrite is mostly observed in areas where gold values are greater than 50 ppb (Fig. 43r). Three common modes of pyrite occurrence have been observed by Hutcherson (2002) at the Murray mine: 1) euhedral to subhedral cubes or aggregates of cubes 0.01-0.1mm in size; 2) anhedral, ratty textured and commonly pitted grains <0.01-0.5 mm in size; and 3) framboidal grains. Hofstra (1994) stated that the gold resides on the surfaces of oxidized framboidal pyrite, on the surfaces and in the rims of oxidized cubic pyrite, and within and on oxidized pyrite dodecahedrons. The pyrite observed in the project specific logging was euhedral to subhedral cubes or aggregates of cubes. The nature of the pyrite in the original logging was not documented. Therefore, it is conceivable that the pyrite documented during this study is probably not ore-stage, but rather diagenetic. Fine-grained ore-related pyrite is probably present in many other samples logged for this project, but was not visible in hand sample. There are very few occurrences of stibnite, barite, realgar, or orpiment at the bottommost 5 feet of the DSrm.

Figure 40: All point maps are presented with deposit outlines and the 50 – 300 and >300 ppb gold halo.

a. Yukon Nevada Gold's previously logged decarbonatized rock.

b. Project specific logged decarbonatized rock.

c. Yukon Nevada Gold's previously logged silicified rock.

d. Project specific logged silicified rock.

e. Yukon Nevada Gold's previously logged dolomitized rock and dolomitic siltstone.

f. Project specific logged dolomitized rock.

g. Classified gridded image of the magnesium to calcium molar ratio. Legend is for calculated grid values,

not actual values.

h. Yukon Nevada Gold's previously logged oxidized rock.

i. Yukon Nevada Gold's previously logged veining.

j. Project specific logged calcite veining.

k. Project specific logged dolomite veining.

l. Project specific logged ferroan dolomite veining.

m. Project specific logged quartz veining.

n. Visually estimated vein density percentage stretched gridded image. Deposit outlines in white. Legend

is for calculated grid values, not actual values.

o. Visually estimated vein density percentage point map.

p. Rock carbonate staining map.

q. Yukon Nevada Gold's previously logged mineralized rock.

r. Project specific logged mineralized rock.
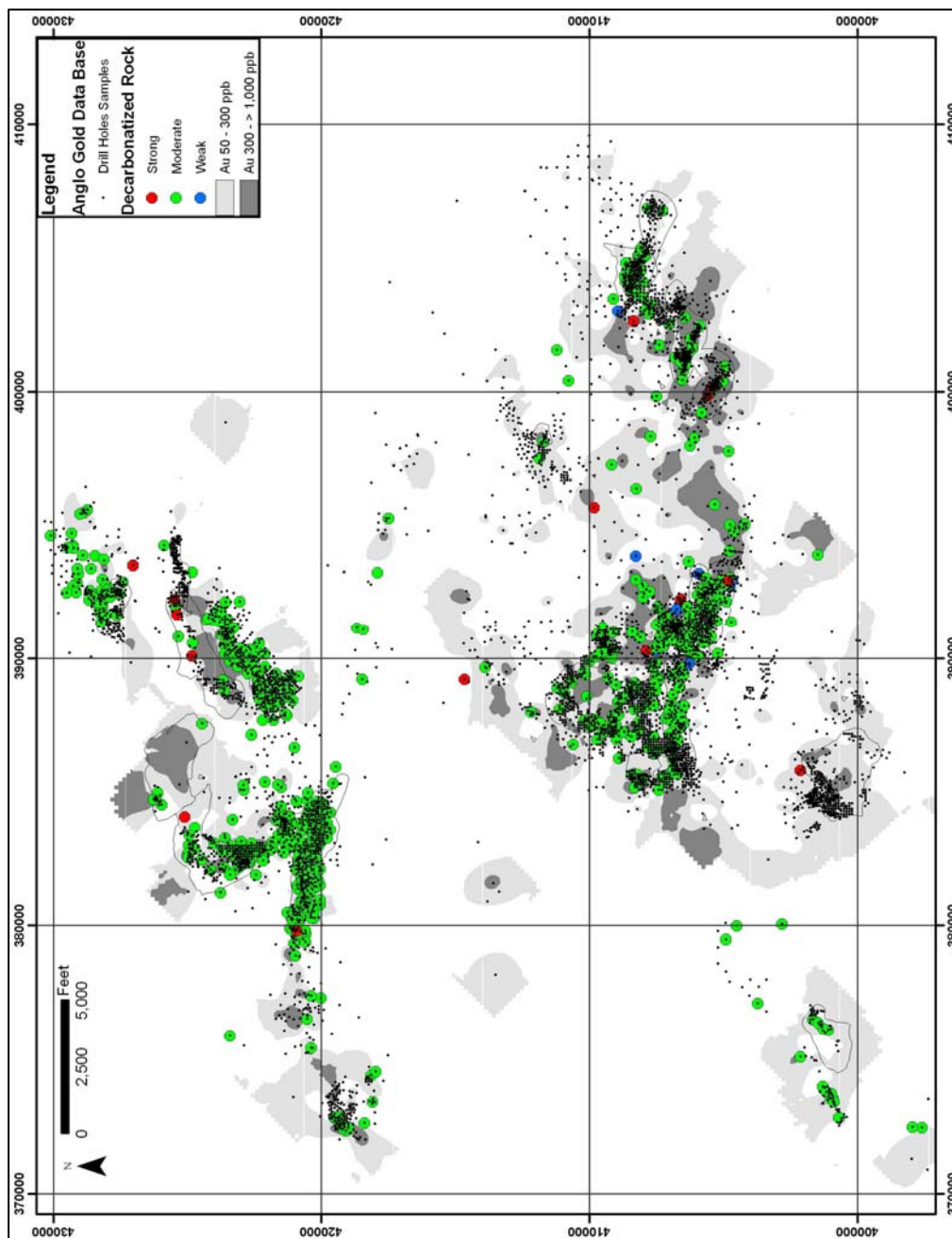
Figure 40a

Figure 40b

128

Figure 40c

129
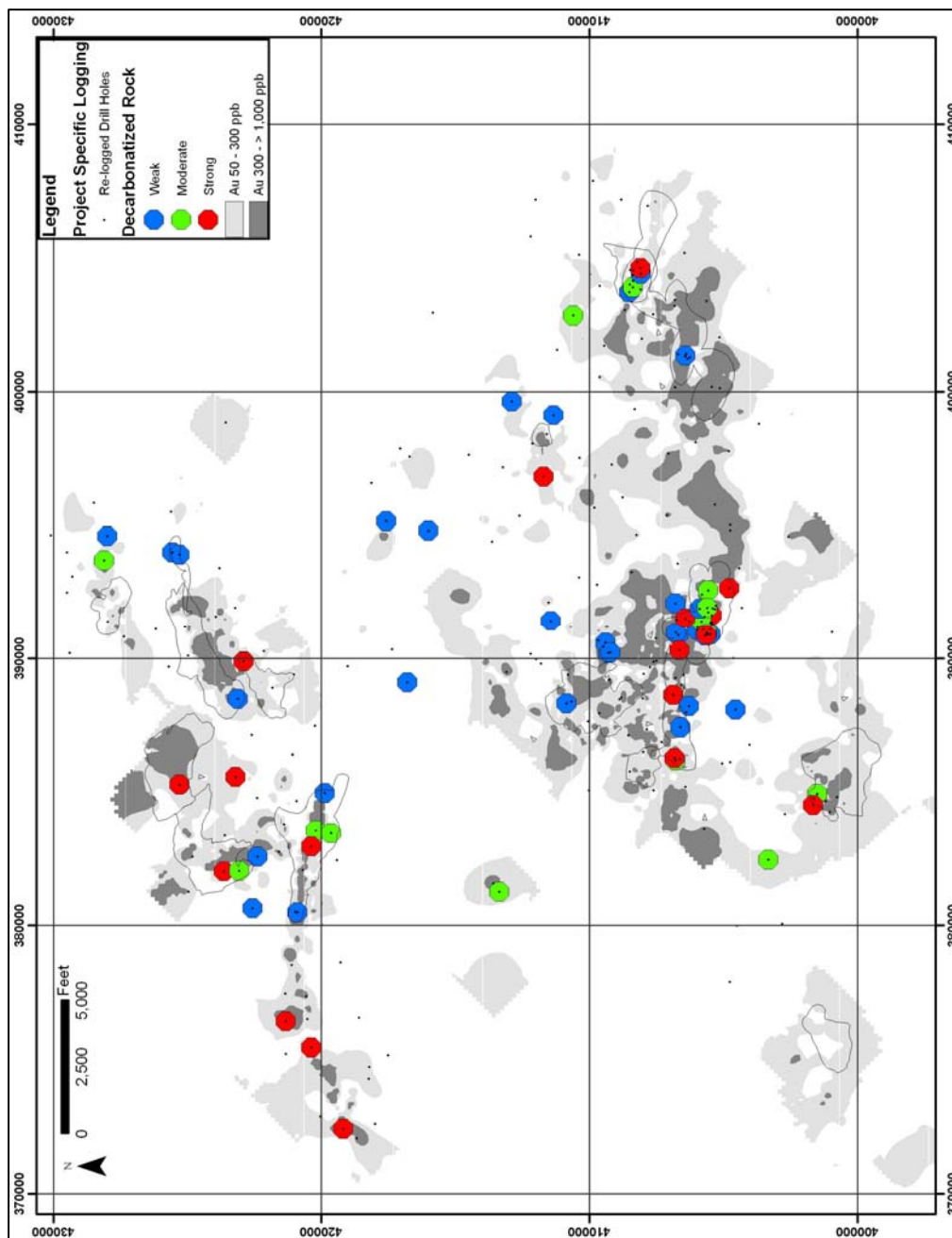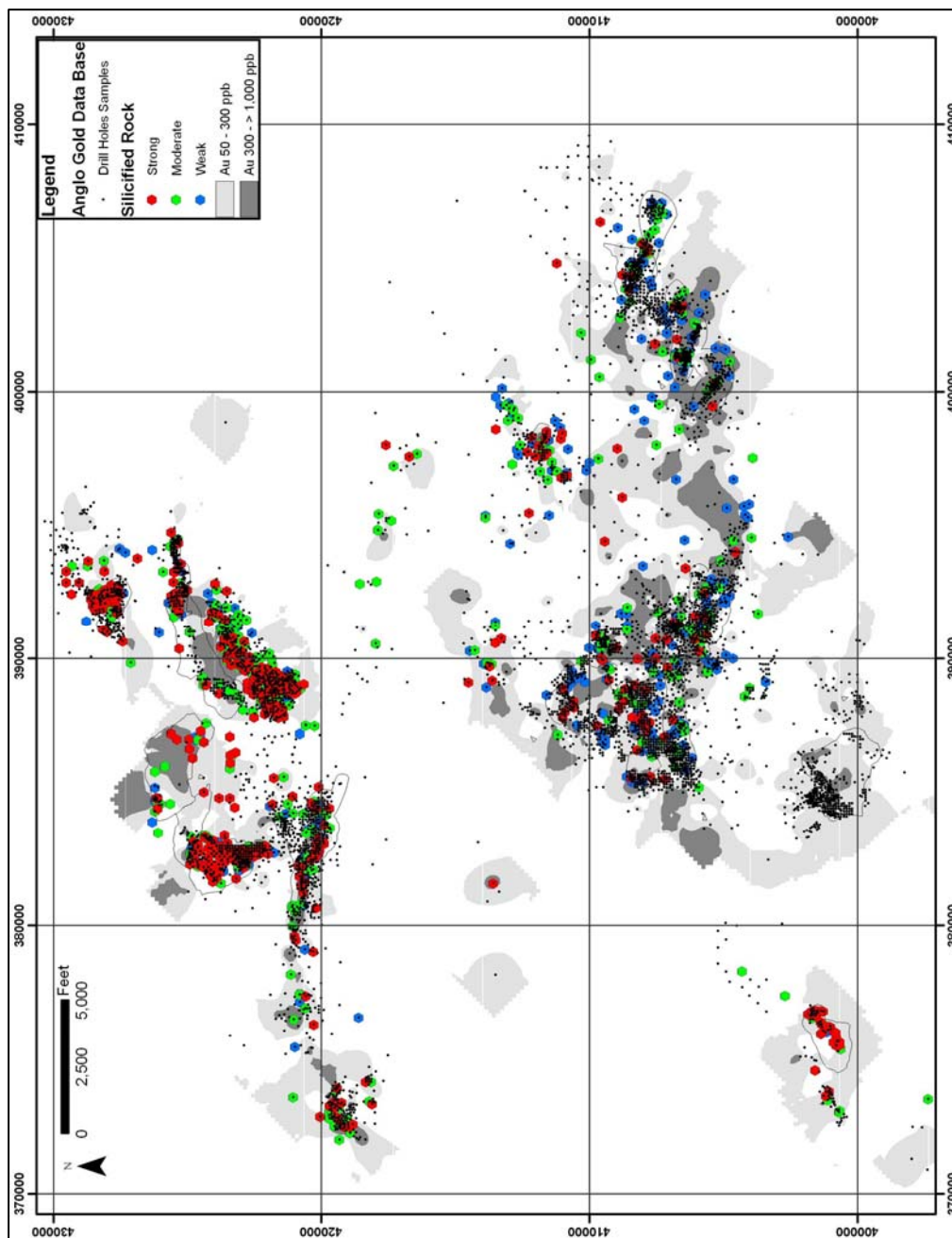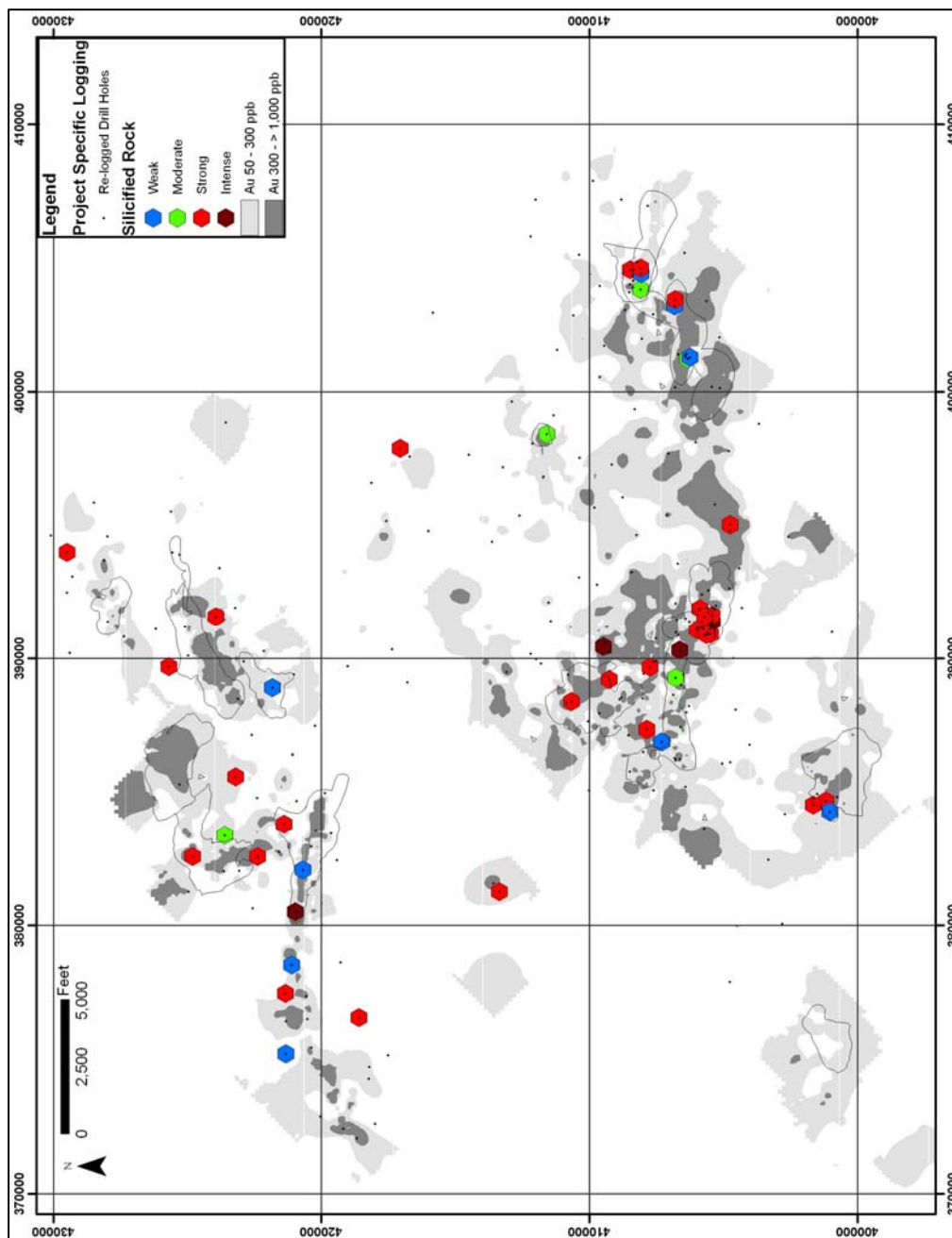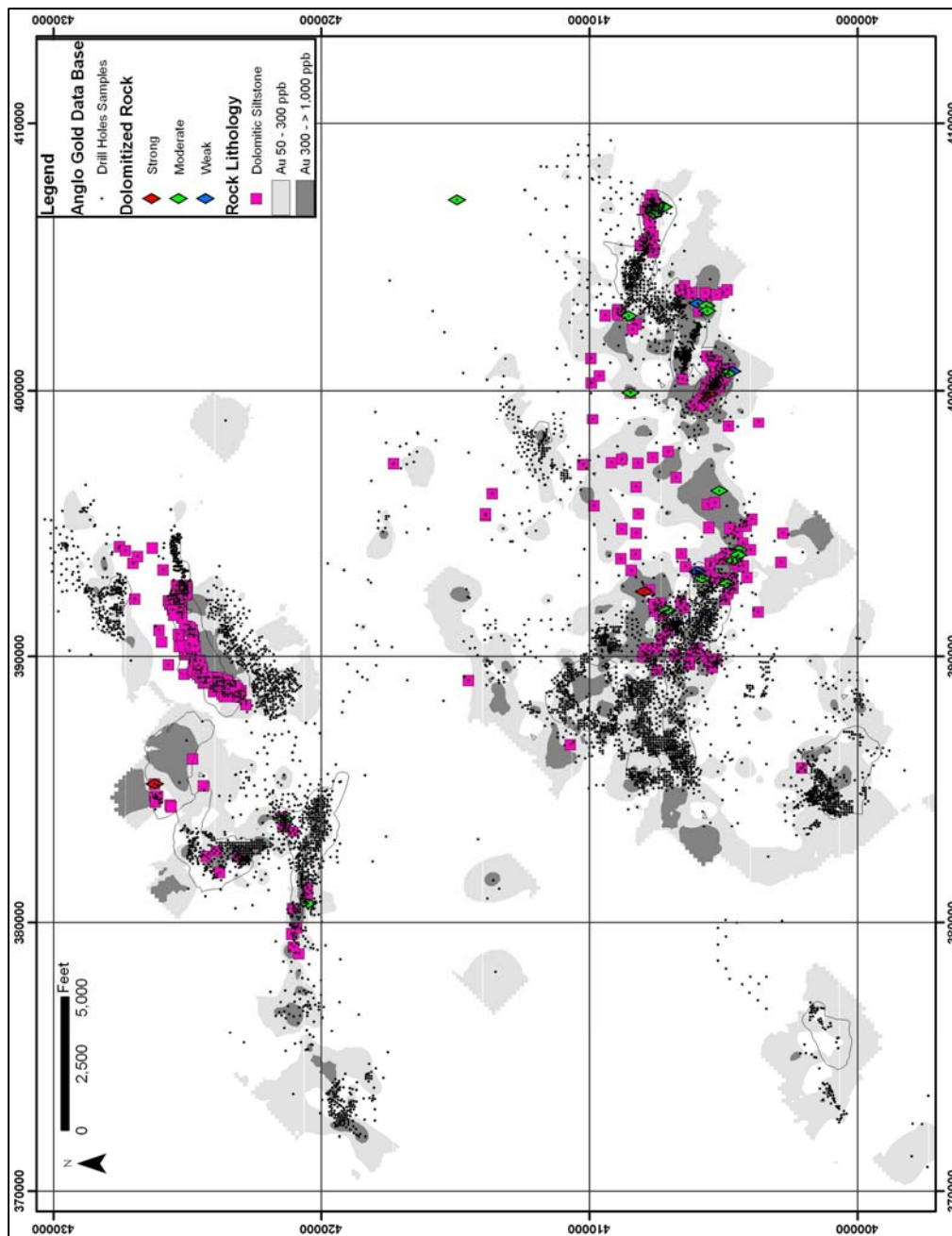
Figure 40d

Figure 40e
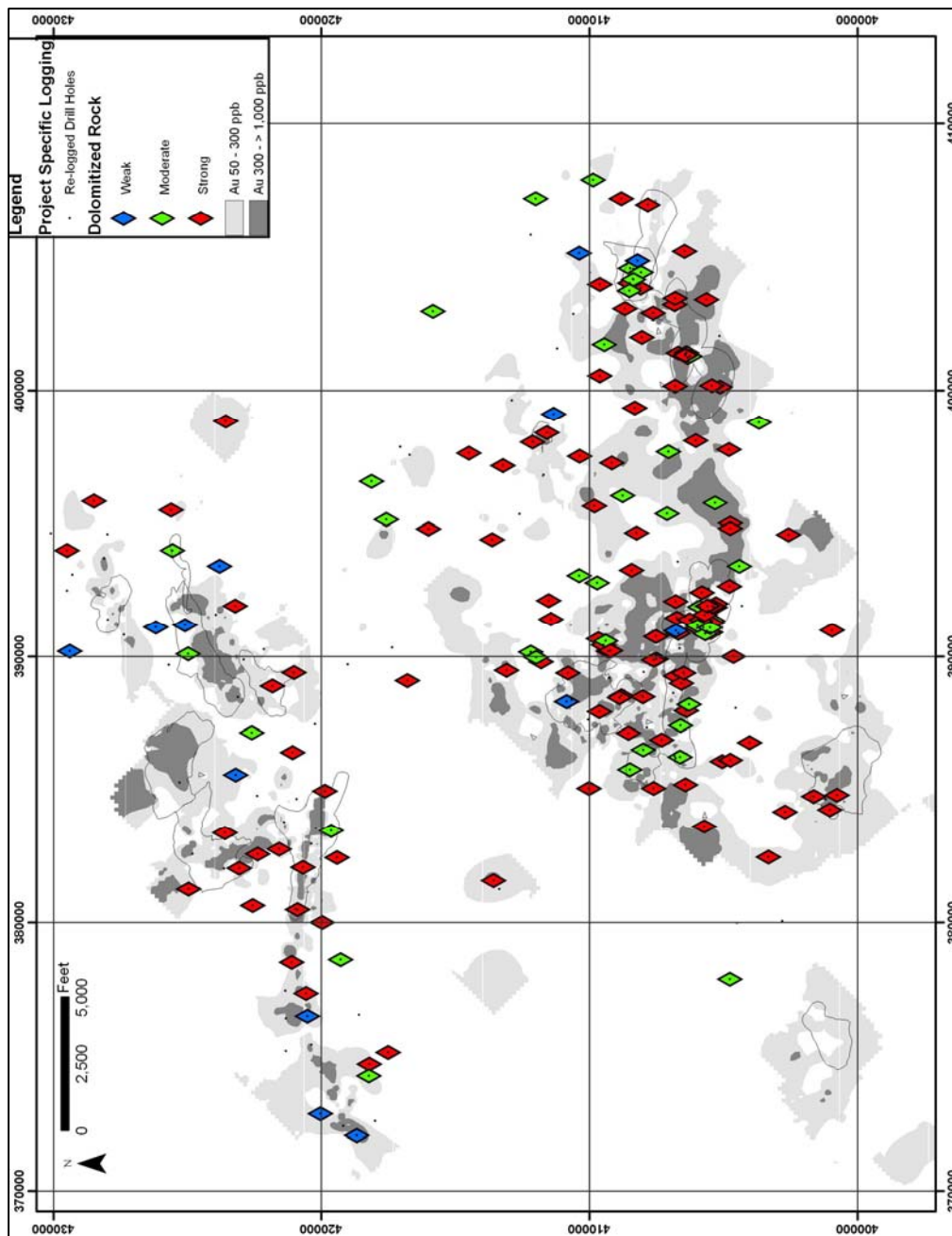
Figure 40f
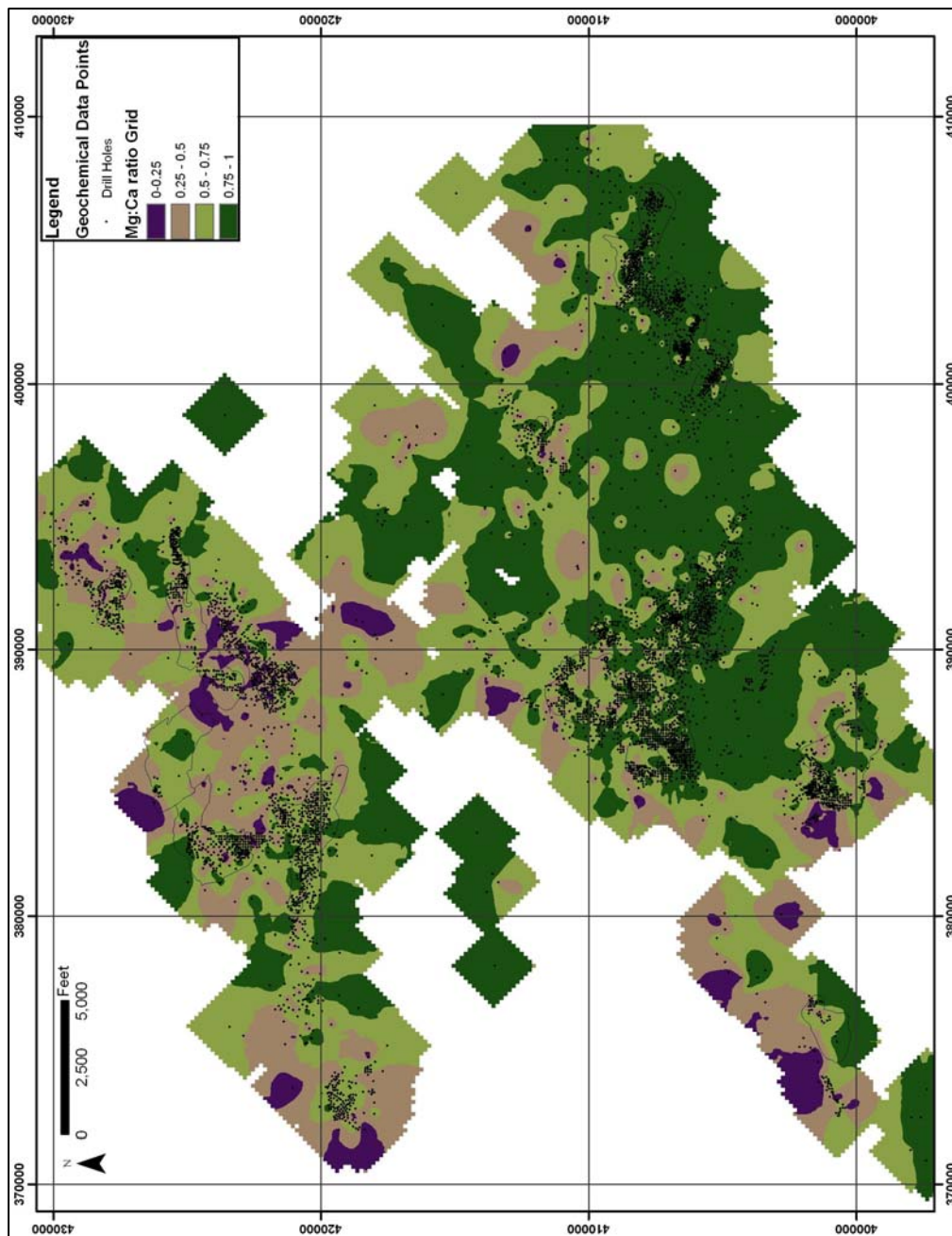
Figure 40g
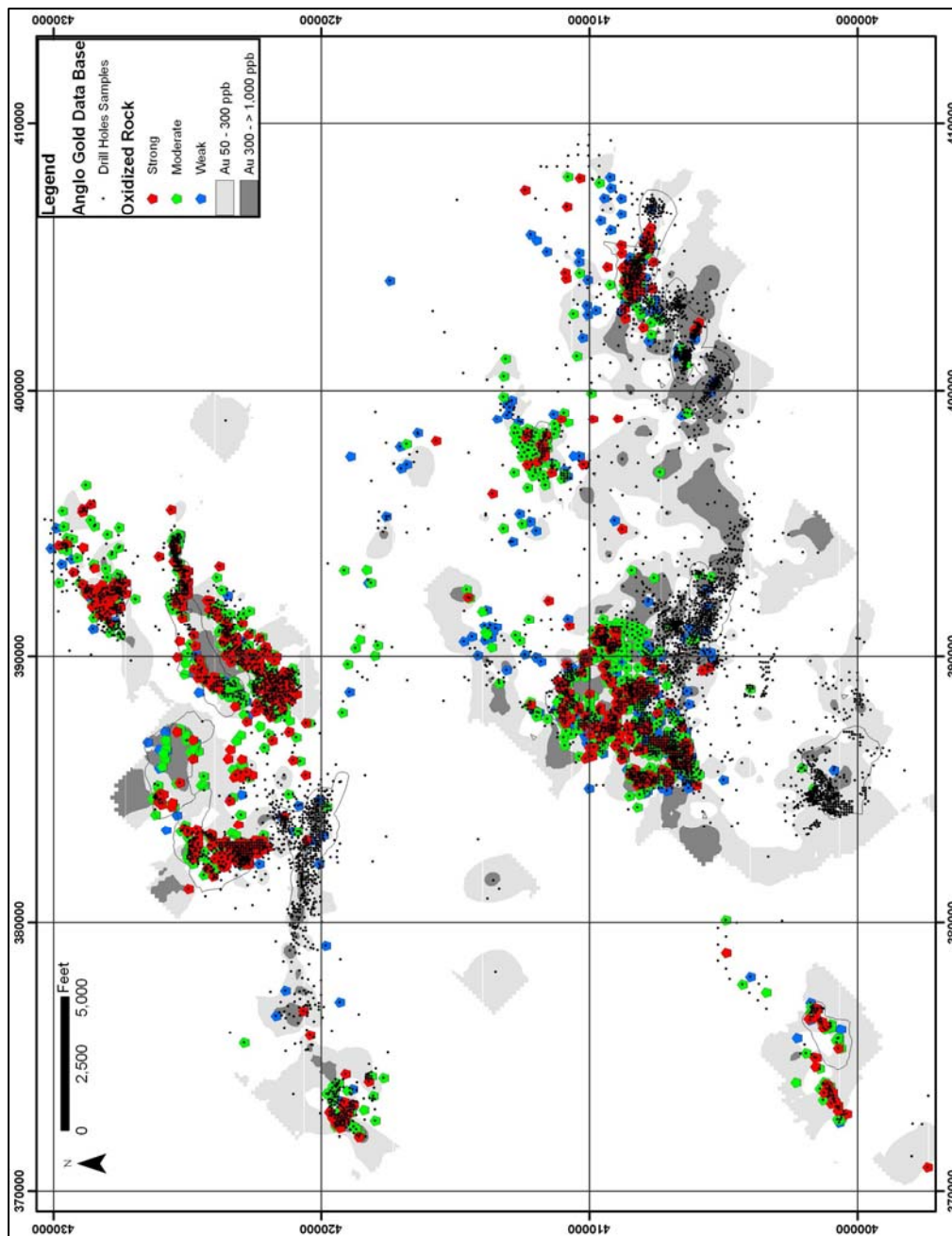
Figure 40h

Figure 40i

135
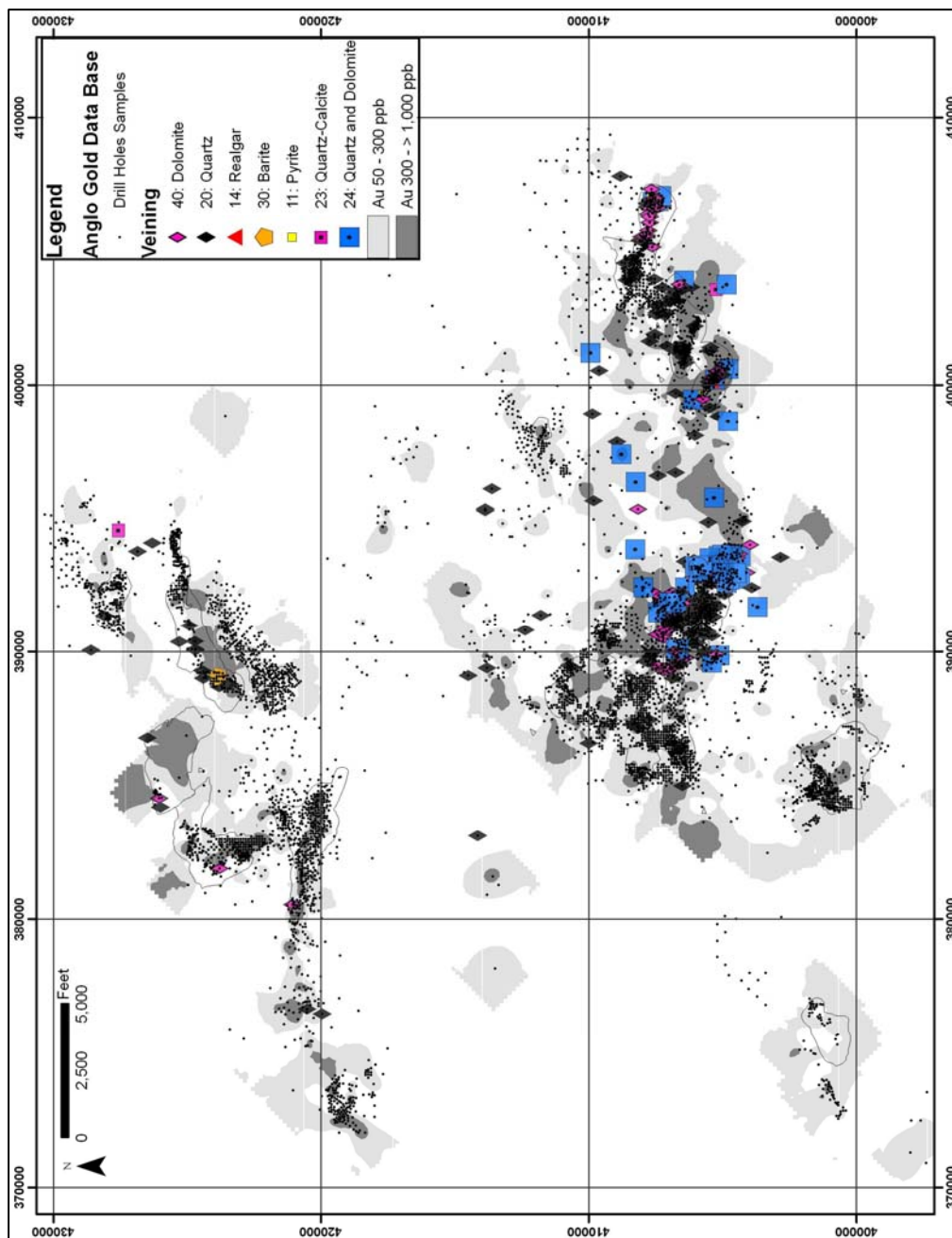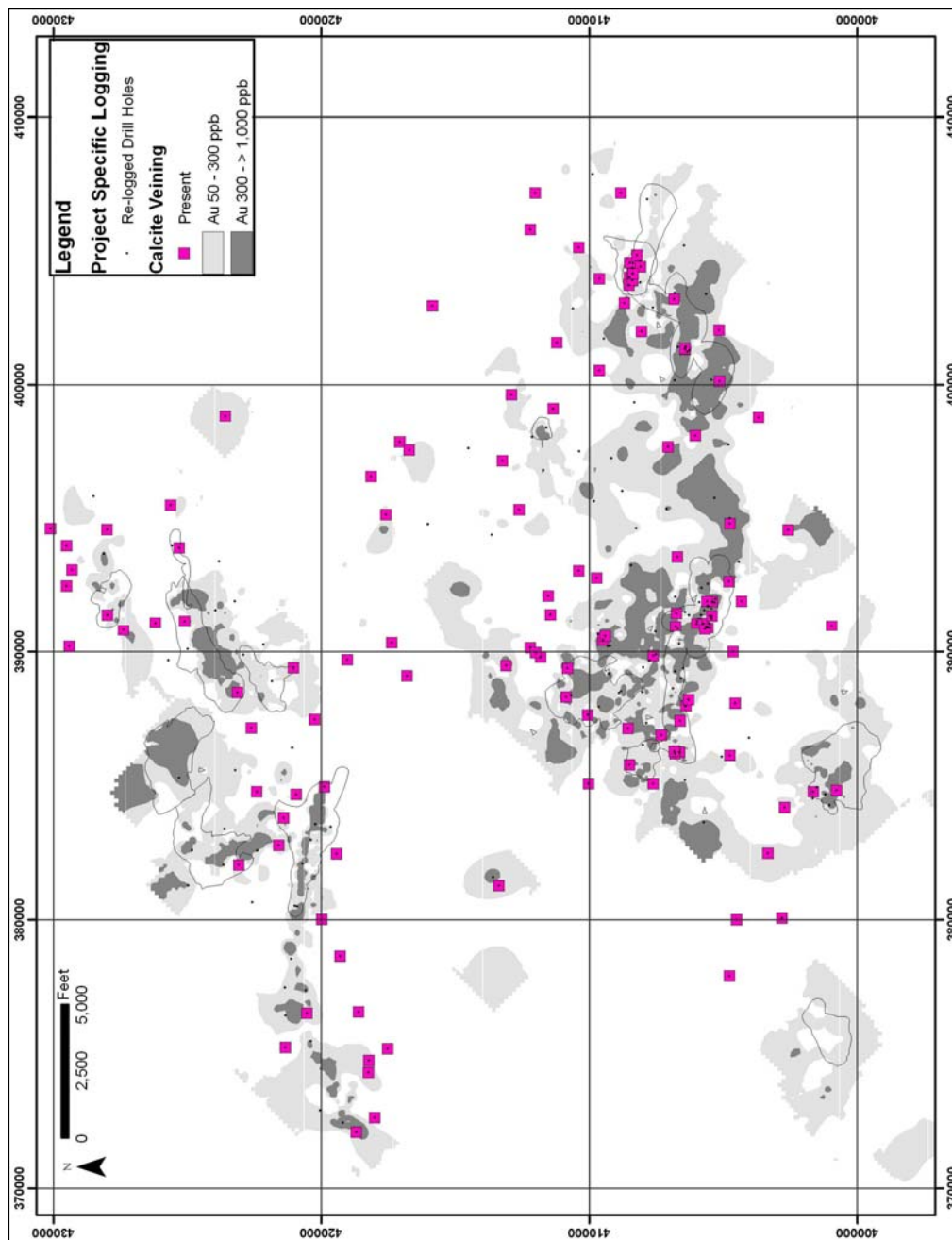
Figure 40j

Figure 40k

137
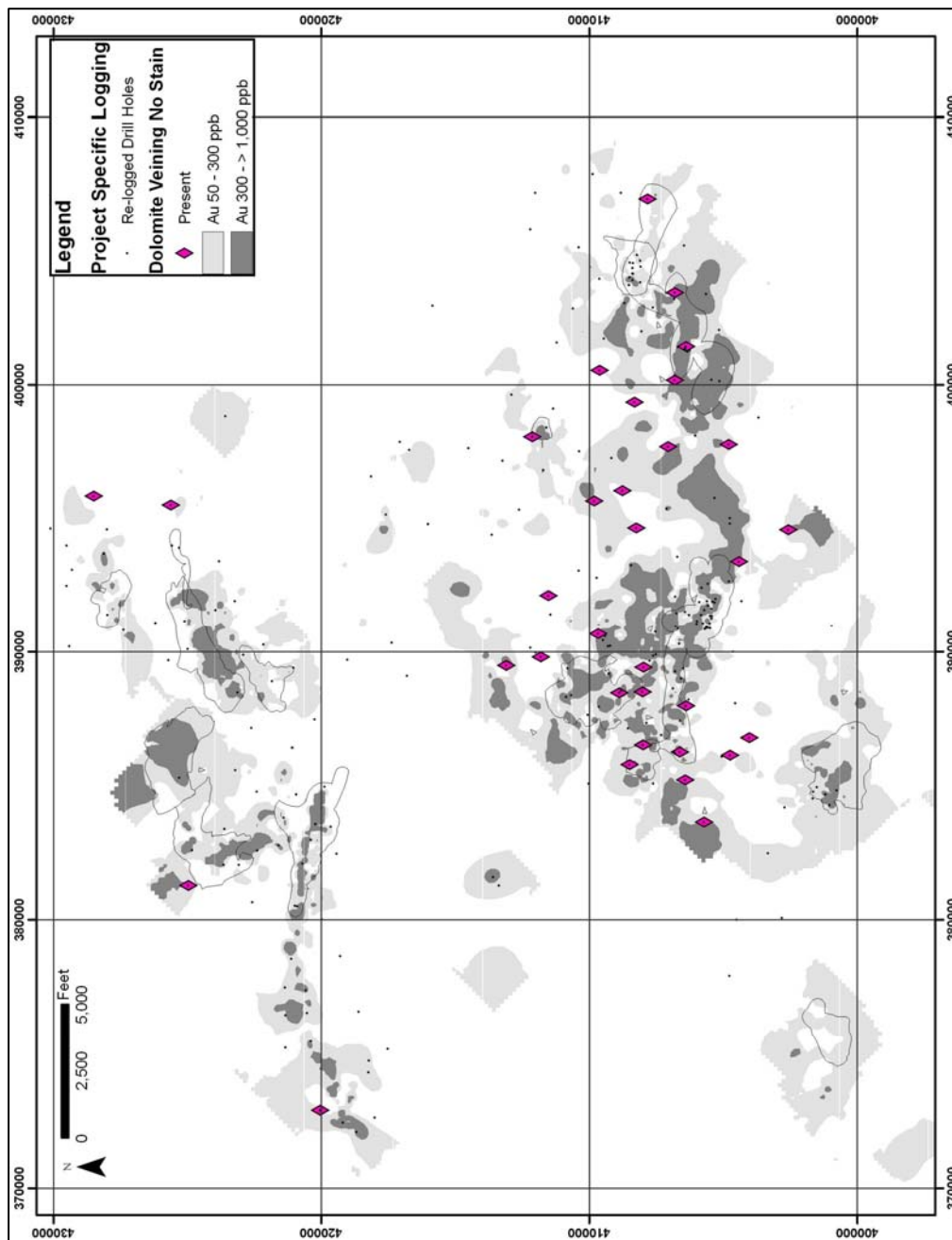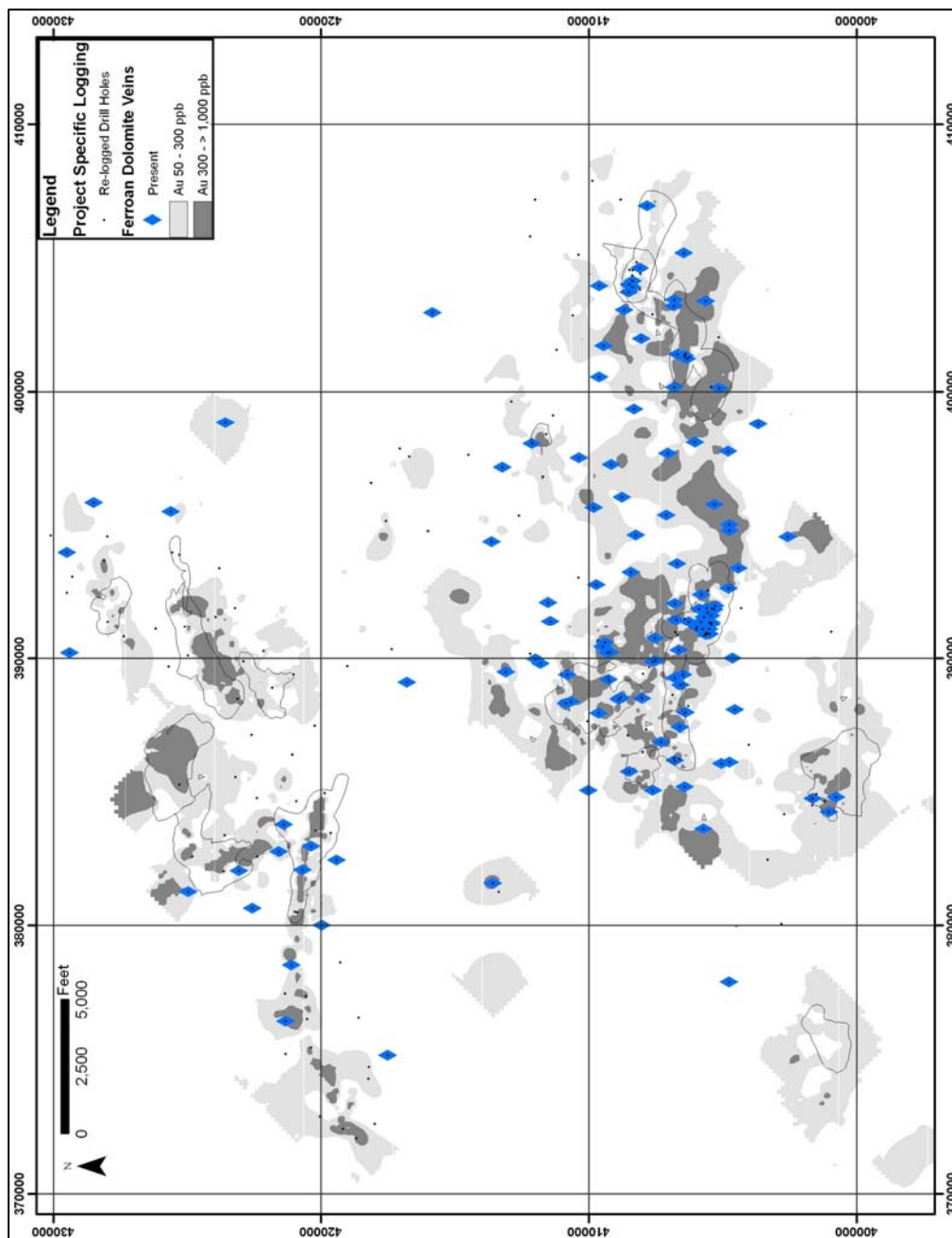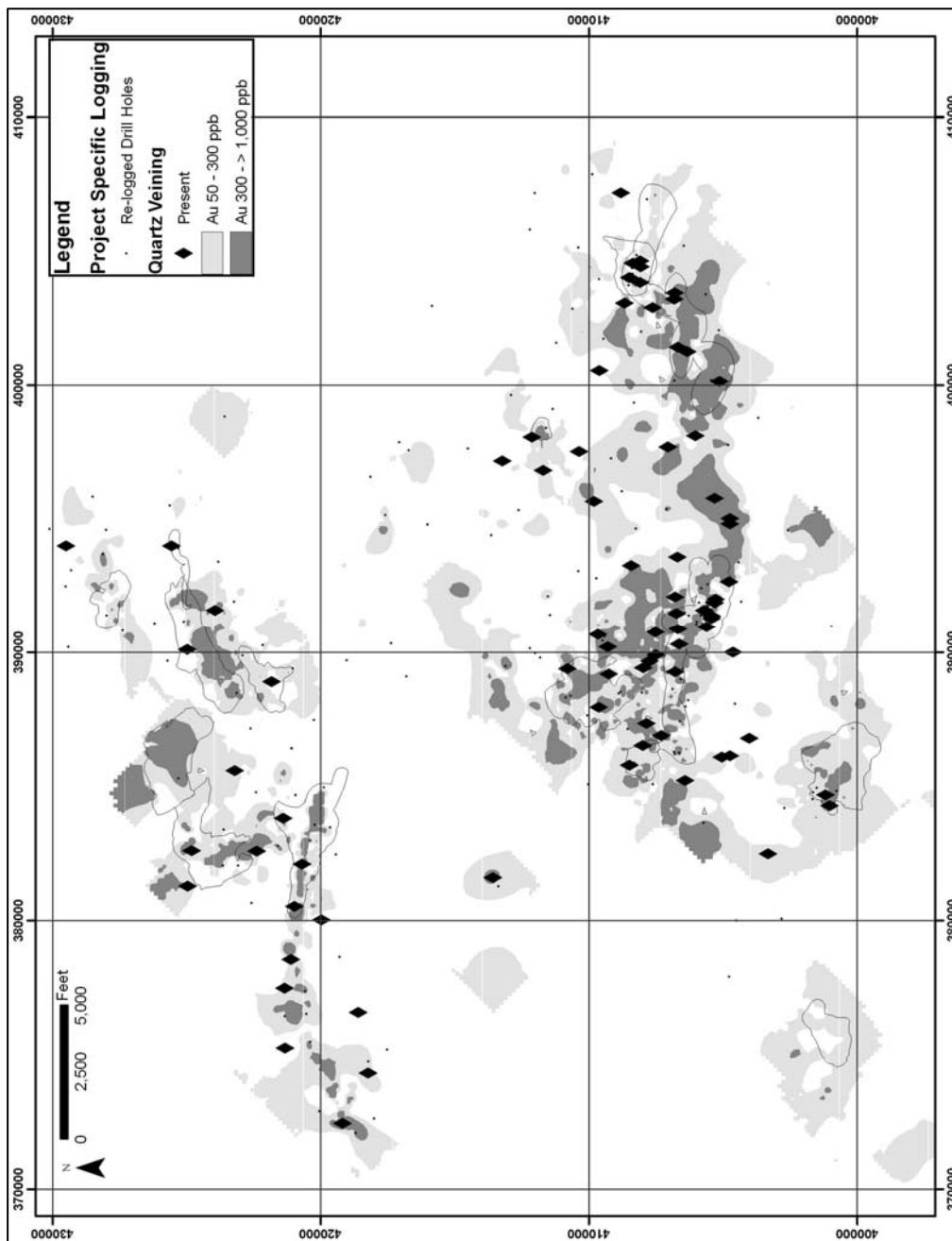
Figure 40l
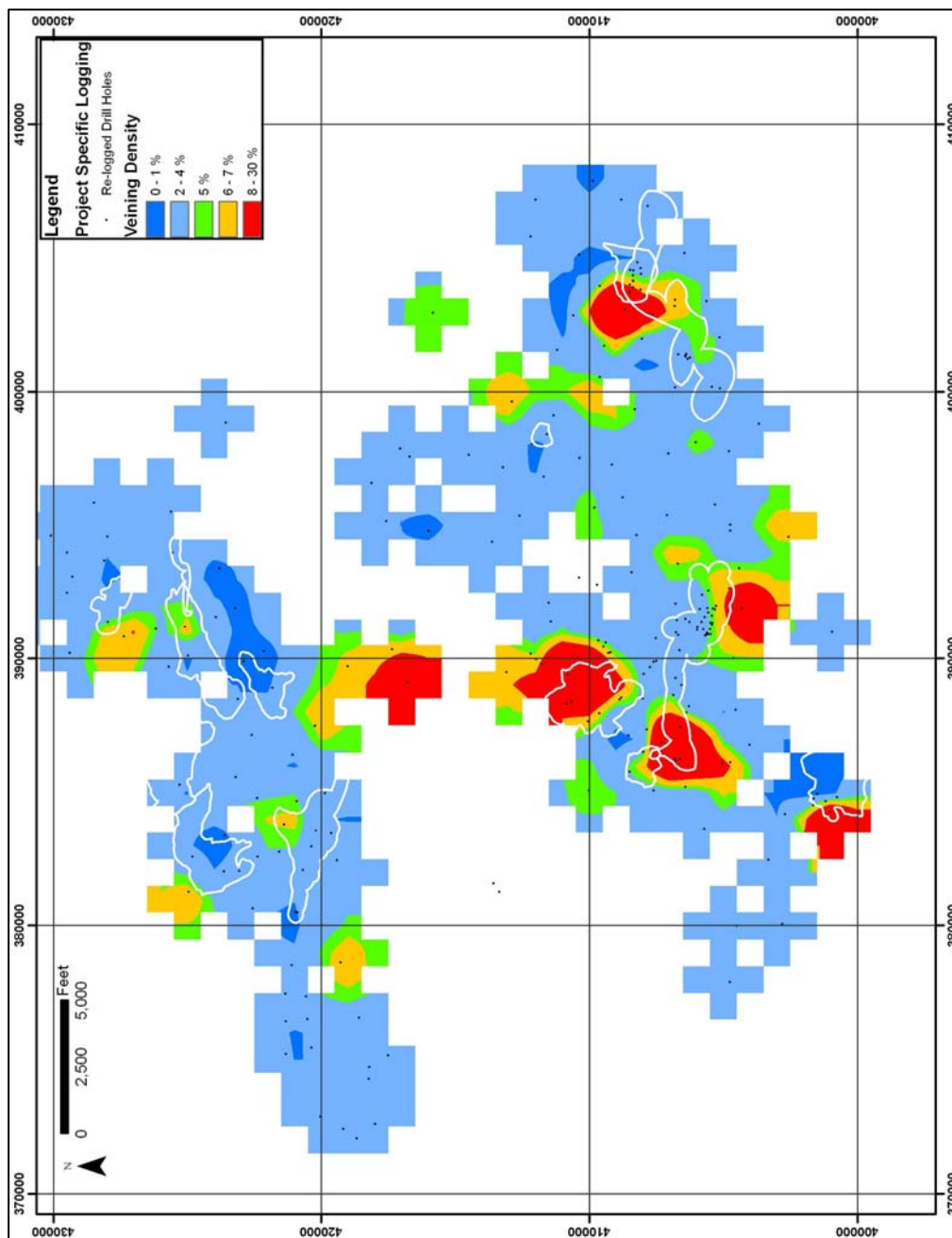
Figure 40m

Figure 40n
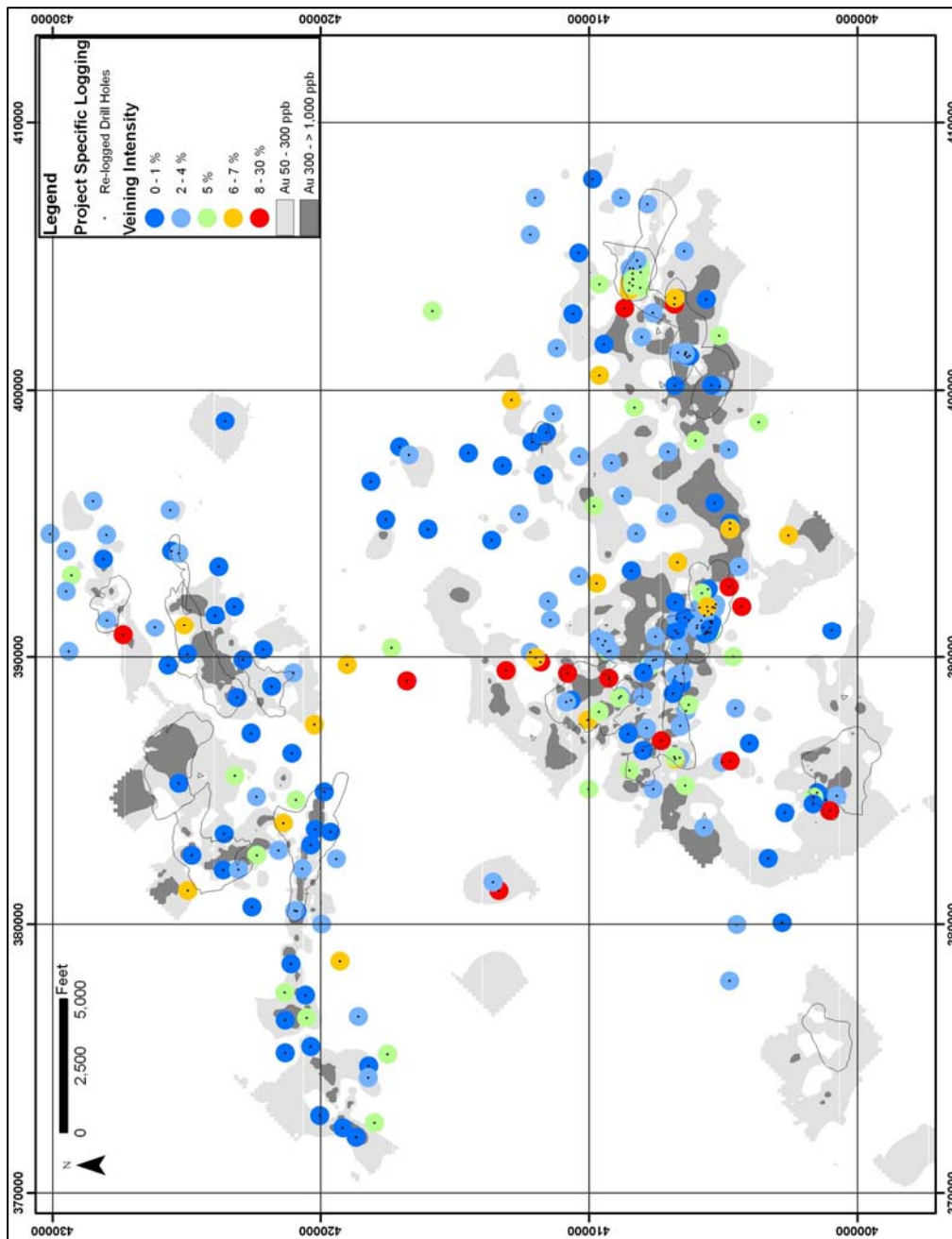
Figure 40o

Figure 40p

142
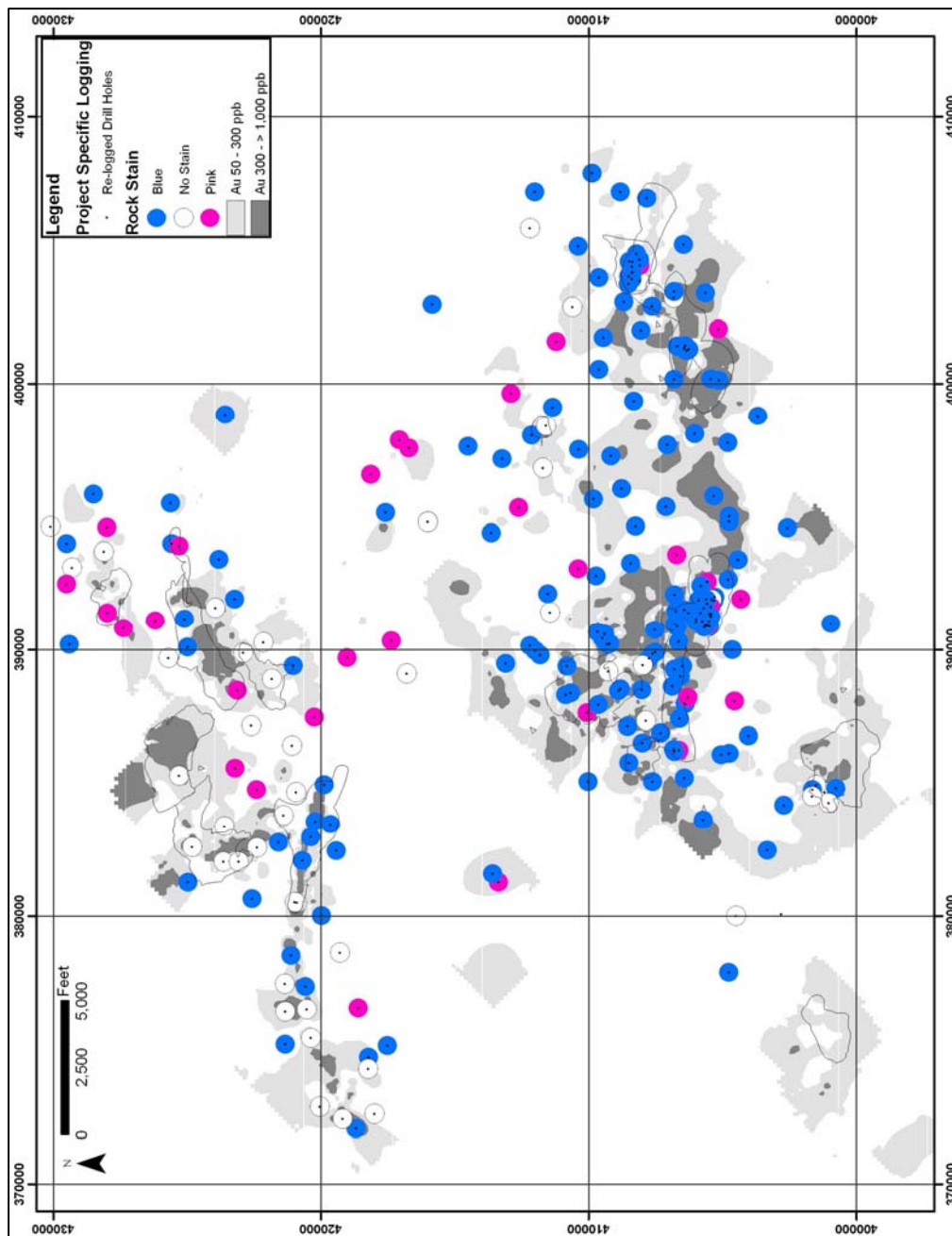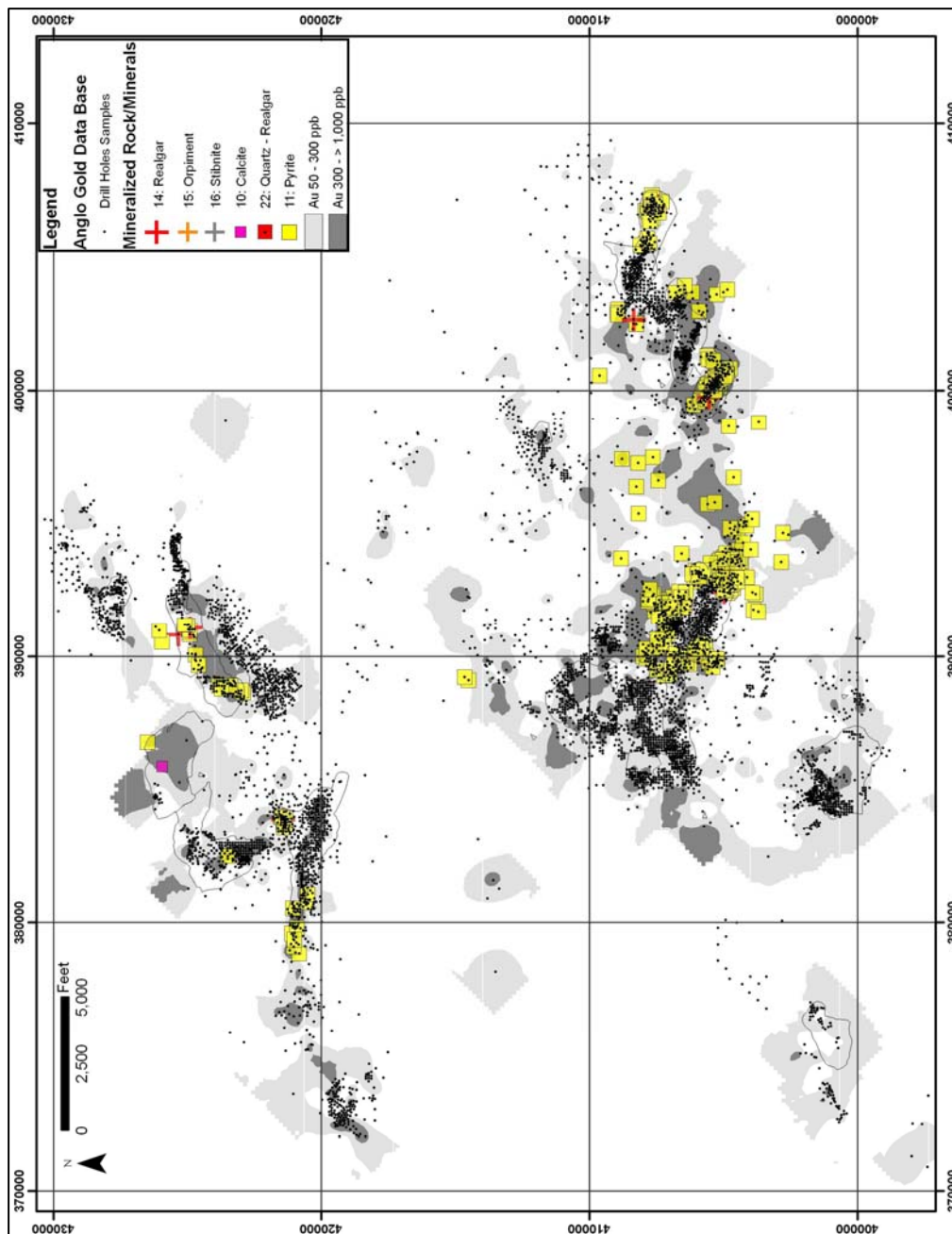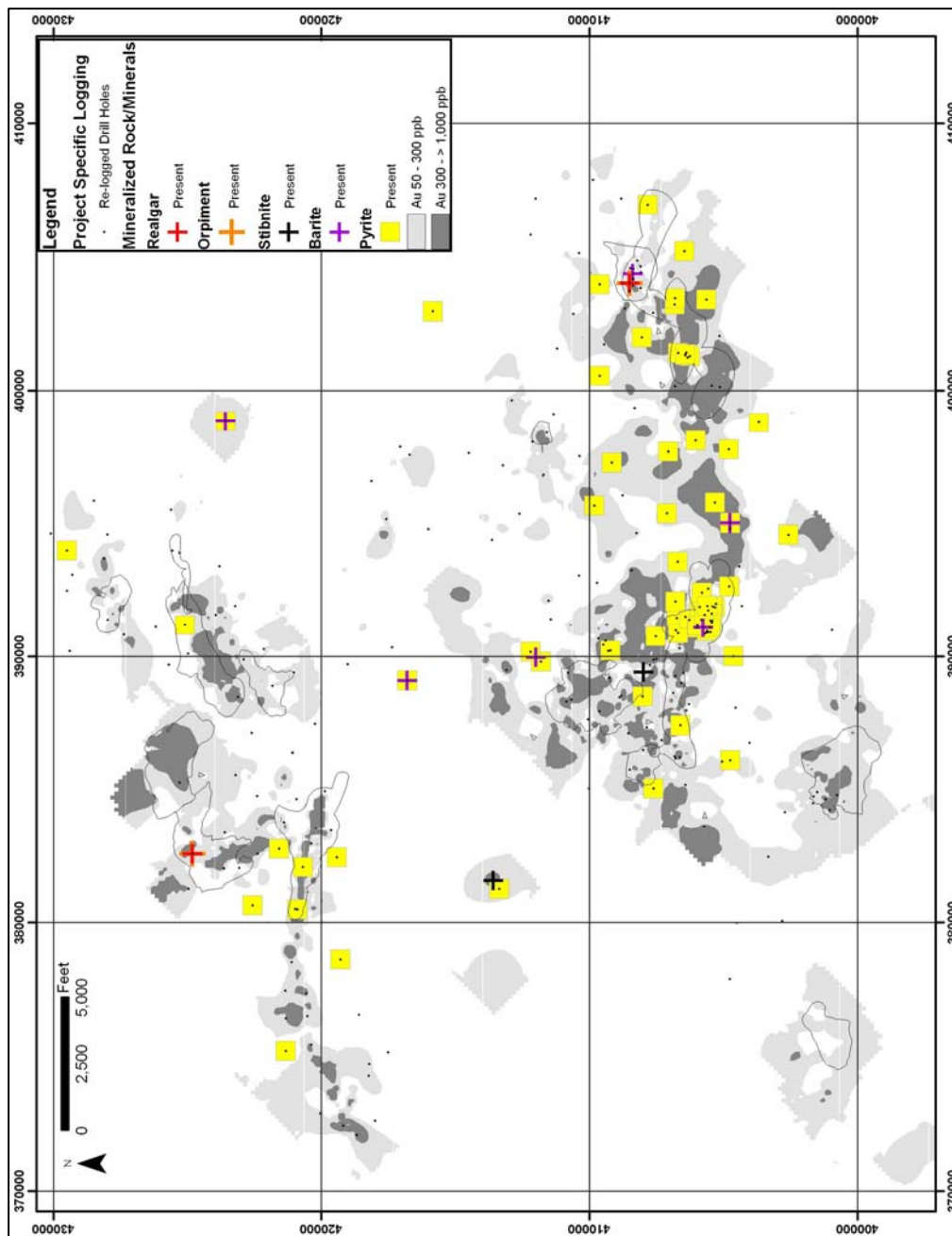
Figure 40q

Figure 40r

X-ray Diffraction

X-ray diffraction (XRD) analyses were completed to test whether or not there was any zoning in mineralogy, especially clays, along the Saval in and around the vertical projection of the known gold deposits at Jerritt Canyon. Splits of pulverized rock (pulps) from 297 holes from the entire 5 foot interval that was originally assayed for the Anglo Gold geochemical data set were analyzed in this study using the X-ray diffractometer at the Nevada Bureau of Mines and Geology. Of the analyses completed, 174 samples were from intervals that were re-logged for this project, and the rest of the samples were chosen based on proximity to missing pulp samples. No attempt was made to concentrate the clays; therefore, the sample can be considered a whole rock sample that contains both rock and vein material. The objective was to see if there were patterns in the clays and other minerals in the whole rock rather than only the clays. The next logical step would be to analyze clay concentrates. The pulps were made into a slurry using acetone in order to preferentially orient any clays in the sample. Initially 100 samples were analyzed using a 2-theta angle of 0° to 60°. Based on the initial results the range was decreased to a 2-theta angle of 6° to 40°. The mineral phases were identified using the software package JADE, which qualitatively categorizes the abundances of identified minerals as major, minor, or trace.

The minerals that were identified by JADE included quartz, dolomite, ankerite, calcite, muscovite (1M, 3T, $2M_1$, and $2M_2$), illite ($2M_1$ and $2M_2$), kaolinite (1Md and 1A), pyrite, marcasite, and arsenopyrite. Despite identification of polytypes by JADE software, the polytypes could not be reliably distinguished when the diffractograms were inspected. Samples are required to have about 5 % or more of a mineral phase in order to

be detectable. The clays in the analyzed samples represented a very minor fraction of the bulk sample therefore, the clay peaks were small, masked by other minerals present in the study, and were indistinguishable due to very similar 2-theta angles. Also without completing clay separates the illite and muscovite polytypes are also indistinguishable. Due to the inability to distinguish clay polytypes the illite-muscovite polytypes and the kaolinite polytypes were grouped together.

Twelve samples that were utilized for the calculation of elemental background, were analyzed by XRD in order establish the background mineralogy prior to Carlin-type mineralization in the Eocene (Table 7): Quartz, calcite, dolomite, and ankerite are major and minor mineral phases in most samples and appear to be characteristic of the rocks prior to gold mineralization. Along with quartz, calcite, and dolomite; pyrite has also been described to be common to the DSrm (Mullens, 1980). Also, illite-muscovite has commonly been observed in unaltered DSrm and was observed in thin section during this study (Fig. 9). Therefore, illite and/or muscovite in the DSrm could be of hydrothermal, authigenic, and/or detrital in origin. Hofstra (1994) indicated the presence of kaolinite in samples that have been strongly weathered and Mullens (1980) identified trace kaolinite during petrographic work but not in XRD analyses. Therefore, whether the kaolinite was present pre or post mineralization is not clear.

Sample	Quartz	Calcite	Dolomite	Ankerite	Muscovite-Illite	Kaolinite	Pyrite	Arsenopyrite
BB-875			Major	Major	Major			
GH-934C	Major	Minor	Major	Major	Trace	Trace	Trace	
GR-286	Major	Major	Major	Minor	Trace			
CM-335	Major	Major	Major					
BB-1008	Major	Major	Major	Major	Trace			
WW-224	Major	Major	Major	Major			Trace	
WC-495A	Major	Major	Major	Major				
CM-083A	Major		Major	Major				Minor
GR-286	Major	Major	Major	Minor	Minor			
CM-335	Major	Major						
CM-083A	Minor		Major					
GH-934C	Major		Major					

Table 7: Minerals present in samples that were chosen to represent calculated geochemical background.

Quartz, calcite, and dolomite are major or minor mineral phases in almost every analysis and do not exhibit a pattern to mineralization (Fig. 41a & 41b). Again, quartz, calcite, and dolomite have been documented as being the dominant mineral phases present in the DSrm (Mullens, 1980). Where present, ankerite occurs as a major or minor phase (Fig. 41c). Ankerite exhibits a spatial relationship with areas of elevated gold values, where it is most commonly found in areas with gold values greater than 50 ppb (Fig. 41c). Ankerite, identified by XRD analysis seems to form a continuous halo to gold values greater than 300 ppb and a spotty halo to gold values greater than 50 ppb. However, like the ferroan dolomite documented during the project specific logging, XRD-ankerite exhibits a closer spatial relationship to areas where gold values are greater than 50 ppb than dolomite, quartz, or calcite (Fig. 41c). Also, in every sample that had logged ferroan dolomite, ankerite was identified by the XRD analyses (Figs. 40l & 41c).

Muscovite-illite is present in 152 samples. Muscovite-illite share some spatial patterns with areas of gold mineralization (Fig. 41d). Though there are several samples with muscovite-illite outboard of gold values greater than 50 ppb, the most concentrated

occurrences of these minerals are within areas where gold values are greater than 300 ppb. The close association between illite-muscovite and areas of mineralization is best observed in the Steer/Saval/SSX area and along the New Deep Fault at the Murray mine (Fig. 41d). Kaolinite is present as a minor and trace mineral phase in 61 samples (Fig. 41e). The samples that have kaolinite are closely associated, but not necessarily restricted to areas where gold values are greater than 50 ppb (Fig. 41e). Like illite/muscovite, kaolinite is also more concentrated in areas where gold values are greater than 300 ppb and forms a discontinuous halo to the 300 ppb gold contour. There was no evidence for dickite but it is difficult to distinguish dickite from kaolinite in whole rock diffractograms.

Pyrite, marcasite, and arsenopyrite were detected in the XRD analyses and are present locally as minor or trace mineral phases (Fig. 41f). All sulfides are spatially associated with mineralized areas. Pyrite is the only sulfide that consistently appears outside of areas where gold values are less than 50 ppb (Fig. 41f), which likely reflects diagenetic pyrite in the DSrm.

Though the maps show some patterns that appear to be related to mineralization bar and whisker and cumulative distribution plots were generated using SYSTAT 11 to test the relationship between the identified mineral phases identified and gold grade (Fig. 41g & 41h). The bar and whisker plots show that the median gold value for samples with pyrite, marcasite or no carbonate is higher than samples with quartz, calcite, dolomite, ankerite, or clays (Fig. 41g). However, in the upper quartile, gold values are the highest for samples with quartz, dolomite, and ankerite (Fig. 41g). The distribution of gold values for samples with illite-muscovite or pyrite is very similar except the upper quartile

for the samples with illite-muscovite have higher gold values than samples with kaolinite (Fig. 41g). The cumulative distribution plots of gold values for samples with quartz, dolomite, ankerite, calcite, illite-muscovite, kaolinite, and pyrite, and samples without carbonate are shown in Figure 41h. Samples with pyrite and marcasite, and samples with no carbonate have higher gold values compared to the samples with quartz, dolomite, ankerite, calcite, illite-muscovite, or kaolinite, which show no significant differences in their cumulative distribution plots (Fig. 41h).

The lack of a statistical relationship between illite-muscovite and gold could be indicating that the spatial association between gold and illite observed during this study may not necessarily be real. As mentioned before, it is very difficult to distinguish muscovite and illite polytypes without making clay separates. The DSrm contains about 7 % clay, most of which is illite (Mullens, 1980). In the North Generator Hill pit Hofstra (1994) also documented the presence of detrital and authigenic $2M_1$ illite within and outboard of the ore zones. Therefore, without clay separates it is difficult to determine whether illite and muscovite formed during mineralization or was mainly of sedimentary origin and was locally enriched in areas of mineralization by leaching of carbonate. As the fluids leach carbonate, the illite would be effectively concentrated enough to show peaks on the XRD. In other words, the pattern may not necessarily be strictly due to acidic attack on silicate minerals, but from concentration of detrital and/or authigenic illite-muscovite within the sample interval during hydrothermal alteration. Also, the generation of late stage acidic fluids by supergene processes have been correlated with some occurrences of kaolinite in the Jerritt Canyon district (Hofstra, 1994). However, most of the samples used for this study were not oxidized.

Similar associations between ore, kaolinite/dickite, and illite have been documented at other Carlin-type deposits. Kuehn and Rose (1992) documented that within the Carlin mine dickite-kaolinite are found within the feeder zones where illite is present just outboard of the feeder zones and within unaltered rocks. At the Genesis and Blue Star deposits Drews-Armitiage *et al*. (1996) documented that the least altered rock of the Popovich Formation contains few to no clay minerals. In unaltered rocks where clay is present kaolinite was observed replacing carbonate. However, hydrothermally altered Popovich is comprised of 10-35% clay minerals where the abundance of illite and kaolinite increases in proximity to ore zones. At the Getchell deposit, Cail and Cline (2001) documented that kaolinite was present in low abundances in mineralized and unmineralized rocks. Kaolinite did not show a strong statistical correlation with gold however, illite exhibited a positive correlation with gold and was also texturally, spatially, and volumetrically associated with gold (Cail and Cline, 2001). A spatial relationship between gold and kaolinite was documented by Heitt *et al*. (2003) at the Deep Star deposit. A zoning sequence extended outward from high grade ore where gold and intense kaolinite were found in the core of the system. Outboard of the gold and intense kaolinite zone the alteration assemblage changed to a weak to moderate kaolinite zone and finally to smectite + kaolinite and illite zone.

Figure 41: Image showing XRD mineral phase distributions are shown with deposit outlines, the 50 – 300 ppb gold halo, and the > 300 ppb gold halo.

a. XRD analysis-point map of dolomite distribution.

b. XRD analysis-point map of calcite distribution.

c. XRD analysis-point map of ankerite distribution.

d. XRD analysis-point map of muscovite-illite distribution.

e. XRD analysis-point map of kaolinite distribution.

f. XRD analysis-point map of sulfide distribution.

g. XRD bar and whisker plots of gold values for samples that contain quartz, samples do not carbonate, samples that contain dolomite, samples that contain calcite, samples that contain ankerite, samples that contain illite-muscovite, samples that contain kaolinite, and samples than contain pyrite-marcasite.

h. XRD cumulative distribution plots of gold values for samples that contain quartz, samples do not contain carbonate, samples that contain dolomite, samples that contain calcite, samples that contain ankerite, samples that contain illite-muscovite, samples that contain kaolinite, and samples than contain pyrite-marcasite.
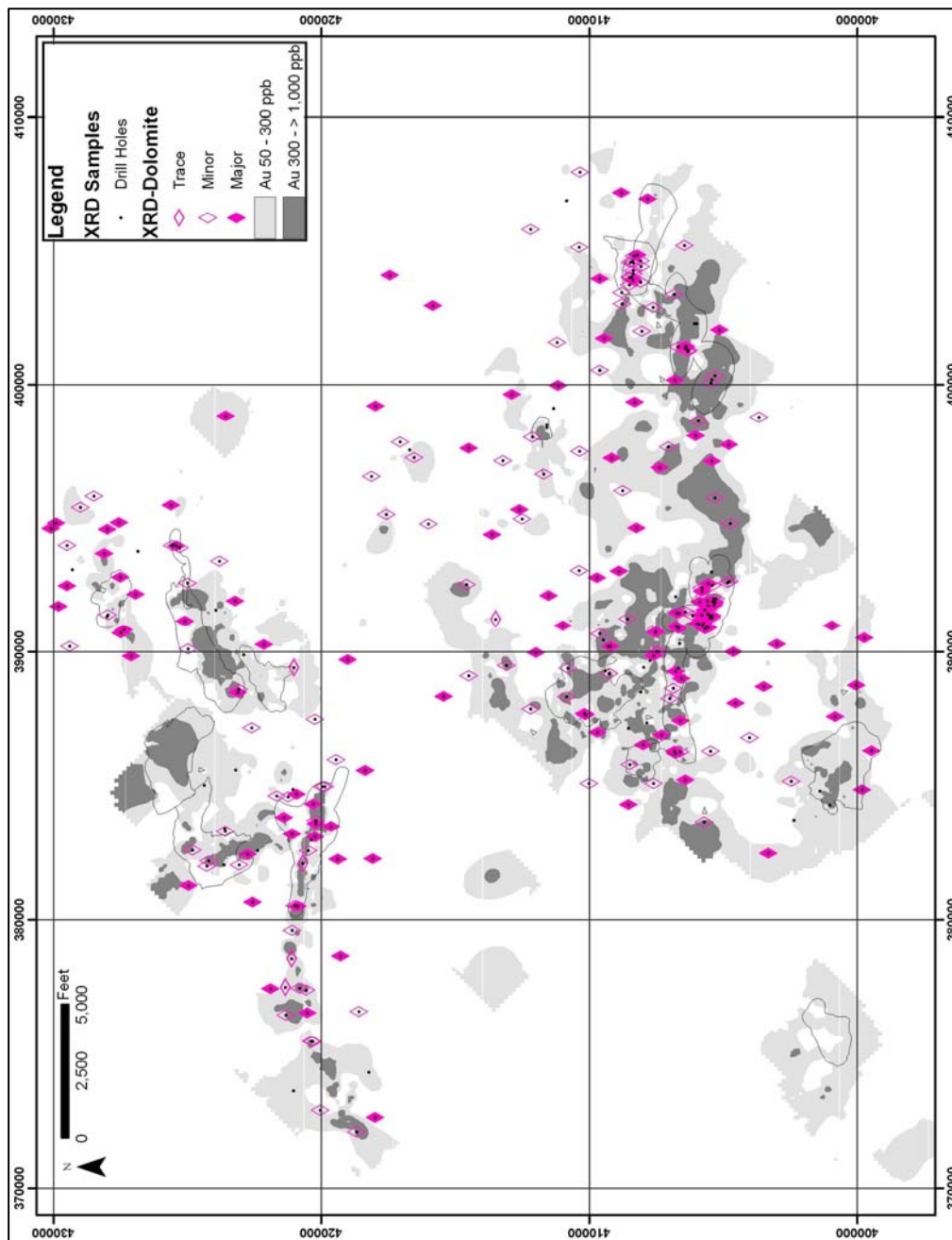
Figure 41a
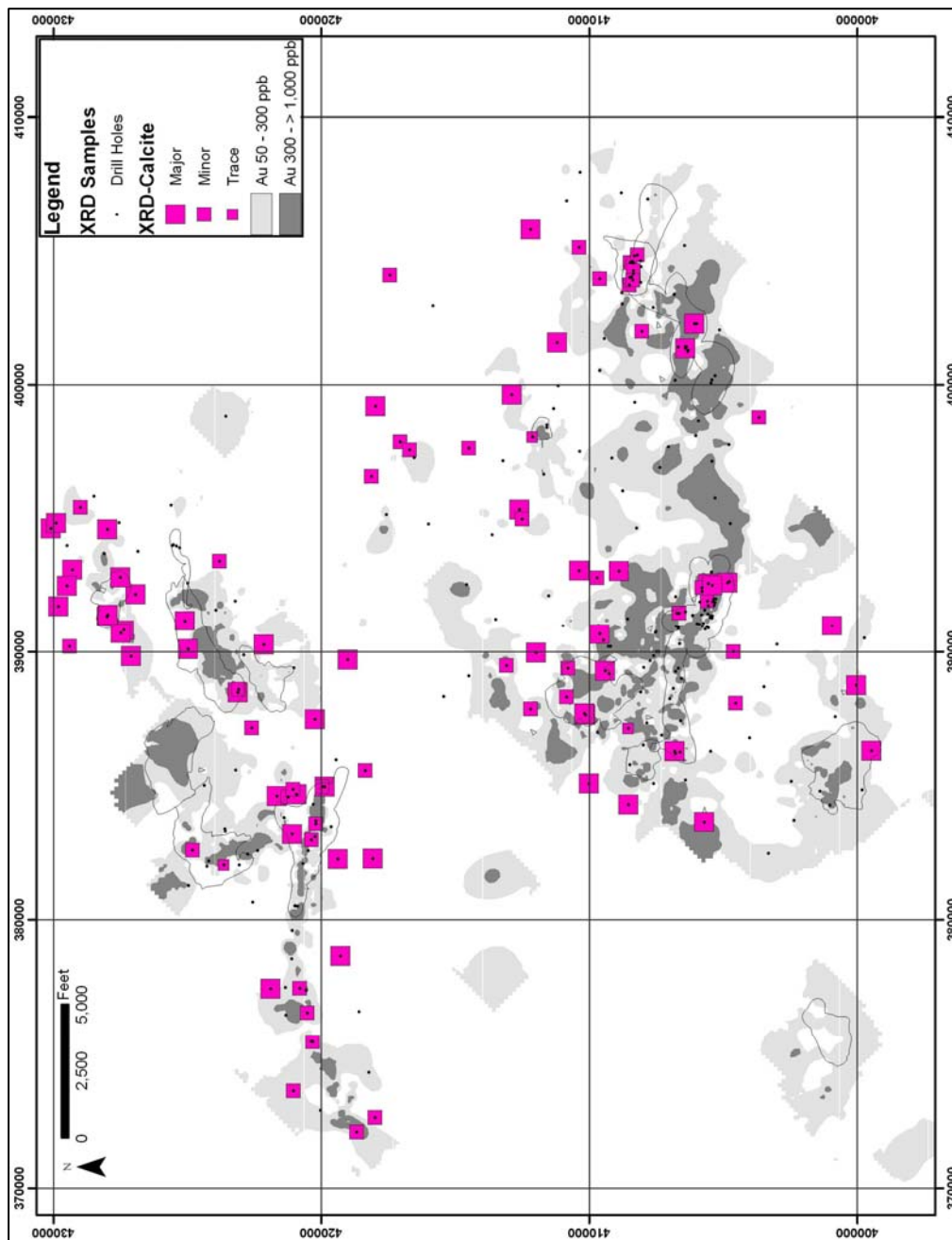
Figure 41b
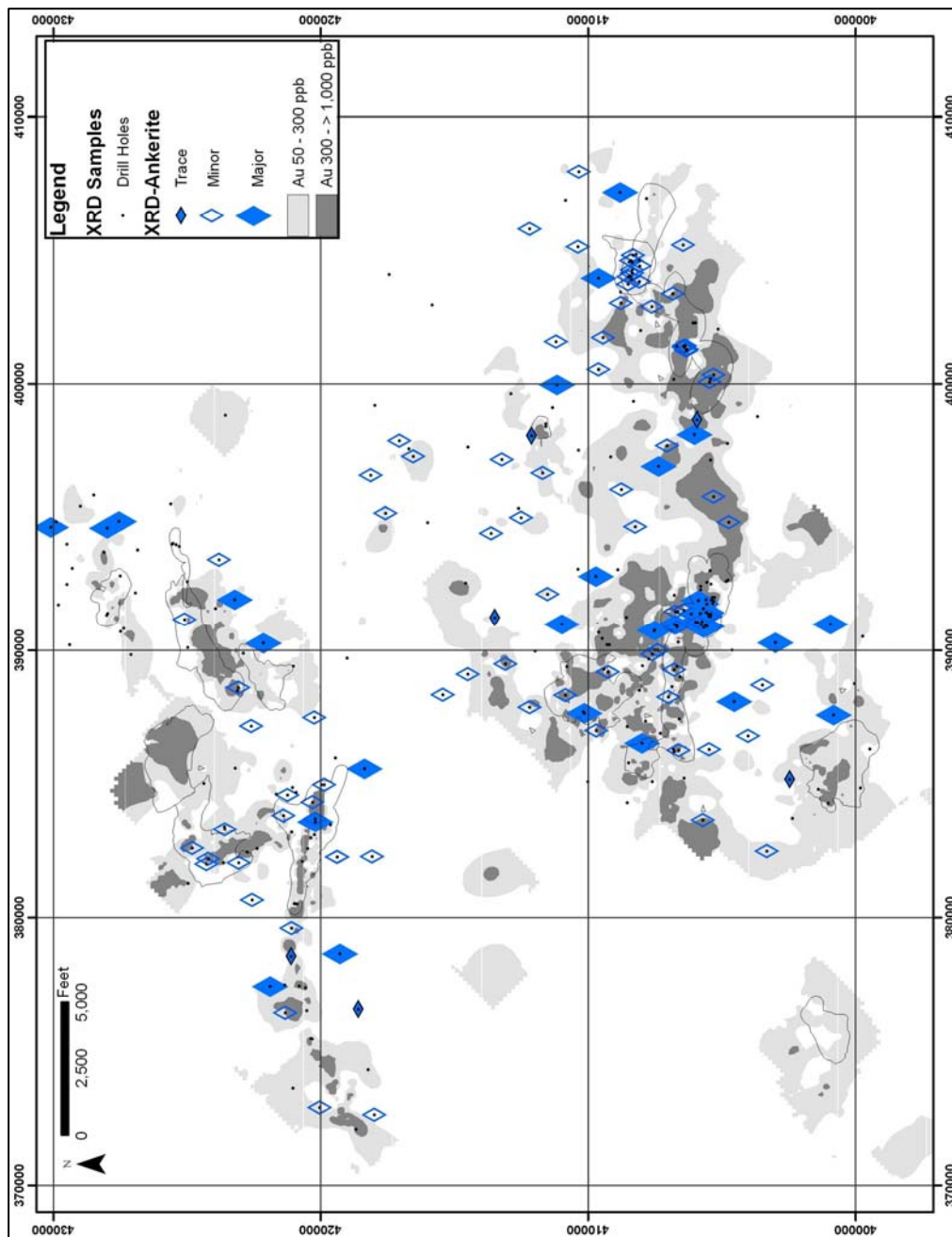
Figure 41c
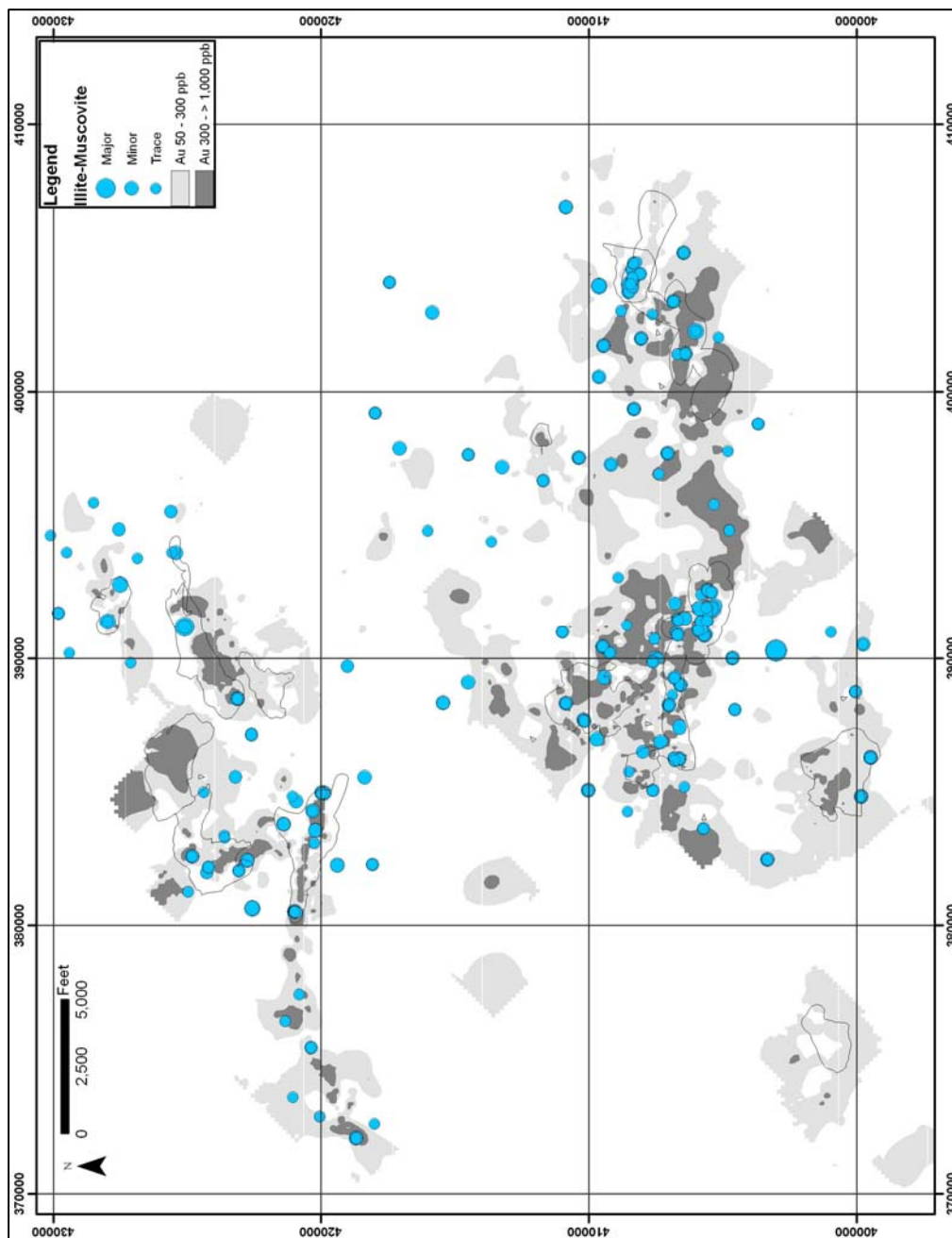
Figure 41d
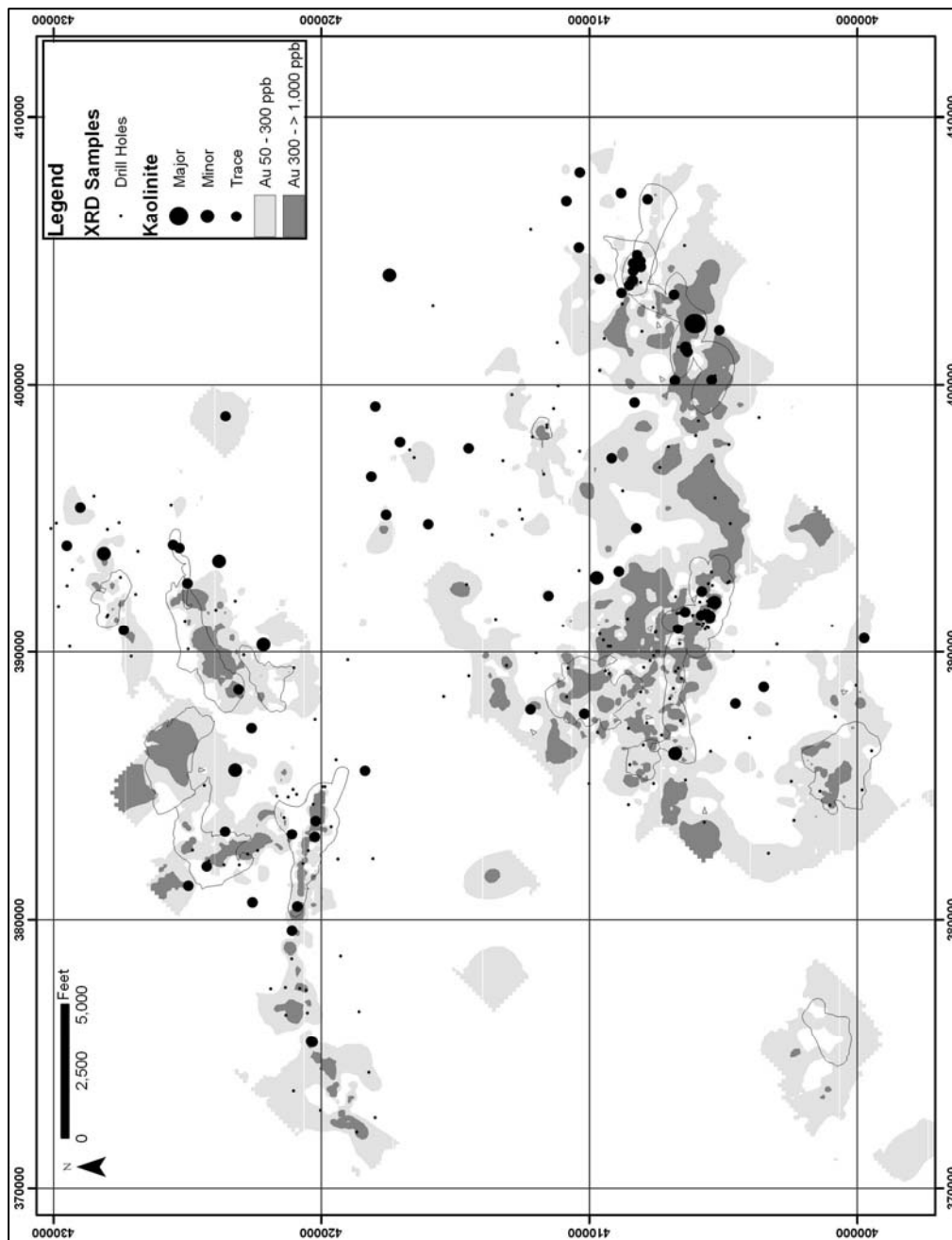
Figure 41e

Figure 41f

156
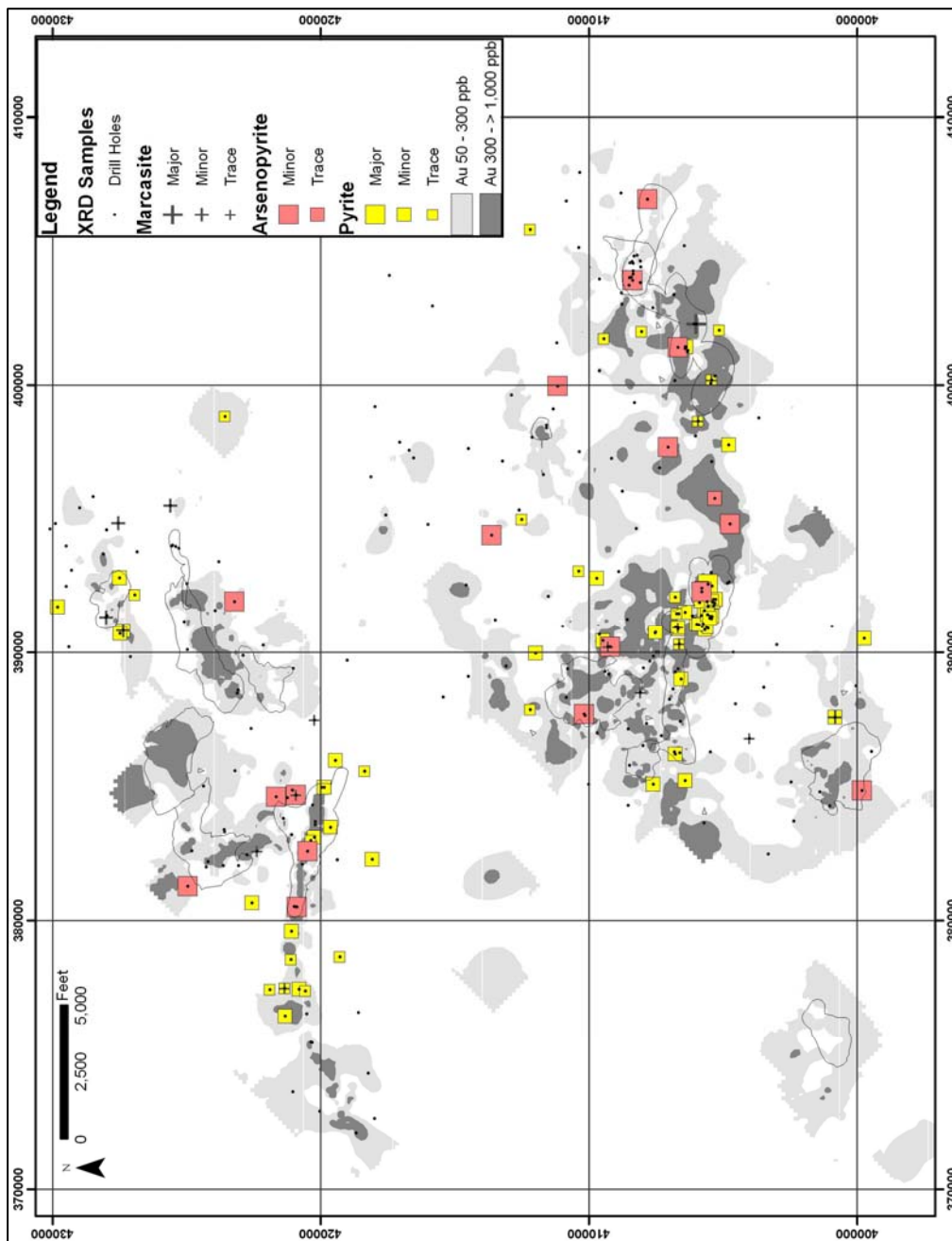
Bar and Whisker Plots
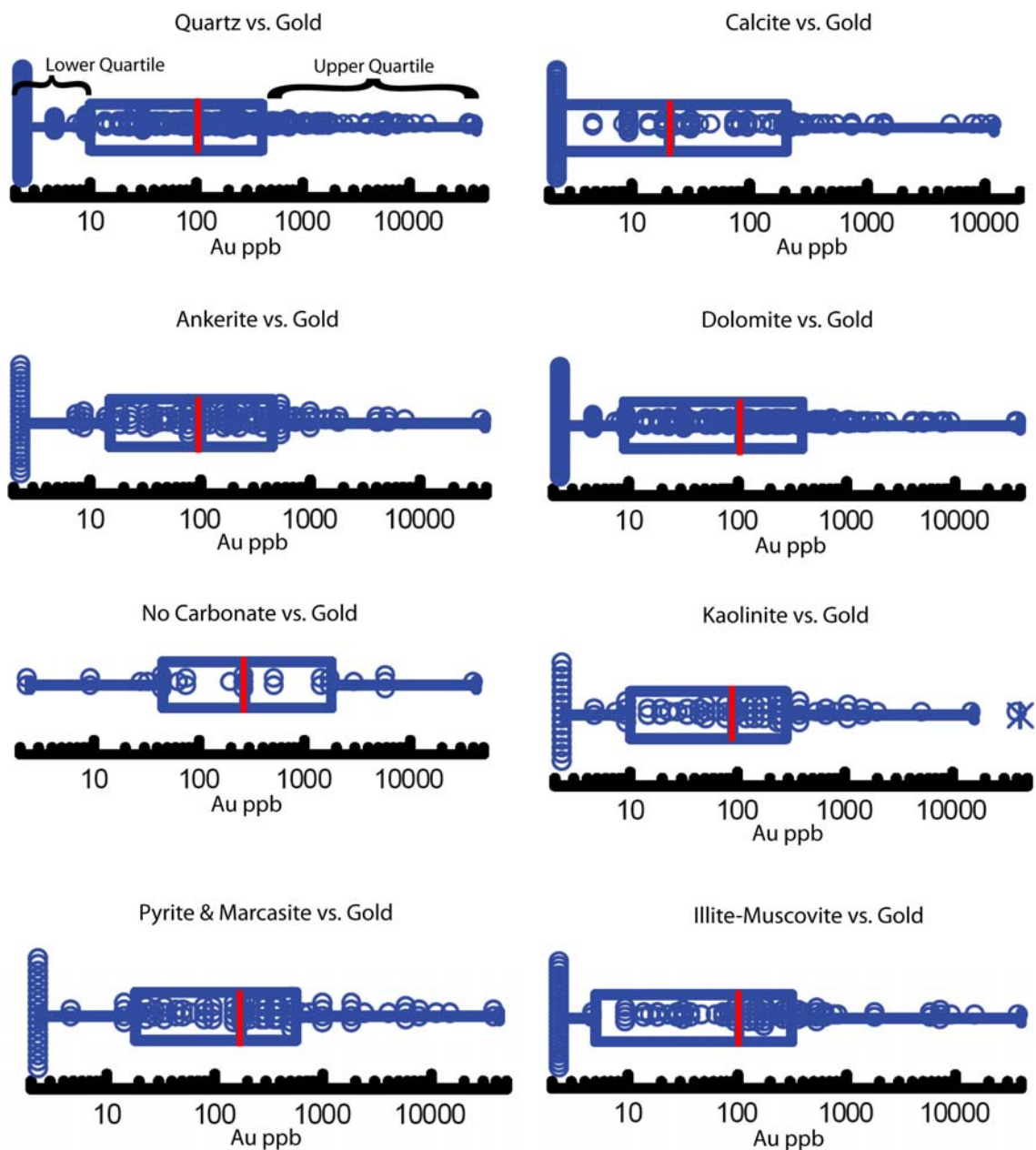
Figure 41g: The red lines indicate the median gold values for the samples used in each plot. The Quartz vs. gold (top left) bar and whisker plot shows where the upper and lower quartiles of the data can be located on all of the plots, and the blue box in-between the upper and lower quartiles represents the remaining 50% of the data used.
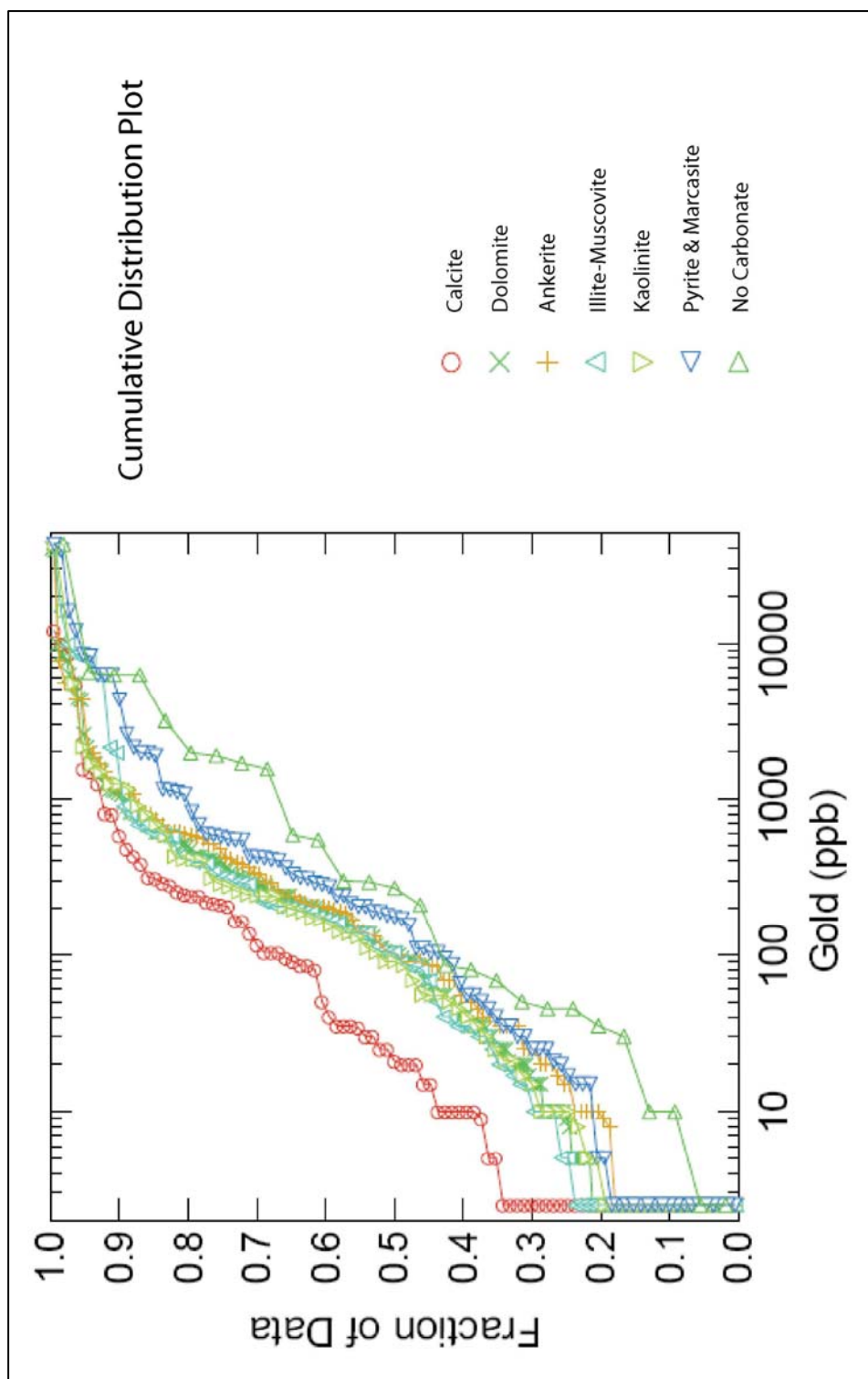
Figure 41h

Isotopic Analyses of Carbonates

Oxygen and carbon isotope data were collected to see whether patterns of $\delta^{13}C$ and $\delta^{18}O$ values occur around areas of known mineralization. Since depleted $\delta^{18}O$ values have been documented in other Carlin-type deposits (Stenger *et al*., 1998, Arehart and Donelick, 2005; Arehart *et al*., 2006), the primary objective was to analyze whether or not depleted $\delta^{18}O$ values form a larger halo to the vertical projection of known gold deposits in the Jerritt Canyon district. Areas of mineralization and visible hydrothermal alteration may be surrounded by visibly unaltered, unmineralized rocks that, nevertheless, underwent isotopic exchange with hydrothermal fluids. The more fluid that passes through a rock the lower the $\delta^{18}O$ values become. If the hydrothermal fluids had a significant amount of lateral fluid flow, then low $\delta^{18}O$ values should extend significantly outboard from the vertical projection of known gold deposits.

Rock carbonate was separated from 179 samples from the bottommost 5 feet of the DSrm, the same interval as the Anglo Gold geochemical database. Carbonate samples from drill core were separated by drilling 67 holes with a ¼ inch bit throughout the 5 foot interval to try to get a representative sample of the interval. Special care was taken to avoid visible veins. Carbonate samples from rotary holes that had representative chips of intervals stored in Phillips boxes were hand-picked, again avoiding veins, and were then crushed to a powder. Rotary holes that had representative chips of intervals on glued boards were not sampled, because of the improbability that all the glue could be removed from the samples. All samples were cooked for 1 hour at 225°C to drive off any organic material. From the baked samples four milligrams from each of the baked samples were weighed out for the analyses. The carbonate isotope analyses were done at

the Nevada Stable Isotope Laboratory. Samples were analyzed using the phosphoric acid reaction method of McCrea (1950). However, in contrast to the method of McCrea (1950), the reaction was performed at 90°C. Analyses were performed using a Micromass MultiPrep preparation device interfaced with a Micromass IsoPrime stable isotope ratio mass spectrometer in dual inlet mode. The $\delta^{13}C$ results are reported relative to PDB. The $\delta^{18}O$ results are reported relative to SMOW. An uncertainty of ± 0.1 ‰ is estimated for both $\delta^{13}C$ and $\delta^{18}O$; therefore, the data are expressed to one decimal place. Yukon Nevada Gold also supplied carbonate isotope data from the bottom five feet of the DSrm from 29 additional holes. Those analyses were also completed at the Nevada Stable Isotope Laboratory.

Of the 179 samples analyzed in this study, 150 samples yielded data. The remaining samples had insufficient carbonate. The samples were corrected for presence of dolomite, or were corrected so that all the sample data were reported in terms of calcite. Using a temperature of 225°C, a reasonable estimate for the temperature of ore formation (Hofstra, 1994), the difference between the fractionation factors for dolomite and calcite was calculated (Table 8). At this temperature there was a 3.08 ‰ difference between calcite and dolomite. Based on Mg/Ca molar ratio values, which were calculated from Anglo Gold's data set, the dolomite/calcite ratio was estimated for each sample, and corrections were made (Table 8).

Mineral	A	B	Temperature Range °C
Calcite	2.78	-2.89	0 to 500
Dolomite	3.2	-1.5	300 to 510

1000In α (mineral/water) = A(10^6 * T^-2) + B

Calcite Temperature °C	°K	1000In α (Calcite/Water)
225	498.15	8.31

Dolomite Temperature °C	°K	1000In α (Dolomite/Water)
225	498.15	11.40

Difference in 1000In α1/2 Calcite vs. Dolomite
3.08

Mg/Ca Ratio		
0.00 - 0.20	0.62	‰ Correction subtracted from δ18O values
0.21 - 0.40	1.23	‰ Correction subtracted from δ18O values
0.41 - 0.60	1.85	‰ Correction subtracted from δ18O values
0.61 - 0.80	2.47	‰ Correction subtracted from δ18O values
0.81 - 1.00	3.08	‰ Correction subtracted from δ18O values

Table 8: Table showing the correction made for dolomite. Corrections made for 225°C.

Of the 150 samples that yielded data, 2 samples came from the data set which was used to calculate elemental background before the Carlin-type event, and, thus, could represent background values prior to Carlin-type mineralization. The average $\delta^{13}C$ isotopic value calculated from the two samples was 0.5 ‰, and the average $\delta^{18}O$ value was 24.2 ‰. From the entire carbonate isotope data set the $\delta^{13}C$ values ranged from 4.5 ‰ to -6.9 ‰ with an average of -4.5 ‰. The $\delta^{18}O$ values ranged from 25.4 ‰ to 7.2 ‰ with an average of 20.1 ‰.

The isotope data were gridded in ArcMap using Target software. The type of grid generated was obtained using a linear gridding method because the data for both $\delta^{18}O$ and $\delta^{13}C$ were normally distributed. The grids were classified using changes in slope in

cumulative distribution curves of the data and breaks where values deviate from unaltered rock. A 1,000 foot cell size/search radius was used for the grids.

The δ^{13}C isotopic values do not show a pattern with respect to the vertical projection of known gold deposits or the 50 ppb and 300 ppb gold contours (Figs. 42a & 42b). Ordovician marine limestones have δ^{18}O values between 22 ‰ and 24 ‰ (Stenger, 1998; Hofstra and Cline, 2000). Rye *et al*. (1974) reported δ^{18}O values between 21.2‰ - 22.5‰ for unaltered DSrm near the Cortez deposit. Therefore, values less than 22 ‰ determined during the analysis will herein be considered depleted which is consistent with the values from background samples used for this study. Zones of depleted δ^{18}O values do show a pattern similar to the vertical projection of known gold deposits and the 50 ppb and 300 ppb gold contours (Figs. 42c & 42d). Low δ^{18}O values are most depleted (between 7 ‰ and 22 ‰) within the vertical projection of known gold deposits and within the 50 ppb gold contour (Figs. 42c & 42d). Depleted δ^{18}O values between 7 and 22 ‰ are most pervasive in the SSX-Smith area. Depleted δ^{18}O values extend out up to 2,000 feet from the 300 ppb gold contour and make a halo to the 50 ppb good halo; however, lack of data inhibits an accurate measurement of the extent of the halo (Figs. 42c & 42d). Zones of depleted δ^{18}O values in the Murray-Winters Creek area are present in a northeast trend extending from Alchem to Winters Creek and in a northwest trend extending from the Murray to West Generator (Fig. 42c). Depleted δ^{18}O values extend out 0 – 800 feet from the 300 ppb gold contour in the Murray-Winters Creek area. Depleted δ^{18}O values extend out to the northern portion of Wright Window (Fig 42c). Similar to logged alteration, depletions in δ^{18}O values are irregular and discontinuous in several localities. Several examples in can be observed in figure 42c, especially within

the SSX deposit, where samples with depleted $\delta^{18}O$ values are within 50 feet of samples with $\delta^{18}O$ values of typical Ordovician marine limestones.

Neither the $\delta^{18}O$ values nor gold values exhibit any relationship with $\delta^{13}C$ values (Figs. 43a & 43b). Also, $\delta^{18}O$ values do not show any clear relationship with gold (Fig. 43c). However, Figure 43d does show a crude pattern of decreasing $\delta^{18}O$ values with increasing factor 3 scores, suggesting a relationship between Carlin-type gold mineralization and depletion of $\delta^{18}O$ values. To review, factor 3 is the factor most closely associated with gold, thallium, mercury, arsenic and tellurium, as determined from factor analysis. On the other hand, $\delta^{18}O$ values do not show any pattern with factor 4, suggesting little relationship between depletion of $\delta^{18}O$ values and the migration of brines believed to be responsible for Zn, V, U, Ni, Cu, Ag, Cd, Se (the elements with high loadings for factor 4). Since there are no known Mesozoic intrusions at Jerritt Canyon, zones of $\delta^{18}O$ depletion, are mostly likely related to fluid flow associated with Carlin-type mineralization.

Depletions of $\delta^{18}O$ values have been documented in the North Generator Hill deposits by Hofstra (1994) and at the Murray deposit by Hutcherson (2002). Hofstra (1994) documented depletions in both $\delta^{13}C$ and $\delta^{18}O$ values where depletions were inversely related to the gold-related suite of elements and depletions in $\delta^{18}O$ values in dolomite correlate with increasing gold values. An attempt was made to see if depleted values in rocks with at least 50% magnesium correlated with elevated gold values, which they did not. Also, ferroan dolomite occurs in areas where $\delta^{18}O$ values are not depleted. Hutcherson (2002) indicated that both $\delta^{13}C$ and $\delta^{18}O$ can be used to identify fluid flow paths but their lack of correlation with gold makes them unreliable when exploring for

gold mineralization. It is important to note that Hofstra's (1994) and Hutcherson's (2002) data are not from one interval or one formation. Depletions of $\delta^{18}O$ values in and around areas of mineralization have also been documented at other Carlin-type deposits including Twin Creeks and Pipeline (Stenger *et al.*, 1998; Arehart and Donelick, 2005). At Twin Creeks, Stenger *et al.* (1998) made similar observations to this study, where $\delta^{18}O$ values were depleted in the Ordovician host rock rocks around the Twin Creeks deposit and $\delta^{13}C$ values did not show a distinct pattern. They reported a weak correlation between high gold values and depleted $\delta^{18}O$ values. Arehart and Donelick (2006) also made similar observations to this study at Pipeline, where $\delta^{18}O$ values were depleted several kilometers from the Pipeline deposit, albeit discontinuously. $\delta^{13}C$ values did not show a distinct depletion pattern around the deposit, and neither $\delta^{13}C$ nor $\delta^{18}O$ depletions clearly correlated with high gold values.

Figure 42:

a. $\delta^{13}C$ classified grid with the 50 ppb and 300 ppb gold contours and white deposit outlines. Legends are for calculated grid values, not actual values.

b. $\delta^{18}O$ classified grid with the 50 ppb and 300 ppb gold contours and white deposit outlines. Legends are for calculated grid values, not actual values.
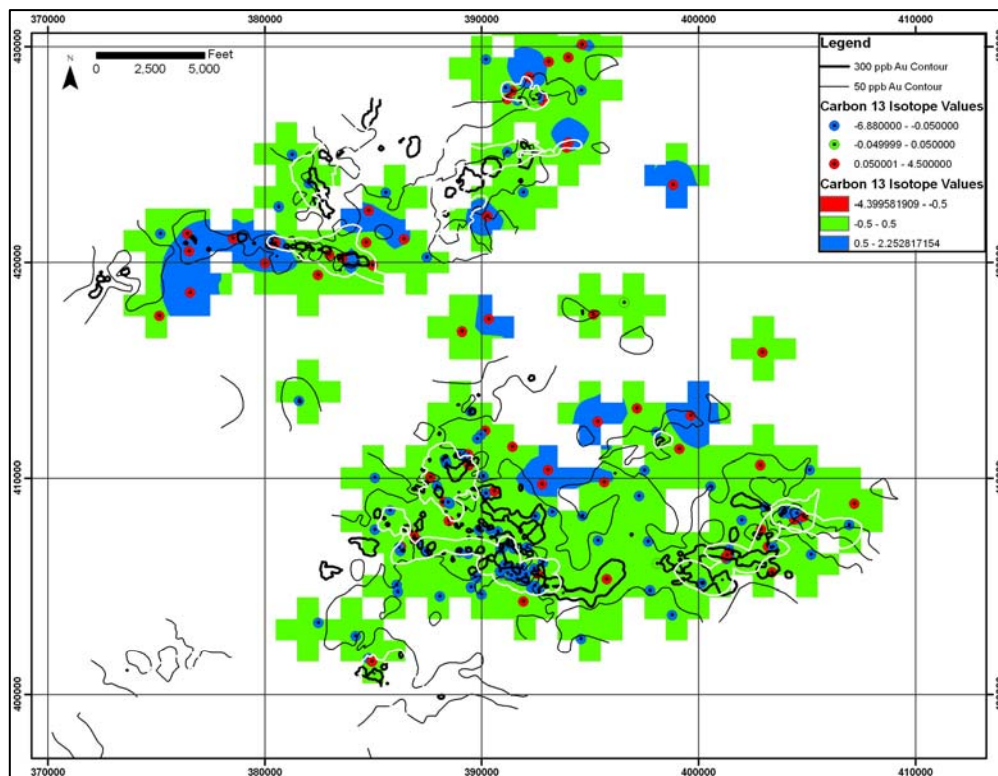
Figure 42a
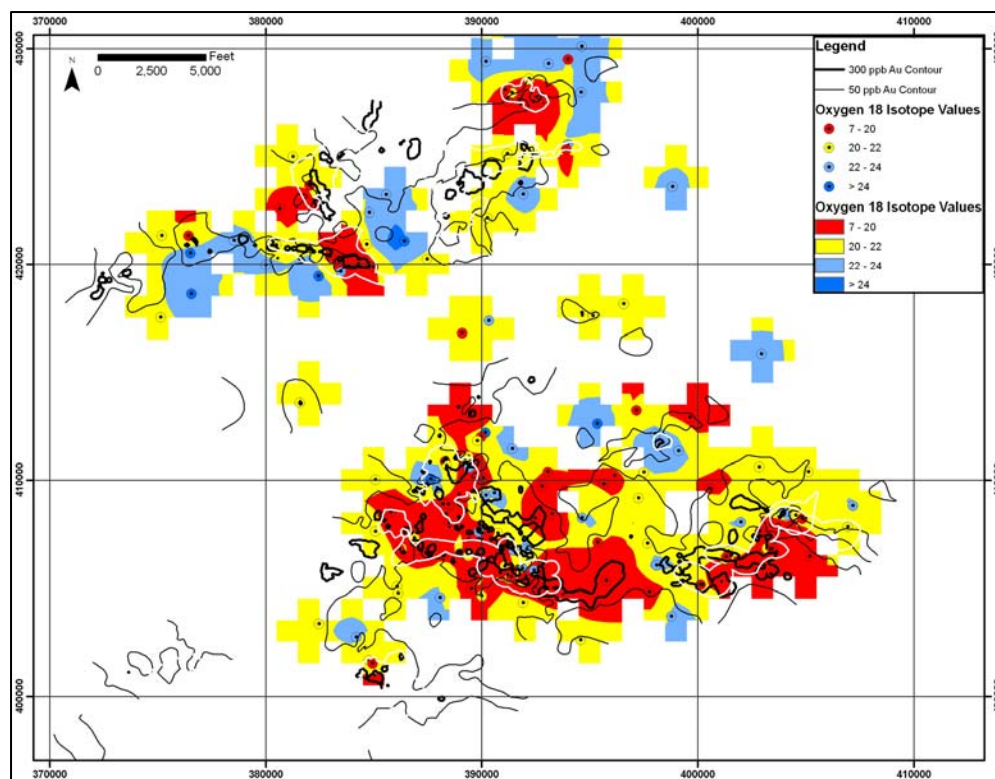
Figure 42b

Figure 43:

a. $\delta^{13}C$ versus $\delta^{18}O$ values.

b. $\delta^{13}C$ values versus gold values.

c. Gold values versus $\delta^{18}O$ values.

d. Factor 3 factor scores versus $\delta^{13}O$ values
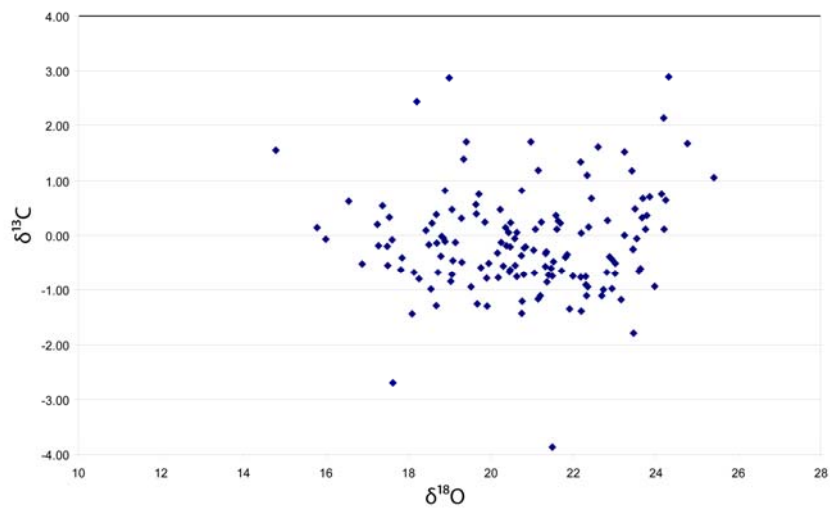
Figure 43a
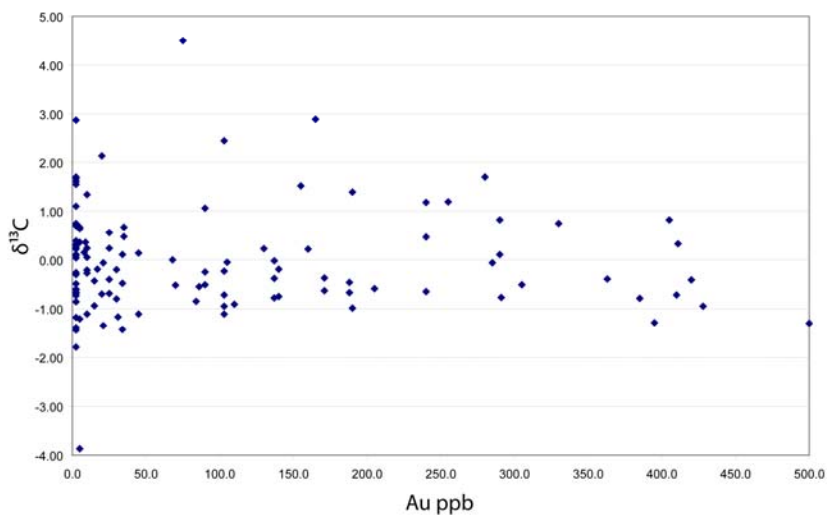
Figure 43b
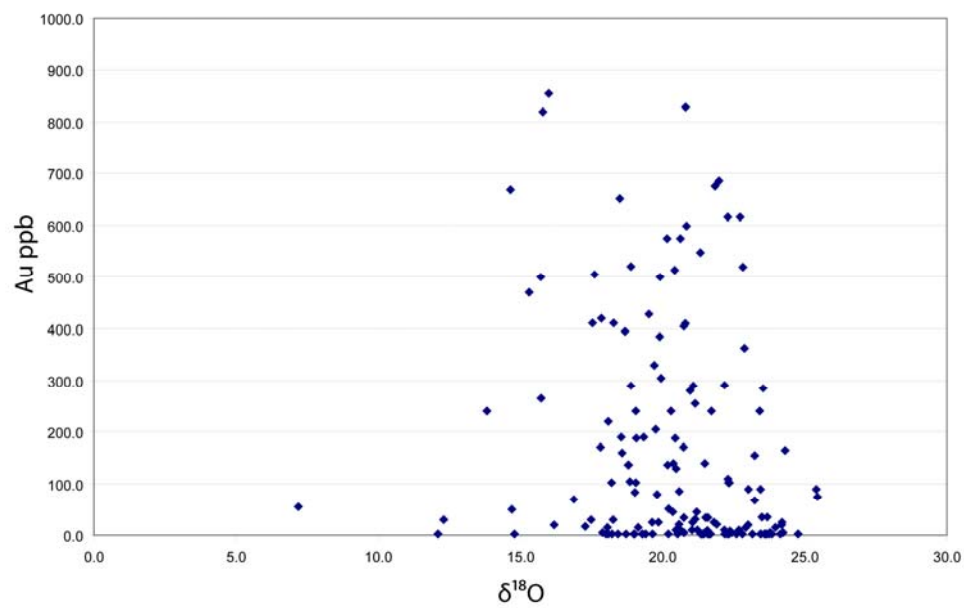
Figure 43c
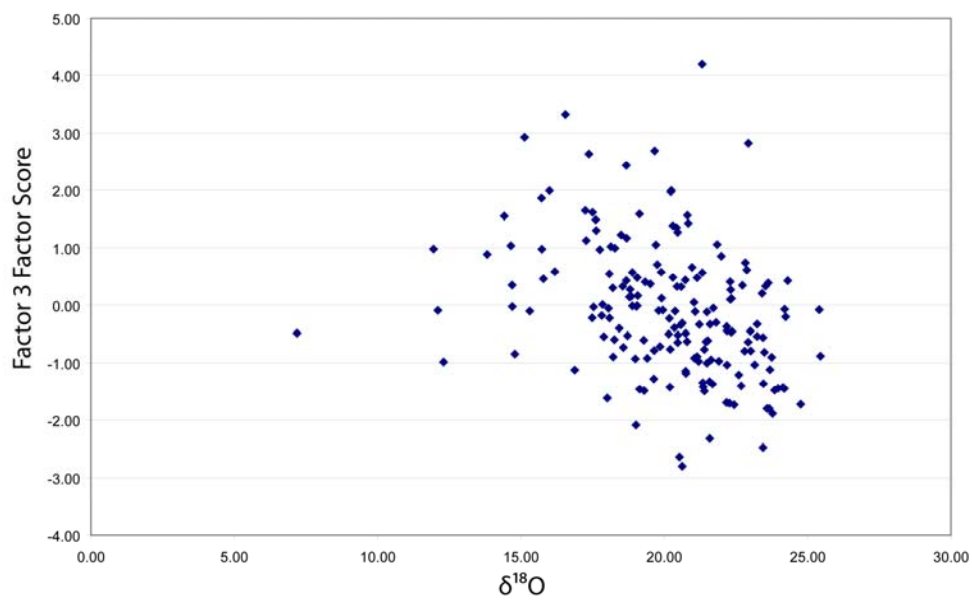
Figure 43d
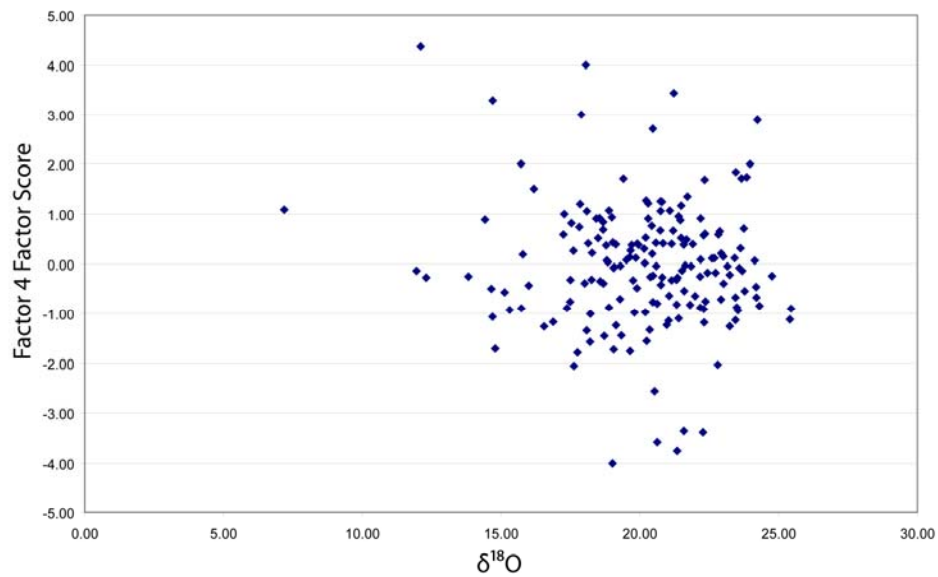
Figure 44: Factor 4 (BSE factor) factor scores versus $\delta^{18}O$ values.

Discussion

Extent of the Hydrothermal System associated with Carlin-type Gold mineralization

The objective of this study was to document and characterize the hydrothermal footprint of Carlin-type deposits at the district-scale by looking at trace elements, logged alteration and mineralization, XRD mineralogy, and carbonate isotopes. Maps of elemental distributions, correlation coefficients, correspondence analyses, and factor analyses all indicated a gold-thallium-arsenic-mercury-tellurium signature associated with ore formation. Maps showing the distribution of gold, thallium, mercury, arsenic, and, to a lesser extent, tellurium exhibit very similar patterns that are spatially associated with the vertical projection of known gold deposits at Jerritt Canyon. Anomalous gold (>50 ppb, Fig. 17), thallium (>0.5 ppm, Fig. 21a), mercury (>3 ppm, Fig. 21d), arsenic (>100 ppm, Fig. 21g), and tellurium (>0.05 ppm, Fig. 21j) generally extend from 1,000 to 8,000 feet from the vertical projections of the deposits (Table 3). Furthermore, anomalous thallium (<2 ppm, Fig. 21b), mercury (<10 ppm, 21e), arsenic (<200 ppm, Fig. 21h), and tellurium (<0.2 ppm, Fig. 21k) values extend out, up to 2,000 feet from gold values >300 ppb. Maps of decarbonatized and silicified rock, ferroan dolomite/ankerite, quartz-bearing veins, illite/muscovite, kaolinite, and depleted δ^{18}O values in rock carbonate (<22‰) also show a close spatial association with the vertical projection of the gold deposits. The patterns in alteration, however, are not nearly as continuous or do not form significant lateral halos like δ^{18}O values, gold, thallium, mercury, tellurium, and arsenic. An exception is ferroan dolomite, which is discussed below. The lack of large, continuous halos and zoning patterns in all of the data sets around the deposits at Jerritt Canyon stands in stark contrast to other deposit types such

as base metal lodes and porphyry copper deposits that show large, pervasive, zoned patterns in trace elements (Goodell and Peterson, 1974; Guilbert and Park, 1975; John, 1978). The observation at Jerritt Canyon that fresh-looking rocks with near background concentrations of ore-related elements can be in close proximity to visually altered rocks that are highly anomalous in trace elements suggests complex fluid flow, which was predominantly vertical rather than horizontal.

The spatial association between gold, arsenic, mercury, thallium, and tellurium is consistent with Carlin-type elemental associations documented in other studies on individual deposits in the Jerritt Canyon district. Hofstra (1994) utilized factor analysis and isocon diagrams on samples taken from the North Generator Hill pit to identify elemental associations or enrichments which were related to the Carlin-mineralization event. The factor analysis completed by Hofstra (1994) exhibited a statistical association between gold, arsenic, mercury, and thallium. Isocon diagrams where interpreted by Hofstra (1994) to show an introduction of gold, arsenic, mercury, and thallium during the Carlin-event. Dewitt (1999) utilized a correlation matrix to demonstrate a statistical correlation between gold, mercury, arsenic, and thallium in the SSX deposit. Tellurium was not analyzed for Hofstra's (1994) or Dewitt's (1999) studies. Hutcherson (2002) used samples from the Murray mine to generate correlation matrices, isocon diagrams, and transects through the mineralized New Deep fault in the Murray mine to identify elemental associations and enrichments related to the Carlin-gold event. Hutcherson (2002) demonstrated a statistical correlation between and an enrichment of gold, arsenic, mercury, thallium, and tellurium during the Carlin-mineralization event, and a general decrease of the Carlin-elemental values away from the New Deep fault.

This study shows that the halo of the Carlin-mineralization system can be observed at the district scale, which can be utilized to target larger deposits at depth. Based on the 50 ppb halo in Figure 17, the size of the Carlin-mineralizing system through the SSX-Smith area is 22,000 feet long and 5,000 feet wide. In the Murray-Winters Creek area the system is 9,000 feet long and 1,500 feet wide in the Murray mine, 4,500 feet long and 1,000 feet wide in the West Generator mine, and 5,500 feet long and 1,500 feet wide in the Marlboro Canyon area. Though the other Carlin-type elements can be utilized to define the extent of the Carlin-system, anomalous gold is most representative of the Carlin-mineralizing system as most elevated values of arsenic, mercury, thallium, and tellurium fall within the 50 ppb gold halo. The size of the Carlin-mineralization system is also depicted by the CTE factor from the factor analysis (factor 3 in Table 6), where most of the high factor scores are confined to the 50 ppb halo (Fig. 27). Published studies on other Carlin-type deposits to date have mostly been focused individual deposits. Therefore, a district scale comparison of size of other Carlin-type deposits with respect to the Jerritt Canyon district cannot be readily made. The lack of elemental zoning shown in this study is unlike other deposit types, such porphyry copper and epithermal systems. For example, at Bingham porphyry copper-gold-molybdenum deposit, John (1978) demonstrated a strong zoning of sulfide minerals with a central 2,500 foot wide zone of molybdenite surrounded by a 100-200 foot halo of copper mineralization, which is further surrounded by a 200-500 foot pyrite zone with a distal 5,500 foot zone of lead-zinc-silver. Such classic zoning is not present in the Jerritt Canyon district. Gridded ratio images for the Carlin-type elements indicate that the Carlin-type elements, with the exception of arsenic and to a lesser extent tellurium,

simply attenuate at almost the same rate away from areas of known mineralization (Figs. 21c, 21f, 21i, & 21l). The lack of elemental zoning at Jerritt is likely characteristic of all Carlin-type deposits. Other Carlin-types deposits, such as those in the Carlin trend (i.e. Getchell and Cortez) are located near Mesozoic intrusions, which complicates interpretation due to the difficulty of sorting out which trace elements are related to Mesozoic hydrothermal activity and which ones are related to Tertiary Carlin-type mineralization.

Similar to other Carlin-type deposits, decarbonatization/argillization and silicification are the alteration types most closely and temporally associated with the gold deposits at Jerritt Canyon. However, the zones of where decarbonatization/argillization and silicification have taken place along the base of the DSrm are not much larger than the vertical projection of the gold deposits (Figs. 40a, 40b, 40c, 40d, & 40f). More importantly, the alteration is irregular or spotty and is not pervasive. Furthermore, there appears to be no zoning patterns between decarbonatized/argillized and silicified rocks with respect to the deposits. In addition, paragenetically late minerals in the Carlin-type deposits at Jerritt Canyon, such as stibnite, orpiment, and realgar are sparse along the base of the DSrm, suggesting they do not form any significant halo to mineralization, even within the vertical projection of the deposits. Illite-muscovite and kaolinite also exhibit a lack of pervasive alteration. The lack of pervasive alteration and alteration zoning at Jerritt Canyon stands, again, in marked contrast to porphyry and epithermal deposits. In porphyry deposits alteration may extend out in a continuous bulls-eye pattern greater than 4,000ft from the mineralized area forming a distinct zoning outward pattern of potassic to phyllic to argillic to propylitic alteration (Guilbert and Park, 1975).

Though variable in size due to permeability factors, Hedenquist *et al* (2000) generalize zoning patterns exhibited by high-sulfidation epithermal deposits. In general high-sulfidation epithermal systems exhibit an alteration zone that is at least 200m wide in which the central mineralized zone is surrounded by a 50m quartz alunite zone that is further surrounded by a 100m wide clay alteration zone. On the other hand, ferroan dolomite does form a significant halo to gold mineralization at Jerritt Canyon and is consistently found within the 50 ppb gold contour along the Saval discontinuity. However, as will be discussed below, ferroan dolomite is not considered to be temporally associated with Carlin-type gold mineralization at Jerritt Canyon, but presents, instead, a pre-ore alteration event that prepared the rocks for subsequent mineralization.

Similar to the alteration products, $\delta^{18}O$ values show a strong spatial relationship to the vertical projection of the deposits and the 50 ppb gold halo along the Saval, but, when examined in detail, the patterns break down as unaltered rocks with undepleted $\delta^{18}O$ values are commonly found in close proximity to altered and isotopically depleted rocks (Figs. 42c & 42d). However, the grid of $\delta^{18}O$ values, suggests depleted $\delta^{18}O$ values form a larger, more continuous halo to the gold deposits than does the distribution of the alteration products. There is little correlation between gold values and $\delta^{18}O$ values in individual samples (Fig. 43c), but low $\delta^{18}O$ values do correspond, albeit crudely, with elevated factor 3 scores, which represents the elements that best represent Carlin-type mineralization (Fig. 43d). Increasing factor 3 scores correlate with decreasing $\delta^{18}O$ values, which is consistent with increased water:rock ratios associated with deposition of the CTEs.

Although locally spotty, the distribution of CTEs form more continuous and larger halos around the gold deposits than those observed for alteration products. Why is this the case? First of all the geochemical data are available for all 6,416 data points, whereas between 150 and 300 drill holes were examined during this study. Therefore, the sample spacing for the logging completed during this study and the isotope and XRD analyses are much wider spaced than that for the trace elements (e.g., compare Figs. 16 and 32). Therefore, one would expect a more spotty distribution of alteration or depleted $\delta^{18}O$ values, simply because of the lower sample density. Secondly, the data set was collected from samples along the Saval that are mostly above, but locally below, known orebodies (e.g., see Fig. 20 and Table 6). Finally, and probably most importantly, the explanation for the spotty nature of the CTEs, alteration, and depleted $\delta^{18}O$ values could be the nature of fluid flow in the Jerritt canyon district. Visually unaltered samples within 50 feet of samples that are strongly altered suggest fluid flow was not pervasive and that water:rock ratios were highly variable. The data and the patterns presented during this study suggest fluid flow during Carlin-type gold mineralization was focused along high-angle faults and fractures, and water:rock ratios sharply decreased away from such fractures. The data presented here do not support extensive lateral fluid flow along low-angles features such as gently dipping stratigraphic units or low-angle faults. The lack of continuity in CTEs, alteration, and depleted $\delta^{18}O$ argues against the Saval discontinuity acting as a major aquifer during Carlin-type gold mineralization. The lack of continuity argues instead for multiple zones of upwelling fluids instead. This differs from porphyry and epithermal deposits because elevated pressures from forceful

ascending hydrothermal fluids induces hydrofracturing enhancing permeability around and above the intrusion enabling large volumes of rock to be altered.

Figure 45 and 46 schematically depict patterns one would expect in systems dominated by lateral fluid flow along favorable stratigraphy versus fluid flow focused in high-angle faults and fractures. Rather than fluid upwelling along just a few major structures and moving thousands of feet laterally along potentially favorable low-angle features, like the Saval discontinuity, I envision multiple zones of passive upwelling fluids that moved up major high-angle faults, but were then distributed into complex secondary fracture systems and locally bled out hundreds of feet laterally into favorable stratigraphy or other favorable, low-angle features. Such a complex fracture flow network would result in highly variably water:rock ratios and the spotty nature of CTEs alteration and isotopic values.
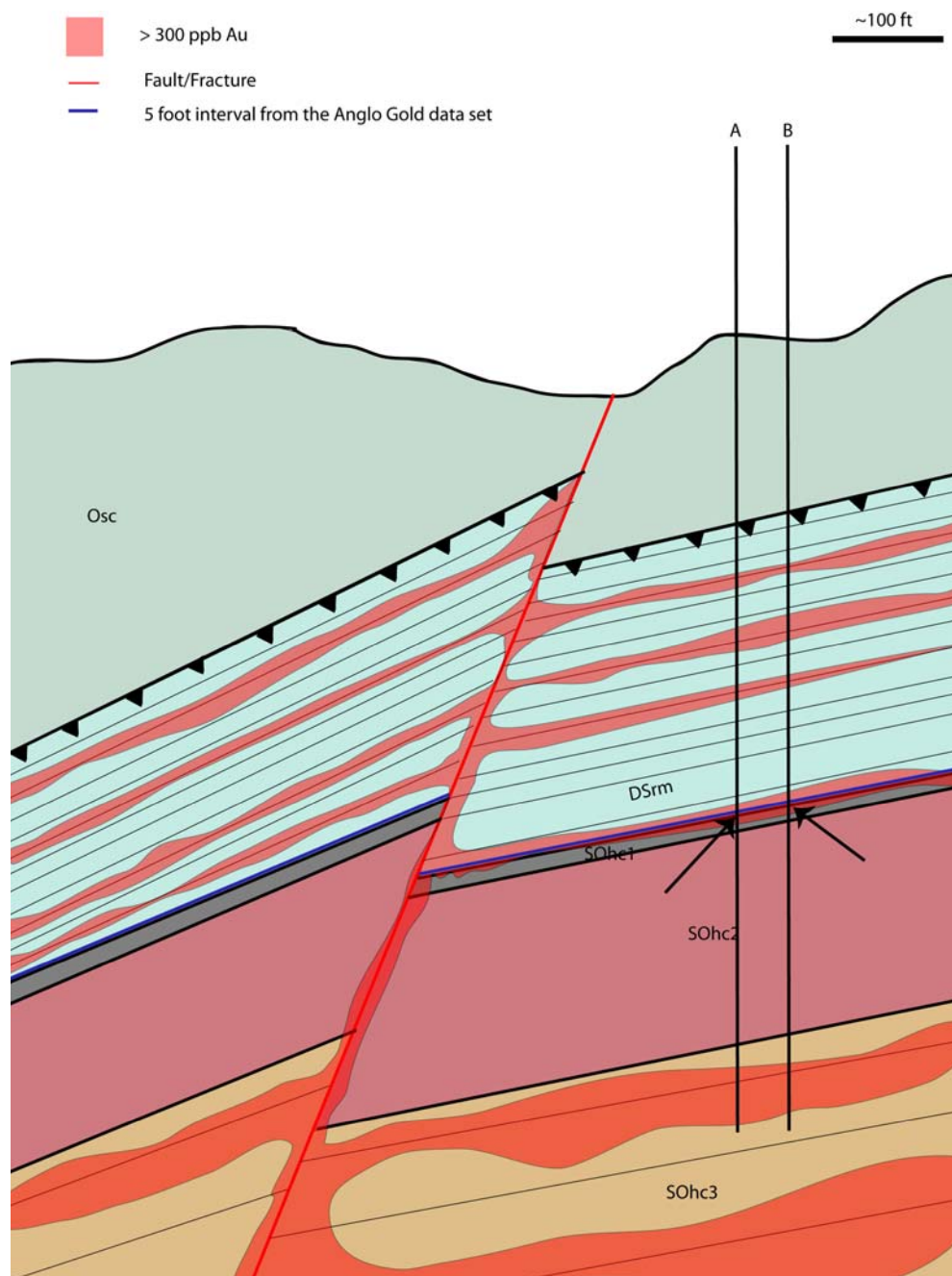
Figure 45: A schematic example of what the mineralizing system would look like if the Carlin-ore fluids exhibited a significant amount of lateral fluid flow. If holes A and B were drilled 50 feet from one another at a given stratigraphic interval, such as the Saval (indicated by the black arrows) mineralization would be intersected by both holes. If the red areas indicate altered rock both holes would have intersected alteration at the base of the DSrm.
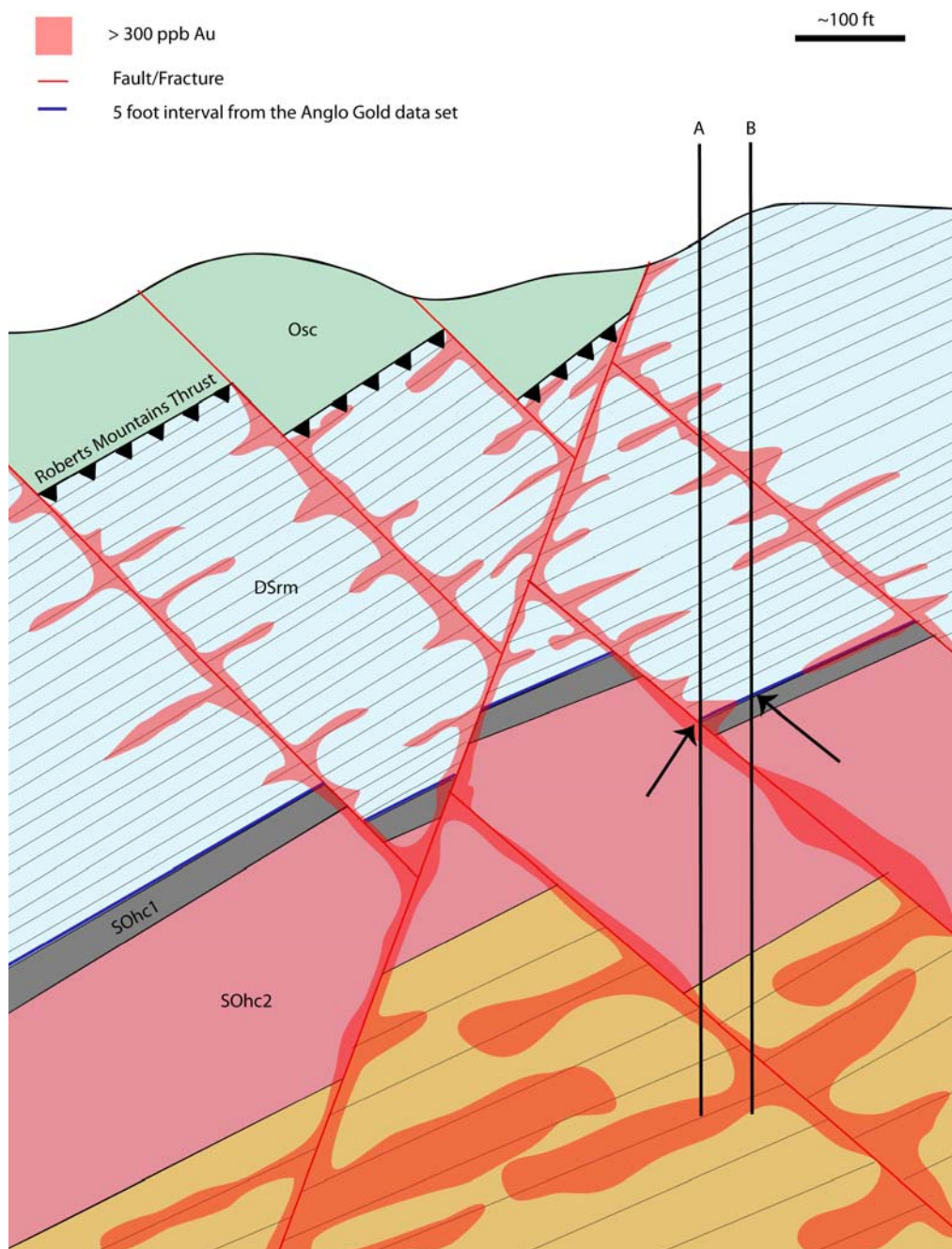
Figure 46: A schematic example of what the mineralizing system would look like if the Carlin-ore fluids were fracture controlled. If holes A and B were drilled 50 feet from one another at a given stratigraphic interval, such as the Saval (indicated by the black arrows) mineralization would be intersected by hole A but not hole B. A similar conclusion would be drawn if the red areas represented hydrothermal alteration. Note minor lateral fluid flow along bedding planes within the stratigraphic units.

The more widespread and more continuous halos of CTEs, silicified, decarbonatized/argillized, and depleted $\delta^{18}O$ values around the gold deposits in the SSX-Smith area strongly suggest this area was the major zone of upwelling fluids in the Jerritt Canyon district during Carlin-type mineralization. In addition, the South Boundary fault in the SSX-Smith area seems to have acted as a true barrier to fluid flow, as many of the CTE patterns are abruptly truncated against it, and there is no evidence for significant post-ore movement on the fault. The SSX-Smith area also seems to be considerably more structurally complex than the Murray-Winters Creek area with numerous faults and fractures allowing for multiple paths of fluid penetration, resultant alteration, and distribution of trace elements. Mineralization in the Murray-Winters Creek area is much more restricted. The best example of restricted mineralization and alteration can be observed in the Murray mine along the New Deep fault extending out to the northern portion of Wright Window, where the CTEs and depleted $\delta^{18}O$ values are generally less than14,000 feet long and 800 feet wide.

In addition, the largest zone of high tellurium values occur around the Steer, Saval, and SSX deposits in the SSX-Smith area. Tellurium is commonly associated with epithermal deposits related to alkalic magmatism (cf. Jensen and Barton, 2000). Its common association in both high-sulfidation epithermal deposits and Carlin-type deposits has been pointed out by Kesler *et al*. (2003). Tellurium is a moderately volatile element whose volatility is similar to rhenium, antimony, thallium, and lead (MacKenzie and Canil, 2008). Williams-Jones and Heinrich (2005) discuss the mechanisms by which volatile elements partition into magmatic-hydrothermal vapors that rise away from the source magma. The vapor can evolve as its ascends through the rock pile expanding with

increasing permeability. The elements found in ore-stage arsenian pyrite and/or marcasite rims are arsenic, gold, mercury, thallium, tellurium, copper and antimony (cf. Cline *et al*., 2005). Williams-Jones and Heinrich (2005) indicate that copper, arsenic, antimony, and gold consistently partition in favor of the vapor phase where zinc, thallium, and lead have no systematic preference. Heinrich (2005) proposed that vapor transport of gold and associated trace elements from a deeper magmatic source could be a viable model to explain Carlin-type deposits. Since tellurium has a similar volatility to thallium, magmatic vapor as a source for the tellurium and other CTEs is a viable hypothesis. If magmatic vapor from an underlying magmatic source is responsible for mineralization at Jerritt Canyon, the main intrusion is likely beneath the Steer, Saval and SSX deposits.

Ferroan Dolomite/Dolomite

As stated above, ferroan dolomite forms the best halo to gold values greater than 300 ppb along the Saval. Ferroan dolomite is consistently found in almost every sample that has gold values greater than 50 ppb (Fig. 40l). Ferroan dolomite forms a spotty halo, upwards of 500 feet, to gold values less than 50 ppb upwards of 500 feet (Fig. 40l). The formation of ferroan dolomite could have been a result of carbonation of iron-bearing minerals during Carlin-type gold mineralization or could be the result of pre-ore iron metasomatism due to hydrothermal alteration or diagenesis (Hofstra and Cline, 2000). Pre-ore iron metasomatism could have been a critical rock preparation event, enabling sulfidation to effectively take place and deposit gold in pyrite during the Carlin-type mineralization. Sulfidation is the process by which aqueous sulfide in the hydrothermal fluid reacts with iron in the rock to form pyrite or marcasite, which destabilizes aqueous

gold bisulfide complexes and precipitates gold in trace element-rich pyrite or marcasite (Hofstra and Cline, 2000). The spatial association between ferroan dolomite and gold mineralization has also been documented in other Carlin-type deposits such as Storm, Miekle, Twin Creeks, and Deep Star, though the timing of ferroan dolomite formation has been debated. In the Roberts Mountains Formation at the Deep Star deposit, a quartz + dolomite mineral assemblage is present in the orebody that is overprinted or replaced by a suite of minerals, typical of Carlin-type mineralization, which included quartz + kaolinite + sooty sulfide (Clode *et al*., 2002; Heitt *et al*., 2003). The quartz + dolomite assemblage was interpreted by Clode *et al*. (2002) to be part of the hydrothermal event associated with Carlin-type mineralization, but did not offer evidence for why. Heitt *et al*. (2003) further addressed the paragenesis at Deep Star and noted that the chalcedonic quartz from the quartz + kaolinite + sooty sulfide assemblage from the Carlin-ore event is intergrown with carbonate minerals from the quartz + dolomite event representing a continuum between the two assemblages. At the Storm deposit Dobak *et al*. (2002) noted two events of ferroan dolomite breccias that are found only in close proximity and serve as host rocks to ore stage silica-sulfide breccias. The breccias are found both capping the upper contact of and within the Bootstrap limestone. The ferroan dolomite breccias at Storm are interpreted to be younger than Jurassic intrusions, based on the presence of fragments of 162 Ma lamprophyre dike in the older breccia and fragments of a mineralized 37.57 Ma basalt dike in the younger breccia (Doback *et al*., 2002). Mineralized ore-stage breccias at Meikle are commonly found within the ferroan dolomites along with high grade gold mineralization (Evans, 2000; Emsbo *et al*., 2003). High grade gold values drastically decrease outboard of ferroan dolomite zones at

Meikle, indicating the ferroan dolomite was a critical rock preparation event which determined where the gold would precipitate. Evans (2000) reported that ferroan dolomite at Meikle formed during a Paleozoic Mississippi Valley Type (MVT) base metal mineralization, which followed a Paleozoic karsting event. However, Emsbo *et al*. (1999) interpreted ferroan dolomite and base metal mineralization at Meikle and other deposits in the northern Carlin Trend to be the result of syngenetic sedimentary exhalative (SEDEX) processes during the Devonian. Finally, at Twin Creeks Stenger *et al*. (1998) and Fortuna *et al*. (2003) both documented the spatial relationship between ferroan dolomite and gold mineralization. Fortuna *et al*. (2003) interpreted the ferroan dolomite to have formed from a pre-Tertiary hydrothermal event which mobilized iron from the interbedded basalt flows into the surrounding sedimentary rocks, resulting in the formation of ferroan dolomites which later served as a source for iron for sulfidation to take place during Tertiary Carlin-type gold mineralization event.

There is no clear-cut evidence at Jerritt Canyon that constrains formation of ferroan dolomite prior to or during Tertiary Carlin-type gold mineralization. The ferroan dolomite veins observed during this study are partially decarbonatized (leached, etched), indicating that they formed prior to and were altered during Carlin-type hydrothermal activity. Ferroan dolomite veins cut the 320 Ma dikes, which excludes the possibility of a SEDEX origin. The SSX-Smith area contains the most widespread, pervasive zone of ferroan dolomite. Numerous Pennsylvanian basalt dikes also transect the SSX-Smith area. Ferroan dolomite is more localized in the Murray-Winters Creek area, which corresponds with much fewer dikes in that area. Fluid inclusions from Carlin-type systems contain an appreciable amount of CO_2 (up to 4 mole %) and chemical modeling

predicts that iron-bearing carbonate minerals should form outboard of the sulfidation halo by carbonation of iron-bearing minerals (Hofstra *et al*., 1991). Therefore, CO_2 metasomatism of iron-bearing minerals in the numerous basalt dikes in the SSX-Smith area during Carlin-type mineralization might account for the distribution of the ferroan dolomite. However, replacement of iron bearing minerals by ferroan dolomite was not observed during this study. Also, there are no significant iron-bearing minerals in the sedimentary rocks of the SOhc and DSrm formations, which hosts much of the ferroan dolomite. Event 1 silicification as defined by Hofstra (1994) resulted in a mineral assemblage consisting of sphalerite, milky quartz, baroque dolomite, anhydrite, barite, pyrite, and graphitic carbon. Hofstra (1994) documented an intimate association between baroque dolomite, milky quartz veins, sphalerite, and hydrocarbons. Baroque dolomite can have a significant amount of iron present (up to 15 mole % $FeCO_3$, Tucker *et al*., 1996). Due to the fact that the baroque dolomite can have appreciable amounts of iron, its intimate association with event 1 sphalerite, alteration of ferroan dolomite veins, and lack of evidence indicating replacement of iron-bearing minerals in the dikes, SOhc and DSrm, ferroan dolomite likely formed prior to the Carlin-type mineralization, a pre-ore event similar to that postulated for Miekle and Twin Creeks.

It is not clear whether the formation of ferroan dolomite and non-ferroan dolomite were the result of one event or two separate events. No cross-cutting relationships between the two were observed. The distribution of non-ferroan dolomite-bearing rocks, as documented in this study, is much more pervasive than rocks containing ferroan dolomite veins (e.g., compare figures 40f and 40l). It appears that non-ferroan dolomitic rock surrounds rocks which have ferroan dolomite veins. The formation of ferroan

dolomite/baroque dolomite is interpreted here to have formed after emplacement of the early Pennsylvanian dikes as ferroan dolomite was observed cutting a Pennsylvanian dike. Sphalerite and baroque dolomite (possibly ferroan) were considered by Hofstra (1994) to be part of his event 1 silicification because they are intimately associated with quartz, anhydrite, barite, pyrite, and graphitic carbon (former liquid hydrocarbon). The graphitic carbon occurs as fractured particles cemented with event 1 quartz (Hofstra, 1994). Sphalerite and pyrite are intergrown with event 1 quartz and jasperiod along with the baroque dolomite (Hofstra, 1994). Based on fluid inclusions in quartz, Hofstra (1994) determined salinities of the event 1 fluids, which could be related to formation of baroque dolomite, to be up to about 15 wt% equivalent NaCl. If sufficiently oxidized, such saline fluids would be capable of transporting iron and reacting with surrounding carbonates to form ferroan dolomite.

The timing of formation is non-ferroan dolomite in the Roberts Mountain Formation at Jerritt Canyon and elsewhere in northern Nevada is not clear. Mullens (1981) in his regional study of the Roberts Mountains Formation, interpreted the dolomite in the Roberts Mountains Formation to be primary in origin; whereas, Armstrong et *al.* (1997), Evans (2000), and Cook and Corboy (2004) interpreted the formation of non-ferroan dolomite in the Northern Carlin trend to be the result of early diagenesis. In addition to early diagenesis, Evans (2000) documented formation of later non-ferroan dolomite during a subsequent Paleozoic base metal event, which resulted from migrating basinal brines, which also formed ferroan dolomite at the Miekle Carlin-type gold deposit in the northern Carlin trend. He documented a temporal progression from ferroan dolomite to non-ferroan dolomite as dolomite crystals filled open space in

the rocks. Observations made during this study appear to be analogous with the sequence of events documented during Evan's (2000) detailed study at Miekle. Similar to Evan's (2000) conclusions at Meikle it is herein believed that early diagenetic processes probably resulted in the formation of non-ferroan dolomitic rocks in the DSrm. Later migrating basinal brines resulted in the formation of ferroan dolomite veins and minor non-ferroan dolomite as iron was progressively removed from the fluid.

<u>Development of the Black Shale Elemental Signature</u>

As described above, The BSEs (black shale elements) consist of a large group of elements which are not related to the Carlin-type mineralization in space or time as evidenced spatially by elemental maps and statistically by Spearman rank correlation, correspondence, and factor analyses as well as by petrographic work from the current and previous studies. The BSEs are redox-sensitive elements, which are commonly observed in black shales around the world. The BSEs are transported as chloride, oxide, anionic, and hydroxide species in oxidized fluids (Rose, 1980). Interaction with organic mater or mixing with a reduced sulfide fluid causes deposition (Rose, 1980; Krauskopf, 1955). The factor analysis indicated two groups of black shale elements along the Saval. The first group consists of lanthanum, phosphorous, uranium, gallium, and vanadium. The second group consists of zinc, vanadium, uranium, selenium, nickel, molybdenum, copper, cadmium, and silver.

Studies at Jerritt Canyon and other Carlin-type deposits have also identified similar elemental associations. Hofstra (1994) indicated the presence of a black shale or phosphatic signature in the SOhc at the North Generator Hill pit. He identified an association between phosphorous, vanadium, cadmium, mercury, silver and chromium.

At SSX, Dewitt (1999) documented, using correlation coefficients, a black shale type signature from 164 holes that included cadmium, vanadium, and zinc all of which have a lesser degree of correlation with silver, molybdenum, nickel, and copper. Hutcherson's (2002) statistical analysis of geochemical data from the Murray deposit showed correlations between zinc, selenium, copper, and molybdenum from 84 hand and rock chip samples. Other Carlin-type systems have similar black shale-type signatures, though the origins of the signatures are not clear. At Deep Star within the Gen-Post fault corridor iron, magnesium, cobalt, nickel, phosphorous, copper, molybdenum, uranium, and vanadium correlate with one another; however, the timing of deposition with respect to gold is unclear (Heitt *et al*., 2003). Emsbo *et al*., (1999) used factor analysis and documented two groups of elements that were associated with gold at the Goldstrike property. The first group consists of a Carlin-type suite of elements consisting of arsenic, mercury, antimony, thallium, tellurium, and tungsten. The second group consists of a sedex suite of elements consisting of zinc, lead, silver, cadmium, barium, mercury, antimony, arsenic, and copper. Emsbo *et al*. (1999) concluded that the second group of elements constitutes mineral phases associated with documented SEDEX mineralization. At Gold Quarry Sha (1993) also used factor analysis to demonstrate a strong elemental association between organic carbon, molybdenum, vanadium, nickel, zinc, and silver, which was interpreted to be syn-sedimentary to early diagenetic in age.

Phosphorous, uranium, lanthanum, and gallium, which constitute the first group of BSEs identified in this study, was probably an initial syn-depositional elemental signature obtained by absorption of uranium, phosphorous, lanthanum, and gallium by organic matter (Krauskopf, 1955) and upwelling oceanic waters enriched in phosphorous

that formed apatite, which contains lanthanum and uranium (Boggs, 2006). The group one BSEs exhibit a spotty distribution in the SSX-Smith area and pervasive elevated values in the Murray-Winters Creek area (Figs. 23a, 23e, & 23f). The presence of the phosphate nodules and lenses in the DSrm along the Saval is consistent with the group one BSE signature.

Similar to the group one, group two BSEs have a spotty distribution in the SSX-Smith area and are more pervasively elevated in the Murray-Winters Creek area. The most pervasive highest values occur in and around the Winters Creek, Mill Creek, and Burns Basin deposits (Figs. 23a, 23b, 23c, 23d, 23g, 23h, 23i, 23j, 23k, & 23l).

Geologic and petrographic data presented in previous studies of Jerritt Canyon as well as the current study strongly suggest a pre-Tertiary origin for the group 2 BSEs and ferroan dolomite. Hofstra (1994) documented that the minerals associated with event 1 silicification were composed of graphitic carbon or fractured particles of former hydrocarbon cemented with quartz along with pyrite which was intergrown with event 1 milky quartz, event 1 jasperiod, and baroque dolomite, which Hofstra (1994) interpreted as possible MVT mineralization where zinc mineralization was accompanied or followed by hydrocarbons. This is similar to observations made by Kuehn and Rose (1995) who documented pre-ore pyrobitumen veinlets which were cut by pre-ore barite ± base metal veins. Chalcopyrite was documented to be intimately associated with sphalerite in the SSX deposit by Dewitt (2000). Intimate intergrowths of chalcopyrite and sphalerite replacing mafic mineral sites in a Pennsylvanian dike at SSX were interpreted by Dewitt (2000) to be pre-Tertiary in age. Hutcherson (2002) found pyrite intergrown with sphalerite and interpreted them as forming prior to or during the early stages of Carlin-

type mineralization. During this study, samples from Winters Creek have: 1) V-As-Zn-(Pb) sulfides in calcite veins containing pyrobitumen + quartz + apatite + pyrite + sphalerite; and 2) quartz veins containing sphalerite + pyrobitumen + pyrite (Fig. 30). At California Mountain carbon seams were documented in a calcite-dolomite host rock (Fig. 31).

The best interpretation for the presence of the group two elements is the migration of an oxidized basinal brine associated with hydrocarbon migration in the Jerritt Canyon district, which as mentioned above, likely was the cause for the formation of ferroan dolomite. With the data presented in this study and other studies from Jerritt Canyon, namely Hofstra (1994), it appears that the basinal brine was epigenetic and resulted in very minor base metal mineralization and hydrocarbon accumulation at Jerritt Canyon, somewhat similar to MVT deposits A similar conclusion was reported at Meikle by Evans (2000) for base metal mineralization at Meikle and by Kuehn and Rose (1995) for base metals and hydrocarbon-bearing veins at the Carlin deposit.

Oxidized saline basinal fluids scavenged the black shale elements and iron from the sedimentary pile and deposited them via reduction by organic carbon. Thermal sulfate reduction occurs when sulfate comes into contact with some organic matter preferentially hydrocarbons or sour gas (Machel, 2001). The sulfate commonly derived from pore fluids with dissolved sulfate is reduced by the hydrocarbons or sour gas to produce products such as sphalerite, galena, and lesser pyrite dolomite and or calcite (Machel, 2001; Sangster, 1996). Observations made by Hofstra (1994) and during this study show no evidence of a SEDEX system as mineralization. Rather than stratiform, the minor base metal mineralization at Jerritt Canyon was associated with a breccia body

with a mineral assemblage consistent with a MVT system. The presence of hydrocarbons also supports an MVT, in that organic carbon or sour gas may have caused reduction of the sulfate in the fluid and the formation of aqueous sulfide, resulting in the deposition of ferroan dolomite and group 2 BSEs, mainly as sulfides. Hofstra (1994) reported homogenization temperatures between 140° and 220°C and salinities ranging up to 15 wt% NaCl equivalent for fluid inclusions hosted by event 1 quartz, which could be related to the basinal brine. Liquid-rich inclusions coexist with methane-bearing gas-rich inclusions. He estimated the fluid inclusions were trapped at depths of 1.5 to 8 km. Some of these fluid inclusions, however, might represent conditions of burial metamorphism that turned the hydrocarbons into pyrobitumen and cryptocrystalline graphite.

Hydrocarbon migration and formation of the minor MVT-type mineralization at Jerritt Canyon is interpreted to have occurred in the late Paleozoic or early Mesozoic. In other Carlin-type gold deposits such as the Carlin (Kuehn and Rose, 1995) and Meikle deposits (Emsbo *et al*., 2003; Evans, 2000), petroleum generation and MVT mineralization has been interpreted to have formed prior to late Jurassic intrusions, likely due to burial during the Mississippian Antler and subsequent late Paleozoic and early Mesozoic orogenies. Maturation of hydrocarbons to pyrobitumen and CH_4 gas production took place during the Late Jurassic to Early Cretaceous low grade metamorphism as interpreted for Jerritt Canyon by Hofstra (1994). At Meikle, Evans (2000) documented Paleozoic MVT mineralization. The MVT mineralization event consisted of early ferroan dolomitization that was followed by pyrite ± sphalerite that replaced a considerable portion of the DSrm massive limestone unit. Evans (2000)

concluded that ferroan dolomite and base metal sulfides pre-dated hydrocarbon migration and burial metamorphism, similar to the conclusion reported by Emsbo *et al*. (2003).

Applications to Exploration

The data sets presented in this study, including trace element patterns and statistical analyses, mineralogical zoning (logging and XRD), carbonate staining, and carbonate isotopes potentially can serve as exploration tools for Carlin-type deposits. Gold concentrations along the Saval form the best halo to the vertical projections of the gold deposits at Jerritt Canyon. As indicated above, the 300 ppb gold contour along the Saval forms a rather continuous halo of up to1,000 feet around the vertical projections of the deposits in the Murray/Winters Creek area and up to 3,700 feet to the vertical projections of the deposits in the SSX-Smith area. It is important to stress again that the 300 ppb gold contour is derived from the grid values. Samples with less than 300 ppb gold do occur within the 300 ppb gold contour. Depleted $\delta^{18}O$ values form a rather continuous halo of –up to 800 feet around the vertical projections of the deposits in the Murray/Winters Creek area and up to 2,000 feet around the vertical projections of the deposits in the SSX-Smith area. The patterns from the point maps of clays documented during from XRD analyses and the logged alteration point maps vary in continuity with respect to the vertical projection of known gold deposits along the Saval. Though some spatial associations can be observed, when observed in detail the patterns are very erratic and do not form consistent halos to areas of mineralization. Table 9 summarizes the distribution of the data sets presented in this study with respect to the 300 ppb gold contour along the Saval. Although it is important to document and understand alteration types associated with mineralized areas, this study has shown alteration should be a

secondary tool in district targeting, because it is commonly very discontinuous and mostly restricted to high grade ore zones. Whole rock XRD also did not show a distinct spatial association with gold. Though many samples do have clay within higher grade ore zones, clays were also present in many areas outboard of known mineralization and clay-bearing samples did not have higher gold values than samples without clay.

This study has shown that gold is the best vectoring tool to find gold. However, CTEs do form significant halos to the deposits, which are more continuous than the gold values themselves. Furthermore, the presence of tellurium seems to indicate areas in which major upwelling of ore fluids occurred. Factor analysis is a viable tool because high factor scores for gold and gold-related elements (factor 3 in this study) outline areas where gold mineralization is present. If individual gold values are low, but mercury, thallium, arsenic, and tellurium values are high, the resultant factor score will also be high, offering the possibility that higher gold values are present nearby. A high factor score for all the CTEs is more robust and reliable than simple high values of individual CTEs. Furthermore, this study has shown that the factor scores for the CTEs increase with decreasing $\delta^{18}O$ values, which could collectively be used as an exploration tool. For example, a drill hole with a high factor score (all of the CTEs have high values) and a depleted $\delta^{18}O$ value would warrant further exploration rather than a hole with a low factor score (some of the CTEs, possibly gold have low values) and a depleted $\delta^{18}O$ value. In districts with more than one hydrothermal signature, such as a Mesozoic intrusion-related signature and Carlin-type gold signature, factor analysis should generate factors that represent both mineralizing systems. For example, if two holes were drilled and both had intervals that assayed 0.02 opt gold, but one hole had a high factor score for

the Mesozoic intrusion related system and the second hole had a high factor score for the Carlin-mineralization, the next hole, everything else being equal, should offset second hole because Mesozoic intrusion-related systems typically do not yield the amount and grade of ore that Carlin-type systems do.

Also, thousands of samples are not required to see the patterns. To test this, the elemental values for the Carlin-type elements were gridded by Target using only the holes that were chosen to be re-logged for this project (247 holes). Even though the patterns were not as detailed, the areas of elevated Carlin-type elements and their patterns were very similar (Fig. 47a, 47b, 47c, 47d, & 47e). For example, Figure 47a shows the grid for gold values from samples that were logged from the project specific logging and the gold contours generated using the Anglo Gold dataset. The gridded gold values closely resemble the gold contours that were made from the entire Anglo Gold data set where the 300 ppb gold contour generally outlines gold values greater than 300 ppb in the gridded image. The same observation can be made between the 50 ppb gold contour, generated from the Anglo Gold data base, and the gold values greater than 50 ppb in the gridded image. The fundamental result here is that 247 holes showed patterns that were similar to 6,417 holes, and 247 samples could be all that is needed to help vector in on Carlin-type gold deposits at the district scale. The cost for ultra trace level methods for multielement geochemical data would cost anywhere from $20.00 to $27.00 per sample. Using the 247 samples to generate a geochemical grid similar to the grid used in Fig. 46a would cost $5,000 to $6,700.

Another even more cost effective vectoring tool is the use of carbonate staining. Ferroan dolomite was documented during this study to consistently occur within the 50

ppb contour, making a halo upwards of 1,000 feet to gold values greater than 300 ppb. Patterns may not be the same in all districts as some districts may have ferroan calcite instead of ferroan dolomite. Carbonate staining is inexpensive and easily utilized, as long as caution is taken to ensure that iron staining is not the result of bleeding from pyrite or other iron-bearing minerals in the rocks and veins. One should not simply the paint the stain on drill core with a brush.

Depletions in $\delta^{18}O$ values also form a large, semi-continuous halo up to 2,000 feet around the vertical projection of known gold deposits and the 300 ppb gold contour along the Saval. Within mineralized areas there are samples present that have $\delta^{18}O$ values consistent with unaltered rocks however; the overall pattern exhibited by depleted $\delta^{18}O$ values is consistent with areas where Carlin-type mineralization is present. There is no statistical or spatial association between depleted $\delta^{18}O$ values, ferroan dolomite or the factor scores for the BSEs, lending further support that the $\delta^{18}O$ depletion halos are the result of the Carlin-type gold mineralization (Fig. 44).

The major zone of upwelling ore fluids in the SSX-Smith area indicates that this area is a candidate for further exploration. Before Yukon-Nevada Gold suspended exploration efforts in the summer of 2008 the SSX-Smith area was their primary target. They had a successful drilling program while drilling between the Smith and SSX mines. Extending the SSX-Smith zone to the area west-northwest of the SSX area, referred to as Cow Canyon, yields a viable exploration target. Though a window into the lower plate is not present in the Cow Canyon area (Fig. 18), lower plate rocks have been intersected at 1,700 feet below the surface. Using the targeting tools presented in this paper viable exploration targets within the northern portion of the Jerritt Canyon District include not

only Cow Canyon, but an area north of California Mountain, where depleted $\delta^{18}O$ values, elevated values for thallium, tellurium, arsenic and mercury, high factor scores for the gold factor from the factor analysis, ferroan dolomite, and exposed lower plate host rocks occur.

	Occur Within the 300 ppb Gold Contour	Form a Halo to the 300 ppb Gold Contour	Halo Distance from 300 ppb - Murray-Winters Creek Area (feet)	Halo Distance from 300 ppb - Steer/Saval/SSX-Smith/DASH area (feet)
XRD analyses				
Kaolinite	YES	YES - (D)		
Illite-Muscovite 2M1 & 3T	YES	YES - (D)		
Ankerite XRD	YES	YES - (C)	100 - 1,000	100 - 700
Dolomite XRD				
Marcasite XRD	YES			
Pyrite XRD	YES			
Arsenopyrite XRD	YES			
Calcite XRD				
Isotopes				
δ13C				
δ18O	YES	YES - (SC) (<22 ‰)	0 - 800	0 - 2,000
Geochemistry				
Arsenic	YES	YES - (C) (50 - 100 ppm)	0 - 800	0 - 1500
Mercury	YES	YES - (C) (1 - 3 ppm)	0 - 1,500	0 - 2,500
Thallium	YES	YES - (C) (0.3 0 0.5 ppm)	0 - 1,500	0 - 2,000
Tellurium	YES	YES - (C) (0.05 - 0.1)	0 - 1,500	0 - 1,500
Antimony				
Logging				
Cacite Veining				
Ferroan Dolomite Veining	YES	YES - (C)	100 - 1,000	100 - 700
Dolomite Veining				
Quartz Veining	YES			
Silicification	YES			
Decalcification	YES			
Dolomitization				
Oxidation				
Pyrite	YES			
Orpiment				
Realgar				
Rock Staining				
Pink				
Blue	YES	YES (SC)	0 - 800	0 - 1,000
No-Stain				

(C): Continuous   (SC): Semi-Continuous   (S): Spotty

Table 9: Table showing the all of the attributes documented during this study and their relationship to gold mineralization.

Figure 47

a. Gridded image of gold values from only the samples re-logged during this study, and the gold contours generated from the Anglo Gold data set. Legend is for calculated grid values, not actual values.

b. Gridded image of arsenic values from only the samples re-logged during this study, and the gold contours generated from the Anglo Gold data set. Legend is for calculated grid values, not actual values.

c. Gridded image of mercury values from only the samples re-logged during this study, and the gold contours generated from the Anglo Gold data set. Legend is for calculated grid values, not actual values.

d. Gridded image of tellurium values from only the samples re-logged during this study, and the gold contours generated from the Anglo Gold data set. Legend is for calculated grid values, not actual values.

e. Gridded image of thallium values from only the samples re-logged during this study, and the gold contours generated from the Anglo Gold data set. Legend is for calculated grid values, not actual values.
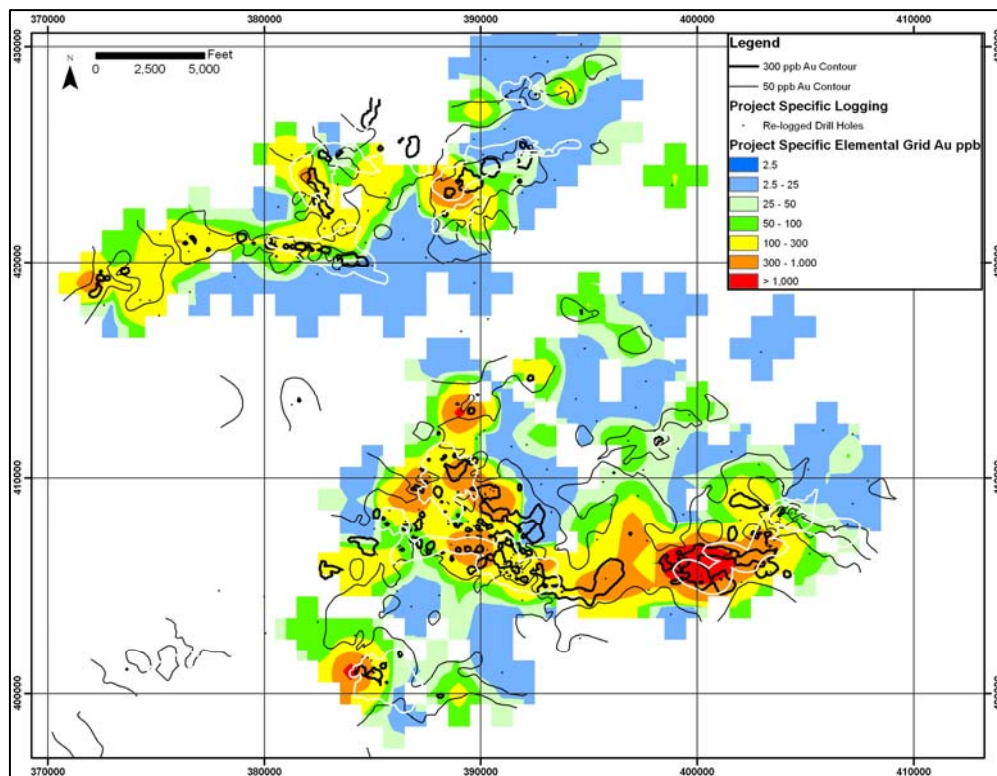
Figure 47a
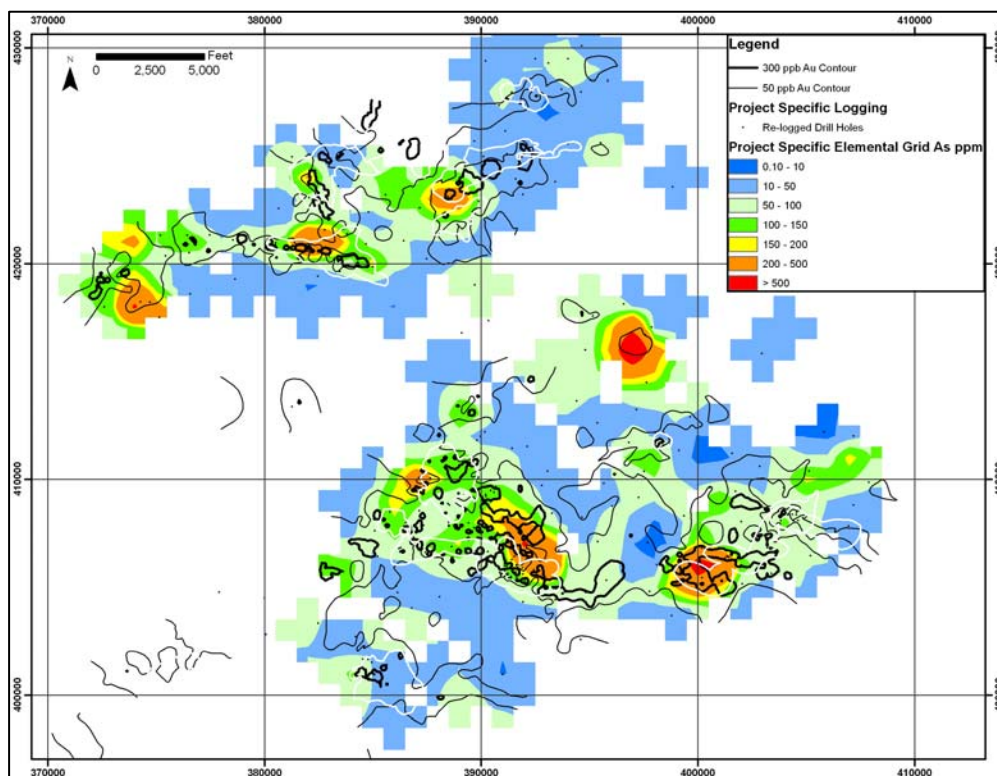
Figure 47b
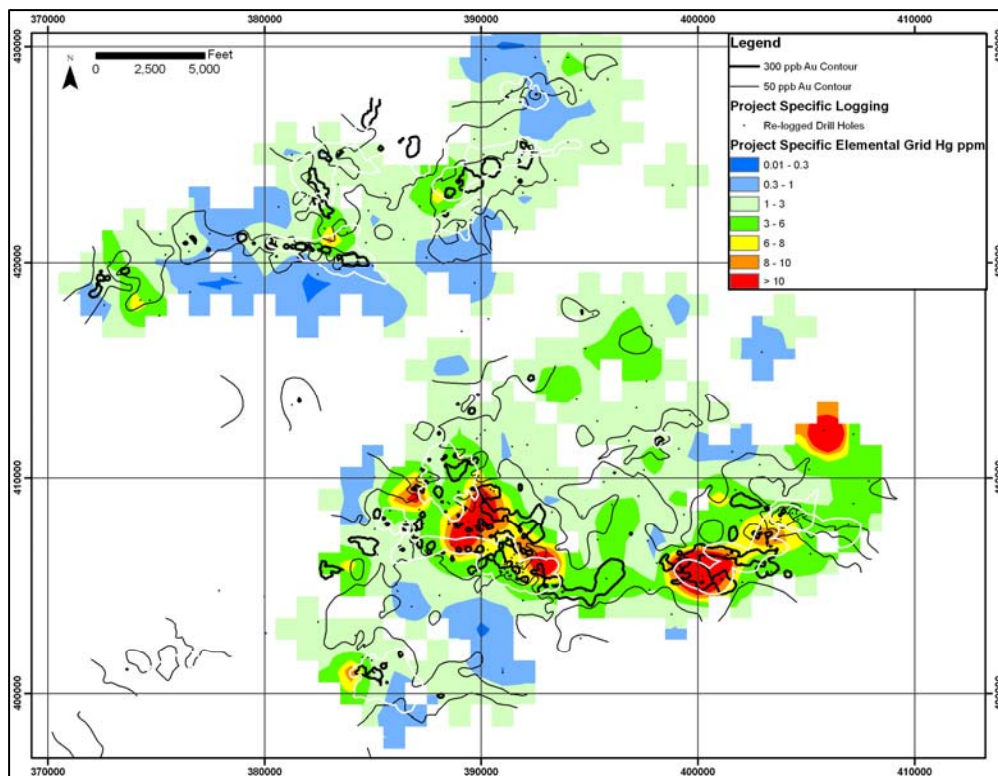
Figure 47c
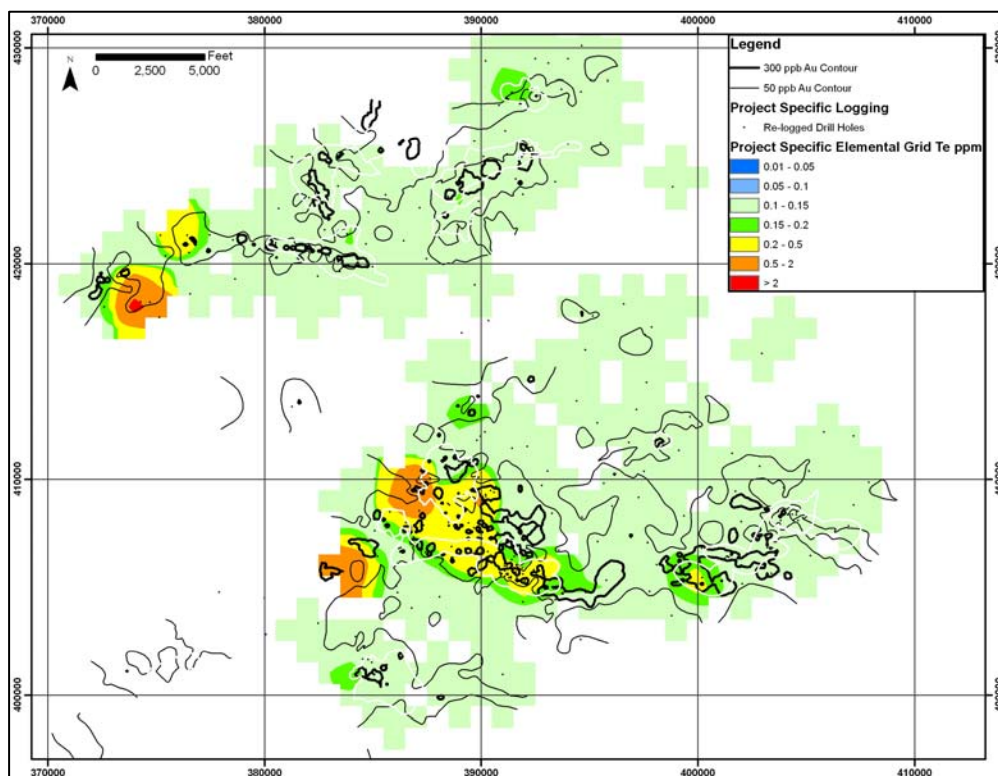
Figure 47d
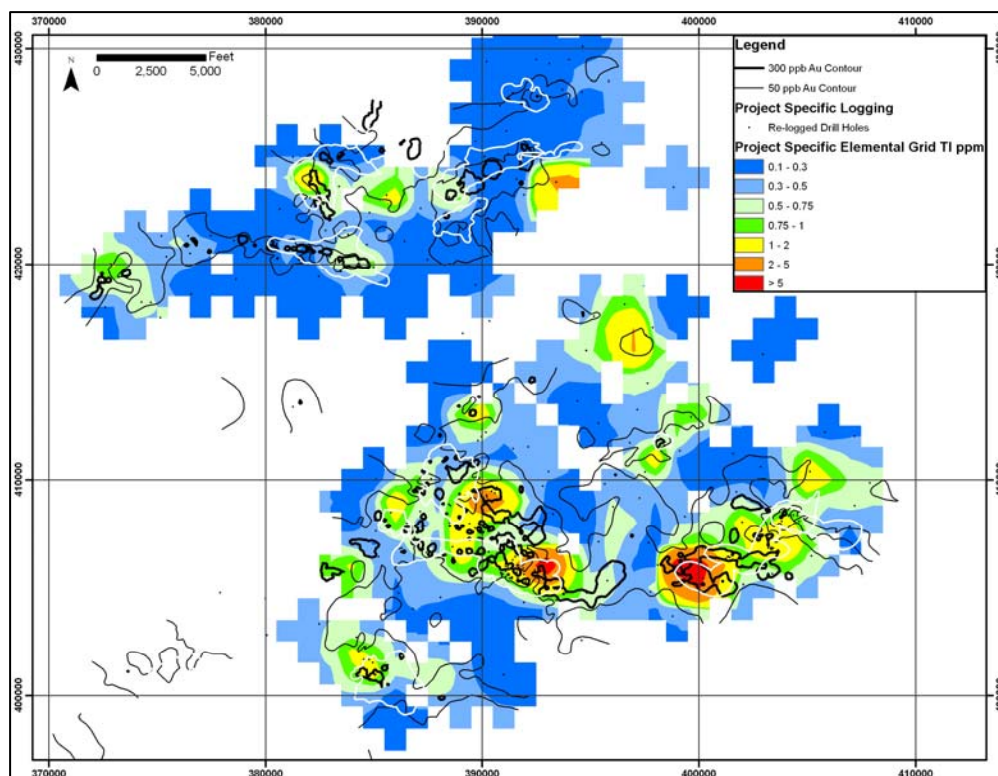
Figure 47e

Conclusions

The Saval Discontinuity in the Jerritt Canyon district is a sub-aerial karsted unconformity that has locally been structurally activated. After deposition of the Hanson Creek Formation the rocks were sub-aerially exposed during a global low-stand. The Roberts Mountains Formation was then deposited in a transgressive sequence over karsted and brecciated $SOhc_1$.

Geochemical analyses of drill cuttings and core from the base of the Roberts Mountain Formation in 6,416 drill holes indicate there are two groups of elements: the Carlin-type elements (CTEs) and the black shale elements (BSEs). The CTEs were precipitated during formation of the Carlin-type gold deposits in the Eocene and consist

of gold, arsenic, thallium, mercury, and tellurium. The Carlin-type elements show a more widespread, continuous pattern in the SSX-Smith area, whereas they form much narrower patterns in Murray-Winters Creek area. Based on the 50 ppb gold contour along the Saval, the west-northwest mineralized trend through the SSX-Smith area is 22,000 feet long and 5,000 feet wide. The CTEs form consistent halos from the 300 ppb gold contour extending out as much as 0-1,500 feet.

Beside the CTEs, ferroan dolomite and depleted $\delta^{18}O$ values in carbonates form the most continuous halos to gold values greater than 300 ppb along the Saval. Ferroan dolomite/ankerite, determined by staining and XRD, is consistently found in samples where gold values were greater than 50 ppb along the Saval, forming a halo of at least 100 feet to the 300 ppb gold contour. Silicification and decarbonatization products do not consistently occur within the 300 ppb gold contour and only occur erratically outside the 50 ppb gold contour. Illite and kaolinite, determined by whole rock XRD, do not form consistent patterns around gold.

The large, continuous zones of elevated CTEs in the SSX-Smith area suggest it was the major zone of upwelling hydrothermal fluids during the formation of the Carlin-type gold deposits in the Jerritt Canyon area. The presence of widespread elevated tellurium only in the Steer-Saval-SSX deposits may be indicating a deep magmatic source. The irregular nature of most of the data sets, especially of logged features like hydrothermal alteration, argues against extensive lateral fluid flow along the Saval during ore formation and suggests complex, fluid flow controlled by interactions between high-angle fracture systems and favorable stratigraphy. More irregular, less extensive CTEs and logged features in the Murray-Winters Creek area, relative to the SSX-Smith area,

suggest weaker or more restricted fluid flow, which appear to be controlled by a few major fault zones, which tapped the main fluid source at depth, rather than numerous high-angle fault and fractures as evidenced in the SSX-Smith area.

Statistical analyses of the geochemical data indicate the black shale elements (BSEs) consist of two groups. Group one consists of uranium, phosphorous, lanthanum, and gallium which was probably inherited during initial deposition of the DSrm by upwelling of deep oceanic waters during a transgressive sequence. The second group consists of zinc, molybdenum, nickel, copper, cadmium, and silver, which along with ferroan dolomite, appear to be the result of migrating basinal brines and mineralization similar to that of MVT deposits. Migration of brines may have been an important rock preparation event, producing ferroan dolomite, which subsequently reacted with auriferous hydrothermal fluids rich in reduced sulfur to deposit gold by sulfidation and formation of gold-bearing pyrite.

The most promising exploration tools derived from this research that could be applied at Jerritt Canyon and other districts of Carlin-type deposits are the collection and analysis of trace elements, the identification of ferroan carbonates and the recognition of zones of depleted $\delta^{18}O$ isotope values. Analysis of the patterns of low levels of gold (e.g., the 300 and 50 ppb contours discussed in this study) should continue to be the most important tool. However, the combination of using GIS to evaluate similar map patterns, statistical analyses, and factor analysis, is critical in determining where CTEs are most closely associated with the gold. In this study, thallium, mercury, arsenic and tellurium are strongly associated spatially and statistically with gold, form halos to gold, and in the case of tellurium, potentially point to the major ore fluid upwelling zones. Thousands of

samples are not required to see the signature and the patterns. Factor analysis can be a very effective exploration tool when exploring in districts that experienced multiple hydrothermal events. Given its spatial coincidence with the CTEs, low cost, and "real time" nature, careful staining of carbonates to determine zones of ferroan dolomite should be routine. However, patterns in other districts might differ. For example, ferroan calcite, rather than ferroan dolomite might be present and gold might be associated with boundaries between ferroan and non-ferroan carbonates. Given the large halos of depleted $\delta^{18}O$ values demonstrated in this study, isotopic analysis of carbonates could be worth the cost in evaluating large areas.

References

Abdi, H., 2003, Factor Rotations in Factor Analyses *in* Lewis-Beck M., Bryman, A., and Futing, T. eds. Encyclopedia of Social Sciences Research Methods. Thousand Oaks (CA): Sage, p. 1-8.

Anderson, G.M., and Macqueen, R.W., 1988, Mississippi Valley-Type Lead-Zinc Deposits: *in* Roberts, R.G., and Sheahan P.A., eds., Ore Deposit Models, Reprint Serires 3, p. 79-90.

Arehart, G.B., and Donelick, R.A., 2006, Thermal and isotopic profiling of the Pipeline hydrothermal system: Application to exploration for Carlin-type gold deposits: Journal of Geochemical Exploration, p. 27-40 p.

Arehart, G.B., Schmauder, G.S., and Donelick, R., 2006, Apatite fission-track and stable isotope geochemistry in the Bald Mountain district, Nevada: GSN Special Publication No. 43, p. 75-101.

Armstrong, A.K., Theodore, T.G., Oscarson, R.L., Kotlyar, B.B., Harris, AG., Bettles, K.H., Lauha, E.A., Hipsley, R.A., Griffen, G.L., Abbott, E.W., and Cluer, J.K., 1997, Preliminary facies analysis of Silurian and Devonian autochthonous rocks that host gold along the Carlin trend, Nevada: U.S. Geological Survey Open-File Report 98-338, p. 38-68.

Baily, S.W., 1984, Classification and Structures of the MICAS: *in* Bailey, S.W., ed., Mineralogical Society of America, Reviews in Mineralogy, v. 13, p. 1-12.

Bettles, K., 2002, Exploration and Geology, 1962 to 2002, at the Goldstrike Property, Carlin Trend, Nevada *in* Thompson, T.B., Teal, L., and Meeuwig, R.O., eds.,

Gold Deposits of the Carlin Trend: Nevada Bureau of Mines and Geology, v. 111, p. 54-75.

Birak, D.J., and Hawkins, R.B., 1985, The Geology of the Enfield Bell Mine and the Jerritt Canyon District, Elko County, Nevada, in Tooker, E.W., ed., Geologic characteristics of sediment-and volcanic-hosted disseminated gold deposits-search for an occurrence model: U. S. Geological Survey Bulletin 1646, p. 95-106.

Blatt, H., and Tracy, R.J., 1992, Petrology Igneous, Sedimentary, and Metamorphic: W. H. Freeman and Company, v. 2, p. 345.

Boggs, S. Jr., 1992, Principles of Sedimentology and Stratigraphy: Pearson Education, ed. 4, p. 484-513.

Boggs, S. Jr., 2006, Petrology of Sedimentary Rocks: Macmillan Publishing Company, ed. 4, p. 227.

Bratland, C.T., 1991, Geology of the Winters Creek gold deposit, Independence Mountains, Elko County, Nevada, in Rains G.L., Lisle, R.E., Schafer, R.W., and Wilkinson, W.H., eds., Geology and Ore Deposits of the Great Basin: Geological Society of Nevada Symposium, Reno, 1990, Proceedings, v. 1, p. 607-618.

Breitsprecher, K., Thorkelson, D.J., Groome, W.G., and Dostal, J., 2003, Geochemical confirmation of the Kula-Farallon slab window beneath the Pacific Northwest in Eocene time: Geology v. 31, p. 351-354.

Cail, T.L., and Cline, J.S., 2001, Alteration Associated with Gold Deposition at the Getchell Carlin-Type Gold Deposit, North-Central Nevada: Economic Geology, v. 96, p. 1343-1359.

Carr, J.R., 2002, Data Visualization in the Geosciences: Prentice Hall, Upper Saddle River, New Jersey, 267 p.

Chakurian, A.M., Arehart, G.G., Donelick, R.A., Zhang, X., and Reiners, P.W., 2003, Timing constraints of gold mineralization along the Carlin trend utilizing apatite fission-track, ^{40}Ar/^{39}Ar, and apatite (U-Th)/He: Economic Geology, v. 98, p. 1159-1171.

Christiansen, R.L., and Lipman, P.W., 1972, Cenozoic volcanism and plate tectonic evolution of the western United States. II. Late Cenozoic: Philosophical Transactions of the Royal Society of London, Series A: Mathematical and Physical Sciences, v. 271, p. 249-284.

Cline, J.S., 2001, Timing of Gold and Arsenic Sulfide Mineral Deposition at the Getchell Carlin-Type Gold Deposit, North-Central Nevada: Economic Geology, v. 96, p. 75-89.

Cline, J.S., Hofstra, A.H., Muntean, J.L., Tosdal, R.M. and Hickey, K.A., 2005, Carlin-type gold deposits in Nevada, USA: Critical geologic characteristics and viable models, *in* Hedenquist, J. and Thompson, T.B. eds. *100th Anniversary Volume.* Society of Economic Geologists, p. 451-484.

Clode, C.H., Grusing, S.R., Johnston, I.M., and Heitt, D.G., 2002, Geology of the Deep Star Gold Deposit, *in* Thompson, T.B., Teal, L., and Meeuwig, R.O., eds., Gold Deposits of the Carlin Trend: Nevada Bureau of Mines and Geology, v. 111, p. 76-90.

Cook, H.E., and Corboy, J.J., 2003, Great Basin Paleozoic Carbonate Platform: Facies, Facies Transitions, Depositional Models, Platform Architecture, Sequence

Stratigraphy, and Predictive Mineral Host Models: USGS Open-File Report 2004-1078, p. 10.

Daly, W.E., Doe, T.C., and Loranger, R.J., 1991, Geology of the northern Independece Mountains, Elko County , Nevada, *in* Raines, G.L., Lisle, R.E., Schafer, R.W., and Wilkinson, W.H., eds., Geology and Ore Deposits of the Great Basin: Geological Society of Nevada Symposium, Reno, 1991, Proceedings, p. 583-602.

Dewitt, A.B., 1999, Alteration, Geochemical Dispersion, and Ore Controls at the SSX Mine, Jerritt Canyon District, Elko County, Nevada: Unpublished M.S. thesis, Reno, University of Nevada, 95 p.

Doback, P. J., Arbonies, D., Hipsley, R., Visher, M., 2002, Geology of the Storm Gold Deposit, *in* Thompson, T.B., Teal, L., and Meeuwig, R.O., eds., Gold Deposits of the Carlin Trend: Nevada Bureau of Mines and Geology, v. 111, p. 46-53.

Drews-Armitiage, S.P., Romberger, S.B., and Whitney, C.G., 1996, Clay alteration and gold deposition in the Genesis and Blue Star deposits, Eureka county, Nevada, Economic Geology, v. 81, p. 1383-1393.

Drits, V.A., Zvyagin, B.B., and Tokmakov, P.P., 1966, Gümbelite, a dioctrahedral $2M_2$ mica. Dok1. Acad. Sci. USSR 170, p. 156-159.

Dunham, J.B., and Olson, E.R., 1980, Shallow Subsurface Dolomitization of Subtidally Deposited Carbonate Sediment in Hanson Creek Formation (Ordovician-Silurian), Central Nevada--Evidence for Groundwater Mixing: Society of Economic Paleontologist and Mineralogist, Special Publication no. 28, p. 139-161.

Eliason, R., and Wilton, D.T., 2005, Relation of gold mineralization to structure in the Jerritt Canyon mining district, Nevada, *in* Rhoden, H.N., Steininger, R.C., and

Vikre, P.G., eds., Geological Society of Nevada Symposium 2005: Window to the World, Reno, Nevada, May 2005, p. 335-356.

Emsbo, P., Hutchinson, R. W., Hofstra, A. H., Volk, J. A., Bettles, K. H., Baschuk, and G. J., Johnson, C. A., 1999, Syngenetic Au on the Carlin trend: Implications for Carlin-type deposits: Geology, v. 27, no. 1, p. 59-62.

Emsbo, P., Hofstra, A.H., Lauha, E.A., Griffin, G.L., and Hutchinson, R.W., 2003, Origin of high-grade gold ore, source of ore fluid components, and genesis of the Meikle and neighboring Carlin-type deposits, northern Carlin trend, Nevada: Economic Geology, v. 98, p. 1069-1100.

Evans, D.C., 2000, Carbonate-hosted breccias in the Meikle mine, Nevada and their relationship with gold mineralization: Unpublished M.S. thesis, Golden, Colorado, Colorado School of Mines, 266 p.

Farmer, G.L., and DePaolo, D.J., 1983, Origin of Mesozoic and Tertiary granite in the western United States and implications for pre-Mesozoic crustal structure. 1. Nd and Sr isotopic studies in the geocline of the northern Great Basin: Journal of Geophysical Research, v. 88, p. 3379-3401.

Folger, H.W., Hofstra, A.H., Eberl, D.D., and Snee, L.W., 1998, Importance of clay characterization to interpretation of $^{40}Ar/^{39}Ar$ dates on illite from Carlin-type gold deposits: Insights from Jerritt Canyon Nevada: U.S. Geological Survey Open File Report 98-338, p. 193-201.

Folger, H.W., Snee, L.W., Mehnert, H.H., Hofstra, A.F., and Dahl, A.R., 1996, Significance of K-Ar and $^{40}Ar/^{39}Ar$ dates from mica in Carlin-type gold deposits: Evidence from the Jerritt Canyon District, Nevada: *in* Coyner, A.R., and Fehey,

P.L., eds., Geology and Ore Deposits of the American Cordillera, Geological Society of Nevada Symposium Proceedings, Reno/Sparks, Nevada, April, 1995, p. 41-60.

Fortuna, J., Kesler, S.E., and Stenger, D.P., 2003, Source of iron for sulfidation and gold deposition, Twin Creeks Carlin-type deposit, Nevada Economic Geology, v. 98, p. 1213-1224.

Goodell, P.C., and Peterson, U., 1974, Julcani Mining District, Peru: A Study of Metal Ratios: Economic Geology, v. 69, p. 347-361.

Guilbert, J.M., and Park Jr., C.P., 1986, The Geology of Ore Deposits, W.H. Freeman and Company, New York, 985 p.

Harlan, J.B., Harris, D.A., Mallette, P.M., Norby, J.W., Rota, J.C., Sagar, J.J., 2002, Geology and Mineralization of the Maggie Creek District *in* Thompson, T.B., Teal, L., and Meeuwig, R.O., eds., Gold Deposits of the Carlin Trend: Nevada Bureau of Mines and Geology, v. 111, p. 115-142.

Hawkins, R.B., 1982, Discovery of the Bell gold mine, Jerritt Canyon district, Elko County, Nevada: Mining Congress Journal, v. 68, no. 2, p. 28-32.

Hedenquist, J.W., Arribas, A.R., Gonzalez-Urien, E., 2000, Exploration for Epithermal Gold Deposits: Reviews in Economic Geology, v. 13, p. 245-277.

Heinrich, C.A., 2005, The physical and chemical evolution of low-salinity magmatic fluids at the porphyry to epithermal transition: a thermodynamic study: Mineralium Deposita, v. 39, p. 864-889.

Heitt, D.G., Dunbar, W.W., Thompson, T.B., Jackson, R.G., 2003, Geology and Geochemistry of the Deep Star Gold Deposit, Carlin Trend, Nevada: Economic Geology, v. 98, p. 1107-1135.

Hesse, R., 1988, Diagenesis #13. Origin of chert: Diagenesis of biogenic siliceous sediments: Geoscience Canada, v. 13, no. 3, p. 171-192.

Hitzman, M.W., 1999, Routine staining of drill core to determine carbonate mineralogy and distinguish carbonate alteration textures: Mineralium Deposita, v. 34, p. 794-798.

Hofstra, A.H., Daly, W.E., Birak, D.J., and Doe, T.C., 1991, Geologic framework and genesis of Carlin-type gold deposits in the Jerritt Canyon district, Nevada, USA, *in* Ladeira, E.A., eds., Brazil Gold '91: Rotterdam, Balkema, p. 77-87.

Hofstra, A.H., 1994, Geology and genesis of the Carlin-type gold deposits in the Jerritt Canyon district, Nevada: Unpublished Ph.D. dissertation, Golden, Colorado School of Mines, 1287 p.

Hofstra, A.H., Snee, L.W., Rye, R.O., Folger, H.W., Phinisey, J.D., Loranger, R.J., Dahl, A.R., Naeser, C.W., Stein, H.J., and Lewchuck, M., 1999, Age Constraints on Jerritt Canyon and Other Carlin-Type Gold Deposits in the Western United States-Relationship to Mid-Tertiary Extension and Magmatism: Economic Geology, v. 94, p. 769-802.

Hofstra, A.H., and Cline, J.S., 2000, Characteristics and models for Carlin-type gold deposits: Reviews in Economic Geology, v. 13, p. 163-220.

Humphreys, E.D., 1995, Post-Laramide removal of the Farallon slab, western United States: Geology, v. 23, p. 987-990.

Humphreys, E., Hessler, E., Dueker, K, Farmer, G.L., Erslev, E., and Atwater, T., 2003, How Laramide-age hydration of North American lithosphere by the Farallon slab controlled subsequent activity in the western United States, *in* Klemperer, S.L., and Ernst, W.G., eds., The George A. Thompson Volume: The lithosphere of Western North America and its geophysical characterization: Geological Society of America, International Book Series, v. 7, p. 524-542.

Hutcherson, S.K., 2002, Geology, Geochemistry and Alteration of Zone 5 of the Murray Mine, Jerritt Canyon District, Elko County Nevada: Unpublished M.S. thesis, Reno, University of Nevada, 114 p.

Ilchik, R.P., 1990, Geology and Geochemistry of the Vantage Gold Deposits, Alligator Ridge-Bald Mountain Mining District, Nevada: Economic Geology, v. 85, p. 50-75.

Jensen, E.P, and Barton, M.D., 2000, Gold Deposits Related to Alkaline Magmatism: Reviews in Economic Geology, v. 13, p. 279-314.

John, E.C., 1978, Mineral Zones in the Utah Copper Orebody: Economic Geology, v. 73, p. 1250-1259.

John, D.A., 2001, Miocene and early Pliocene epithermal gold-silver deposits in the northern Great Basin, western United States: Characteristics, distribution, and relationship to magmatism: Economic Geology, v. 96, P. 1827-1854.

Jones, C., Sonder, L., and Unruh, J.R., 1998, Lithospheric gravitational potential energy and past orogenesis: Implications for conditions of initial Basin and Range and Laramide deformation: Geology, v. 26, p. 639-642.

Jones, M., 2005, Jerritt Canyon District Independence Mountains, Elko County, Nevada, Gold's at Fault, *in* Rhoden, H.N., Steininger, R.C., and Vikre, P.G., eds., Geological Society of Nevada Symposium 2005: Window to the World, Reno, Nevada, May 2005, p. 99-122.

Kerr, J.W., 1962, Paleozoic sequences and thrust slices of the Seetoya Mountains, Independence Range, Elko County, Nevada: Geological Society of America Bulletin, v. 73, no. 4, p. 714.

Ketner, K.B., 1977, Late Paleozoic orogeny and sedimentation, southern California, Nevada, Idaho, and Montana, *in* Stewart, J.H., Stevens, C.H., and Fritsche, A.E., eds., Paleozoic paleogeography of western United States: Pacific Section, Society of Economic Paleontologists and Mineralogists, Pacific Coast Paleogeography Symposium 1, p. 363-369.

Kuehn, C.A, and Rose, A. W., 1992, Geology and geochemistry of wall-rock alteration at the Carlin gold: Economic Geology, v. 87, p. 1697-1721.

Kuehn, C.A., and Rose, A.W., 1995, Carlin Gold Deposits, Nevada: Origin in a Deep Zone of Mixing between Normally Pressured and Overpressured Fluids: Economic Geology, v. 90, p. 17-36.

Kistler, R.W., and Peterman, Z.E., 1973, Variations in Sr, Rb, K, Na, and Initial Sr ^{87}/Sr ^{86} in Mesozoic Granitic Rocks and Intruded Wall Rocks in Central California: *GSA Bulletin*; v. 84; no. 11; p. 3489-3512.

Krauskopf, K.B., 1955, Sedimentary Deposits of Rare Metals: Economic Geology, 50th Anniversary Volume, p. 411-463.

Krumbein, W.C., Sloss, L.L., 1951, Stratigraphy and Sedimentation: W. H. Freeman and Company, city, 497p.

Land, L.S., 1979, Chert-Chalk Diagenesis: The Miocene Island Slope of North Jamaica: Journal of Sedimentary Petrology, v. 49, n. 1, p. 223-232.

Laschet, C.A., 1984, On the Origin of Cherts: Facies, v. 10, p. 257-290.

Lawerence, E.F., 1963, Antimony deposits in Nevada: Nevada Bureau of Mines Bulletin 61, p. 248.

Liu, M., and Shen, Y., 1998, Crustal collapse, mantle upwelling, and Cenozoic extension in the North America Cordillera: Tectonics, v. 17, p. 311-321.

Machel, H.G., 2001, Bacterial and thermochemical sulfate reduction in diagenetic settings—old and new insights: Sedimentary Geology, v. 140, p. 143-175.

MacKenzie, J.M., and Canil, D., 2008, Volatile heavy metal mobility in silicate liquids: Implications for volcanic degassing and eruption prediction: Earth and Planetary Science Letters 269, p. 488-469.

McCrea, J.M., 1950, On the isotopic chemistry of carbonates and a paleotemperature scale: Journal of Chemical Physics, v. 18, p. 849-857.

Miller, D.M., Nilsen, T.H., and Bildeau, W.L., 1992, Late Cretaceous to early Eocene geologic evolution of the U.S. Cordillera: Geological Society of America, Geology of North America, v. G-3, p. 205-260.

Miller, E.L., Hodsworth, B.K., Whiteford, W.B., and Rodgers, D., 1984, Stratigraphy and structure of the Schoonover sequence, northeastern Nevada: Implications for Paleozoic plate-margin tectonics: Geological Society of America Bulletin, v. 95, p. 1063-1076.

Muntean, J. L., Coward, M. P., Tarnocia, C. A., 2007, Reactivated Paleozoic normal faults: controls on the formation of Carlin-type gold deposits in north-central Nevada, Geological Society, London, Special Publications, v. 272, p. 571-587.

Muntean, J.L., and Henry, C.D., 2007, Preliminary Geologic Map of the north half of the Jerritt Canyon Mining District, Elko County, Nevada: Nevada Bureau of Mines and Geology, Open File Report OF07-3.

Mullens, T.E., 1980, Stratigraphy, Petrology, and Some Fossil Data of the Roberts Mountains Formation, North-Central Nevada: U.S. Geological Survey Professional Paper 1063, p. 1-67.

Nevada Bureau of Mines and Geology, 2007, The Nevada mineral industry 2007: Nevada Bureau of Mines and Geology Special Publication MI-2007, 182 p.

Peters, S.G., Armstrong, A.K., Harris, A.G., Oscarson, R.L., Noble, P.J., Biostratigraphy and Structure of Paleozoic Host Rocks and Their Relationship to Carlin-Type Gold Deposits in the Jerritt Canyon Mining District, Nevada: Economic Geology, v. 98, p. 317-337.

Phinisey, J.D., 1995, Petrography, alteration, and mineralization of igneous dikes of the Jerritt Canyon district, Elko County, Nevada: Unpublished M. S. thesis, Reno, University of Nevada. 173 p.

Phinisey, J.D., Hofstra, A.H., Snee, L.W., Roberts, T.T., Dahl, R.J., and Loranger, R.J., 1996, Evidence for multiple episodes of igneous and hydrothermal activity and constraints on the timing of gold mineralization, Jerritt Canyon district, Elko County, Nevada, *in* Coyner, A.R., and Fahey, R.L., eds., Geology and Ore

Deposits of the American Cordillera: Geological Society of Nevada Symposium, Reno, 1995, Proceedings, v. 1, p. 15-39.

Poole, F.G., Stewart, J.H., Palmer, A.R., Sandberg, C.A., Madrid, R.J., Ross, Jr., R.J., Hintze, L.F., Miller, M.M., and Wrucke, C.T., 1992, Latest Pre-Cambrian to latest Devonian time; Development of a continental margin, *in* Burchfiel., B.C., Lipman, P.W., and Zoback, M.L. eds., The Cordilleran Orogen: Conterminous U.S.: Boulder, Colorado: Geological Society of America, The Geology of North America, v. G-3, p. 9-56.

Rahl, J.M., McGrew, A.J., and Foland, K.A., 2002, Transition from contraction to extension in the northeastern Basin and Range: New evidence from the Copper Mountains, Nevada: Journal of Geology, v. 110, p. 179-194.

Roberts, R.J., Hotz, P.E., Gilluly, J., and Ferguson, H.G., 1958, Paleozoic rocks of north-central Nevada: American Association of Petroleum Geologists Bulletin, v. 42, no. 12, p. 2813-2857.

Roberts, R.J., Montgomery, K.M., and Lehner, R.E., 1967, Geology and Mineral Resources of Eureka County, Nevada: Nevada Bureau of Mines and Geology, Bulletin 64, p. 20-21.

Rose, A.W., Hawkes, E.H., and Webb, J.S., 1980, Geochemistry in Mineral Exploration: Academic Press, 2nd edition, 657 p.

Rye, R.O., Doe, B.R., and Wells, J.D., 1974, Stable isotope and lead isotope study of the Cortez, Nevada, gold deposit and surrounding area: U. S. Geological Survey Journal of Research, v. 2, p. 13-23.

Sangster, D.F. (Ed.), 1996, Carbonate-hosted lead-zinc deposits. Society of Economic Geologists Special Publication No. 4, 664 p.

Sha, P., 1993, Geochemistry and genesis of sediment-hosted disseminated gold mineralization at the Gold Quarry mine, Nevada: Unpublished Ph.D. thesis, University of Alabama, 228 p.

Shimoda, S., 1970, A hydromuscovite from the Shakanai mine, Akita prefecture, Japan: Clays and Clay Minerals 18, p. 269-274.

Silberling, N.J., 1975, Age relationships of the Golconda thrust fault, Sonoma Range, north-central Nevada: Geological Society of America Special Paper 163, 28 p.

Silberling, N.J., and Roberts, R.J., 1962, Pre-Tertiary stratigraphy and structure of northwestern Nevada: Geological Society of America Special Paper 72, 58p.

Stenger, D.P., Kesler, S.E., and Vennemann, T., 1998, Carbon and oxygen isotope zoning around Carlin-type gold deposits: a reconnaissance survey at Twin Creeks, Nevada: Journal of Geochemical Exploration, v. 63, p. 105-121.

Stewart, J.H., 1972, Initial deposits in the Cordilleran geosyncline: Evidence of a Late Precambrian separation: Geological Society of America Bulletin, v. 83, p. 1345-1360.

Stewart, J.H., 1980, Geology of Nevada: Nevada Bureau of Mines and Geology Special Publication 4, 136 p. 1 plate.

Takeda, H., and Ross, M., 1995, Mica polytypism: Identification and origin: American Mineralogist, v. 80, p. 715-724.

Theodore, T.G., Berger, V.I., Singer, D.A., Harris, A.G., and Stevens, C.H., 2004, Synthrusting deposition of the Pennsylvanian and Permian Strathern Formation, northern California trend, Nevada: Sedimentary Geology, v. 165, p. 1-28.

Tucker, M.E., Wright, V.P., Dickson, J.A.D, 1996, Carbonate Sedimentology: Blackwell Publishing, Oxford 482 p.

Wells, J.D., Stoiser, L.R., Elliot, J.E., 1969, Geology and Geochemistry of the Cortez Gold Deposit, Nevada: Economic Geology, v. 64, p. 526-587.

Williams-Jones, A.E., Heinrich, C.A., Vapor Transport of Metals and the Formation of Magmatic-Hydrothermal Ore Deposits, *in* Hedenquist, J. and Thompson, T.B., J.F.H, Goldfarb, R.J., and Richards, J.P., eds. *100th Anniversary Volume.* Society of Economic Geologists, v. 100, p. 1287-1312.

Wilton, T., 2004, A Commentary on the structural Setting at Jerritt Canyon, Nevada and its Relationship to High-Grade, Sediment-hosted Gold Deposits in the District: GSN Special Publication No. 39, p 73-85.

Wright, V.P., 1982, The Recognition and Interpretation of Paleokarsts: Two examples from the Lower Carboniferous of South Wales: Journal of Sedimentary Petrology, v. 52, n. 1, p. 83-94.

Zoback, M.L., Anderson, R.E., and Thompson, G.A., 1981, Cainozoic evolution of the state of stress and style of tectonism of the Basin and Range province of the western United States: Royal Society of London Philosophical Transactions, Part A, v. 300, p. 407-434.

<u>Appendix</u>

Appendix 1

Geologic Maps illustrating rock units, hydrothermal alteration types, and

textural/mineralogical features.

<u>Key to Mapping</u>

Qal   ▢   Quaternary alluvium/Mine Tailings

DSrm   ▢   Devonian-Silurian Roberts Mountains Formation

$SOhc_1$ ▢   Silurian-Ordovician Hanson Creek Formation Unit 1

$SOhc_2$ ▢   Silurian-Ordovician Hanson Creek Formation Unit 2

$SOhc_3$ ▢   Silurian Ordovician Hanson Creek Formation Unit 3

Cave Fill   ▢

<u>Alteration</u>

Silicified Rock   Weak   · · · · · · · ·   Moderate   — — —

                Strong   ——————

Dolomitized Rock   Weak   · · · · · · · ·   Moderate   — — —

                Strong   ——————

Carbon   Weak   · · · · · · · ·   Moderate   — — —

                Strong   ——————

Oxidized Rock   Weak   · · · · · · · ·   Moderate   — — —

                Strong   ——————

Fault   ——————————   Inferred Fault   — — — —

Key to Mapping Continued

Contact ———————— Inferred Contact - - - - - - - - - -

Breccia △ △ △ △

B-Barite **Sk-Stibiconite**

Base map for Thomas Jose

Interpreted geology map of Thomas Jose

Out crop map for Thomas Jose

Alteration map for Thomas Jose

Saval Jr. Base Map

Interpreted geology map for Saval Jr..

Outcrop map for Saval Jr..

Alteration map for Saval Jr..

South Bidart Base Map and Outcrop map.

10 Feet
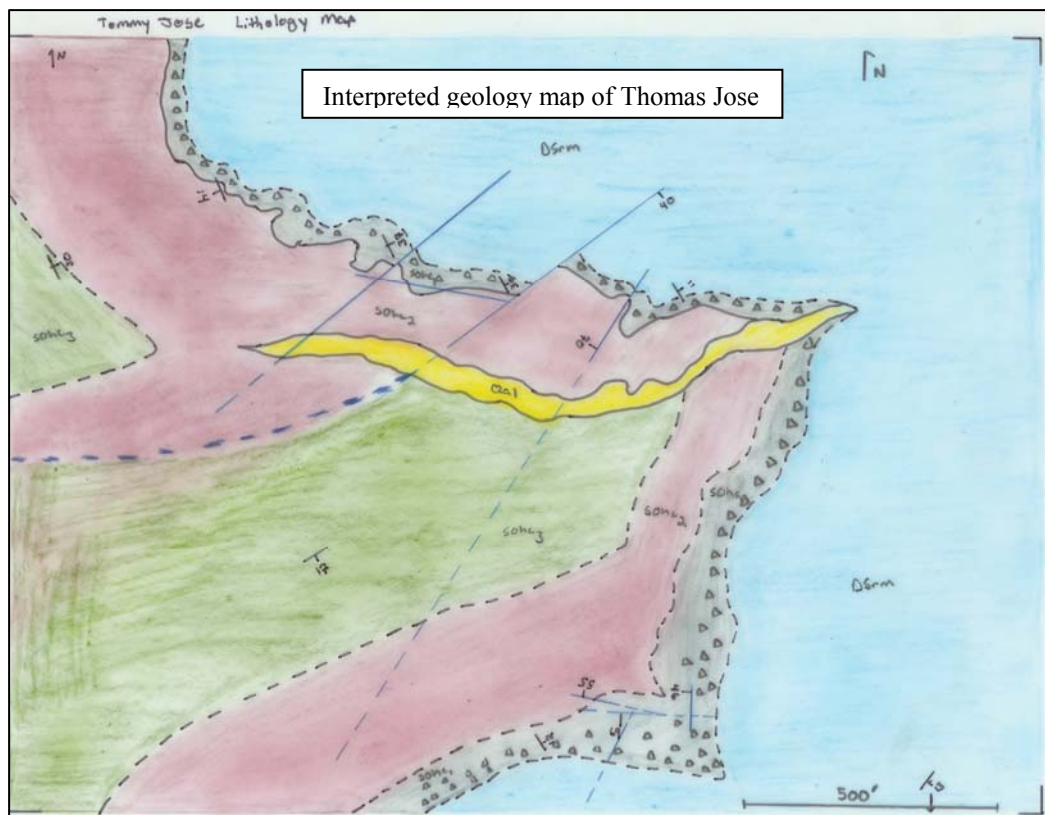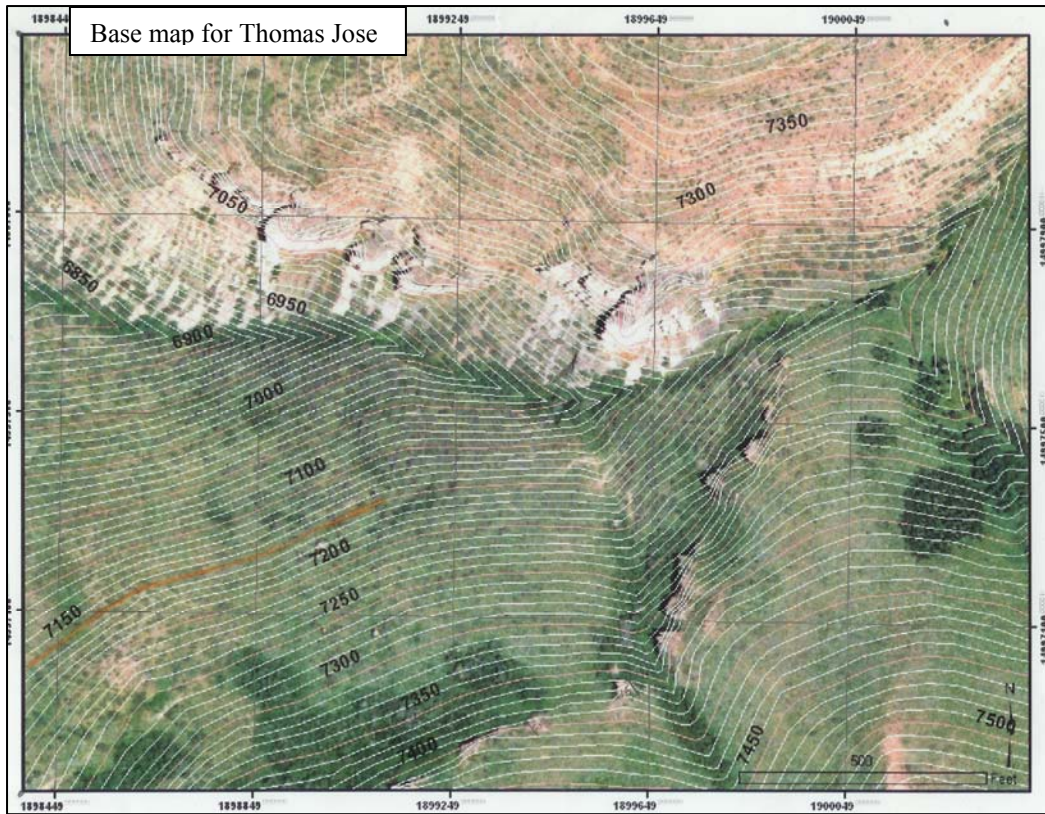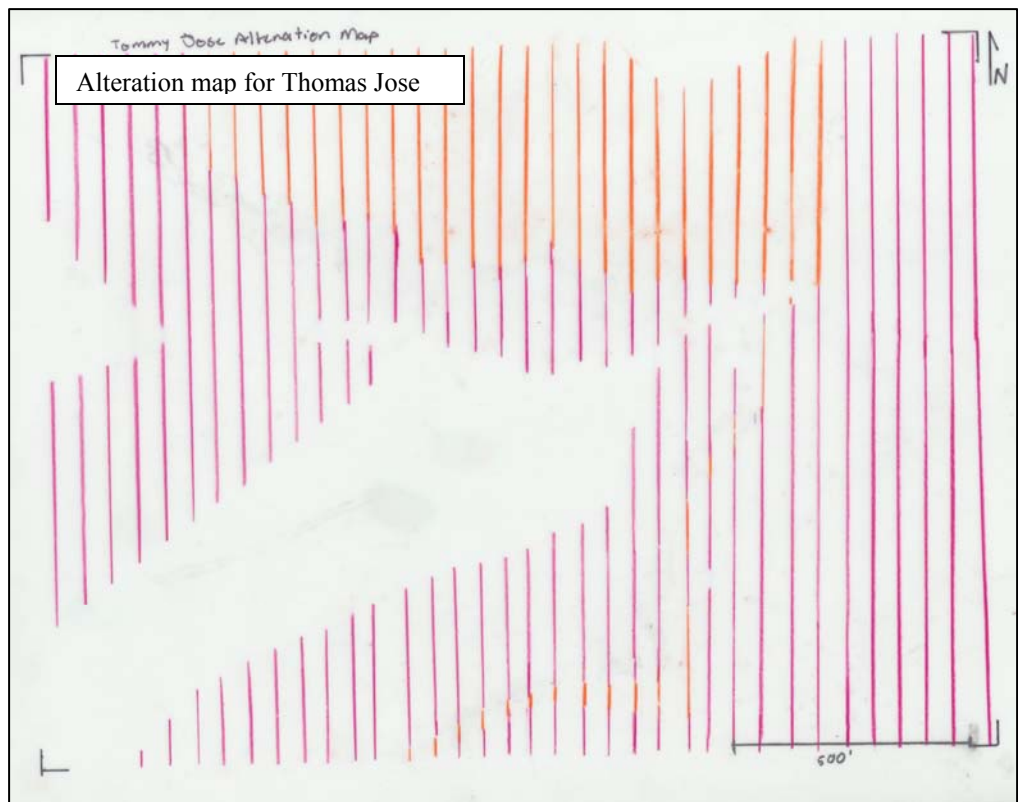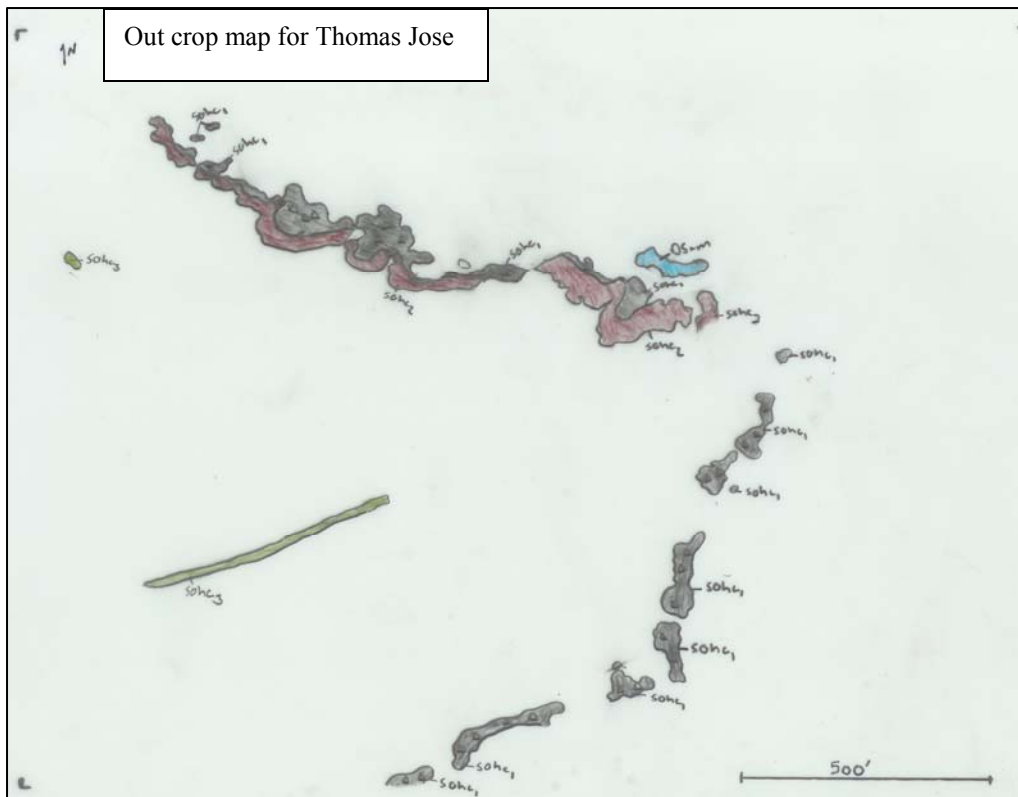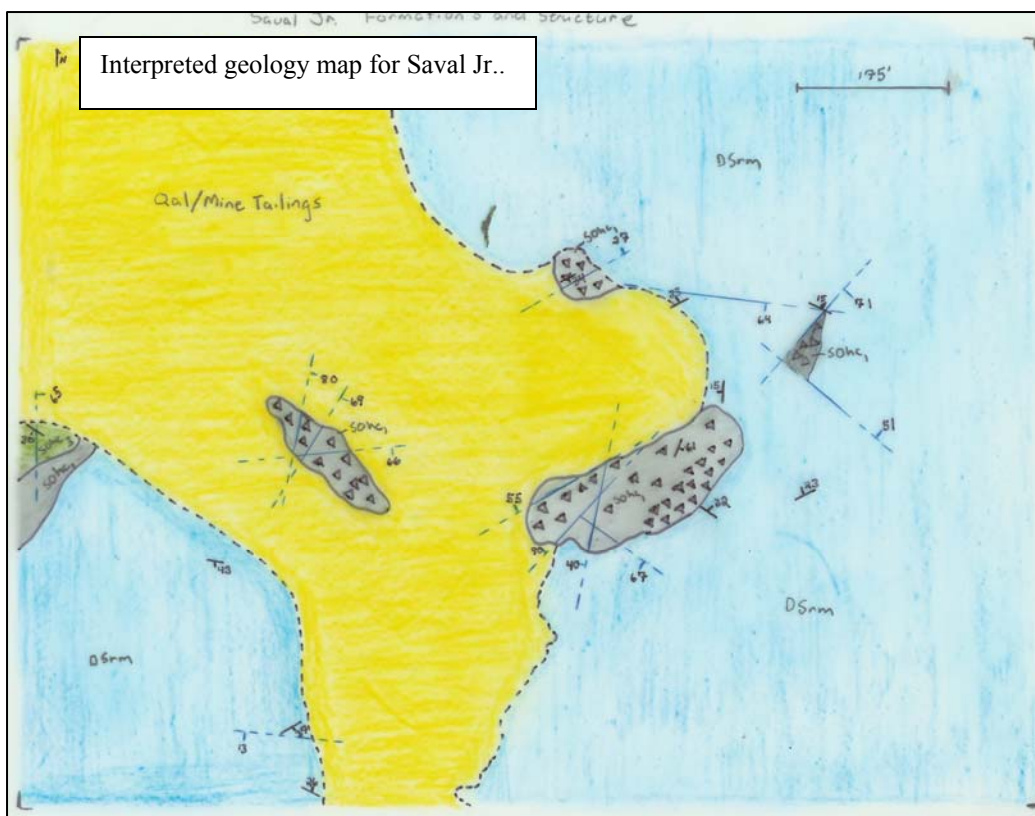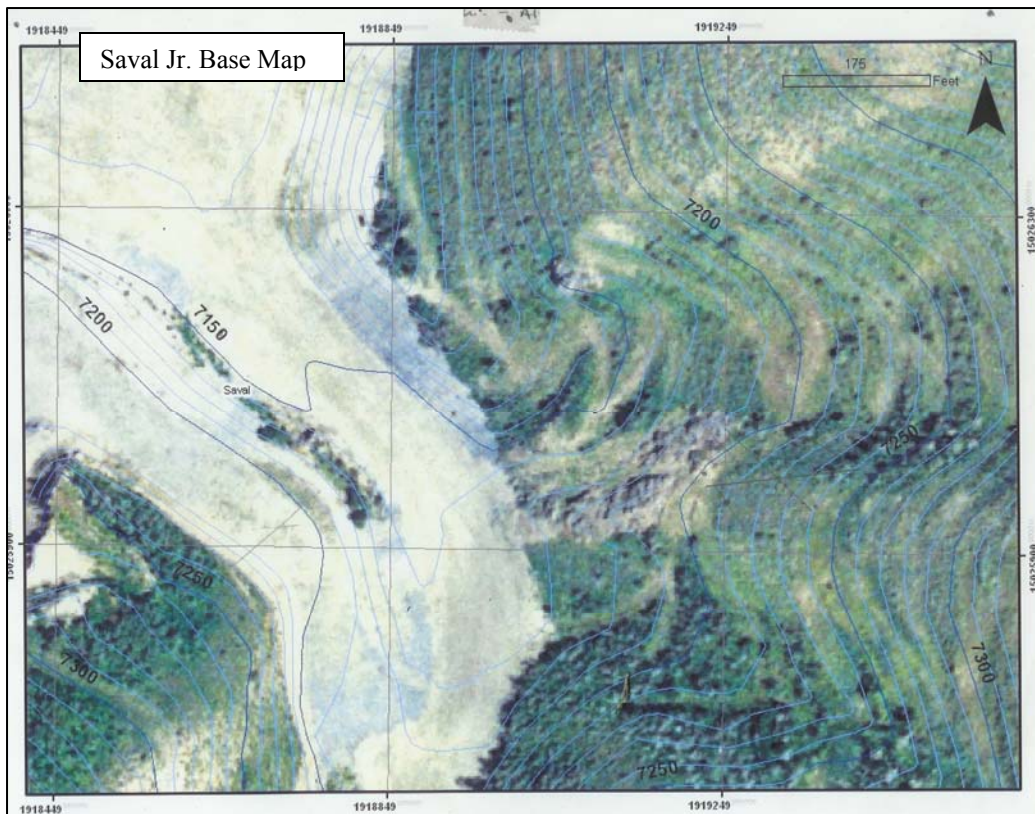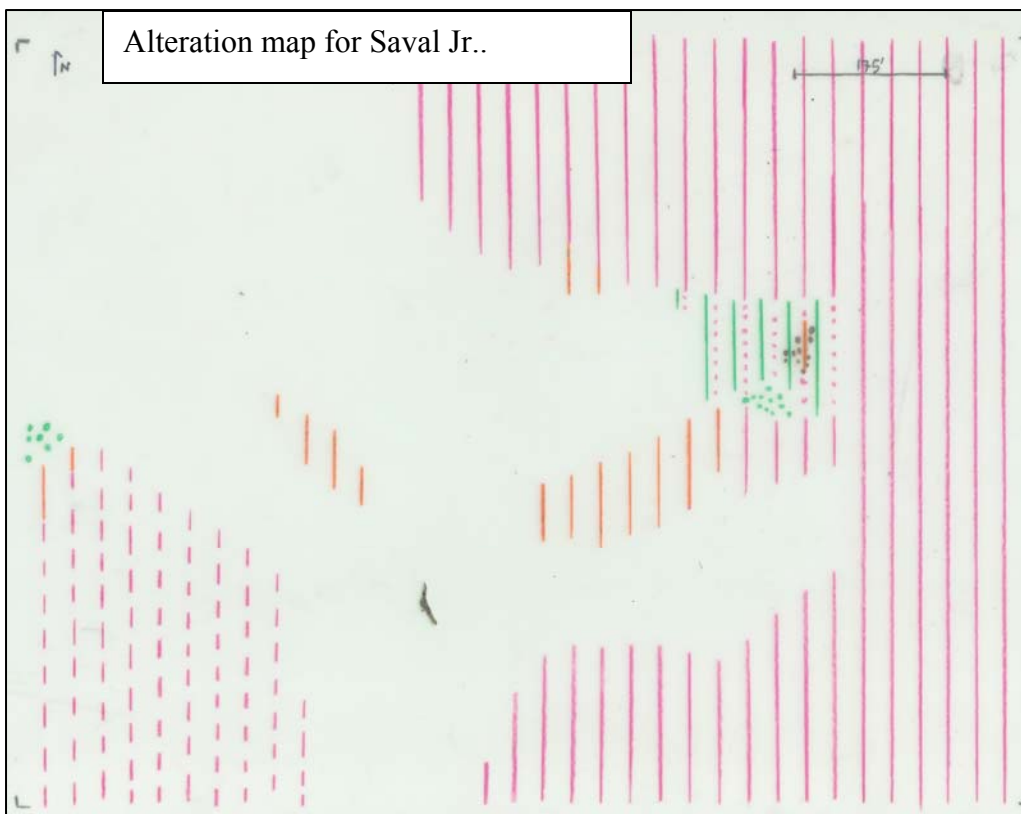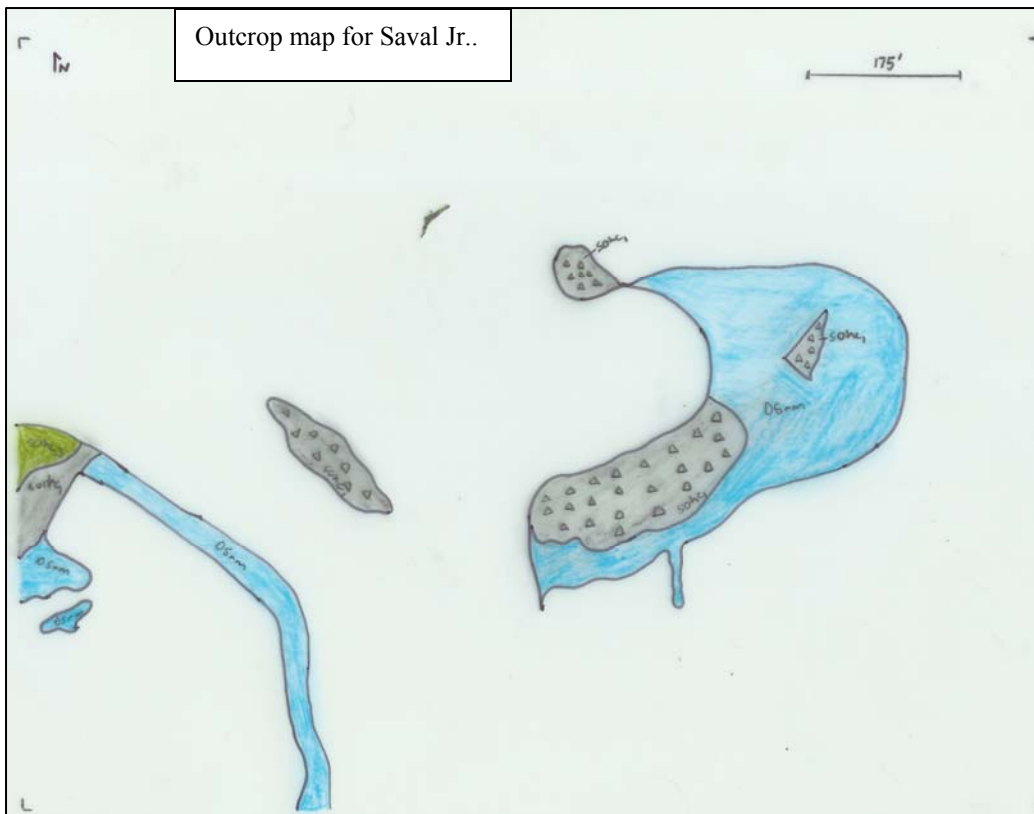
Appendix 2: Samples used to establish background geochemical concentrations.

Sample	Au ppb	Al %	Sb ppm	As ppm	Ba ppm	Be ppm	Bi ppm	B ppm	Cd ppm	Ca %	Cr ppm	Co ppm	Cu ppm	Ga ppm	Ge ppm	Fe %	La ppm	Pb ppm	Mg %
BB-1008	2.50	0.48	2.50	7.40	130.00	0.55	0.07	5.00	2.72	11.15	64.00	5.00	24.20	1.20	0.05	1.27	5.00	8.00	5.60
BB-1154	2.50	0.34	1.90	6.20	810.00	0.90	0.07	5.00	0.22	7.63	44.00	4.60	12.60	1.10	0.05	0.92	5.00	4.00	4.12
BB-800	2.50	0.24	1.10	5.20	180.00	0.35	0.06	5.00	0.54	11.30	56.00	5.80	14.60	0.70	0.05	1.33	5.00	1.00	4.36
BB-875	2.50	0.11	1.30	7.20	274.40	0.30	0.03	5.00	0.84	13.65	3.00	5.30	10.60	0.25	0.03	1.07	8.40	5.20	6.73
BI-024	2.50	0.09	13.00	6.00	1190.00	0.15	0.02	5.00	0.08	15.00	4.00	4.00	12.60	0.30	0.05	0.55	5.00	8.00	0.28
CM-083A	2.50	0.02	0.30	1.00	30.00	0.05	0.05	5.00	0.10	15.00	26.00	0.40	2.00	0.05	0.05	0.07	5.00	1.00	9.74
CM-112	2.50	0.17	0.70	1.00	80.00	0.25	0.02	5.00	0.01	15.00	5.00	4.80	7.40	0.50	0.05	0.86	5.00	14.00	1.46
CM-320	2.50	0.15	0.60	1.00	150.00	0.40	0.04	5.00	0.02	15.00	6.00	3.80	8.80	0.50	0.05	0.69	5.00	12.00	1.88
CM-335	2.50	0.08	1.30	2.00	100.00	0.20	0.05	5.00	0.58	15.00	18.00	1.80	8.40	0.50	0.05	0.25	5.00	2.00	1.45
GH-238	2.50	0.32	2.80	8.80	230.00	0.65	0.06	5.00	1.86	6.69	15.00	5.20	19.40	0.80	0.05	1.17	5.00	6.00	3.57
GH-337	2.50	2.83	0.40	2.60	120.00	0.70	0.19	5.00	0.26	4.87	42.00	14.00	14.80	5.70	0.05	3.14	10.00	2.00	2.44
GH-367	2.50	0.09	1.10	1.00	130.00	0.25	0.01	5.00	0.02	15.00	0.00	3.00	5.00	0.30	0.05	0.54	10.00	1.00	2.41
GH-424	2.50	0.22	0.65	7.40	103.40	0.15	0.05	5.00	0.08	11.30	13.00	3.30	36.60	0.60	0.03	0.76	13.40	4.60	2.85
GH-577	2.50	0.15	2.50	7.60	170.00	0.30	0.05	5.00	0.44	12.70	21.00	2.60	23.00	0.40	0.05	1.05	5.00	2.00	5.26
GH-578	2.50	0.24	2.00	1.00	80.00	0.60	0.06	5.00	0.46	15.00	26.00	2.20	20.20	1.00	0.05	0.62	10.00	6.00	3.58
GH-584	2.50	0.30	1.60	6.00	70.00	0.65	0.01	5.00	0.44	15.00	25.00	3.40	32.20	1.00	0.05	1.04	10.00	1.00	4.35
GH-585	2.50	0.28	1.20	9.00	90.00	0.45	0.07	5.00	0.44	13.85	28.00	2.80	24.80	0.90	0.05	0.92	10.00	1.00	5.06
GH-597	2.50	0.26	3.30	2.00	90.00	0.50	0.05	5.00	0.38	15.00	19.00	2.40	15.40	0.90	0.05	0.69	10.00	6.00	3.92
GH-601	2.50	0.20	4.60	2.00	60.00	0.45	0.01	5.00	0.44	15.00	15.00	2.40	19.00	0.70	0.05	0.58	10.00	1.00	3.47
GH-621C	2.50	0.11	3.00	8.00	450.00	0.20	0.04	5.00	0.24	15.00	7.00	1.80	8.60	0.30	0.05	0.41	5.00	1.00	3.38
GH-683C	2.50	0.32	4.10	7.60	80.00	0.35	0.05	5.00	0.12	10.20	54.00	2.40	9.40	0.70	0.05	0.69	5.00	1.00	4.81
GH-687	2.50	1.98	1.20	4.40	170.00	0.40	0.10	5.00	1.04	5.66	94.00	19.00	51.80	4.60	0.05	3.71	10.00	4.00	2.53
GH-690	2.50	0.01	0.10	2.00	320.00	0.15	0.01	5.00	0.02	15.00	22.00	1.00	9.40	0.05	0.05	0.09	5.00	4.00	0.41
GH-704	2.50	0.44	1.90	8.40	240.00	0.55	0.06	5.00	1.44	8.23	37.00	5.00	14.00	1.10	0.05	0.89	10.00	6.00	3.31
GH-728	2.50	0.28	1.50	1.00	170.00	0.25	0.04	5.00	0.24	15.00	26.00	2.20	10.00	0.60	0.05	0.56	5.00	1.00	4.36
GH-858A	2.50	0.09	3.40	10.00	110.00	0.30	0.03	5.00	0.34	15.00	23.00	2.20	11.20	0.30	0.05	0.44	5.00	50.00	3.99
GH-902	2.50	0.55	7.80	6.00	430.00	0.60	0.08	5.00	0.76	15.00	46.00	2.80	23.20	1.50	0.05	0.77	10.00	6.00	4.09
GH-909	2.50	0.30	8.40	5.60	30.00	0.30	0.05	5.00	0.32	8.66	60.00	2.80	11.80	0.60	0.05	0.81	5.00	1.00	3.23
GH-934C	2.50	0.32	2.20	5.00	80.00	0.35	0.05	5.00	0.20	10.10	94.00	2.40	13.80	0.70	0.05	0.73	5.00	1.00	5.49
GR-078	2.50	0.22	4.20	6.60	130.00	0.35	0.06	5.00	0.32	12.30	46.00	2.60	14.20	0.70	0.05	0.64	10.00	1.00	5.12
GR-095	2.50	0.26	1.90	5.20	200.00	0.50	0.06	5.00	2.42	10.85	30.00	3.80	14.80	0.70	0.05	1.00	5.00	6.00	4.48
GR-165	2.50	0.36	2.20	6.60	430.00	0.65	0.08	5.00	1.92	10.80	47.00	4.60	12.00	1.00	0.05	1.06	10.00	4.00	4.33
GR-266	2.50	0.37	1.50	8.40	210.00	0.60	0.06	5.00	1.86	9.97	56.00	4.80	16.60	0.90	0.05	1.04	5.00	8.00	4.14
GR-272	2.50	0.30	1.00	3.00	260.00	0.45	0.06	5.00	0.88	8.28	26.00	3.80	10.60	0.80	0.05	0.79	5.00	10.00	3.72
GR-286	2.50	0.23	3.60	6.40	240.00	0.40	0.06	5.00	3.42	12.55	28.00	3.80	15.80	0.60	0.05	0.98	10.00	6.00	5.00
GR-295C	2.50	0.21	2.40	2.80	170.00	0.40	0.06	5.00	0.34	13.30	41.00	3.80	17.20	0.50	0.05	0.91	10.00	4.00	4.82
GR-300	2.50	0.09	3.30	1.00	190.00	0.25	0.03	5.00	0.22	15.00	29.00	5.00	9.20	0.20	0.05	0.39	5.00	2.00	3.08
HC-039	2.50	0.23	3.10	8.80	295.40	0.15	0.06	5.00	1.48	7.30	8.00	6.40	17.60	0.65	0.03	1.10	7.20	8.80	3.30
LM-023	2.50	0.36	2.50	4.00	60.00	0.60	0.06	5.00	0.40	6.57	23.00	3.80	14.80	0.80	0.05	1.07	5.00	6.00	3.73
LM-084	2.50	0.53	4.55	8.10	107.40	0.60	0.04	5.00	0.10	13.45	30.00	1.90	6.60	1.50	0.03	0.40	32.40	4.20	5.23
LM-089	2.50	0.21	4.85	7.90	68.40	0.25	0.04	5.00	0.24	12.30	36.00	1.80	6.00	0.60	0.03	0.55	7.20	4.20	4.88
NF-704	2.50	0.07	2.25	1.00	117.80	0.50	0.03	5.00	0.45	15.00	13.00	2.50	2.80	0.30	0.05	0.21	10.20	4.40	2.63
NF-921	2.50	0.56	4.60	1.00	373.80	0.80	0.09	30.00	3.33	15.00	47.00	3.90	13.00	3.30	0.03	0.38	73.40	12.00	2.87
NF-942	2.50	0.29	2.95	1.00	83.40	0.40	0.07	5.00	0.43	15.00	48.00	2.90	14.60	1.10	0.03	0.54	21.40	6.20	3.91
NG-1051	2.50	0.24	12.50	8.00	40.00	0.60	0.10	5.00	5.98	15.00	22.00	4.40	38.60	1.30	0.05	0.83	10.00	8.00	4.60
PC-064	2.50	0.12	2.30	7.40	120.00	0.30	0.03	5.00	0.36	10.75	25.00	1.80	6.00	0.20	0.05	0.46	5.00	2.00	6.47
PC-120	2.50	0.11	2.05	8.10	207.60	0.30	0.04	5.00	0.32	13.75	12.00	2.80	8.00	0.35	0.03	0.42	7.00	5.00	8.62
PC-133	2.50	0.43	1.50	9.60	160.00	0.20	0.03	5.00	0.30	8.87	36.00	2.00	6.80	0.90	0.05	0.52	5.00	1.00	5.08
RC-052	2.50	0.15	1.10	6.20	244.40	0.20	0.05	5.00	0.66	12.65	34.00	3.20	14.40	0.55	0.03	0.72	9.60	5.40	3.05
SC-556	2.50	0.21	2.50	9.00	220.00	0.20	0.05	5.00	0.24	10.70	22.00	2.20	10.00	0.50	0.05	0.48	5.00	1.00	5.27
SC-053	2.50	0.19	1.90	6.00	110.00	0.25	0.03	5.00	0.90	15.00	9.00	1.80	12.00	0.60	0.05	0.43	5.00	8.00	3.69
SC-494	2.50	0.09	0.90	1.00	210.00	0.40	0.03	5.00	0.01	15.00	0.00	4.00	7.80	0.30	0.05	0.63	5.00	1.00	0.69
SC-551	2.50	0.16	1.30	1.00	170.00	0.15	0.02	5.00	0.04	15.00	15.00	2.40	5.60	0.30	0.05	0.52	5.00	1.00	1.23
SC-692	2.50	0.12	1.10	6.00	90.00	0.10	0.03	5.00	0.02	15.00	3.00	3.60	8.00	0.30	0.05	0.54	5.00	1.00	1.09
SC-697	2.50	0.28	2.45	6.60	224.60	0.55	0.05	5.00	1.38	11.70	13.00	3.10	9.40	0.85	0.03	0.75	11.00	6.00	4.99
SC-885	2.50	0.33	5.50	8.80	500.00	0.30	0.04	5.00	0.26	14.10	11.00	2.00	13.80	0.70	0.05	0.45	5.00	2.00	4.95
SC-908	2.50	0.44	5.70	6.00	130.00	0.55	0.15	5.00	8.94	15.00	25.00	3.40	35.20	1.80	0.05	0.42	10.00	10.00	3.11
SP-013	2.50	0.03	0.60	7.60	390.00	0.25	0.01	5.00	0.10	7.44	110.00	0.50	3.20	0.10	0.05	0.29	5.00	1.00	4.16
SP-093	2.50	0.29	1.00	9.80	160.00	0.25	0.02	5.00	0.40	11.50	59.00	1.00	15.00	0.80	0.05	0.51	10.00	1.00	4.71
SP-133	2.50	0.20	2.10	8.00	560.00	0.25	0.04	5.00	0.20	15.00	28.00	3.00	8.40	0.60	0.05	0.93	5.00	10.00	3.24
SP-742	2.50	0.32	2.20	8.20	100.00	0.35	0.05	5.00	2.36	4.86	95.00	5.40	43.60	1.00	0.05	1.65	5.00	6.00	1.74
SS-202	2.50	0.03	1.30	2.00	240.00	0.05	0.01	5.00	0.02	15.00	22.00	1.00	2.00	0.10	0.05	0.10	5.00	4.00	0.60
SS-542	2.50	0.04	1.80	8.00	580.00	0.05	0.01	5.00	0.02	15.00	12.00	1.20	3.60	0.10	0.05	0.09	5.00	4.00	1.45
TJ-059	2.50	0.15	1.30	9.20	2390.00	0.15	0.01	5.00	0.28	12.55	25.00	2.00	8.80	0.10	0.05	0.29	5.00	4.00	7.79
TJ-093	2.50	0.09	1.80	7.00	440.00	0.20	0.03	5.00	0.26	13.30	25.00	1.80	7.20	0.20	0.05	0.34	5.00	10.00	8.41
TJ-097	2.50	0.11	1.20	5.60	250.00	0.25	0.01	5.00	0.64	13.90	13.00	1.20	18.80	0.40	0.05	0.28	10.00	10.00	8.66
TJ-100	2.50	0.12	1.80	6.80	160.00	0.20	0.01	5.00	0.60	11.80	36.00	1.60	7.40	0.50	0.05	0.28	10.00	2.00	7.67
WC-037	2.50	0.02	0.60	1.00	360.00	0.10	0.01	5.00	0.04	15.00	0.00	1.20	2.40	0.10	0.05	0.09	5.00	1.00	4.39
WC-273	2.50	0.15	0.05	1.00	60.00	0.35	0.02	5.00	0.06	15.00	4.00	3.40	6.00	0.40	0.05	0.55	5.00	6.00	2.09
WC-382	2.50	0.47	0.70	6.50	440.60	0.15	0.05	10.00	0.37	10.25	58.00	2.30	18.00	1.80	0.03	0.53	8.60	4.00	4.52
WC-445	2.50	0.48	0.80	8.60	40.00	0.70	0.07	5.00	0.32	14.10	37.00	3.40	27.60	1.60	0.05	0.69	10.00	2.00	5.14
WC-495A	2.50	0.28	2.30	8.00	950.00	0.40	0.05	20.00	0.40	15.00	36.00	2.00	21.80	0.70	0.05	0.67	10.00	12.00	4.29
WH-008	2.50	0.29	4.10	8.20	75.60	0.40	0.06	5.00	1.13	7.70	45.00	5.00	11.60	0.80	0.03	0.99	11.40	8.00	3.59
WP-005	2.50	0.17	1.10	1.00	530.00	0.10	0.01	5.00	1.14	15.00	24.00	2.80	11.40	0.50	0.05	0.42	10.00	1.00	1.01
WT-075	2.50	0.17	3.30	6.00	110.00	0.30	0.04	5.00	2.46	15.00	9.00	2.20	8.40	0.40	0.05	0.54	10.00	8.00	3.91
WT-126	2.50	0.61	0.95	3.90	126.20	0.50	0.07	5.00	0.99	10.45	32.00	3.70	13.60	1.70	0.03	0.86	15.20	6.00	3.64
WT-131	2.50	0.14	5.40	1.00	90.00	0.15	0.03	10.00	4.82	15.00	8.00	2.20	27.20	0.40	0.05	0.60	10.00	2.00	3.46
WW-224	2.50	0.26	3.40	8.00	540.00	0.30	0.07	5.00	0.30	11.05	26.00	2.80	13.60	0.70	0.05	0.69	5.00	4.00	4.82
WW-309	2.50	0.15	3.90	1.00	260.00	0.15	0.03	5.00	0.02	15.00	5.00	3.20	3.40	0.30	0.05	0.63	5.00	26.00	1.64
Average Values	2.50	0.29	2.58	5.37	258.01	0.35	0.05	5.63	0.87	12.53	29.58	3.33	14.17	0.80	0.05	0.72	8.63	5.46	3.96

Sample	Mn ppm	Hg ppm	Mo ppm	Ni ppm	P ppm	K %	Sc ppm	Se ppm	Ag ppm	Na %	Sr ppm	S %	Te ppm	Tl ppm	Ti %	W ppm	U ppm	V ppm	Zn ppm
BB-1008	170.00	0.27	10.00	25.00	2290.00	0.24	3.00	4.00	0.52	0.01	183.00	0.69	0.03	0.02	0.01	0.05	4.95	89.00	222.00
BB-1154	195.00	0.45	1.40	17.00	250.00	0.19	3.00	1.00	0.02	0.01	73.00	0.04	0.03	0.20	0.01	0.25	0.75	11.00	74.00
BB-800	240.00	0.14	11.60	22.00	300.00	0.13	3.00	1.50	0.08	0.01	199.00	0.87	0.05	0.16	0.01	0.05	2.50	16.00	56.00
BB-875	610.00	0.16	1.70	26.50	190.00	0.08	3.10	0.40	0.01	0.01	255.00	0.05	0.02	0.24	0.01	0.05	1.35	4.00	46.00
BI-024	240.00	0.13	0.80	5.00	200.00	0.05	0.50	0.25	0.02	0.01	1600.00	0.03	0.15	0.08	0.01	0.15	0.35	3.00	18.00
CM-083A	110.00	0.36	0.20	0.50	420.00	0.01	0.50	0.25	0.01	0.01	133.00	0.01	0.03	0.18	0.01	0.05	0.50	1.00	8.00
CM-112	275.00	0.12	0.40	6.00	220.00	0.15	0.50	0.25	0.01	0.01	1925.00	0.36	0.10	0.10	0.01	0.15	0.25	2.00	24.00
CM-320	265.00	0.24	0.60	5.00	200.00	0.13	0.50	0.25	0.01	0.01	1425.00	0.33	0.05	0.06	0.01	0.05	0.40	3.00	20.00
CM-335	45.00	0.34	6.40	8.00	1070.00	0.05	1.00	0.50	0.10	0.01	196.00	0.23	0.05	0.10	0.01	0.80	5.15	25.00	36.00
GH-238	155.00	0.54	3.40	19.00	450.00	0.19	2.00	2.50	0.36	0.01	70.00	0.68	0.03	0.10	0.01	0.25	1.25	36.00	82.00
GH-337	680.00	0.16	1.20	31.00	430.00	0.13	3.00	0.50	0.06	0.01	210.00	0.15	0.03	0.10	0.01	0.10	0.35	32.00	90.00
GH-367	190.00	0.32	0.60	6.00	190.00	0.07	0.50	0.25	0.01	0.01	1175.00	0.45	0.03	0.02	0.01	0.05	0.30	3.00	12.00
GH-424	120.00	0.20	0.85	14.50	930.00	0.14	2.20	1.20	0.08	0.01	176.40	0.56	0.01	0.06	0.01	0.50	0.90	7.00	42.00
GH-577	95.00	0.64	2.40	22.00	350.00	0.10	1.00	4.00	0.48	0.01	158.00	0.85	0.03	0.12	0.01	0.50	0.95	18.00	46.00
GH-578	80.00	0.29	8.00	24.00	6860.00	0.12	0.50	2.50	0.24	0.01	261.00	0.55	0.03	0.08	0.01	0.25	6.35	62.00	56.00
GH-584	100.00	0.63	5.00	33.00	4090.00	0.15	2.00	3.00	0.52	0.01	199.00	0.86	0.03	0.02	0.01	0.40	3.90	36.00	84.00
GH-585	85.00	0.40	3.20	25.00	3790.00	0.14	1.00	3.50	0.44	0.01	197.00	0.85	0.03	0.12	0.01	0.15	4.25	36.00	90.00
GH-597	80.00	0.45	11.00	26.00	8080.00	0.13	0.50	2.50	0.16	0.01	249.00	0.58	0.03	0.16	0.01	0.40	13.30	43.00	88.00
GH-601	70.00	0.46	5.80	25.00	4020.00	0.10	1.00	2.50	0.46	0.01	237.00	0.62	0.03	0.02	0.01	0.35	3.70	39.00	70.00
GH-621C	75.00	0.30	9.00	15.00	1680.00	0.05	1.00	1.50	0.14	0.01	242.00	0.41	0.03	0.14	0.01	0.30	2.45	27.00	48.00
GH-683C	140.00	0.44	4.20	8.00	1860.00	0.14	3.00	0.50	0.16	0.01	64.00	0.62	0.03	0.10	0.01	0.30	1.75	15.00	30.00
GH-687	645.00	0.21	5.40	82.00	1750.00	0.17	5.00	2.50	0.20	0.01	185.00	0.75	0.03	0.12	0.01	0.20	2.20	81.00	148.00
GH-690	65.00	0.11	1.20	3.00	310.00	0.01	0.50	0.25	0.01	0.01	357.00	0.06	0.05	0.01	0.01	0.50	2.60	4.00	8.00
GH-704	150.00	0.34	2.60	14.00	540.00	0.25	2.00	2.00	0.44	0.01	117.00	0.65	0.03	0.06	0.01	0.55	1.65	36.00	80.00
GH-728	95.00	0.41	4.20	9.00	850.00	0.16	1.00	0.50	0.14	0.01	180.00	0.51	0.03	0.08	0.01	0.40	1.55	15.00	46.00
GH-858A	95.00	0.16	8.80	15.00	1390.00	0.06	1.00	1.50	0.20	0.01	249.00	0.46	0.03	0.08	0.01	0.45	2.75	23.00	68.00
GH-902	125.00	0.43	10.00	30.00	7100.00	0.22	1.00	3.50	0.44	0.01	243.00	0.78	0.03	0.10	0.01	0.90	5.95	77.00	94.00
GH-909	120.00	0.26	2.20	12.00	730.00	0.17	3.00	2.00	0.14	0.01	31.00	0.65	0.03	0.06	0.01	1.10	0.85	18.00	66.00
GH-934C	95.00	0.38	2.60	15.00	140.00	0.18	2.00	2.00	0.26	0.01	70.00	0.69	0.03	0.06	0.01	0.20	0.70	16.00	76.00
GR-078	110.00	0.40	4.60	13.00	1930.00	0.11	2.00	1.50	0.24	0.01	127.00	0.54	0.03	0.10	0.01	0.55	3.05	13.00	54.00
GR-095	165.00	0.16	5.20	18.00	630.00	0.17	3.00	3.00	0.36	0.01	163.00	0.58	0.03	0.06	0.01	0.15	1.85	29.00	124.00
GR-165	180.00	0.14	3.40	17.00	1430.00	0.20	2.00	3.00	0.42	0.01	150.00	0.65	0.05	0.12	0.01	0.35	2.30	37.00	110.00
GR-266	230.00	0.16	7.60	21.00	410.00	0.18	4.00	0.50	0.16	0.01	116.00	0.70	0.03	0.04	0.01	0.10	1.60	45.00	116.00
GR-272	170.00	0.14	4.40	13.00	250.00	0.16	3.00	0.25	0.04	0.01	126.00	0.54	0.03	0.08	0.01	0.15	1.10	14.00	64.00
GR-286	110.00	0.12	3.80	22.00	2490.00	0.14	2.00	5.00	0.86	0.01	196.00	0.87	0.05	0.06	0.01	0.10	3.05	45.00	156.00
GR-295C	120.00	0.13	2.00	20.00	1260.00	0.16	2.00	3.00	0.36	0.01	190.00	0.70	0.03	0.06	0.01	0.03	1.40	16.00	110.00
GR-300	65.00	0.14	8.00	15.00	490.00	0.05	0.50	0.50	0.10	0.01	269.00	0.36	0.03	0.08	0.01	0.50	2.05	26.00	22.00
HC-039	125.00	0.24	51.34	59.00	230.00	0.14	3.80	3.80	0.01	0.02	120.90	0.93	0.06	0.24	0.01	0.05	3.25	59.00	236.00
LM-023	305.00	0.09	1.00	10.00	310.00	0.12	1.00	0.50	0.12	0.01	90.00	0.28	0.03	0.04	0.01	0.03	0.70	12.00	50.00
LM-084	85.00	0.29	2.65	12.00	8580.00	0.28	1.90	0.60	0.08	0.01	182.30	0.41	0.02	0.10	0.01	0.25	5.55	9.00	8.00
LM-089	160.00	0.15	0.65	11.00	460.00	0.12	2.50	1.00	0.13	0.01	80.80	0.47	0.03	0.02	0.01	0.25	0.95	12.00	18.00
NF-704	110.00	0.26	3.95	28.50	150.00	0.04	1.10	0.80	0.05	0.01	328.00	0.23	0.10	0.01	0.01	0.15	4.05	35.00	38.00
NF-921	55.00	0.51	13.25	49.40	10000.00	0.32	4.80	3.00	0.24	0.05	534.00	0.46	0.10	0.02	0.01	0.15	98.00	149.00	182.00
NF-942	110.00	0.33	7.25	35.00	5930.00	0.13	2.80	2.20	0.23	0.01	182.60	0.61	0.08	0.02	0.01	0.40	5.70	52.00	48.00
NG-1051	115.00	1.34	48.40	71.00	2510.00	0.13	3.00	4.50	0.72	0.01	204.00	0.96	0.05	0.02	0.01	0.75	27.40	298.00	688.00
PC-064	110.00	0.17	6.00	13.00	150.00	0.07	1.00	0.50	0.12	0.01	67.00	0.46	0.03	0.06	0.01	0.25	1.90	37.00	44.00
PC-120	95.00	0.13	11.50	29.00	170.00	0.06	2.40	0.60	0.06	0.02	128.30	0.32	0.04	0.02	0.01	0.20	2.20	35.00	68.00
PC-133	145.00	0.26	6.00	12.00	360.00	0.21	1.00	0.50	0.14	0.01	56.00	0.48	0.03	0.08	0.01	0.25	1.80	32.00	32.00
RC-052	125.00	0.01	9.55	22.00	950.00	0.10	2.30	1.80	0.31	0.01	217.00	0.60	0.03	0.10	0.01	0.15	3.40	16.00	54.00
SC-556	80.00	0.28	3.80	10.00	730.00	0.14	1.00	1.00	0.12	0.01	124.00	0.46	0.03	0.14	0.01	0.45	2.10	12.00	32.00
SC-053	90.00	1.04	4.60	12.00	530.00	0.12	1.00	1.50	0.34	0.01	220.00	0.53	0.05	0.14	0.01	0.20	2.25	34.00	48.00
SC-494	235.00	0.24	0.20	6.00	190.00	0.07	1.00	0.25	0.01	0.01	1510.00	0.03	0.03	0.10	0.01	0.05	0.30	2.00	12.00
SC-551	180.00	0.33	0.80	3.00	230.00	0.11	0.50	0.25	0.01	0.01	1630.00	0.37	0.03	0.06	0.01	0.20	0.35	2.00	12.00
SC-692	205.00	0.57	0.40	6.00	180.00	0.10	1.00	0.25	0.01	0.01	1475.00	0.20	0.03	0.12	0.01	0.15	0.25	2.00	16.00
SC-697	120.00	0.51	2.90	17.00	1480.00	0.16	2.80	3.80	0.49	0.01	153.20	0.61	0.07	0.12	0.01	0.15	1.50	41.00	66.00
SC-885	85.00	0.24	3.20	8.00	340.00	0.22	1.00	0.50	0.14	0.01	168.00	0.47	0.03	0.08	0.01	0.30	1.50	14.00	34.00
SC-908	70.00	0.84	8.80	22.00	8670.00	0.23	1.00	7.50	0.88	0.01	273.00	0.54	0.15	0.20	0.01	0.30	18.60	118.00	316.00
SP-013	345.00	0.13	1.40	8.00	370.00	0.01	0.50	0.00	0.01	0.01	68.00	0.02	0.03	0.05	0.01	0.25	0.90	13.00	16.00
SP-093	90.00	0.54	3.00	16.00	1890.00	0.14	1.00	0.00	0.26	0.03	105.00	0.18	0.05	0.10	0.01	0.03	3.15	29.00	74.00
SP-133	290.00	0.54	2.00	11.00	300.00	0.13	2.00	0.00	0.04	0.01	1040.00	0.45	0.03	0.20	0.01	0.05	3.70	6.00	40.00
SP-742	395.00	0.49	8.80	29.00	2150.00	0.16	2.00	4.50	0.64	0.01	138.00	0.81	0.05	0.06	0.01	0.10	2.50	45.00	214.00
SS-202	25.00	0.02	0.20	3.00	1800.00	0.02	0.50	0.25	0.01	0.01	674.00	0.01	0.05	0.01	0.01	0.45	0.45	1.00	2.00
SS-542	25.00	0.15	0.10	1.00	1270.00	0.02	0.50	0.25	0.01	0.01	845.00	0.01	0.05	0.01	0.01	0.30	0.40	2.00	2.00
TJ-059	125.00	0.18	4.60	16.00	120.00	0.08	1.00	0.25	0.20	0.01	176.00	0.08	0.03	0.12	0.01	0.55	1.00	22.00	60.00
TJ-093	100.00	0.10	6.40	13.00	160.00	0.05	1.00	0.25	0.14	0.01	109.00	0.35	0.03	0.02	0.01	0.65	1.95	24.00	24.00
TJ-097	110.00	0.23	4.40	12.00	1720.00	0.05	1.00	0.25	0.14	0.01	109.00	0.01	0.03	0.06	0.01	0.25	2.65	62.00	74.00
TJ-100	75.00	0.20	6.20	14.00	1010.00	0.06	1.00	0.50	0.22	0.01	87.00	0.31	0.03	0.06	0.01	0.20	2.20	47.00	54.00
WC-037	80.00	0.01	0.60	0.50	80.00	0.01	0.50	0.25	0.01	0.01	186.00	0.13	0.05	0.02	0.01	0.05	1.35	1.00	8.00
WC-273	205.00	0.51	0.20	4.00	200.00	0.13	1.00	0.25	0.01	0.01	1825.00	0.39	0.05	0.02	0.01	0.03	0.40	3.00	16.00
WC-382	75.00	0.33	1.30	27.00	670.00	0.26	4.30	0.60	0.29	0.01	112.90	0.02	0.03	0.10	0.01	0.20	1.55	34.00	46.00
WC-445	75.00	0.36	2.20	31.00	3170.00	0.25	3.00	3.50	0.54	0.03	242.00	0.87	0.03	0.06	0.01	0.30	3.50	32.00	120.00
WC-495A	100.00	0.79	3.20	25.00	1150.00	0.16	3.00	1.50	0.32	0.01	148.00	0.01	0.03	0.10	0.01	0.40	1.65	40.00	108.00
WH-008	195.00	0.19	7.40	27.50	360.00	0.19	4.60	0.60	0.07	0.01	120.00	0.73	0.01	0.12	0.01	0.20	1.50	24.00	68.00
WP-005	100.00	0.18	1.80	26.00	930.00	0.06	0.50	0.50	0.14	0.01	326.00	0.04	0.03	0.06	0.01	0.15	2.40	15.00	100.00
WT-075	80.00	0.31	5.80	14.00	700.00	0.12	0.50	2.00	0.34	0.01	261.00	0.66	0.03	0.06	0.01	0.10	2.40	49.00	128.00
WT-126	135.00	0.14	1.75	27.00	1000.00	0.33	3.60	0.80	0.32	0.01	160.30	0.01	0.03	0.10	0.01	0.05	1.35	29.00	66.00
WT-131	100.00	0.33	8.40	19.00	280.00	0.10	1.00	2.50	0.48	0.01	512.00	0.55	0.03	0.02	0.01	0.10	3.65	76.00	238.00
WW-224	90.00	0.15	1.80	15.00	860.00	0.16	2.00	2.00	0.24	0.01	119.00	0.68	0.03	0.02	0.01	0.30	1.75	19.00	74.00
WW-309	230.00	0.24	0.60	6.00	200.00	0.13	0.50	0.25	0.01	0.01	1565.00	0.19	0.03	0.10	0.01	0.10	0.30	2.00	24.00
Average Values	154.56	0.31	5.34	18.52	1545.70	0.13	1.76	1.52	0.21	0.01	362.89	0.45	0.04	0.08	0.01	0.26	3.96	32.27	77.75

Appendix 3: Target grids for all elements, not presented in the thesis.

Appendix 4: Codes and criteria used by Yukon-Nevada Gold forcore and chip logging.

Queenstake Resources USA, Inc.
Jerritt Canyon Mine
JERRITT CANYON GEOLOGIC CODES

ROCK I - FORMATION

Null No Data	1 SOhcI	6 Eastern Facies	25 Om	
0 Cavity	2 SOhcII	7 DSrm	30 Mwp	
9 Alluvium/Colluvium	3 SOhcIII	10 Oe	40 Intrusive (undiff.)	
99 Dump	4 SOhcIV	16 Op	60 Tert. Volc. &	
	5 SOhcV	20 Osc	Assoc. Sed. Rxs.	

ROCK II - FORMATION

40 Intrusive (undiff.)

ROCK - LITHOLOGY

Null No Data	30 Conglomerate	40 Claystone	50 Volcanic Rocks
0 Cavity	31 Sandstone	41 Shale	(undifferentiated)
1 Alluvium/Colluvium	32 Quartzite/Quartz Arenite	42 Argillite	51 Tuff
2 Dump	33 Calcareous Sandstone	43 Chert-argillite	52 Tuffaceous Seds
10 Limestone	34 Calcareous Quartzite	44 Chert	(waterlain)
11 Micritic Limestone	35 Siltstone	45 Chert-siltstone	53 Greenstone
12 Debris Flow Limestone	36 Calcareous Siltstone	46 Siltstone-argillite	70 Intrusive
13 Silty Limestone	37 Dolomitic Siltstone	47 Claystone-argillite	(undifferentiated)
14 Cherty Limestone	38 Siliceous Siltstone	48 Chert-claystone	71 Equigranular
20 Dolomite	39 Cherty Siltstone	49 Argillite-sandstone	72 Subequigranular
23 Silty Dolomite			73 Porphyritic
24 Cherty Dolomite			
25 Wispy* bed slty ls/ls			80 Cave/karst fill
26 Wispy* bed calc sltst			
27 Wispy* bed dol'c sltst			

ALTERATION TYPE

Null Unaltered	50 Argillic Alteration (Clay: Kaol, Mont, Allophane, etc.)
10 Oxidation	60 Propylitic Alteration (Epidote, Chlorite +/- Carbonate)
20 Silicification	70 Contact Metamorphism
30 Decalcification	80 Phyllic Alteration (Quartz, Sericite, Pyrite)
40 Carbon	90 Dolomitization

VEIN / MINERAL TYPE

1 Native Gold	20 Quartz	30 Barite	50 Clay
9 Undifferentiated	21 Quartz-pyrite	31 Barite-pyrite	51 Kaolinite
10 Calcite	22 Quartz-realgar	32 Barite-sphalerite	52 Kaolinite-pyrite
11 Pyrite	23 Quartz-calcite	35 Alunite	
12 Marcasite	24 Quartz-dolomite	36 Jarosite	60 Fe-Ox
13 Calcite-Pyrite	25 Quartz-FeOx		61 Hematite
14 Realgar	26 Sphalerite	40 Dolomite	62 As-Ox
15 Orpiment	27 Galena	41 Dolomite-pyrite	63 Cu-Ox
16 Stibnite	28 Chalcopyrite	45 Variscite	67 Carbon
17 Cinnabar			
18 Calcite-realgar			
19 Arsenopyrite			

DEFORMATION TYPE

10 Breccia	
20 Gouge	
30 Broken/Fractured	
40 Sheared	
50 Heterolithic Breccia	

INTENSITY

		(Realgar/Orpiment)
1 Weak	{	Visible
2 Moderate	{	~ 5%
3 Strong	{	~ 10%

* Wispy, wavy, bioturbated

Lithology

42 Argillite
49 Argillite-sandstone
34 Calcareous Quartzite
33 Calcareous Sandstone
36 Calcareous Siltstone
80 Cave/karst fill
44 Chert
43 Chert-argillite
48 Chert-claystone
45 Chert-siltstone
24 Cherty Dolomite
14 Cherty Limestone
39 Cherty Siltstone
40 Claystone
47 Claystone-argillite
30 Conglomerate
12 Debris Flow Limestone
20 Dolomite
37 Dolomitic Siltstone
53 Greenstone
70 Intrusive (undiff.)
10 Limestone
11 Micritic Limestone
32 Quartzite/
Quartz Arenite
31 Sandstone
41 Shale
38 Siliceous Siltstone
35 Siltstone
46 Siltstone-argillite
23 Silty Dolomite
13 Silty Limestone
51 Tuff
52 Tuffaceous Sediments
(waterlain)
50 Volcanic Rocks
(undifferentiated)
25 Wispy bed slty ls/ls
26 Wispy bed calc sltst
27 Wispy bed dol'c sltst

Minerals

35 Alunite
19 Arsenopyrite
30 Barite
10 Calcite
67 Carbon
28 Chalcopyrite
17 Cinnabar
50 Clay
27 Galena
61 Hematite
36 Jarosite
51 Kaolinite
12 Marcasite
1 Native Gold
15 Orpiment
11 Pyrite
20 Quartz
14 Realgar
26 Sphalerite
16 Stibnite
45 Variscite

Appendix 4: Criteria used for logging alteration in the samples logged for this project, and key to logging.

Silicified Rock:

4-Intense: If silica etching produced vugs, and textures were not visible the rock was classified as intensely silicified.

3-Strong: Based off of presence of silica etching and texture destruction. If silica etching produced vugs but textures were still visible then it was strongly silicified.

2-Moderate: If the rock was harder than it should have been, had no RXN with HCl, and no silica etching it was classified as moderately silicified. In moderately silicified rocks textures were well preserved.

1-Weak: Wasn't really documented while core logging. Weakly silicified rock was where the entire rock was not silicified only portions concentrated around quartz veins.

Dolomitized Rock:

3-Strong: RXN only when scratched. Strongly dolomitized rock was when the fizz was very weak after scratch (only heard by holding the rock to my ear). Rock looks gritty, like material is missing.

2-Moderate: RXN only when scratched and took 1-3 seconds to occur. The RXN was vigorous. Rock looks gritty but there is still a decent reaction with HCl.

1-Weak: RXN was not as strong as it should have been. The rock reacted without being scratched, but the RXN was hesitant.

Decarbonatized Rock:

   3-Strong-weak to no fizz, punky very porous 60-100% clay present

   2-Moderate-Weak to moderate fizz, porous 10-60% clay present

   1-Weak-moderate to strong fizz 5-10% clay present

Oxidized Rock:

   3-Strong: More than 60% of the rock was oxidized

   2-Moderate: More than 25% but less than 60% of the rock was oxidized

   1-Weak: Less than 25% of the rock was oxidized

Core Logging Key

Silicified Rock:	Strong		Moderate		Weak
Dolomitized Rock:	Strong		Moderate		Weak
Decarbonatized Rock:	Strong		Moderate		Weak
Oxidized Rock:	Strong		Moderate		Weak

Fe Calcite Veining:

Pink Calcite Veining:

Veining with Fe calcite and pink calcite, colors drawn in the order they appear in the

veins:

No Stain Dolomite Veining:

Fe Dolomite Veining:

Quartz Veining

Mineralization:

Stibnite ●   Orpiment ●   Realgar   ●   Calcite ●   Quartz ●   Pyrite ●

Core Logging Key Continued

Faults:

Breccia:
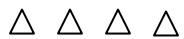
Planar Bedding DSRM

Wavy Bedding DSRM

SOHC1

SOHC2

SOHC3

SOHC4

Form 1

Hole ID: SH-280C **Project:** Sava l **Logged By:** Lucia **Start Date:** 7/20/07 **Finish Date:** 7/20/07

Depth	Lithology/Structure		Alteration/Mineralization		Veins		Estimated Percentages		
	Graphic	Description	Graphic	Description	Graphic	Description	Sulfidation		
249.5		DSRM: Finely laminated calc-siltstone medium gray Except in fault zones where it turns black/Carbonacrious Bedding planar to wavy. Wavy bedds correlate with influx of veining which correlates with fault zones In the two major faultzones the rock is very brittle & crumbled it almost looks like it has been cooked for to long Brecciation due to veining Clasts angular to subangular Stain: Blue		Strongly dolomitized Rxn only when scratched through this section. Clay is present but it seems to be argillic/ fault related because Rock still reacts moderat dolo Rxn 3-5 sec after contact w/Rx Slightly mlsic hesitant not as vigorous as it should be Mod decal no Rxn volume loss mod dolo Rxn 3-5 sec delay strong dolo Rxn only when scratched mod dolo Rxn 3-5 sec after contact Moderate oxidation limonite but w/ hematite inbetween bedding planes mod dolo weak argillic Alt		Veining moderate ave 1mm 1.5" Dominately Fe calcite veining minor pink calcite veining cutting fe calcite veining Pink calcite veining only light 1/1" be 1" wide Pink in center Fe calcite on margins (sample taken) Veins going everywhere .01mm-4cm wide only pink			
259.5									
265.5									
269.5									

Form 2

Hole ID: SH-280C **Project:** Sava l **Logged By:** Lucia **Start Date:** 7/20/07 **Finish Date:** 7/20/07

Depth	Lithology/Structure		Alteration/Mineralization		Veins		Estimated Percentages		
	Graphic	Description	Graphic	Description	Graphic	Description	Sulfidation		
		269-274.5 very broken appearing wavy bedded dark gray-black Calc-siltstone Cannot see the stain		Mod. Dolo Still Calcareous Rxn hesitant but weakly happens Weak argillic alt due to faulting		No veining from 269-274.5			
		some C_2 massive light gray to buff limestone Some bedding apparent in the last foot of the section Stain - Pink through section 2 minor areas of brecciation clasts subrounded to subangular very faint		Section weakly limonite oxidized Strong whimnoted Mod Dolo Rxn weak but Stronger when Scratched weak dolo Rxn quick but not vigorous mod dolo Rxn weak but stronger when scratched		Weak pink calcite veining Veining a little more intense Mostly Fe Calcite pink not showing up			
279.5									
TD									
89.5									

Sheet 1 of 3

Hole ID: SH-359C   Project: Saval   Logged By: Lucia   Start Date: 7/10/07   Finish Date: 7/10/07

Depth	Graphic	Lithology/Structure Description	Graphic	Alteration/Mineralization Description	Graphic	Veins Description	Sulfidation	Estimated Percentages		
298		DSRM: Finely planar laminated calc-siltstone, slightly dark to lighter gray except when oxidized then it is tan/buff. The lighter colored layers are more calcareous though it is not clear in the oxidized areas whether or not it is these layers that are oxidizing to hematite or if it is more the silty layers. Stain Blue. Small irregular chert lenses throughout section. Breccia zone associated with moderate calcite veining & fault zone		weak dolo no oxidation, mod dolo no oxidation. Intense dolo & Intense Oxidation limonite & hematite. mod dolo intense limonite. weak dolo weak oxides/limonite. weak Dolo. weak Dolo. strong dolo strong oxides limonite & hematite. mod dolo intense oxide lim & hem. weak oxide. weak Dolo/weak oxide		(Fe) Calcite veining cutting calcite veining. minor calcite veining ~1" apart. Dilation the NE vein seems to be filled around the margins of Fe dolo paragensis. Not totally clear. minor calcite veins cutting Ddis placing NW Calcite veins				
308										
318										

Sheet 2 of 3

Hole ID: SH-359C   Project: Saval   Logged By: Lucia   Start Date: 7/10/07   Finish Date: 7/10/07

Depth	Graphic	Lithology/Structure Description	Graphic	Alteration/Mineralization Description	Graphic	Veins Description	Sulfidation	Estimated Percentages		
		DSRM: Finely laminated planar calc-siltstone. Veining is really weird here this section looks a little jumbled up. Faulted contact		mod dolo mod limonite & hem. Moderate dolo & Intense oxidation mostly limonite. Intense dolo & lim minor argillic alt		Calcite veining gets irregular here, some veins look oriented but there are a whole bunch that are not towards the contact that is				
		SORC: silicified breccia chert & limestone fragments 3mm stain Blue		silicification no etching textures preserved minor oxidation		Brecciated veining or veining follows breccia				
		DSRM: laminated calc siltstone. This whole section appears to be a fault zone. Stain: Blue		Possible minor minor argillic alt & minor dol. Oxidized limonite & hematite hematite in bedding		Again veining very broken up not very continuous				
328		327.2 SORC, Brecciated Silicified chert & limestone. Clasts are angular to sub angular .1-3mm long some are large chunks of bedding that have been ripped up		Intensely silicified except for late calcite & (Fe) dolomite veins. Silica etching present leaving angular vugs		Fe dolo vein. The veins look like they are in a shot gun pattern there are very few that hold their continuity. Sample taken this one is difficult. Calcite & qtz veins scattered in matrix				
338										

Appendix 5: Sample excel sheet with data entered as it was logged for this project. These are the data that were brought into ArcMap.

Footage_Above_Below_Saval	Hole_ID	Isotope_num_Al_only	Footage_Actual	X	Y	Elevation	Formation	Lithology	Formation_2	Lithology_2	Argillic_alteration	Decalcification	Silicification	Dolomitization	Oxidation	Dolomite_Veins_NS	Fe_Dolomite_Veins	Calcite_Veins	Calcite_Veins_Pink	Fe_Calcite_Veins
0 ft - 5 ft	SC-1060		45-50	390209	409303	7184	7	36							3		y			
5 ft - 10 ft	SC-1060		50-55	390209	409303	7184	7	36							3		y			
10 ft - 15 ft	SC-1060		55-60	390209	409303	7184	7	36				1		3	3		y			
15 ft - 20 ft Assay_Int	SC-1060	75	60-65	390209	409303	7184	7	36				1		3	3		y			
20 ft - 25 ft	SC-1060		65-70	390209	409303	7184	7	36					3		2					
25 ft - 30 ft	SC-1060		70-75	390209	409303	7184	1	14					3		1					
30 ft - 35 ft	SC-1060		75-80	390209	409303	7184	2	10					3		2					
35 ft - 40 ft	SC-1060		80-85	390209	409303	7184	3	11										y		
0 ft - 5 ft	BB-1004		430-435	382479	403323	7284	7	36						2	3			y		
5 ft - 10 ft	BB-1004		435-440	382479	403323	7284	7	36						2	3			y		
10 ft - 15 ft	BB-1004		440-445	382479	403323	7284	7	36						3	3		y	y		
15 ft - 20 ft Assay_Int	BB-1004	80	445-450	382479	403323	7284	7	36				2		3	1			y		
20 ft - 25 ft	BB-1004		450-455	382479	403323	7284	1	14					3		1			y		
25 ft - 30 ft	BB-1004		455-460	382479	403323	7284	1	14	2	10			3	3			y			
30 ft - 35 ft	BB-1004		460-465	382479	403323	7284	1	14	2	10			3	3			y			
35 ft - 40 ft	BB-1004		845-850	382479	403323	7284	2	10							1			y		
0 ft - 5 ft	GH-823		850-855	383585	420209	6157	7	36				2	2							
5 ft - 10 ft	GH-823		855-860	383585	420209	6157	7	36				2	2							
10 ft - 15 ft	GH-823		860-865	383585	420209	6157	7	36				1	1							y
15 ft - 20 ft Assay_Int	GH-823	79	865-870	383585	420209	6157	7	36				2	2					y		
20 ft - 25 ft	GH-823		870-875	383585	420209	6157	7	36										y		
25 ft - 30 ft	GH-823		875-880	383585	420209	6157	7	36										y		
30 ft - 35 ft	GH-823		880-885	383585	420209	6157	7	36										y		
35 ft - 40 ft	GH-823		885-890	383585	420209	6157	7	36				1						y		
0 ft - 5 ft	GH-312		60-65	385598	423206	7142	7	33					1	2			y		
5 ft - 10 ft	GH-312		65-70	385598	423206	7142	7	33				1		1	2			y		
10 ft - 15 ft	GH-312		70-75	385598	423206	7142	7	33				3		1	3					
15 ft - 20 ft Assay_Int	GH-312	78	75-80	385598	423206	7142	7	33	1	14		3	3	1	3					
20 ft - 25 ft	GH-312		80-85	385598	423206	7142	1	14					3							
25 ft - 30 ft	GH-312		85-90	385598	423206	7142	1	14					3							
30 ft - 35 ft	GH-312		90-95	385598	423206	7142	1	14					3							
35 ft - 40 ft	GH-312		95-100	385598	423206	7142	1	14				1	3	1					
0 ft - 5 ft	BB-1208		370-375	384204	402704	7077	7	36						3	3		y			
5 ft - 10 ft	BB-1208		375-380	384204	402704	7077	7	36				1		2	2					y

Quartz_Veins	Veining_Intensity	Rock_Stain	Lithology_2_Stain	Realgar_Min	Barite	Orpiment_Min	Pyrite_Min	Stibnite_Min	Wavy_bedding	Phosphate_Lenses	Stiolites	Structure_Zone_Present	Breccia	Color_Onlythe_5ft	Comments
y	2	b		n	n	n	n	n	n	n	n	n	n		Rock still scratches and rxn is weak when scratched
y	1	b		n	n	n	n	n	n	n	n	n	n		Dolomite veins seem to be with the milky quartz veins
y	3	b		n	n	y	n	n	n	n	n	n	n		There appears to be minor clay formation and the rock looks less competent.
y	5	b		n	n	n	n	n	n	n	n	n	n		Leaving steal on the rock, very minor milky quartz veining.
y	5	n		n	n	n	n	n	n	n	n	n	n		There seems to be very minor brecciation present associated with veining.
y	5	n		n	n	n	n	n	n	n	n	n	y		
y	10	n		n	n	n	n	n	n	n	n	n	n		
	7	p		n	n	n	n	n	n	n	n	n	n		
	2	b		n	n	n	n	n	n	y	n	n	n		Rxn hesitant, stain slightly blue.
	1	b		n	n	y	n	n	n	y	n	n	n		
	3	b		n	n	n	n	n	n	n	n	n	y		
y	1	b		n	n	n	n	n	n	n	n	n	n		
y	3	n		n	n	n	n	n	n	n	n	n	y		
y	15	n	b	n	n	n	n	n	n	n	n	n	y		from 455-465 it is a mix of dolomitized SOHC2 (coarse grained limestone) and brecciated silicified SOHC1
y	30	n	b	n	n	n	n	n	n	n	n	n	y		
	10	p		n	n	n	n	n	n	n	n	n	n		
	0	b		n	n	n	n	n	n	n	n	n	n		Clay present hesitant moderate rxn
	0	b		n	n	n	n	n	n	n	n	n	n		
	1	b		n	n	n	n	n	n	n	n	n	n		More reactive with hall, less clay present
	1	b		n	n	n	n	n	n	n	n	n	n		
	3	b		n	n	n	n	n	n	n	n	n	n		
	7	b		n	n	y	n	n	n	n	n	n	n		
	2	b		n	n	n	n	n	n	n	n	n	n		
	7	b		n	n	n	n	n	n	n	n	n	n		Minor clay formation
	1	p		n	n	n	n	n	n	n	n	n	n		Roberts is more sandy looking here, fine grained with fine laminations and still calcareous though rxn is not as strong as usual.
	2	p		n	n	n	n	n	n	n	n	n	n		Minor clay formation
	2	p		n	n	n	n	n	n	n	n	n	n		Lots of clay no rxn w/HALL
y	5	p	n	n	y	n	n	n	n	n	n	n	y		
y	3	n		n	n	n	n	n	n	n	n	n	y		
y	2	n		n	n	n	n	n	n	n	n	n	y		
y	3	n		n	n	y	y	n	n	n	n	n	y		
y	10	n		n	n	n	n	n	n	n	n	y	y		SOHC1 is really shattered here with clay formation here called decal. I assume this is a fault zone
y	1	b		n	n	y	n	n	n	n	n	n	n		Slight rxn when scratched. Finely planar laminated gray calc siltstone.
	1	n		n	n	y	n	n	n	n	n	n	n		

Appendix 6

Carbonate Staining Solution

For each you need 250 ml of 2% HCl:

60 ml of 10% HCl

190 ml of distilled H_2O

For Potassium ferricyanide:

250 ml of 2% HCl (dilute first)

1.25 g of Potassium ferricyanide

For Alizarine red S:

250 ml of 2% HCl (dilute first)

.3 g of Allizuran red S